

PONTIFICIA UNIVERSIDAD CATÓLICA DEL PERÚ

ESCUELA DE POSGRADO



U-Pb Geochronology of Zircon and Cassiterite from the Taucane Sn-polymetallic project, Puno, Peru

**Tesis para obtener el grado académico de Maestro en Química que
presenta:**

Pablo Ernesto Valverde Rodriguez

Asesor:

Lisard Torró i Abat


Lima, 2026

Informe de Similitud

Yo, Lisard Torr3 i Abat, docente de la Facultad de Ciencias e Ingenier3a de la Pontificia Universidad Cat3lica del Per3, asesor de la tesis titulada "U-Pb Geochronology of Zircon and Cassiterite from the Taucane Sn-polymetallic project, Puno, Peru", del autor Pablo Ernesto Valverde Rodriguez de constancia de lo siguiente:

- El mencionado documento tiene un 3ndice de puntuaci3n de similitud de 12 %. As3 lo consigna el reporte de similitud emitido por el software *Turnitin* el 09/01/2026.
- He revisado con detalle dicho reporte y la Tesis y no se advierten indicios de plagio.
- Las citas a otros autores y sus respectivas referencias cumplen con las pautas acad3micas.

Lugar y fecha: Lima a 9 de enero de 2026

Apellidos y nombre del asesor: Torr3 i Abat, Lisard	
DNI : 49088982	Firma 
ORCID: 0000-0002-3557-8334	

ACKNOWLEDGMENTS

This thesis is not only the result of an academic process, but also reflects significant personal growth. This achievement would not have been possible without the valuable collaboration of numerous persons and institutions.

Firstly, I would like to express my gratitude to God for allowing me to reach this point and for giving me the strength and health to achieve my goals.

To my incredible wife, Yomira Loayza, for her immense love, infinite patience, and consistent support, especially during periods of uncertainty and fatigue.

To my parents, Susana Rodriguez and Pablo Valverde, who have always encouraged my dreams and supported me unconditionally in every aspect of my life.

To my sister and brother-in-law, Paola Valverde and Erick Kukurelo, for their unwavering support in all situations.

To my advisor, Lisard Torró, for his constant guidance, patience, and trust in me, as well as his invaluable friendship. I would also like to thank Luís Ortega and Juan Jaramillo for their support and insightful comments, which allowed me to delve deeper into my thesis and improve its quality.

To Cyril Chelle-Michou, Lorenzo Tavazzani, Dawid Szymanowski, and Sava Markovic, for their immense support during my stay at ETH Zurich.

To the Master's program in Chemistry and the Society for Geology Applied to Mineral Deposits (SGA), for their support to present my research at the 18th SGA Biennial Meeting in Golden, Colorado.

In addition, I would like to extend my gratitude to Minsur S.A. for the support during sampling tasks, especially to Miroslav Kalinaj and Daniel Alayza.

Finally, I would like to thank my friends, who celebrated my achievements, understood my absences, and reminded me of the importance of enjoying the process.

This research was funded by the PI1117 project, granted by PUCP.

RESUMEN

El depósito Taucane, ubicado en el departamento de Puno al sureste de Perú, constituye un descubrimiento singular en el cinturón de estaño de los Andes Centrales. Destaca por ser el primer depósito de Sn-polimetálico en la región que está volumétricamente dominado por cuerpos mineralizados tipo manto. También, por su ubicación geológica dentro del dominio morfoestructural del cinturón de retrocabalgamientos de los Andes Centrales, una zona previamente descartada como prospectiva para depósitos de Sn. El objetivo principal de esta tesis es contextualizar la formación del depósito Taucane dentro de la evolución del cinturón de estaño de los Andes centrales mediante dataciones radiométricas U-Pb de zircón en granitoides y casiterita.

La mineralización polimetálica se manifiesta como mantos y vetas alojadas en rocas sedimentarias mesozoicas. Están compuestas principalmente por sulfuros, con menores proporciones de casiterita (variedad *needle-tin*) y sulfosales que definen tres etapas paragenéticas hipogénicas que denotan una transición de condiciones de baja sulfuración hacia una sulfuración intermedia. Asimismo, se observa una transición proximal-distal de un sistema hidrotermal de skarn y reemplazo de carbonatos (CRD).

La geocronología U-Pb de casiterita y zircón confirman el emplazamiento coetáneo de los granitoides de carácter peraluminoso y la mineralización a ca. 24 Ma. Estas edades contextualizan la mineralización de Taucane dentro del evento metalogénico Oligoceno terminal-Mioceno del cinturón de estaño de los Andes Centrales. El descubrimiento de Taucane dentro del cinturón de retrocabalgamientos de los Andes Centrales representa un cambio de paradigma significativo en la exploración de Sn en el sur de Perú, incrementando significativamente las áreas prospectivas.

ABSTRACT

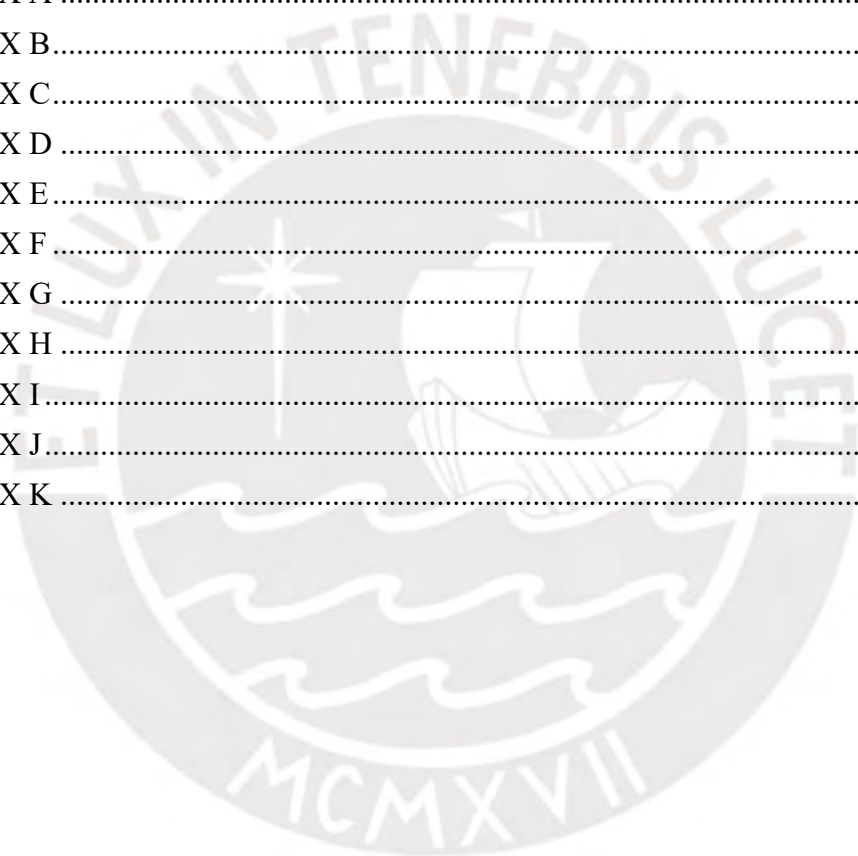
The Taucane deposit, located in the department of Puno in southeastern Peru, constitutes a singular discovery in the Central Andean Tin Belt. It stands out as the first Sn(-polymetallic) deposit in the region that is volumetrically dominated by manto-type orebodies. It is also notable for its geological location within the Central Andean Backthrust Belt morphostructural domain, an area previously ruled out as prospective for Sn deposits. The main objective of this thesis is to contextualize the formation of the Taucane deposit within the evolution of the Central Andes Tin Belt using U-Pb radiometric dating of zircon in granitoids and cassiterite.

Polymetallic mineralization occurs as mantos and veins hosted in Mesozoic sedimentary rocks. They are mainly composed of sulfides, with minor proportions of cassiterite (var. needle-tin) and sulfosalts that define three hypogenic paragenetic stages denoting a transition from low- to intermediate-sulfidation conditions. Likewise, a proximal-distal transition of a skarn and carbonate replacement hydrothermal system (CRD) is observed. U-Pb geochronology of cassiterite and zircon confirms the contemporaneous emplacement of peraluminous granitoids and mineralization at ca. 24 Ma. These ages contextualize the Taucane mineralization within the latest Oligocene-Miocene metallogenic event of the Central Andean Tin Belt. The discovery of Taucane within the Central Andean Backthrust Belt represents a significant paradigm shift in Sn exploration in southern Peru, significantly increasing the prospective areas.

Table of Contents

1. INTRODUCTION	11
1.1. Cassiterite: Tin ore and geologic clock	11
1.2. The Central Andean Tin Belt: Three countries and one major province	14
1.3. The Taucane Project	17
1.4. Conundrum	19
1.5. Objectives	19
1.6. Hypothesis	20
1.7. Justification.....	21
2. METHODOLOGY	21
2.1. Sampling.....	21
2.2. Analytical methods	22
2.2.1. Optical microscopy.....	22
2.2.2. Whole-rock chemical analysis.....	22
2.2.3. Scanning electron microscopy (SEM-EDS).....	24
2.2.4. Electron microprobe (EPMA)	24
2.2.5. LA-ICP-SF-MS: Zircon and cassiterite trace element analysis and dating	26
3. GEOLOGICAL SETTING.....	28
3.1. Geology of the Central Andes in southern Peru	28
3.2. Geology of the Central Andean Tin Belt.....	36
3.3. Geology of the Taucane Project	40
4. RESULTS.....	49
4.1. Petrography.....	49
4.1.1. Intrusive rocks	49
4.1.1.1. Monzogranite.....	49
4.1.1.2. Quartz-monzodiorite.....	52
4.1.1.3. Monzodiorite	54
4.1.1.4. Minette.....	56
4.1.2. Ore samples	58
4.1.2.1. Kelly System	58
4.1.2.2. Lorena System	61
4.2. Whole-rock element geochemistry.....	64
4.3. Cassiterite mineral geochemistry.....	72
4.3.1. Major and minor elements.....	72
4.3.2. Trace elements.....	72
4.3.3. Cassiterite U-Pb dating.....	83

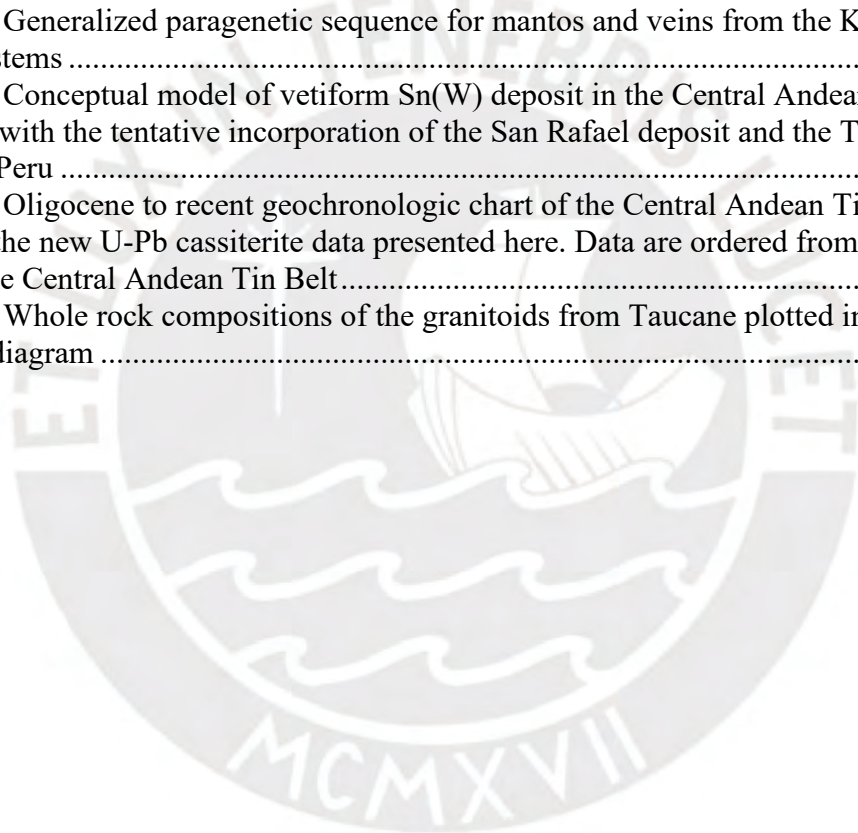
4.4.	Zircon mineral geochemistry.....	84
4.4.1.	Zircon U-Pb dating.....	84
4.4.2.	Trace elements.....	86
5.	DISCUSSION.....	90
5.1.	Kelly vs Lorena systems: exploration constraints.....	90
5.2.	Mineralization style and comparison with other Sn(-polymetallic) deposits.....	93
5.3.	Age of the mineralization and relationship with intrusive rocks.....	98
5.4.	Tin: new horizons for exploration in southern Peru.....	104
6.	CONCLUSIONS.....	105
7.	REFERENCES.....	107
	APPENDIX A.....	125
	APPENDIX B.....	131
	APPENDIX C.....	150
	APPENDIX D.....	173
	APPENDIX E.....	178
	APPENDIX F.....	210
	APPENDIX G.....	223
	APPENDIX H.....	233
	APPENDIX I.....	250
	APPENDIX J.....	289
	APPENDIX K.....	293



List of Figures

Figure 1: Main deposits located within the Central Andean Tin Belt. The thin white arrows indicate the migration of mineralized centers with time in the Central Andean Tin Belt.....	15
Figure 2: Location map of the Taucane project.....	18
Figure 3: "Zeiss Primotech" microscope at the Laboratory of Geology of the Pontificia Universidad Católica del Perú	22
Figure 4: Quanta 650 FEI environmental scanning electron microscope (SEM) at Centro de Caracterización de Materiales (CAM) of the Pontificia Universidad Católica del Perú	24
Figure 5: Electron microprobe equipment available at the Scientific and Technological Centers of the University of Barcelona, Spain	25
Figure 6: Thermo Scientific Element XR device with Laurin Technic S-155 ablation plate at ETH Zurich (Switzerland)	28
Figure 7: Morphostructural domains of the Eastern Cordillera in southern Peru	35
Figure 8: Location of Taucane exploration concessions in regional geologic map with morphostructural domains in the Eastern Cordillera of the Andes in southeastern Peru.	41
Figure 9: Location of Taucane Project in local geologic map.....	42
Figure 10: Geologic map of the Taucane project according to detailed mapping performed by MINSUR S.A. including the location of the studied samples and drill cores.....	44
Figure 11: Preliminary exploration model of the Taucane mineralization system including veins and mantos of the Lorena and Kelly hosted by the Jurassic-Cretaceous sedimentary rocks, and potentially, veins extending to older sedimentary units	45
Figure 12: General aspect of the mineralization in the Kelly system.....	47
Figure 13: General aspect of the mineralization in the Lorena system	48
Figure 14: Intrusive rocks in the Taucane area.....	49
Figure 15: Representative transmitted-light images of monzogranite (sample TC-23-01)	51
Figure 16: Representative transmitted-light images of quartz-monzodiorite (sample TC-23-02)	53
Figure 17: Representative transmitted-light images of monzodiorite (sample TC-23-04).	55
Figure 18: Representative transmitted-light images of minette (sample TC-23-03).....	57
Figure 19: Photomicrographs of polymetallic mineralization in veins and mantos from the Kelly system	60
Figure 20: Generalized paragenetic sequence for orebodies in the Kelly System	61
Figure 21: Photomicrographs of the polymetallic mineralization in veins and mantos from the Lorena System	63
Figure 22: Generalized paragenetic sequence for orebodies in the Lorena System.....	64
Figure 23: Harker diagrams of major and minor oxides from Taucane	65
Figure 24: Geochemical diagrams for intrusive rocks from the Taucane Project.....	68
Figure 25: Normalized multi-element diagrams of major and trace elements in intrusive rocks from Taucane	69
Figure 26: Binary diagrams of major element oxides for the Taucane minette	70
Figure 27: Normalized multi-element diagrams of major and trace elements in minette from Taucane.....	71

Figure 28: Binary SnO ₂ vs FeO correlation diagram for cassiterite from Taucane (EMPA data).....	73
Figure 29: Selected box plots showing element contents in cassiterite from Taucane (LA-ICP-SF-MS data)	79
Figure 30: Correlation binary plots for cassiterite from Taucane	81
Figure 31: REE spider diagrams normalized to C1 chondrite values.....	82
Figure 32: Rare earth element contents normalized to C1 chondrite values	83
Figure 33: Results of in situ U-Pb isotope analyses of cassiterite.....	84
Figure 34: CL images of representative zircon grains from granitoids in the Taucane Project.....	85
Figure 35: Zircon U–Pb concordia diagrams and weighted mean model ages for Taucane granitoids.....	86
Figure 36: REE contents of zircon from Taucane normalized to Chondrite C1 values .	87
Figure 37: Binary diagrams of trace elements and derived parameters for zircon grains from Taucane.....	90
Figure 38: Generalized paragenetic sequence for mantos and veins from the Kelly and Lorena systems	92
Figure 39: Conceptual model of vetiform Sn(W) deposit in the Central Andean Tin Belt in Bolivia with the tentative incorporation of the San Rafael deposit and the Taucane Project in Peru	94
Figure 40: Oligocene to recent geochronologic chart of the Central Andean Tin Belt, including the new U-Pb cassiterite data presented here. Data are ordered from north to south of the Central Andean Tin Belt.....	99
Figure 41: Whole rock compositions of the granitoids from Taucane plotted in the Zr/Hf vs Nb/Ta diagram	101



List of Tables

Table 1: Detection limits for each major and minor oxide.....	26
Table 2: Major and trace element contents.....	66
Table 3: Major and minor element contents of cassiterite from Taucane (EPMA data) 72	
Table 4: Trace element contents of cassiterite from Taucane (LA-ICP-MS data).....	75



1. INTRODUCTION

1.1. Cassiterite: Tin ore and geologic clock

Tin (Sn) is one of the earliest metals to have been utilized by humanity. It is used in the production of sheet metal, cans, containers, and alloys, as well as for brazing and polishing (Kamilli et al. 2017; Haldar 2020). Of particular importance nowadays are indium-tin oxide (ITO) alloys, which are essential in digital technologies such as touchscreens and in green technologies such as photovoltaic panels (Bashar 1998; Aydın and Sezgintürk 2017). Cassiterite, a tin oxide mineral (SnO_2) of the rutile group with a tetragonal lattice structure (Farmer et al. 1991; Kamilli et al. 2017; Haldar 2020), is the principal tin ore (Bowles 2020; Haldar 2020).

Cassiterite can be found in a variety of mineral deposit types with vastly different paragenetic assemblages (Bennett et al. 2024), including:

- **Placer tin deposits:** These deposits have been an important source of tin, accounting for approximately 70% of world cassiterite concentrate production in 2012 (Kamilli et al. 2017). Cassiterite, being heavy and chemically inert, tends to concentrate in residual deposits, in which erosion and weathering processes remove lighter rock material (Lehmann 2021). A classic example is the Kinta Valley in Malaysia (Ingham and Bradford 1960).
- **Granite-related tin deposits:** These represent a significant source of tin (Kamilli et al. 2017). Tin granites have a distinctive chemical composition, which is enriched in certain elements, such as Rb, Cs, Li, and depleted in Sr, Eu, and Ba (Lehmann 1990a; Kamilli et al. 2017), and anomalous textures including unidirectional solidification textures (UST), graphic intergrowths,

and pegmatitic dykes (Kamilli et al. 2017). Granite-related tin deposits can be classified as:

- Stanniferous pegmatites (e.g., Jabal Silsilah, Saudi Arabia, Kamilli and Criss 1996);
- Quartz-cassiterite and sulfide-cassiterite, epithermal/mesothermal veins, lodes, stockworks, and greisen (e.g., Geevor and Wheal Jane, United Kingdom, Dines 1956; Herberton, Australia, Blake and Smith 1970; Chorolque, Bolivia, Sillitoe et al. 1975; San Rafael, Peru, Kontak and Clark 2002); and
- Skarn and carbonate-sulfide replacement deposits (e.g., Cuomolong, China, Hou et al. 2007; Ayawilca, Peru, Benites et al. 2022).

It is common that single deposits or districts host several of these mineralization styles (e.g., greisen, skarn, and veins in the Geyer tin deposit, Erzgebirge, Germany; Meyer et al. 2024).

Cassiterite can incorporate a wide range of minor and trace elements within its structure that substitute for Sn, including Fe, Ti, Mn, Al, Nb, Ta, U, Be, Li, and rare earth elements (REE; Cheng et al. 2019; Gemmrich et al. 2021; Bennett et al. 2024). Among these elements, depending on their charge, ionic radius, and coordination of ions compared to Sn^{4+} , the following cations are considered compatible: Al^{3+} , Fe^{3+} , Ga^{3+} , V^{3+} , Cr^{3+} , Sc^{3+} , Sb^{3+} , W^{4+} , U^{4+} , Zr^{4+} , Hf^{4+} , Ti^{4+} , Nb^{5+} , and Ta^{5+} (Cheng et al. 2019; Mao et al. 2020). Cations similarly charged to Sn can be substituted directly (e.g., $\text{Sn}^{4+} \rightleftharpoons \text{Ti}^{4+}$); otherwise, coupled substitution mechanisms are required (Bennett et al. 2024).

Due to the refractory nature of cassiterite, this mineral can preserve primary information on the physical-chemical characteristics of ore-forming fluids from which they

crystallized (Jiang et al. 2004; Mao et al. 2020). Thus, cassiterite associated with high-temperature systems has higher Nb, Ta, and Zr contents and lower Fe and Mn contents compared to cassiterite associated with lower-temperature systems (Zhang et al. 2017). The Ti/Zr and Ti/Sc ratios in cassiterite decrease from locations proximal to the causative intrusion to those distal to it, and thus can be used as a vector to magmatic-hydrothermal centers (Gemrich et al. 2021). On the other hand, the isotopic composition of oxygen (O), hafnium (Hf), and tin (Sn) in cassiterite can provide information about the formation conditions of Sn deposits, such as the origin, composition, and evolution of fluids (e.g., Yamazaki et al. 2014; Kendall-Langley et al. 2020; Wang et al. 2021; Li et al. 2022; Yang et al. 2022, 2023; Zhou et al. 2022; Wu et al. 2023).

Cassiterite typically incorporates more U^{4+} than Pb^{2+} , which makes it a suitable mineral for U-Pb dating and the most robust and reliable geochronometer for Sn mineralized systems (Neymark et al. 2018 and references therein). Recent developments allow for the high-precision and accuracy dating of cassiterite through Isotope Dilution Thermal Ionization Mass Spectrometry (ID-TIMS) and Laser Ablation Inductively Coupled Plasma Mass Spectrometry (LA-ICP-MS; e.g., Cao et al. 2017; Cheng et al. 2019; Carr et al. 2020; Gemrich et al. 2021; Leopaldi et al. 2024). For example, the ID-TIMS method was applied to measure the U-Pb isotopic compositions of cassiterite from the Yankee deposit of the Mole Granite (Eastern Australia) and yielded a date of 246.48 ± 0.51 Ma, which is consistent with the range of a previously published ID-TIMS U-Pb date of hydrothermal xenotime from the area (Carr et al. 2020). On the other hand, the geochronology in cassiterite has been useful for the study of complex tin ore deposits as the case of the Sadisdorf Sn-Li-(W-Cu) deposit. It is located in the eastern Erzgebirge region of Germany and exhibits two distinct styles of mineralization (Leopaldi et al. 2024). To investigate whether these two types of mineralization were temporally linked,

Leopaldi et al. (2024) conducted LA-ICP-MS analyses. The authors concluded that, since all analyzed samples yielded a narrow range of dates (315.1 ± 3.3 Ma to 311.0 ± 4.0 Ma) that overlap each other considering the analytical error, the mineralization was associated with the same magmatic-hydrothermal event.

The chemical composition and U-Pb dates of cassiterite from tin deposits situated along the Central Andean Tin Belt have been investigated recently. Cassiterite from nine Bolivian deposits/districts was investigated through LA-ICP-sector field (SF)-MS for trace elements and U-Pb dating by Gemmrich et al. (2021). These authors determined the following U-Pb cassiterite dates: 218.3 ± 5.5 Ma (Kellhuani), 24.4 ± 0.4 Ma (Viloco), 24.0 ± 2.4 Ma (Huanuni), and 24.0 ± 5.1 Ma (Llallagua). Using the same methodology, Harlaux et al. (2023) and Markovic et al. (2025) obtained U-Pb cassiterite dates ranging from 24.43 ± 0.32 to 23.47 ± 0.53 Ma in the San Rafael deposit in SE Peru.

1.2. The Central Andean Tin Belt: Three countries and one major province

The Central Andean Tin Belt is a metallogenic province extending over 1,000 km between $\sim 14^\circ$ S and 23° S from southeastern Peru, across Bolivia, to northern Argentina (Fig. 1; Sillitoe et al. 1975; Grant et al. 1979; Mlynarczyk and Williams-Jones 2005; Fontboté 2018). This belt has historically accounted for 13% of global Sn supply (USGS 2025) and hosts hundreds of Sn-W-Ag-polymetallic deposits, occurrences, and mineral showings.

Tin mining in this region has historically been a significant economic activity, with evidence of its occurrence for millennia prior to colonial contact (Cooke et al. 2008). Nevertheless, mining reached its zenith during the colonial era, specifically in the 16th century, when the Spanish discovered the Ag-rich deposits of Cerro Rico de Potosí (Fig. 1). The discovery laid the foundations for the economic growth of the Spanish empire

and, subsequently, of Bolivia (Arce-Burgoa and Goldfarb 2009). In the early 1900s, large tin deposits were discovered, replacing silver as the most valuable metal in the Bolivian economy, a situation that persisted until the collapse of the tin market in 1985 (Arce-Burgoa and Goldfarb 2009). These large deposits were chiefly exploited by the so-called tin barons (Simón I. Patiño, Carlos Víctor Aramayo, and Mauricio Hochschild) until 1952, when the mines were nationalized (Claure 1986).

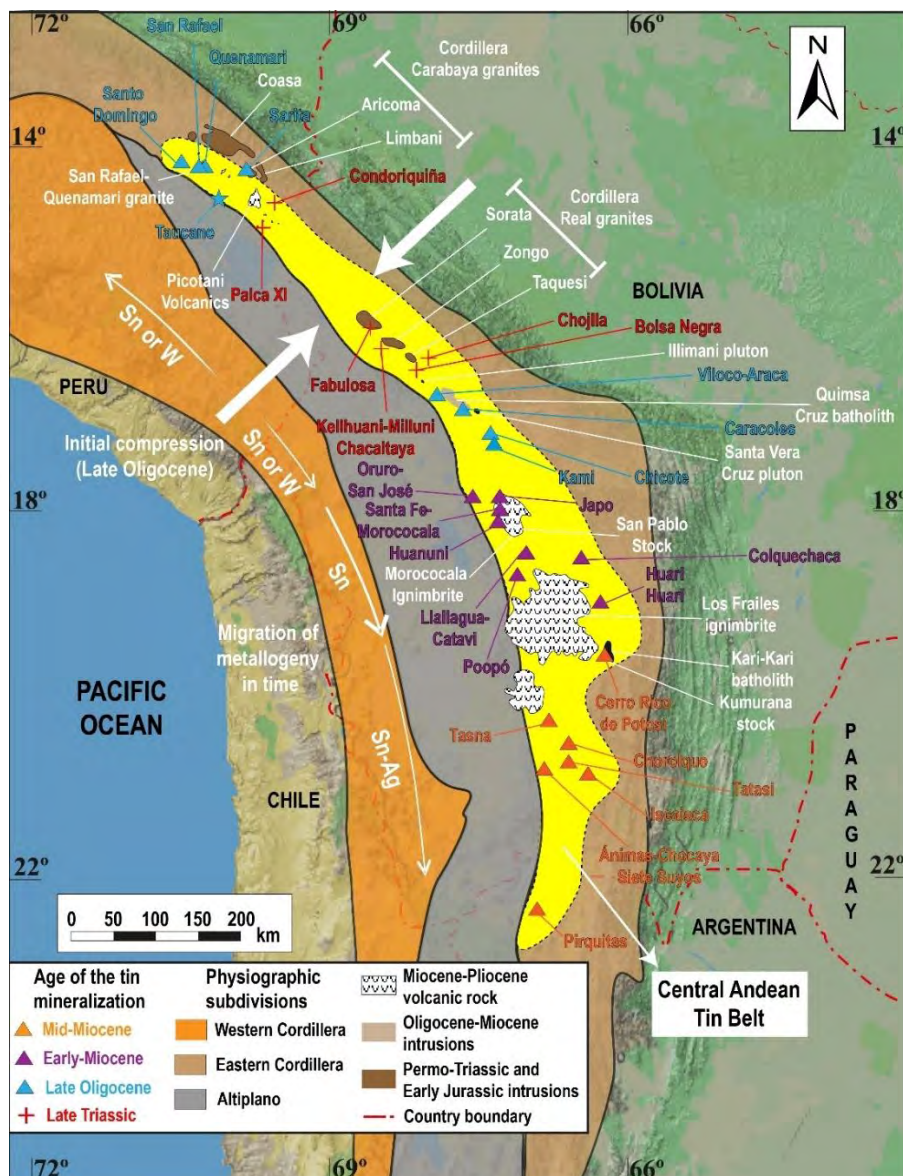


Figure 1. Main deposits located within the Central Andean Tin Belt. The thin white arrows indicate the migration of mineralized centers with time in the Central Andean Tin Belt. The thick white arrows indicate the direction of compression in the late Oligocene. Modified from Sandeman et al. (1995), Mlynarczyk and Williams-Jones (2005), Fontboté (2018), and Gemmrich et al. (2021)

Historically, Bolivia was one of the largest tin producers for much of the 20th century, with mining as the country's principal industry (Arce-Burgoa and Goldfarb 2009). Upon the discovery of the majority of large tin deposits in Bolivia, estimates indicate that >8% of the world's tin reserves are located within this country (USGS 2020). Bolivia's annual tin production has remained relatively constant from 2018 to 2024, in the range between 16,900 and 21,000 t (USGS 2020, 2025). Peru accounted for 12% of global tin production in 2024 from a single active deposit, San Rafael, and exhibited an increase in production from 26,200 t in 2023 to 31,000 t in 2024. Likewise, the current reserves of Bolivia and Peru exceed 0.5 Mt (USGS 2025), thus ensuring future production continuity.

The San Rafael deposit was discovered in 1913, when a Chilean-German company identified Cu mineralization on the slopes of the Quenamari hill. This was later confirmed by Rafael Avendaño, who traced a Cu deposit, hence the name of the San Rafael lode (Arenas 1999). In 1958, Lampa Mining Co. began extracting high-grade copper from the surface. This copper was then used to blend with copper-silver ores from nearby deposits. In 1966, W.R. Grace & Co. acquired a 67% stake in Lampa Mining Co. and formed Minsur Sociedad de Responsabilidad Ltda., which operated the deposit until 1977, when the Brescia Group purchased the entire company and assumed 100% ownership of San Rafael, operating it under the name Minsur S.A. During the initial period, mining operations were concentrated on the shallow Cu ore, as the underlying Sn mineralization was not discovered until 1980 (Arenas 1999; Mlynarczyk et al. 2003). Through exploration work, large ore bodies (lodes) with Sn grades up to 15 wt.% were identified (Mlynarczyk et al. 2003). The San Rafael deposit is predominantly hosted by the San Rafael Intrusive Complex, emplaced at ca. 24 Ma (Kontak and Clark 2002; Harlaux et al. 2021). Harlaux et al. (2023) have constrained the main stage of Sn mineralization at San Rafael to the interval 24.10 ± 0.37 to 23.47 ± 0.53 Ma.

Beyond the world-class San Rafael deposit, exploration in the Peruvian segment of the Central Andes tin belt has led to the discovery of dozens of Sn(-W-polymetallic) deposits and occurrences, including Nazareth, Santo Domingo, Jesica, San Jose, Ocuara, Condoriquiña, Quenamari, Sarita, and Palca XI. The Nazareth Sn-Cu deposit, which is located 6 km NE of the San Rafael mine, is also hosted by the San Rafael Intrusive Complex and has current total resources of 157,111 t of fine tin (Villón 2025). The Santo Domingo Sn-Cu (Pb-Zn-Ag) deposit is located 24 km NW of the San Rafael mine in the Carabaya Province (Acosta et al. 2011; Sánchez 2016). K-Ar dates on biotite from Santo Domingo range from 23.1 ± 0.2 Ma to 27.1 ± 1.0 Ma (Clark et al. 1990). The Sarita W-Sn (Mo-Cu) deposit is located in the northern sector of the Aricoma pluton, associated with the Carabaya Batholith. The dates of the deposit, as determined by K-Ar biotite analyses, range from 187.11 ± 1.18 Ma to 194.1 ± 3.9 Ma (Clark et al. 1990; Acosta et al. 2011). The Palca XI W (Cu-Zn-Ag-Sn) deposit is situated in the Choquene district, near the southern limit of the Precordillera de Carabaya. The obtained $^{40}\text{Ar}/^{39}\text{Ar}$ biotite dates range from ca. 24 to 25 Ma (Clark et al. 1990).

1.3. The Taucane Project

The Taucane project is situated in the San José district of the Azángaro Province in the Puno Department, ~35 km to the southeast of the San Rafael Mine (Fig. 2; Alayza 2016). The deposit was discovered by Minsur in 2014 and represents the first documented occurrence of Sn-rich manto-type mineralization in southern Peru, hosted in Mesozoic sedimentary rocks and containing Ag-Pb-Zn (Alayza 2016; Arias 2023). From a geological perspective, the area is located within the belt of Sn-Cu-W deposits associated with Oligocene-Miocene intrusive events as defined in Carlotto et al. (2009). Taucane lies within the Putina Fold-Thrust Belt, also referred to as the Mesozoic block, due to the predominance of Mesozoic-age of the exposed rocks. This structural domain is part of

the Central Andean Backthrust Belt. Specifically, Taucane is situated near the northern boundary of the Mesozoic block, adjacent to the Macusani Structural Zone (Perez et al. 2016a; Arias 2023), formerly known as the Precordillera de Carabaya (Laubacher 1978). This is a differential fact of Taucane with regard to other Sn systems in SE Peru, such as San Rafael and Santo Domingo, which are situated in the Macusani Structural Zone and hosted by Paleozoic (meta)sedimentary rocks (Alayza 2016).

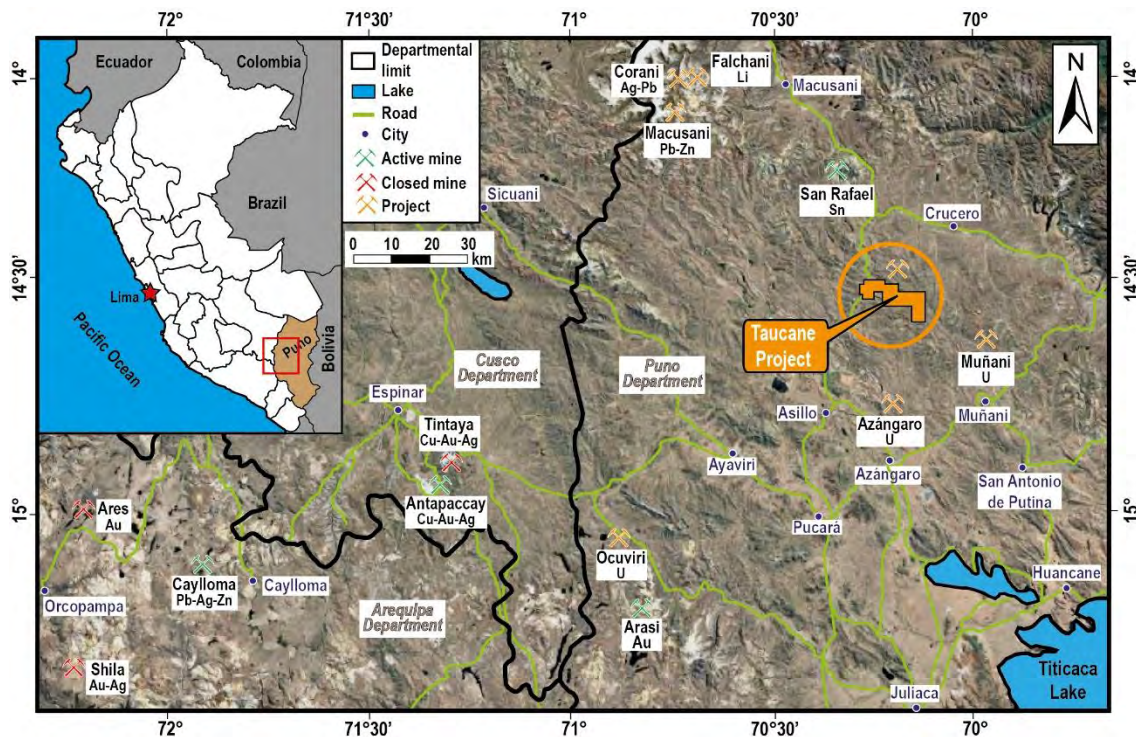


Figure 2. Location map of the Taucane project. Modified from Alayza (2016)

There is evidence of artisanal mining activity in the area, as identified by Minsur during geological reconnaissance work in 2007. In 2008, Minsur conducted a diamond-drilling campaign that intersected mineralized structures, including mantos with prospective Ag, Pb, and Zn contents (Alayza 2016). Subsequently, mineralized structures containing Ag, Pb, Zn, and Sn were also identified at the surface (Alayza 2016; Arias 2023).

There are a few available studies on Taucane. Alayza (2016) and Alayza et al. (2017) produced a local predictive geological model for the Taucane project based on surface

geological mapping, drill core data, geophysics, petromineralogical studies, rock geochemistry, and spectroscopy on alteration minerals. Subsequently, Arias (2023) characterized the mineralogy of the Pb, Zn, Ag, and Sn ore in the Lorena vein.

1.4. Conundrum

The world-class San Rafael deposit in Puno is the only mine currently producing tin in Peru. In addition, other deposits and occurrences are known nearby, and there is a high probability for new discoveries along the Central Andean Tin Belt in Peru. One of the most recently discovered Sn occurrences in the area is Taucane. This prospect is of particular interest since, unlike the other known Sn deposits and occurrences in the area located within the Macusani Structural Zone, Taucane is situated within the contiguous Central Andean Backthrust Belt morphostructural domain. This ushers in the possibility of expanding exploration for Sn south of the Macusani Structural Zone in Mesozoic host rocks. On the other hand, previous descriptions of Taucane mineralization refer the occurrence of Sn as manto-type mineralization, which is a novel mineralization style for Sn in the Peruvian segment of the Central Andean Tin Belt. Despite its strategic interest, few detailed studies on Taucane are available (Alayza 2016; Arias 2023), and the ages of the tin mineralization and associated intrusive units remain unknown.

1.5. Objectives

Main objective

- To contextualize the formation of the Taucane Sn-polymetallic deposit within the evolution of the Central Andean Tin Belt.

Specific objectives

- To petrographically and geochemically characterize the intrusive units spatially related to the tin mineralization;
- To document the textural varieties and paragenetic generations of cassiterite and their contextualization within complete paragenetic sequences in order to delineate tin mineralization events;
- To analyze the composition in terms of major, minor, and trace elements of cassiterite;
- To date cassiterite from mineralized structures and zircon grains from cospatial intrusive units through U-Pb;
- To integrate the new dates within the metallogenic evolution of the Central Andean Tin Belt and, in general, within the tectonic and magmatic evolution of the Central Andes;
- To constrain prospective geological features for the exploration of Sn mineralization along the Central Andean Backthrust Belt in SE Peru.

1.6. Hypothesis

The age of the Sn-polymetallic mineralization at Taucane is probably equivalent or similar to that of other tin deposits and occurrences found in the extension of the Central Andean Tin Belt into Peru, such as San Rafael (ca. 24 Ma) and Santo Domingo (ca. 23-27 Ma; Clark et al. 1990; Harlaux et al. 2020, 2021, 2023). Accordingly, the tin mineralization in the Taucane prospect would have formed during the Oligocene-Miocene metallogenic event recorded along the Central Andean Tin Belt (Mlynarczyk and Williams-Jones 2005; Gemmrich et al. 2021). This ascription is further supported by the fact that the Taucane mineralization is hosted by Jurassic-Cretaceous rocks of the

Mesozoic block of the Central Andean Backthrust Belt, which rules out that it was formed during the previous, Triassic metallogenic event recorded in this metalliferous belt (Fig. 1). Finally, it is plausible that cassiterite from the Taucane prospect exhibits similar trace element signatures (e.g., Nb, Ta, In, Ge, and Ga) as cassiterite from other Oligocene-Miocene Sn deposits of the Central Andean Tin Belt.

1.7. Justification

Tin has a multitude of applications, including the production of cans, containers, construction materials, and solder, as well as being a critical metal in the manufacture of digital and green technologies in the form of ITO alloys (Aydın and Sezgintürk 2017; Kamilli et al. 2017). Consequently, the search for new tin deposits is essential. Situated within the “Mesozoic block” in the Central Andean Backthrust Belt, the Taucane prospect emerges as a notable anomaly relative to the other known Sn deposits in the region (e.g., San Rafael, Santo Domingo), which are systematically located in the Paleozoic block within the Macusani Structural Zone. Therefore, the sole occurrence and documentation of the Taucane mineralization may constitute a major step forward towards enhanced exploration for tin in new geologic domains that were previously discarded as prospective for this metal.

2. METHODOLOGY

2.1. Sampling

A total of 35 samples were collected, including 23 drillhole and 12 surface samples. Of the surface samples, four are representative of the intrusive units exposed in the area, and the remaining eight are mineralized samples. In addition, the drillhole samples are associated with the main mineralized systems at Taucane, including the Lorena (n = 20) and Kelly (n = 10) systems. A list of the studied samples, their coordinates, and brief field

descriptions is provided in Appendix A. The photographs of the samples are provided in Appendix B.

2.2. Analytical methods

2.2.1. Petrography

The petrographic study of the collected samples was conducted on thin and thick polished sections. Thick polished sections ($n = 32$) of mineralized samples were prepared at the QEMSCAN Laboratory of the Pontificia Universidad Católica del Perú (PUCP), and the thin polished sections ($n = 4$) of intrusive rock samples were prepared at the Department of Earth and Planetary Sciences of the ETH Zurich. These sections were examined using a Zeiss Primotech microscope with transmitted and reflected light, equipped with a digital camera, which is available at the Laboratory of microscopy at PUCP (Fig. 3). Individual petrographic descriptions of the thick sections are presented in Appendix C.



Figure 3. "Zeiss Primotech" microscope at the Laboratory of Geology of the Pontificia Universidad Católica del Perú

2.2.2. Whole-rock geochemical analysis

The bulk chemical compositions of the four intrusive samples were determined. The rocks were cut in order to remove weathered parts, then crushed and ground to fine-grained

homogeneous powder in an agate mill. Loss on ignition (LOI) was determined at 1,050 °C on the powder material, which was then melted in a 1:5 ratio with lithium tetraborate ($\text{Li}_2\text{B}_4\text{O}_7$) into homogeneous glass discs at 1,080 °C. The major and minor elements were then determined using a PANalytical AXIOS wavelength-dispersive X-ray fluorescence (WD-XRF) spectrometer, operating at 2.4 kV, at ETH Zurich. Trace element contents were determined in the same fused beads used for XRF analyses by means of LA-ICP-MS with an Excimer 193 nm (ArF) GeoLas (Coherent) laser system coupled to an ELAN 6100 DRC quadrupole mass spectrometer at ETH Zürich. Measurements were conducted at a laser repetition rate of 10 Hz and a laser energy density of $\sim 10 \text{ J/cm}^2$ on the sample surface. The ablation aerosol was mixed in the in-house-built ablation cell with carrier gas consisting of helium ($\sim 1 \text{ L/min}$). The ablated aerosol was then mixed with argon make-up gas and homogenized by flushing through an in-house built squid device before introduction into the plasma torch. An analytical scheme of 30 seconds recording of gas blank, and 40 seconds of target ablation was implemented following the standard sample bracketing procedure. Synthetic glass NIST SRM610 (Jochum et al. 2011) was analyzed every 15 unknowns with a spot size of $40 \mu\text{m}$ and used as primary reference material for normalization and instrumental drift correction. The fluxer blank was ablated using a spot size of $110 \mu\text{m}$ to correct for matrix effects on the glass beads. The secondary standard USGS BCR-2 (Raczek et al. 2001) was also analyzed with a spot size of $110 \mu\text{m}$ to test the accuracy and reproducibility of the analysis (2–10 % depending on the element). Three individual measurements per sample were made following the same parameters as for blanks and secondary standards. Data reduction was carried out in the MATLAB-based SILLS program (Guillong et al. 2008). The SiO_2 contents from XRF measurements were used as an internal standard to convert raw counts to contents.

2.2.3. Scanning electron microscopy (SEM-EDS)

Microtextures and mineral composition semi-quantification were analyzed using a Quanta 650 scanning electron microscope with energy analyzer (SEM-EDS) from FEI, equipped with an Octane Pro EDS detector from AMETEK at the Centro de Caracterización de Materiales (CAM-PUCP; Fig. 4). In addition, the internal textures of zircon grains were characterized by cathodoluminescence (CL) imaging on a JEOL JSM-6390 scanning electron microscope (SEM) at the Institute of Geochemistry and Petrology, ETH Zurich.



Figure 4. Quanta 650 FEI environmental scanning electron microscope (SEM) at Centro de Caracterización de Materiales (CAM) of the Pontificia Universidad Católica del Perú

2.2.4. Electron microprobe (EPMA)

Major and minor element contents in cassiterite were measured on thick polished sections using a five-channel JEOL JXA-8230 electron probe microanalyzer (EPMA) at the Scientific and Technological Centers of the University of Barcelona (CCiT-UB; Fig. 5) following a similar procedure as Gemmrich et al. (2021). The analysis areas were delineated based on petrographic criteria. The operating conditions were 20 kV accelerating voltage, a beam current of 20 nA, and a beam diameter of 1 to 5 μm —

depending on grain size, crystal porosity, or microinclusions of other mineral phases. The analytical standards and lines used were ZrO_2 (Zr, $L\alpha$), Nb_2O_5 (Nb, $L\alpha$), SnO_2 (cassiterite, $L\alpha$), FeO (Fe, $K\alpha$), Ta_2O_5 (Ta, $L\alpha$), MnO (rhodonite, $K\alpha$), and TiO_2 (rutile, $K\alpha$). The respective lower limits of detection are shown in Table 1. EPMA data for cassiterite are reported in Appendix D.



Figure 5. Electron microprobe equipment available at the Scientific and Technological Centers of the University of Barcelona, Spain

Table 1. Detection limits for each major and minor oxide

Oxides	wt.%
SnO ₂	0.20
ZrO ₂	0.20
Nb ₂ O ₅	0.20
FeO	0.10
MnO	0.10
TiO ₂	0.10
Ta ₂ O ₅	0.15

2.2.5. LA-ICP-SF-MS: Zircon and cassiterite trace element analysis and dating

The determination of trace element contents in cassiterite was conducted by means of LA-ICP-SF-MS at the Institute of Geochemistry and Petrology at ETH Zürich (Fig. 6) using a similar configuration as the one described in Gemmrich et al. (2021). The analyses were performed on polished sections using an LA-ICP-SF-MS with a 193 nm RESOLUTION S-155 ArF excimer laser system (ASI/Applied Spectra) coupled to an Element XR sector field ICP-MS (Thermo) was used. Analysis conditions included repetition rates of 3 Hz, a laser diameter of 43 μm , and a laser energy intensity on the sample of approximately 3.5 J cm^{-2} . Ablation was conducted in a Laurin Technic S-155 double-volume cell with a constant carrier gas flow of approximately 0.5 L min^{-1} He, 1 L min^{-1} Ar, and 2 mL min^{-1} N₂. The USGS GSD-1G glass (Guillong et al. 2005) was used as the primary reference material for quantifying trace elements and correcting instrumental drift. The Fe contents obtained by EPMA were used as an internal standard. The intensities of masses 113 and 115 were corrected for interferences by subtracting the contribution of ¹¹³Cd and ¹¹⁵Sn, respectively, based on the measured intensities of ¹¹¹Cd and ¹¹⁸Sn and using the natural isotope ratios for Cd and Sn recommended by IUPAC. Analytical reproducibility and precision were verified by repeated measurements of the

homogeneous reference material NIST glass SRM610 (Jochum et al. 2011). The analytical results were processed with the SILLS software (version 1.3.2; Guillong et al. 2008) in Matlab.

For U-Pb cassiterite dating, the measured intensities were further processed offline using the Igor Pro Iolite v2.5 software (Hellstrom et al. 2008) and the VizualAge data reduction scheme (Petrus and Kamber 2012). Background intensities were used to calculate isotope ratios, which were corrected for laser-induced Pb/U fractionation according to Paton et al. (2010) and for instrumental drift using the rutile R10 as a reference material. Due to the high closure temperature for the U-Pb isotope system in cassiterite (~850 °C; Zhang et al. 2011), this date likely corresponds to the formation age of the Sn mineralization. The cassiterite trace element data are reported in Appendix E, and cassiterite isotopic data are presented in Appendix F.

The same analytical equipment was used for U-Pb dating and trace-element analysis on zircon from the intrusive units. Zircon crystals were obtained from the three granitoid samples, while zircon grains could not be separated from the basaltic (minette) sample. Zircon crystals were separated from rock samples by heavy liquid (methylene iodide) gravity separation. The zircon grains selected for analysis were subjected to a thermal annealing process at 900 °C for a period of 48 hours in a muffle furnace. Following this, the zircon grains were handpicked, mounted on epoxy mounts, and polished to expose their central cross-sections. The procedure followed is detailed in Guillong et al. (2014) and Horstwood et al. (2016). Crystallization temperatures were calculated using the Ti-in-zircon thermometer of Ferry and Watson (2007), considering an $a(\text{SiO}_2) = 1$ and an $a(\text{TiO}_2) = 0.7$ (Chelle-Michou et al. 2014), which reflect the presence of magmatic quartz and rutile (Hayden and Watson 2007; Claiborne et al. 2010). Oxygen fugacity ($f\text{O}_2$) was calculated through the oxybarometer calibration of Loucks et al. (2020), which uses the

contents of trace elements such as Ce, U, and Ti. CL-SEM images of the zircons are presented in Appendix G. The zircon isotopic and trace element data are reported in Appendices H and I, respectively.



Figure 6. Thermo Scientific Element XR device with Laurin Technic S-155 ablation plate at ETH Zurich (Switzerland)

3. GEOLOGICAL SETTING

3.1. Geology of the Central Andes in southern Peru

The Andean Cordillera is the Earth's longest mountain range, extending ~ 8,000 km from Venezuela to Patagonia (Wörner et al. 2018a; Kay and Mpodozis 2020). The formation of the Andes involves over 200-million-year history that includes tectonic convergence and subduction of oceanic domains beneath the western margin of the South American continent with periods of flattening and steepening of the subducting slab, uplift related to compressional deformation, collision of oceanic terranes in the northern Andes and of oceanic ridges in the southern Andes, forearc subduction erosion, and removal of the base of the thickened crust by delamination (Horton 2018; Kay and Mpodozis 2020). The Andes are divided into the Northern, Central, and Southern Andes. The Andes exhibit a curvature at the orocline of the Central Andes, also known as the Bolivian Orocline at

~18 °S (Kley 1999; Capitanio et al. 2011). North of the orocline, the Andean ranges trend NW-SE, while south of it the Andes range N-S (Fig. 1).

The Central Andes constitute the highest (up to 6,800 m.a.s.l.), widest (up to 750 km), and thickest (up to 70 km) segment of the Andes and extend about 4,000 km between ~5 and 33°S, i.e., from northern Peru, through Bolivia, to northern Chile and Argentina (Wörner et al. 2018a; Kay and Mpodozis 2020). According to Ramos (2018), the Central Andes are subdivided into three main tectonic segments. The northern segment comprises the Paracas terrane, a Grenvillian-age basement micro-continent that separated from the Amazonian craton during the Ordovician period, developing oceanic crust. The subsequent subduction of this oceanic crust and the collision of the Paracas terrain with the craton led to the formation of the Famatinian arc along the Cordillera de Marañón (Chew et al. 2007, 2016; Ramos 2008, 2018). As a result of this collision, the segment exhibits middle to high-grade metamorphism (Ramos 2018). The central segment constitutes a transitional domain between the Paracas and Arequipa-Antofalla terranes; the boundary between these coincides with the Abancay deflection, defined as a major tectonic feature of the Central Andes (Marocco 1978). The Abancay deflection limits flat subduction to the north and normal subduction to the south, and contains E–W structures that connect southward with NW–SE structures of the Bolivian Orocline (Carlotto 2013). It controlled the emplacement of different igneous rocks in the tectonic inversion of the Andean Structures and in the synorogenic sedimentary basins developed in southern Peru (Carlotto 2013; Ramos 2018). This segment is defined by the partial reactivation of inherited sutures, without the development of a separation comparable to that of the Paracas Terrane (Ramos 2018). Consequently, Ordovician rocks with low- to medium-grade metamorphic facies were preserved, as evidenced by the Cordillera de Vilcabamba (Egeler and de Booy 1961). The southern segment comprises the Arequipa-Antofalla

terrane, a block amalgamated to the Amazonian craton and was only partially detached, unlike the Paracas Terrane (Ramos 2018). Consequently, no Famatinian oceanic crust developed, and the Paleozoic extension resulted in the formation of large retro-arc basins (Bahlburg et al. 2006). These basins preserved sedimentary sequences from the Ordovician to the Devonian periods (Ramos 2018).

At the southern of Peru, the Central Andes comprise the Coastal Forearc, the Western Cordillera, the Altiplano-Puna Plateau, the Eastern Cordillera, the sub-Andean Fold and Thrust Belt, and the Foreland Basins (Fig. 7; Clark et al. 1990; Mišković et al. 2009; Perez et al. 2016a; Wörner et al. 2018a; Kay and Mpodozis 2020). Along the Central Andes, two main magmatic domains are identified: the Main Arc and the Inner Arc, which are distinguished by the nature of the igneous petrochemical assemblage and have played a pivotal role in metallogenesis (Kontak et al. 1984; Clark et al. 1990). The Main Arc domain stretches along the Coast Range and the Western Cordillera. It is distinguished by the presence of volcanic and plutonic igneous rocks, which have been persistently emplaced throughout the Mesozoic and Cenozoic eras (Pitcher et al. 1985, Clark et al. 1990). These rocks experienced a gradual continentward migration from the late Triassic to the Paleogene (Clark et al. 1990). During the middle Oligocene, the main arc migrated toward the trench, associated with crustal thickening and changes in slab geometry (Mamani et al. 2010). During the late Oligocene, large-scale areal expansion occurred, with the arc broadening rather than migrating. This event resulted in the juxtaposition of igneous lithotypes from the Main Arc and the Inner Arc in the Peruvian segment of the Eastern Cordillera, with a combined arc width of approximately 320 to 350 km (Clark et al. 1990). The Inner Arc or rear arc is restricted to the Eastern Cordillera and the eastern margin of the Altiplano-Puna Plateau, which lie over a thick pile of strongly deformed succession of clastic and, to a lesser extent, calcareous Paleozoic (meta)sedimentary rocks

(Clark et al. 1983, 1990; Kay et al. 2010; Salisbury et al. 2022). These rocks accumulated in an extensive subsidence basin that formed along an ancient zone of weakness in the Precambrian substructure (Ramos 1988, 2008, 2018; Jiménez and López-Velásquez 2008; Ramos and Jiménez 2014). The Inner Arc is characterized by restricted peralkaline rocks and more voluminous moderately to strongly peraluminous, intermediate to acidic, volcanic and intrusive suites formed through metapelite anatexis with variable proportions of mantle-derived melts of mainly Triassic and Miocene (Clark et al. 1983, 1990; Sandeman et al. 1995, 1997; Kay et al. 2010; Salisbury et al. 2022; Pichavant et al. 2024; Ramírez-Briones et al. 2025).

The Eastern Cordillera of Peru is limited to the west by the Altiplano-Puna Plateau and to the east by the sub-Andean thrust and fold belt. The structural boundaries of the Eastern Cordillera are defined by the Main Andean Thrust along its northeastern margin and the Ayaviri fault, which forms part of the Urcos-Ayaviri-Copacabana-Coniri fault system, along its southwestern margin (Carlotto 2013; Perez and Horton 2014; Perez et al. 2016b). Sempere and Jacay (2008) designate the Eastern Cordillera as "the Tectonic Andes" due to the considerable tectonic shortening observed therein. Its formation is the result of a series of tectonic events that began with back-arc basin sedimentation during the Carboniferous-Permian, when the Peruvian territory was covered by an epeiric sea (Dalmayrac et al. 1980; Boekhout et al. 2018), and continues today through ongoing uplift that intensified since the Eocene (Benjamin et al. 1987; Farrar et al. 1988; Kley et al. 1997; Benavides-Cáceres 1999; Sempere et al. 2008; Mišković et al. 2009; Perez et al. 2016b; Spikings et al. 2016).

South of the Abancay deflection ($\sim 11^{\circ}\text{S}$), in central Peru, the exposed crystalline basement along the Eastern Cordillera of Peru comprises phyllite, schist, gneiss, and

amphibolite of the Huaytapallana Massif, covered by Paleozoic and Triassic-Jurassic sedimentary sequences (Pfiffner and González 2013; Chew et al. 2016). Huaytapallana is, in lithostratigraphic terms, equivalent to the Marañón Complex North of the Abancay deflection, composed of Neoproterozoic to the early Paleozoic high-grade orthogneiss and metasedimentary sequences (Wipf 2006; Chew et al. 2016).

In southern Peru, the Eastern Cordillera is composed of a (meta)sedimentary sequence that comprises ~7 km of marine Ordovician to Devonian siliciclastic deposits belonging to the San José, Sandia, and Ananea formations (Perez et al. 2016b). A major unconformity produced by the “Early Hercynian” orogenic event separates the Ordovician strata from the overlying Carboniferous, Permian, Triassic, and Cretaceous rocks (Dalmayrac et al. 1980; Sempere et al. 2004; Perez et al. 2016a). Up to 4 km of carboniferous shale and quartzite and Permian limestone of the Ambo, Tarma, and Copacabana formations are observed (Perez et al. 2016a,b). The Mitu Group, with a thickness > 2 km, overlies the Carboniferous-Permian sequence and preserves non-marine volcanic and siliciclastic rocks (Perez et al. 2016b; Spikings et al. 2016). Previous studies have associated the Triassic Mitu Group deposition with the intrusion of monzogranites along the Eastern Cordillera, suggesting that synrift deposition occurred in multiple hemigrabens with coetaneous magmatism (Laubacher 1978; Dalmayrac et al. 1980; Kontak et al. 1990; Sempere et al. 2002; Mišković et al. 2009; Perez et al. 2016a). Likewise, Jurassic (Muni Formation) and Cretaceous sequences (Huancané Formation and Moho Group) are also present (Perez et al. 2016b). This sedimentary sequence was intruded by a series of igneous suites, which include Ordovician-Early Silurian granitoids, Carboniferous-Early Permian granitoids and diorite, Late Permian-Triassic granodiorite, and Miocene granite (Mišković et al. 2009).

At the latitudes of southern Peru and through Bolivia, the Eastern Cordillera is a doubly-vergent thrust wedge (Eichelberger et al. 2013, 2015). In southern Peru, it comprises three SW-oriented morphostructural domains (Fig. 7), which from northeast to southeast are:

1. The Cordillera de Carabaya: It is located between the Macusani Structural Zone and the sub-Andean zone and is the NW extension of the Cordillera Real in Bolivia (Clark et al. 1983; Perez et al. 2016a). The structural boundaries of the Cordillera de Carabaya are the Main Andean Thrust along its northeastern margin and the Cordillera de Carabaya Backthrust along its southwestern margin (Perez et al. 2016a). The Cordillera de Carabaya forms a geomorphological boundary at high altitude (5-6 km) that acts as a drainage divide and comprises multiple Permo-Triassic plutons and smaller Jurassic plutons, which intruded Ordovician-Carboniferous strata and the deposits of the Triassic Mitu Group, respectively (Kontak et al. 1990b; Mišković et al. 2009; Perez et al. 2016a). The Triassic plutons are found along 130 km from the Cordillera de Carabaya to the Cordillera de Andahuaylas, where their volume decreases, and they disappear completely north of 10°S (Mišković et al. 2009; Spikings et al. 2016). This decrease of Triassic plutonism coincides with the absence of lava flows in the Mitu Group in central and northern Peru (Megard, 1978; Spikings et al. 2016). These Permo-Triassic granites continue into the Cordillera Real of Bolivia (Gillis et al. 2006).
2. Macusani Structural Zone: It is situated between the Cordillera de Carabaya and the Central Andean Backthrust Belt. The structural boundaries of the Macusani Structural Zone are the Cordillera de Carabaya Backthrust along its northeastern margin and the Anta fault system along its southwest margin (Perez et al. 2016a; Rodriguez et al. 2021). The Anta fault system is also known as Quilcapunco-Ccaccapunco (Rodriguez et al. 2010) or San Anton (Perez et al. 2016a), and

belongs to the Pre-Cordillera de Carabaya Fault System (Rodriguez et al. 2021). The Macusani Structural Zone comprises Carboniferous and Permian metasedimentary rocks as well as Triassic Mitu Group conglomerate and bimodal volcanic and siliciclastic rocks (Perez et al. 2016a,b). The thickest and best-exposed sections of the Mitu Group are in the Macusani Structural Zone, where rapid lateral changes in thickness, lithology, and facies are observed (Perez et al. 2016a). The Macusani Structural Zone exhibits an abrupt increase in the depth of the exposed structural levels (>4 km) relative to the Central Andean Backthrust Belt. It is characterized by non-coaxial structures, as evidenced by folds and faults with N-S, NE-SW, and NNW-SSE orientations, in contrast to the NW-SE regional trend typical of southern Peru (Perez et al. 2016a,b). This is due to the reactivation of Late Paleozoic deformation patterns by Andean thrust faults within the Macusani Structural Zone (Perez et al. 2016a). Finally, during the Mesozoic, granite stocks and coeval, cogenetic volcanogenic rocks were deposited within the Macusani Structural Zone (Clark et al. 1990; Alayza 2016), which were grouped under the Crucero Intrusive Supersuite and the Crucero Supergroup by Sandeman et al. (1997).

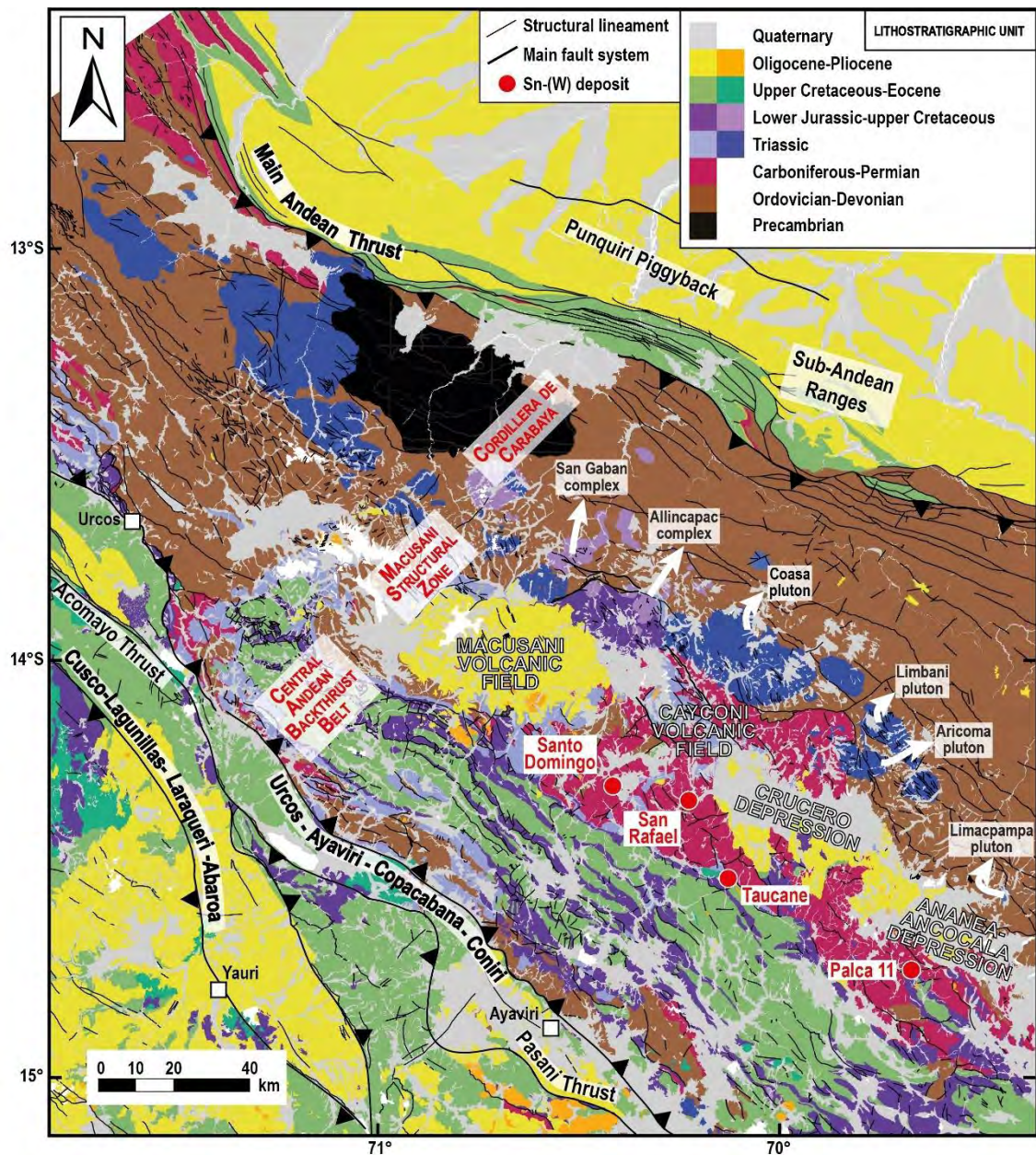


Figure 7. Morphostructural domains of the Eastern Cordillera in southern Peru. Modified from Perez and Horton (2014), Perez et al. (2016a,b), Sundell et al. (2019), INGEMMET (2023), and Ramirez-Briones (2024)

3. Central Andean Backthrust Belt: It is situated between the Macusani Structural Zone and the Altiplano. The structural boundary between the Central Andean Backthrust Belt and the Altiplano is delineated by the Ayaviri fault, (Sempere et al. 1990; Perez and Horton 2014). The Central Andean Backthrust Belt is ~ 50 km wide and extends for more than 1,000 km from south-central Peru to southern Bolivia. It comprises the Putina Fold-Thrust Belt in Peru (Canaza 2018), which

is the NW continuation of the Huarina Fold-Thrust Belt stretching across Bolivia (McQuarrie and DeCelles 2001; Jiménez and López-Velásquez 2008; Perez et al. 2016a,b). The Putina Fold-Thrust Belt is composed of Jurassic-Cretaceous sandstone, limestone, shale, and pelite, which exhibit SE-trending faults and folds (Perez et al. 2016a; Rodriguez et al. 2021). The faults are spaced between 1-3 km apart, and the field relationships suggest the presence of an imbricate fold-thrust belt, as no evidence of a roof thrust has been identified (Perez et al. 2016a). In contrast, the Huarina Fold-Thrust Belt exposes deeper, Lower Paleozoic units (Pérez et al. 2016a,b). This is due to the presence of basement megathrusts in the Huarina Fold-Thrust Belt, which extend eastward, displacing basement sheets measuring 12-15 km in thickness (McQuarrie and DeCelles 2001). This sequence of events led to the activation of thrust faults, causing the erosion of Mesozoic and Cenozoic strata and the uplift and dominance of Paleozoic strata (Murray et al. 2010).

3.2. Geology of the Central Andean Tin Belt

The Central Andean Tin Belt constitutes an elongated metallogenic province, confined to the Eastern Cordillera of the Andean orogen and extending over 1,000 km from Southern Peru, through Bolivia, to Northern Argentina (Mlynarczyk and Williams-Jones 2005; Fontboté 2018). It hosts hundreds of Sn and W rich deposits with secondary commodities such as Ag, Zn, Cu (expressed from now on as “Sn-W ± Ag-Zn-Cu”), occurrences, and mineral showings that are associated with peraluminous granitoids and subvolcanic stocks emplaced during two main metallogenic events: one in the late Triassic (ca. 235 and 190 Ma), which is restricted to the northern part of the belt, and one in the Late Oligocene-early Miocene (ca. 25 and 12 Ma), which is recorded across the entire belt (Fig. 1; Clark et al. 1990; Lehmann et al. 1990; Mlynarczyk and Williams-Jones 2005;

Gemrich et al. 2021; Harlaux et al. 2021, 2023). The latter is of much greater economic importance and includes several world-class deposits such as Huanuni, Llallagua, Cerro Rico de Potosí, Oruro (San José-Itos mines), and Chorolque in Bolivia and San Rafael in Peru (Fig. 1).

Following the general trend of the Eastern Cordillera, the Central Andean Tin Belt shows a NW-SE orientation north of the Central Andean orocline and a N-S orientation south of it. The northern segment consists mainly of Sn-W lodes, veins, and stratabound orebodies (Kelly and Turneaure 1970; Turneaure 1971; Lehmann 1985; Torró et al. 2024). The Sn-W veins and lodes are found in districts such as Sayaquira, Caracoles, Bolsa Negra, and Milluni in Bolivia and in San Rafael and Santo Domingo in Peru, and are characterized by a predominant cassiterite-quartz and wolframite-quartz ore with common scheelite (Turneaure 1971). Stratabound tin mineralization is also common in this sector, with at least three known mining areas: San José/Amarete, Kellhuani, and Mt. Blanco (Lehmann 1990b; Torró et al. 2024). Greisen-type alteration has been identified in San Rafael (Harlaux et al. 2020) and Chacaltaya (Bolivia; Torró et al. 2024), but is comparatively of minor economic importance compared to veins and lodes. The southern segment consists mainly of Sn porphyry deposits, as well as Sn, Sn-W, and Sn-Ag-polymetallic veins and breccias formed in xenothermal and epithermal environments (Sillitoe et al. 1998; Heuschmidt et al. 2002; Mlynarczyk and Williams-Jones 2005; Torró et al. 2019a, b; Cacho et al. 2019; Torres et al. 2020).

There are several hypotheses associated with the origin of the Central Andean Tin Belt. The first suggests that there is a “geochemical heritage”, meaning that the location of the metallogenic province was controlled by a persistent tin anomaly (Ahlfeld 1967; Schuiling 1967). This anomaly is believed to be associated with the host rocks, the underlying Precambrian basement (Ahlfeld 1967), or the upper mantle, which is

periodically tapped (Schuiling 1967). However, these theories have been mostly superseded since high tin content in granitic rocks can be directly related to the degree of magmatic fractionation (Lehmann 1987; Dietrich et al. 2000). Subsequently, Lehmann et al. (1990) proposed that the west-east metallic zonation in the Andes is determined by the compositional difference in the magma source regions of each zone and by the progressive reduction eastward of the role of subduction-associated igneous processes in deposit formation. In this scenario, the magmatism observed in the Central Andean Tin Belt resulted from extensive melting of carbon- and boron-rich pelitic rocks, estimated to be 10-15 km thick (Mlynarczyk and Williams-Jones 2005). The result was the formation of melts of peraluminous and reduced character (S-type granitoids; ilmenite-bearing series of Ishihara 1981). Furthermore, the extensive fractional crystallization of these melts led to the enrichment of Sn and W in the melts and their effective transference to related hydrothermal fluids (Lehman et al. 1990; Mlynarczyk and Williams-Jones 2005).

The northern termination of the Central Andean Tin Belt extends ~150 km into Peruvian territory. This northern extension was poorly delineated by the mid-20th century subsequently become an important source of tin concentrates since 1970 (Clark et al. 1983; Kontak et al. 1990a). The change is attributed to the discovery of the world-class San Rafael deposit, one of the largest and highest-grade primary Sn deposits around the world (Mlynarczyk et al. 2003; Wagner et al. 2009; Harlaux et al. 2020, 2021, 2023; Markovic et al. 2025). Additionally, several other minor deposits, including Nazareth, Santo Domingo, Jesica, San Jose, Ocuara, Condoriquiña, Quenamari, Sarita, and Palca 11, have also been identified (Carlotto et al. 2009). These deposits were formed during the second, “third”, and fourth of the five metallogenic episodes proposed by Zappetini et al. (2001) within the Central Andean Tin Belt.

During the second episode, defined by Zappetini et al. (2001) to occur from the Upper Triassic to the Lower Jurassic, the deposits were associated with strongly peraluminous stocks (Clark et al. 1990). The Condoriquiña and Sarita deposits formed during this geological period. The first significant Sn-dominant bedrock mineralization to be recognized in Peru was the Condoriquiña Sn(-W-Au) deposit (Petersen 1960; Clark et al. 1990). The available K-Ar and $^{40}\text{Ar}/^{39}\text{Ar}$ data for this district indicate that mineralization took place before 112.4 ± 2.4 Ma, whereas the Rb-Sr isotope relations strongly suggest a post-Carboniferous age (Clark et al. 1990). The Sarita, or Oscoroque, Cu-W-Mo(-Sn) deposit was the most significant base and lithophile metal mineralization known to be associated with the Carabaya batholith. Two ages were obtained for the deposit: a K-Ar date of 194.1 ± 3.9 Ma for biotite from a monzogranite taken from an outcrop adjacent to a Cu-rich vein, with presence of chalcopyrite disseminations. Furthermore, a $^{40}\text{Ar}/^{39}\text{Ar}$ step-heating of this biotite yielding an integrated date of 187.11 ± 1.18 Ma (Clark et al. 1990).

During the third episode of Zappetini et al. (2001), which took place from the Upper Oligocene to the Lower Miocene, vein-like Sn mineralization was associated with granitic intrusions. The Santo Domingo, San Rafael, Palca XI, and Nazareth deposits belong to this period. The San Rafael deposit is predominantly hosted by the San Rafael Intrusive Complex, emplaced at ca. 24 Ma (Kontak and Clark 2002; Harlaux et al. 2021). Harlaux et al. (2023) and Markovic et al. (2025) have constrained the main stage of Sn mineralization between 24.43 ± 0.32 and 23.47 ± 0.53 Ma. Nazareth is a satellite deposit located 5 km NE of San Rafael and therefore probably has a similar age to San Rafael (Villón 2025). The Santo Domingo Sn-Cu(-Pb-Zn-Ag) deposit is located 24 km NW of the San Rafael mine in the Carabaya province (Acosta et al. 2011; Sánchez 2016). K-Ar dates on biotite from Santo Domingo range from 23.1 ± 0.2 Ma to 27.1 ± 1.0 Ma (Clark

et al. 1990). The Palca XI W(-Sn-Ag-Cu-Pb-Zn) deposit, located in the Choquene district, was the largest tungsten producer in the Andes (Farrar et al. 1990). The ages of the deposit were determined by $^{40}\text{Ar}/^{39}\text{Ar}$ analysis of hydrothermal biotite and adularia closely associated with scheelite mineralization. The dates were 24.96 ± 0.13 and 24.82 ± 0.15 Ma for two biotite fractions, and 22.60 ± 0.12 Ma for the adularia (Clark et al. 1990; Acosta et al. 2011).

The fourth episode (Zappetini et al. 2001), which occurred in the middle Miocene, is of minimal importance in Peru, including only the Jessica deposit. The Jessica Sn-Zn deposit is located in the Lintere Hill and consists of a series of veins (Clark et al. 1990). A total fusion $^{40}\text{Ar}/^{39}\text{Ar}$ date was determined for magmatic muscovite from the leucogranite of Lintere Hill at 17.40 ± 0.14 Ma (Clark et al. 1990).

3.3. Geology of the Taucane Project

The Taucane Project is situated within the Central Andean Backthrust Belt, close to the northern boundary of this morphostructural domain with the Macusani Structural Zone (Fig. 8). In detail, the area covered by the exploration concessions is geologically subdivided into two lithostratigraphic domains by the Taucane fault, which is part of a structural mega-alignment called the Pre-Cordillera de Carabaya Fault System (Kontak et al. 1987; Alayza 2016; Rodriguez et al. 2021). To the north of the Taucane Fault, Paleozoic and Triassic (meta)sedimentary units within the Macusani Structural Zone are exposed. To the south of the Taucane Fault, where most of the study area is located, Mesozoic sedimentary rocks are discordantly exposed overlying Paleozoic units within the Central Andean Backthrust Belt.

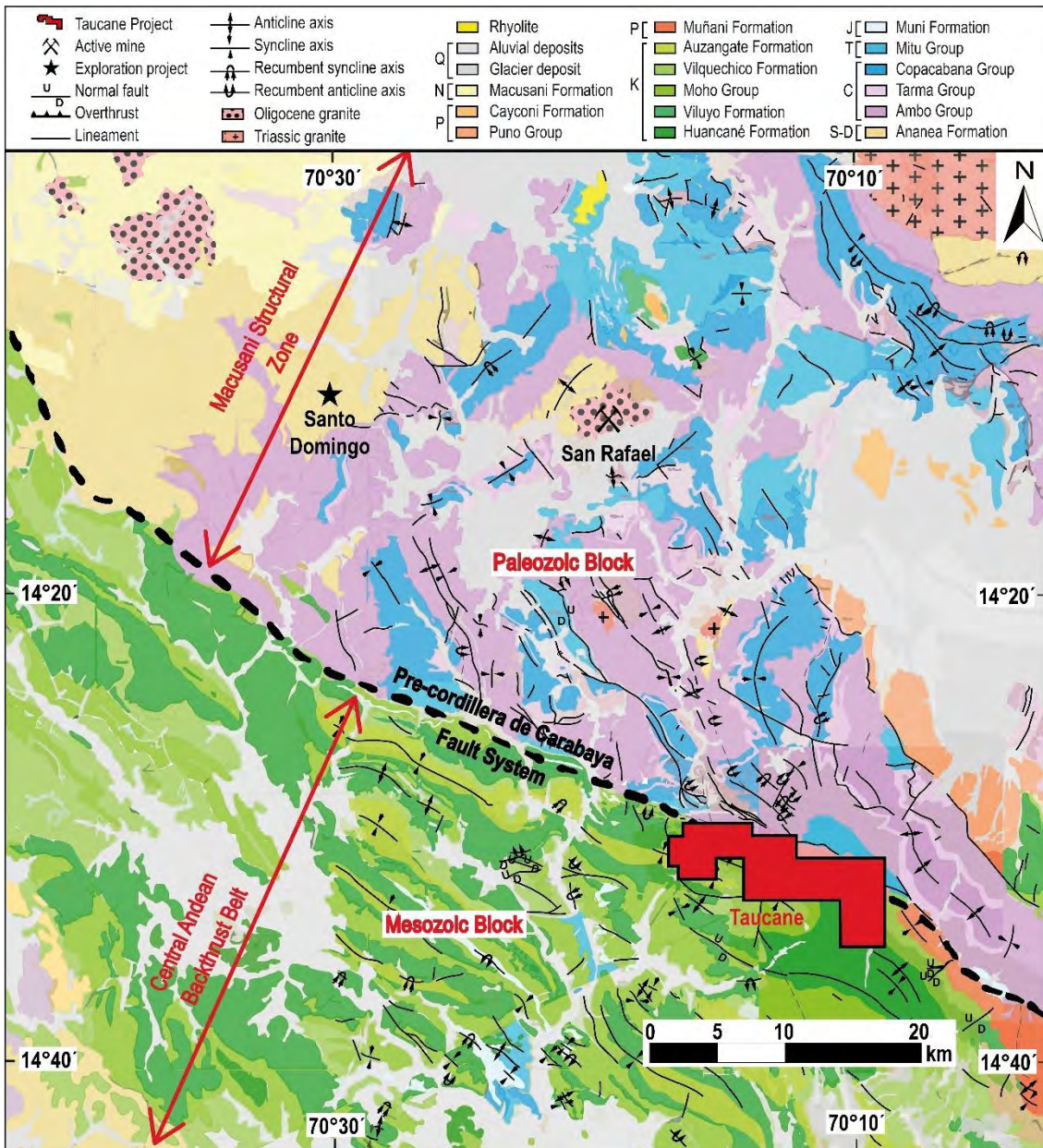


Figure 8. Location of Taucane exploration concessions in the regional geologic map with morphostructural domains in the Eastern Cordillera of the Andes in southeastern Peru. S-D to Q letters correspond to the geological Periods. Modified from Sanchez and Zapata (2003) and Alayza (2016)

In the northern strip of the concessions, four Paleozoic units have been identified (Fig. 9). The Silurian-Devonian Ananea Formation, the oldest in the study area, comprises black phyllite and gray shale with thin sandstone layers (Rodriguez et al. 2021). The Lower Carboniferous Ambo Group overlies the Ananea Formation, consists of layers of gray sandstone and shale. The Late Carboniferous Tarma Group is characterized by an intercalation of green and gray sandstone with parallel lamination and overlies the Ambo

Group. The Permian Copacabana Group overlies the Ambo Group and is composed of gray wackstone-packstone limestone with chert nodules (Alayza 2016; Rodriguez et al. 2021).

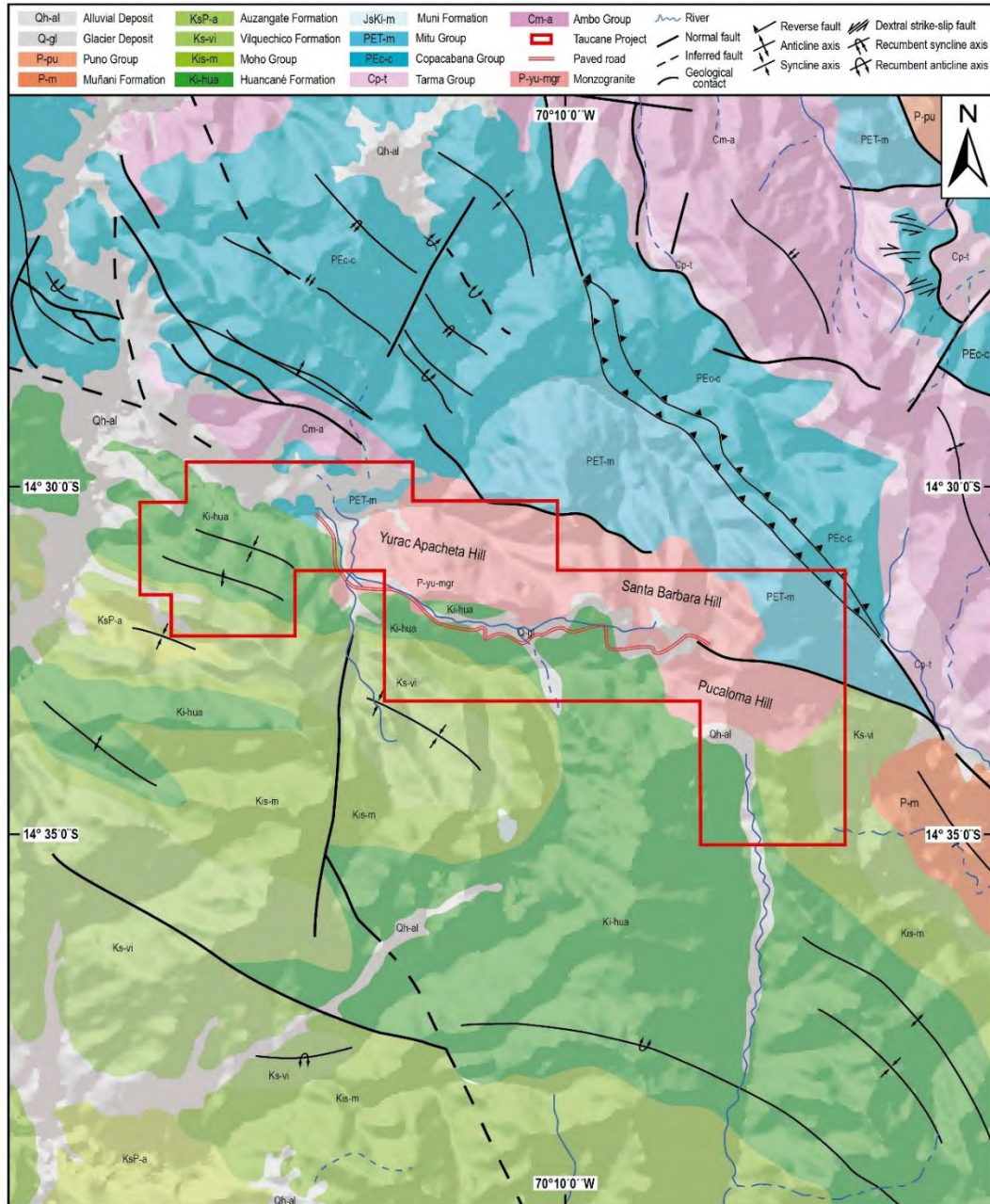


Figure 9. Location of the Taucane Project in the local geologic map. Modified from Sanchez and Zapata (2003)

The rest of the concession is mostly covered by Triassic, Jurassic, and Cretaceous sedimentary rocks (Fig. 9). The Triassic Mito Group unconformably overlies the Copacabana Group and underlies the Muni Formation (Sánchez and Zapata 2003). The

Mitu Group is composed of reddish polymictic conglomerate with subangular clasts of quartzite, limestone, and volcanic rocks (Sánchez and Zapata 2003; Rodríguez et al. 2021). The Upper Jurassic Muni Formation is composed of sandy siltstone and clay, with colors ranging from red, violet, and greenish gray to white, and includes gypsum deposits and limestone horizons, collectively reaching approximately 400 m in thickness (Sempere et al. 2004; Rodríguez et al. 2021). The Muni Formation overlies the Mitu Group and underlies the sandstone of the Huancané Formation with erosional unconformity (Rodríguez et al. 2021). The Lower Cretaceous Huancané Formation consists of quartz sandstone with a characteristic white-pinkish color that are intercalated with red pelites towards their base, exhibiting cross-stratification (Sempere et al. 2004). This Formation underlies the Upper Cretaceous Moho Group, which is composed of limestone and siltstone interbedded with white quartz sandstone (Sánchez and Zapata 2003; Rodríguez et al. 2021)

This sequence is cut by a series of intrusive rocks along the Pre-Cordillera de Carabaya fault system, north of the main mineralized zones, in the Santa Barbara, Yurac Apacheta, and Pucaloma hills (Fig. 9). According to their macroscopic characteristics, they correspond to quartz monzodiorite, monzodiorite, monzogranite, and lamprophyre (minette; Vallance 2015; Alayza 2016). Quartz monzodiorite is the main intrusion in the study area, with its main outcrop located in the Santa Barbara and Yurac Apacheta hills (Fig. 10). The monzodiorite is predominantly exposed in the Yurac Apacheta Hill, where it constitutes a stock. The monzogranite is principally observed as dykes cutting the sedimentary sequences that are associated with the mineralization, as well as the quartz monzodiorite. Finally, the minette occurs as dykes penetrating monzogranite dykes, quartz-monzodiorite intrusive rocks, and to a lesser extent, the sedimentary sequence. The petrographic characteristics of the four intrusive units are described below (Section

4.1.1.). Furthermore, the Jean breccia (Fig. 10)—named after Dr. Jean Vallance, who conducted studies in the area—is associated with the main intrusion in the Santa Barbara Hill. Its surface geometry is defined by an ellipse, with a SE-oriented major axis of ~1,300 m and a minor axis of ~800 m (Vallance 2013; Alayza 2016). On the edges of this ellipsoid, annular breccias developed with widths of up to 100 to 150 m and exhibit abundant iron oxides in the matrix (Alayza 2016).

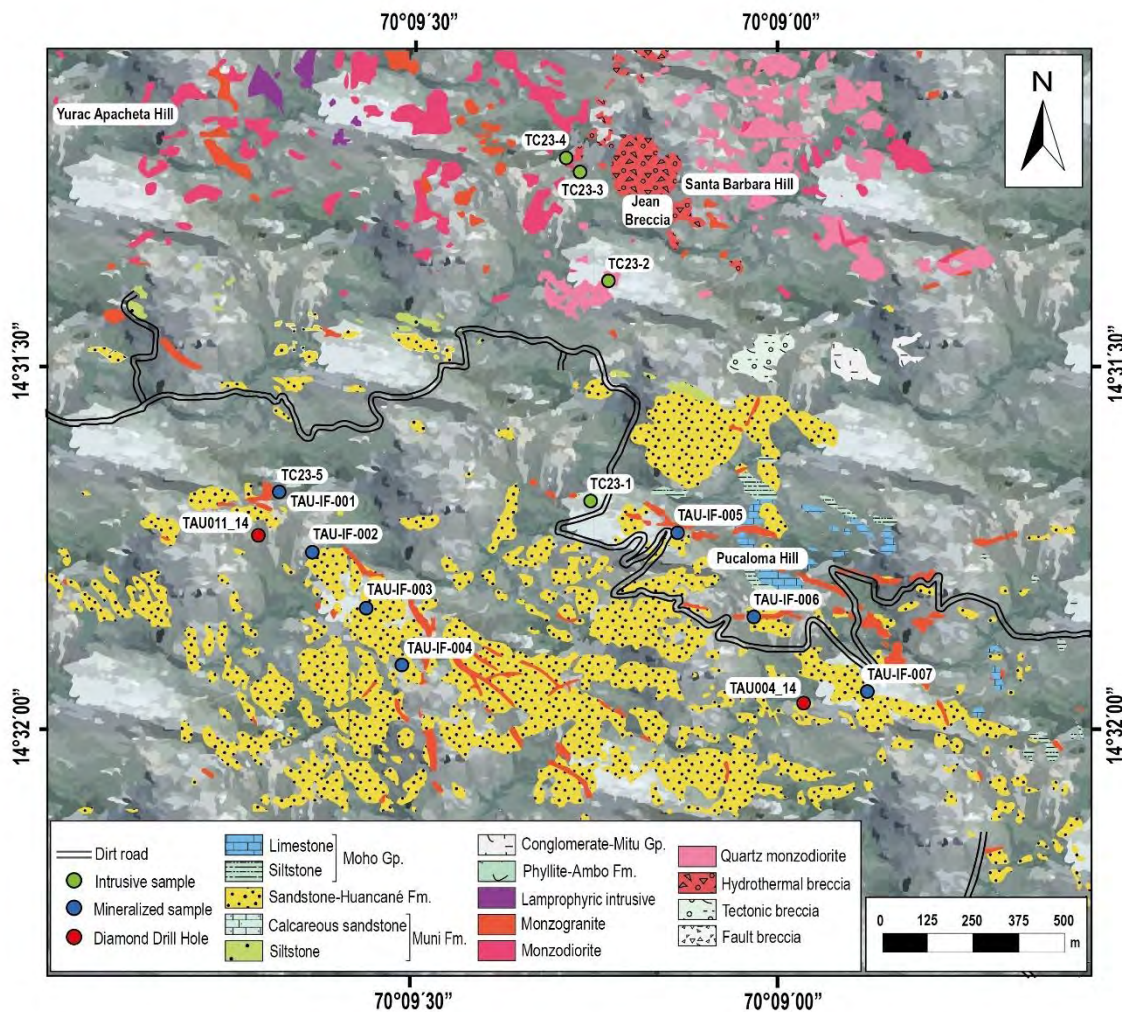


Figure 10. Geologic map of the Taucane project according to detailed mapping performed by MINSUR S.A. including the location of the studied samples and drill cores. Base map modified from Alayza (2016)

In terms of mineralization, Taucane comprises stratiform replacement ore-bodies (mantos) and, to a lesser extent, vein systems, both hosted by the Mesozoic sedimentary sequence. Four sectors of interest have been identified within the Taucane area: the

Lorena vein and manto system, the Kelly vein and manto system, the Taucane West Body, and the Jean Breccia. The Lorena and Kelly systems are the most volumetrically significant (Fig. 11; Alayza 2016).

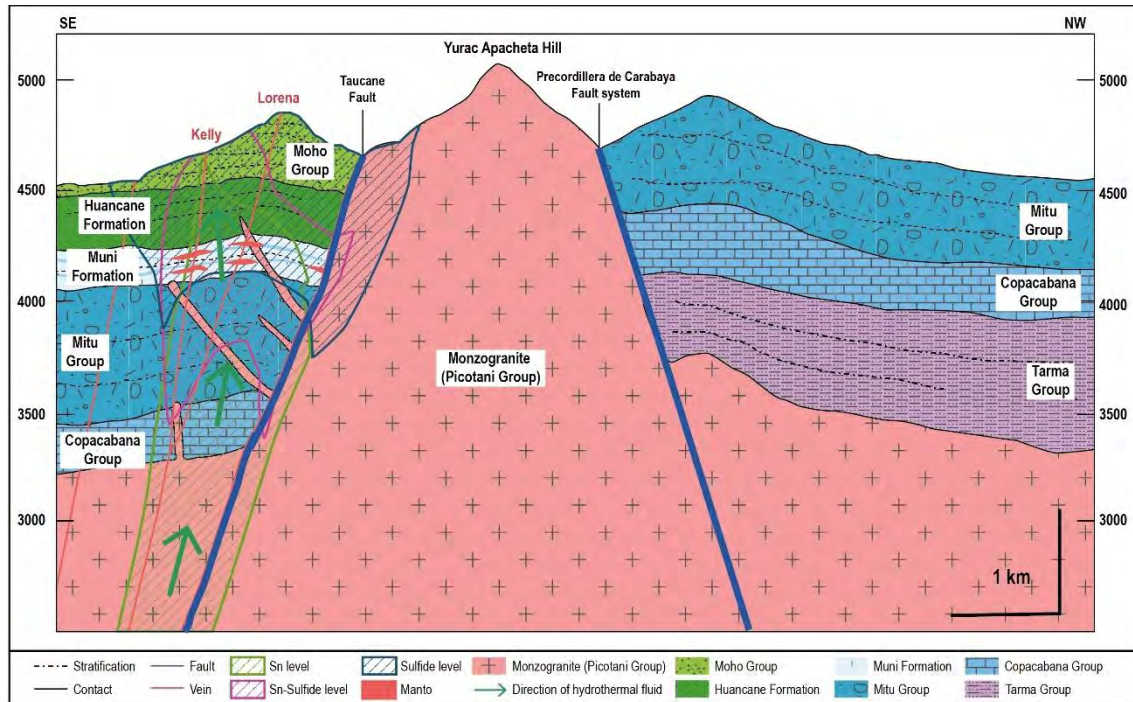


Figure 11. Preliminary exploration model of the Taucane mineralization system, including veins and mantos of the Lorena and Kelly hosted by the Jurassic-Cretaceous sedimentary rocks, and potentially, veins extending to older sedimentary units (inspired in Alayza 2016)

Both systems have comparable hydrothermal alteration patterns regardless of the specific mineralization style. Argillic alteration is the most abundant alteration in the area and is directly related to mineralized structures, faults, and breccias. The alteration minerals in sandstone are essentially clays (kaolinite, montmorillonite), while in intrusive rocks, illite predominates over smectites (Alayza 2016). Sericite alteration has been observed in association with the host rocks of the mineralized structures of both systems, along with pyrite and, in some cases, in association with pyrrhotite and/or chlorite, and late carbonate infills (Vallance 2015, Alayza 2016). In addition, mantos in the Kelly system exhibit skarn mineral assemblages.

The Kelly vein system crops out at the Pucaloma Hill as three narrow sub-parallel structures with variable thicknesses of 0.10-0.50 m, lengths of ~1 km along strike, azimuths of 160°-170°, and dips of 70°-80° SW (Fig. 12A). The mineralized veins cut sandstone of the Huancané Formation and monzogranite dykes. On surface, the structures are discontinuous and have a brecciated texture with a strongly oxidized matrix and abundant barite (Fig. 12B). The mineralization at depth consists of Fe-Cu-Pb-Zn sulfides (mostly pyrite) and Ag-rich sulfides and sulfosalts (Fig. 12C). Furthermore, mantos of the Kelly system were identified at elevations of 4,400-4,600 m, and exhibit thicknesses of up to 24 m and lateral extensions of up to 200 m. They developed along calcareous sandstone horizons of the Muni Formation and the Moho Group, with skarn phases, such as green garnet (Fig. 12D) and pyroxene, associated with mineralization. The mineralization identified consists of Fe-Cu-Zn-As sulfides (mostly pyrrhotite; Fig. 12E), Ag-rich sulfides and sulfosalts, and cassiterite.

The Lorena vein system also crops out along the Pucaloma Hill and exhibits a discontinuous extension of approximately 1.3 km along strike, azimuths of 110°-140°, and dips of 60°-80° SW. The vein system is branched, with individual veins ranging in thickness from 0.10 to 1.50 m. The mineralized veins cut sandstone of the Huancané Formation, siltstone and limestone of the Moho Group, and dykes of monzogranitic composition. On the surface, the structure is brecciated, composed predominantly of patchy barite and sandstone fragments embedded within a strongly oxidized matrix (Fig. 13A). At depth, the mineralization consists of massive Fe sulfides (mostly pyrite; Fig. 13B) and Ag-rich Pb phases. Mantos in the Lorena system occur at elevations between ~4,300 and 4,600 m. They share comparable characteristics to those from the mantos in the Kelly area, including thickness, lateral extensions, and mineralization, the main

differences being that pyrite is more abundant than pyrrhotite (Fig. 13C-E) and that skarn phases are not observed.

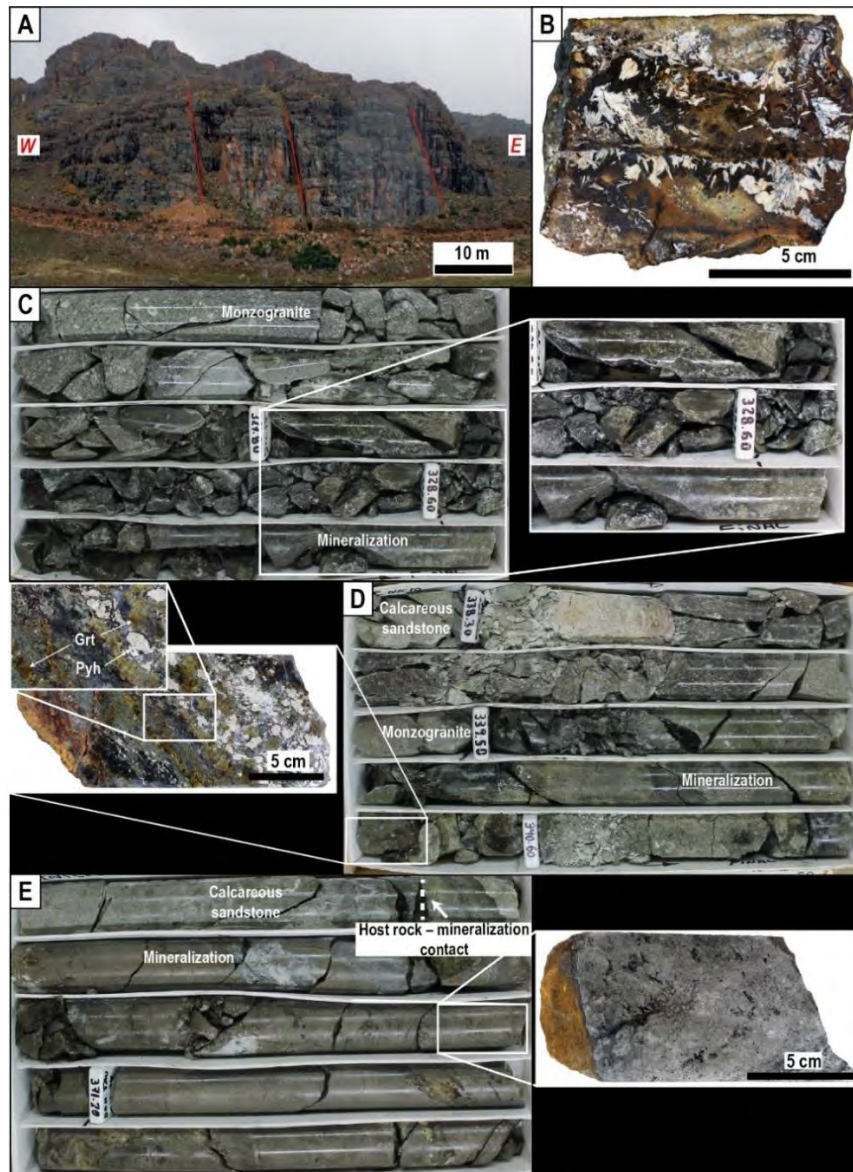


Figure 12. General aspect of the mineralization in the Kelly system. A) Narrow, subvertical structures (red lines) of the Kelly Vein system hosted by sandstone of the Huanané Formation; (B) Quartz-barite vein breccia cemented by iron oxides and lesser amounts of galena; (C) Drill core showing greenish-gray monzogranite with a weak chlorite alteration cut by vein-type mineralization comprising semi-massive pyrite (inset) and, to a lesser extent, galena; (D) Drill core showing calcareous sandstone in contact with monzogranite and manto-type mineralization with skarn phases including green garnets (inset), chlorite in fractures, and calcite in veins forming druses. Mineralization consists of pyrrhotite (<15%), pyrite (<8%) in patches, and disseminated chalcopyrite; (E) Drill core showing brecciated calcareous sandstone with subrounded clasts < 3 cm in size, in contact with manto-type mineralization composed of massive pyrrhotite (<70%; inset), pyrite (8%) in fractures and bands, and galena (2%), sphalerite, and chalcopyrite (1%) in veinlets and disseminations

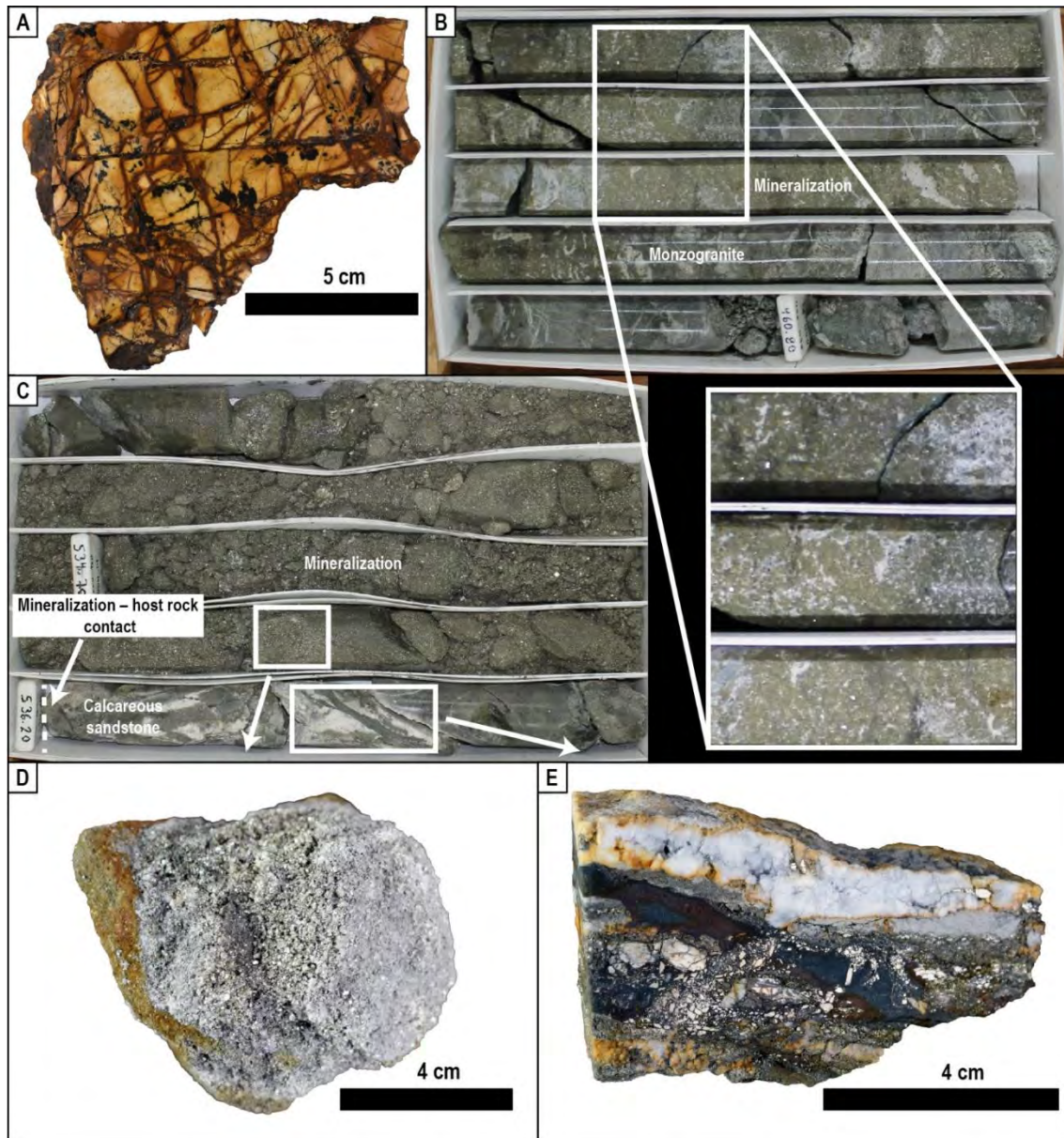


Figure 13. General aspect of the mineralization in the Lorena system. A) Vein breccia with boxwork texture developed by replacement of Fe-oxides (goethite and limonite) cementing barite, galena, and clasts of partially silicified sandstone of the Huanané Formation; (B) Drill-core exhibits pyrite- (<85%) and quartz vein (see inset) cutting an intensely silicified monzogranite filled with calcite filling through fractures; (C) Manto-type mineralization composed of fine-grained powdery pyrite (<75%), in contact with calcareous sandstone with moderate fracturing and calcite veins up to 2 cm wide with pyrite; D) Massive powdery, fine-grained pyrite with minor calcite in matrix; E) Pyritized (<60%) vein breccia with dark sulfide gouge-type groundmass and bands of white quartz

4. RESULTS

4.1. Petrography

4.1.1. Intrusive rocks

The intrusive rocks identified in the Taucane Project can be classified as monzogranite (TC-23-01; Fig. 14A), quartz-monzodiorite (TC-23-02; Fig. 14B), monzodiorite (TC-23-04; Fig. 14C), and minette (TC-23-03; Fig. 14D; Vallance, 2015).

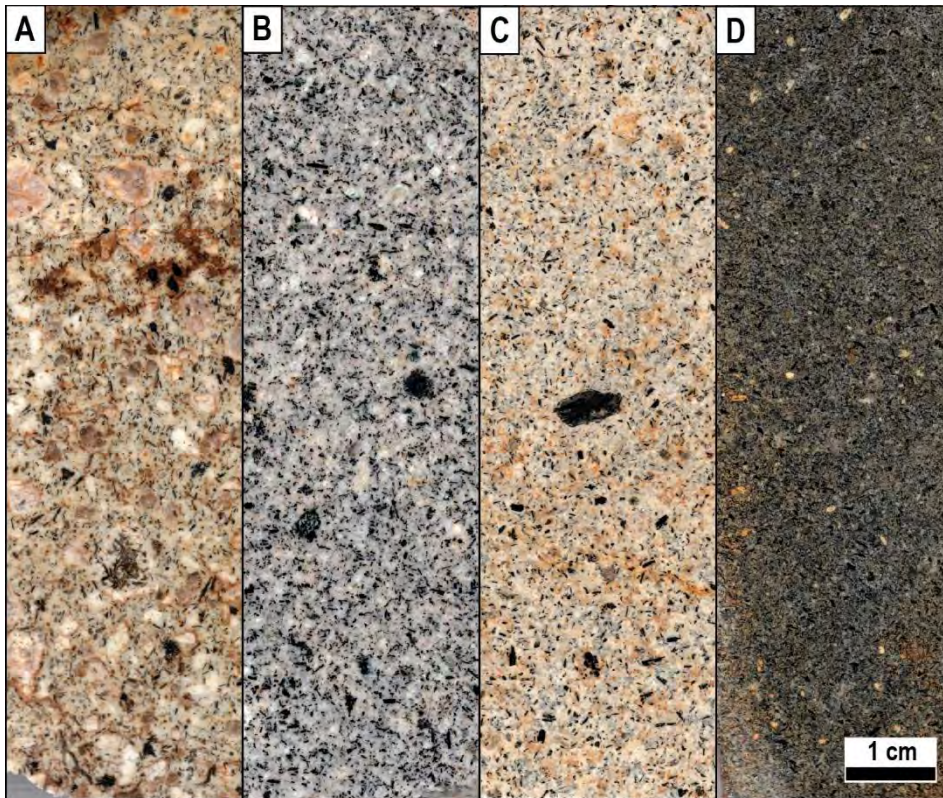


Figure 14. Intrusive rocks in the Taucane area. (A) monzogranite; (B) quartz-monzodiorite; (C) monzodiorite; and (D) minette

4.1.1.1. Monzogranite

In hand sample, the monzogranite is pinkish gray in color, with a predominant porphyritic texture (Fig. 14A). It contains phenocrysts of pinkish K-feldspar up to 0.7 cm in size with a tabular to anhedral habit. There are also whitish plagioclase phenocrysts up to 0.5 cm in size with a tabular habit. To a lesser extent, biotite crystals up to 0.3 cm in size are observed throughout the sample. From a microscopic perspective, the K-feldspar

phenocrysts contain plagioclase and biotite chadacrysts (Fig. 15A). In addition, Baveno-law twins are observed in some K-feldspar phenocrysts (Fig. 15B). Phenocrysts of K-feldspar, plagioclase, biotite, and muscovite are embedded in a groundmass composed of quartz, plagioclase, and to a lesser extent, K-feldspar (Fig. 15C-E). The visually estimated primary mineral composition is as follows: plagioclase (40%), quartz (30%), K-feldspar (25%), and biotite plus muscovite (5%). Occasional grains of rutile and zircon are also observed. Secondary quartz with a mosaic texture and local tourmaline fill interstitial spaces (Fig. 15F). Alteration features include biotite partially altered to chlorite and Fe-Ti oxy-hydroxides (Fig. 15D), as well as plagioclase, and to a lesser extent K-feldspar, altered to sericite (Fig. 15A-C).



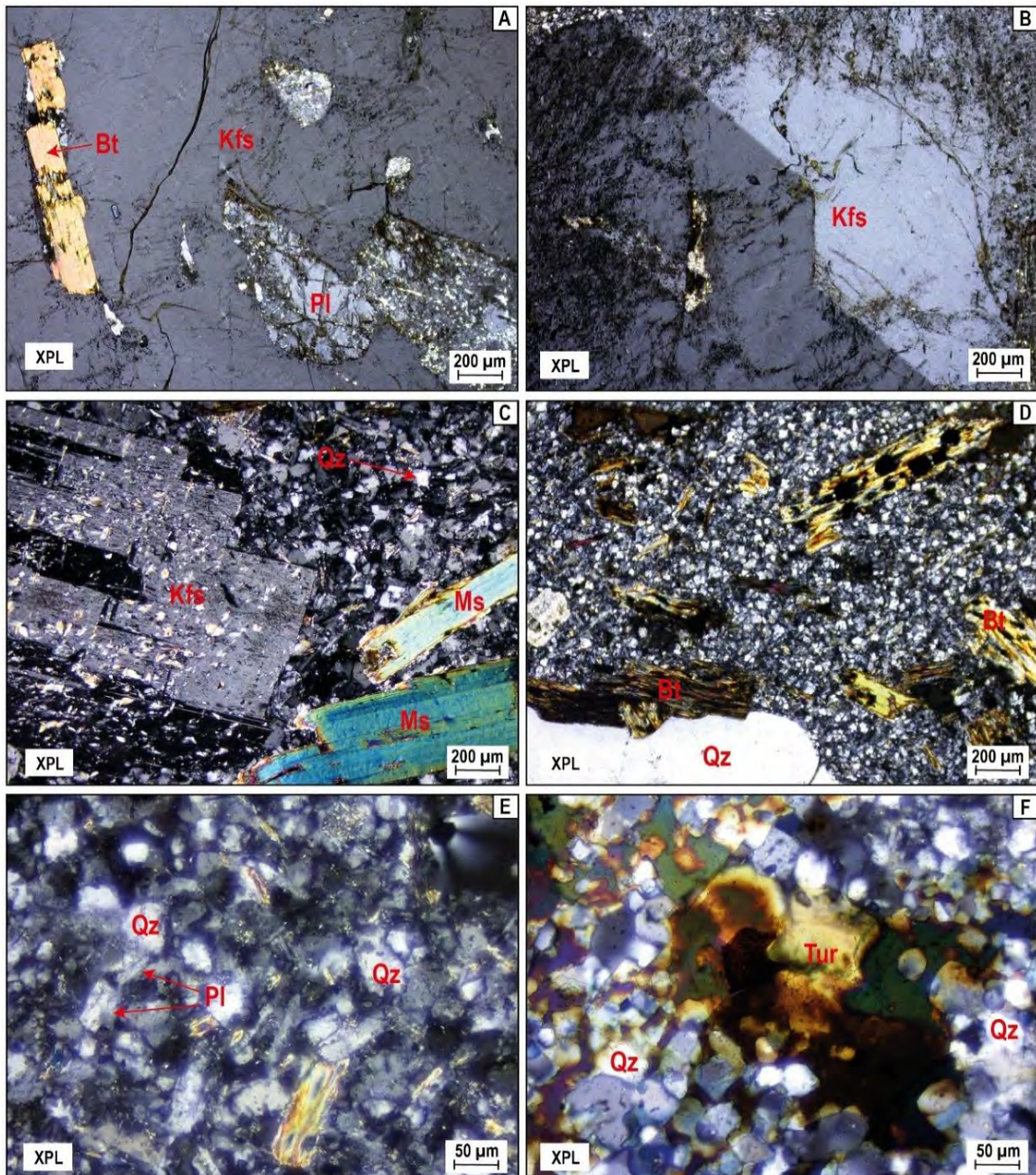


Figure 15. Representative transmitted-light images of monzogranite (sample TC-23-01). (A) K-feldspar phenocryst with plagioclase and biotite chadacrysts; (B) K-feldspar phenocryst with Baveno-law twinning; (C) K-feldspar and muscovite phenocrysts embedded in a fine-grained quartzfeldspatic groundmass; (D) Fine-grained groundmass along with phenocrysts of quartz and altered biotite; (E) Fine-grained groundmass composed mainly of primary quartz, plagioclase, and lesser K-feldspar; (F) Secondary quartz and tourmaline as cavity fillers. Abbreviations: Bt—Biotite, Kfs—K feldspars, Ms—Muscovite, Pl—Plagioclase, Qz—Quartz, Tur—Tourmaline, XPL—Cross polarized light

4.1.1.2. Quartz-monzodiorite

In hand sample, the quartz-monzodiorite is light gray in color, with a phaneritic and broadly equigranular texture (Fig. 14B). It is composed mainly of plagioclase, K-feldspar, quartz, and lesser amounts of tourmaline and biotite. It is dominated mainly by plagioclases up to 0.7 cm in size, with grayish-white tones and tabular to subhedral habits. K-feldspar grains are subhedral, up to 0.4 cm in size, and exhibit pinkish tones. Quartz grains are anhedral, up to 0.3 cm in size, and translucent. Tourmaline and biotite form rosettes (clots) that are up to 0.4 cm in diameter. From a microscopic perspective, the K-feldspars phenocrysts are anhedral and show Carlsbad twinning (Fig. 16A). Plagioclase phenocrysts are subhedral with their characteristic albite-type polysynthetic twinning. Quartz phenocrysts are roundish and have undulatory extinction. Occasionally, cordierite phenocrysts up to 1 mm size are found with characteristic cyclic twinning (Fig. 16B). Irregular clots composed of brown biotite (Fig. 16D-E) and skeletal tourmaline (Fig. 16F) are observed within a groundmass consisting mainly of K-feldspar and minor amounts of quartz, biotite, and plagioclase (Fig. 16C). The visually estimated primary mineral composition is as follows: plagioclase (40%), K-feldspar (30%), quartz (15%), biotite (12%), and tourmaline (3%). The alteration mainly affects biotite, which is partially replaced by sericite and chlorite (Fig. 16D). Plagioclase and K-feldspars phenocrysts are weakly to moderately altered to sericite. Late carbonates flood the groundmass and partially replace biotite and feldspar (Fig. 16E).

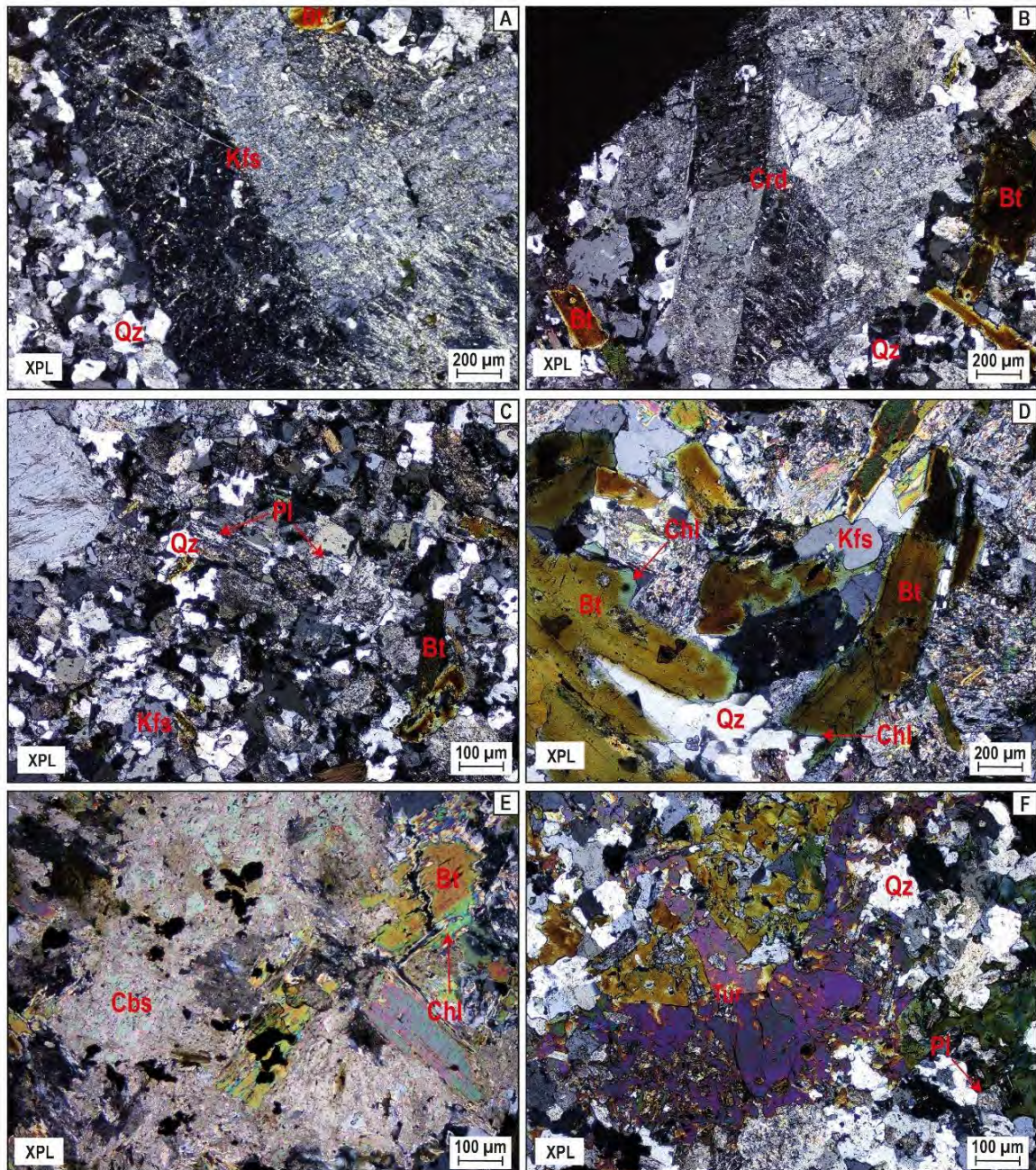


Figure 16. Representative transmitted-light images of quartz-monzodiorite (sample TC-23-02). (A) Sericitized K-feldspar phenocryst with Carlsbad twin, including quartz chadacrysts; (B) Cordierite with its characteristic cyclic texture; (C) Groundmass composed mainly of quartz and K-feldspar, and to a lesser extent, plagioclase; (D) Clot of coarse-grained biotite phenocrysts altered through edges to chlorite; (E) Carbonate masses flooded the groundmass and partially replaced biotite; (F) Clot of coarse-grained, skeletal tourmaline finely intergrown with fine-grained quartz and feldspars. Abbreviations: Bt—Biotite, Cbs—Carbonates, Chl—Chlorite, Crd—Cordierite, Kfs—K feldspars, Pl—Plagioclase, Qz—Quartz, Tur—Tourmaline, XPL—Cross polarized light

4.1.1.3. Monzodiorite

In hand sample, the monzodiorite is grayish white to pinkish in color and exhibits a phaneritic texture (Fig. 14C). It is composed mainly of plagioclase, K-feldspar, biotite, and, to a lesser extent, quartz. It is dominated by subhedral crystals of white to light-gray plagioclase, with sizes up to 0.4 cm. Anhedral K-feldspar crystals with pinkish tones and sizes up to 0.3 cm are observed. In addition, there is the presence of biotite with tabular to subhedral habits up to 0.7 cm and tabular muscovite with sizes up to 0.3 cm. To a lesser extent, translucent anhedral quartz grains are up to 0.2 cm in size. From a microscopic perspective, plagioclase phenocrysts are subhedral and show common polysynthetic twins and local chessboard-like textures (Fig. 17A). K-feldspar phenocrysts are subhedral to anhedral and exhibit Carlsbad-type twinning (Fig. 17B). Biotite crystals are anhedral to subhedral, while muscovite crystals are subhedral, platy, and locally form cross-like twinned specimens (Fig. 17C). The groundmass is formed mainly of K-feldspar, plagioclase, lesser amounts of biotite, and minor quartz. The visually estimated primary mineral composition is as follows: plagioclase (40 %), K-feldspar (30 %), muscovite (10 %), biotite (10 %), chlorite (5 %), and quartz (5%). Alteration features include strong sericitization of K-feldspar (Fig. 17B), and less intense sericitization of plagioclase. Biotite has been partially altered to chlorite (Fig. 17D). In sectors, carbonates have flooded groundmass and partly replaced feldspars (Fig. 17E-F).

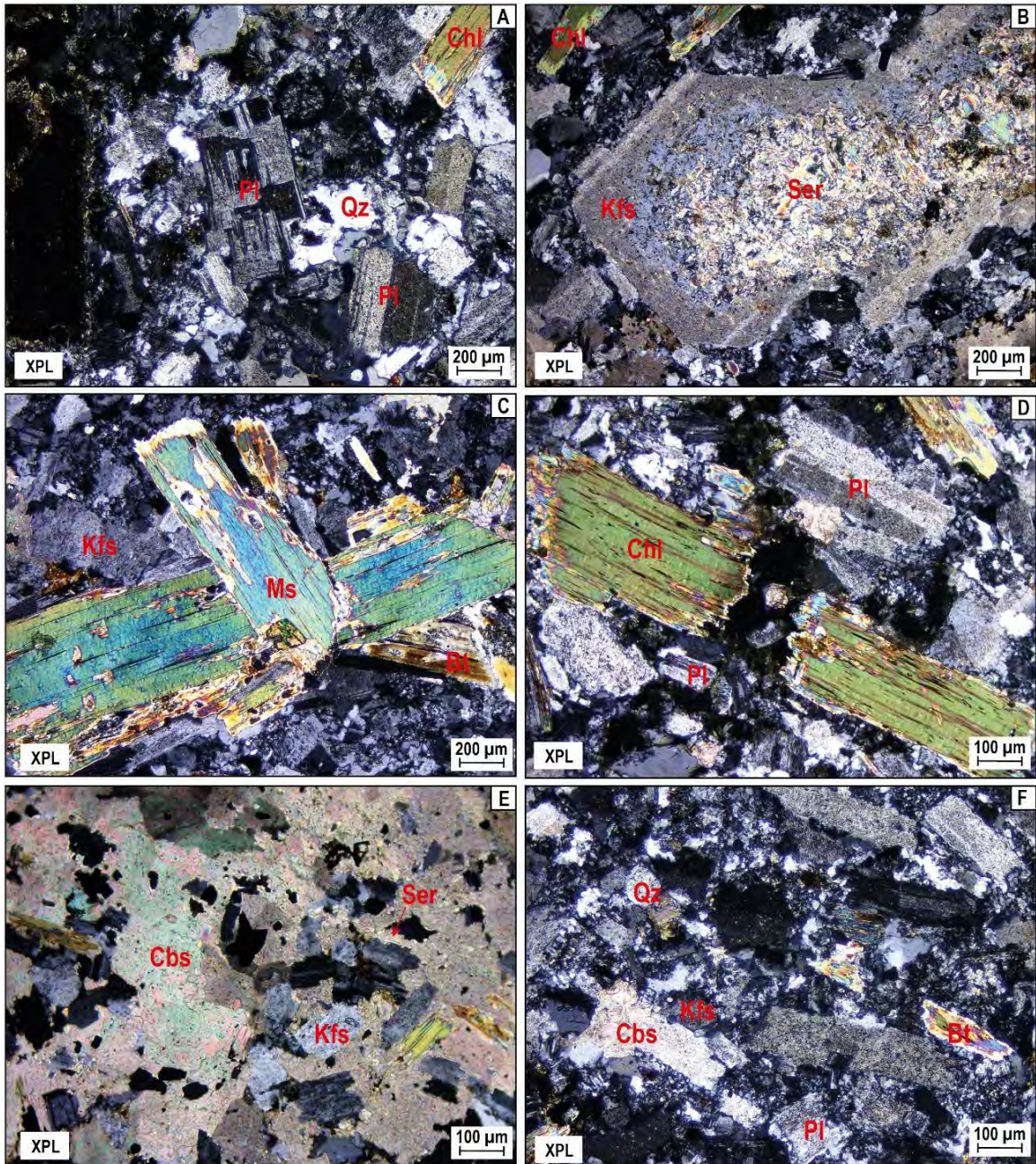


Figure 17. Representative transmitted-light images of monzodiorite (sample TC-23-04). (A) Plagioclase phenocrysts with “chessboard” textures along with less abundant quartz and biotite phenocrysts; (B) K-feldspar phenocryst that has been strongly sericitized within a quartzfeldspatic groundmass; (C) Subhedral muscovite laths partly altered to chlorite in a groundmass rich in K-feldspar; (D) Subhedral grains of mica obliterated by chlorite alteration within a quartzfeldspatic groundmass; (E) Patches of carbonates flooding the groundmass and partly replacing the phenocrysts; (F) Detail of the groundmass, which is mostly formed by K-feldspar and plagioclase and less abundant biotite laths; carbonate patches occur locally. Abbreviations: Bt—Biotite, Cbs—Carbonates, Chl—Chlorite, Kfs—K-feldspar, Ms—Muscovite, Pl—Plagioclase, Qz—Quartz, Ser—Sericite, XPL—Cross polarized light

4.1.1.4. Minette

In hand sample, the minette is greenish gray to black in color and exhibits a phaneritic texture with abundant black to dark brown phlogopite and whitish K-feldspar (Fig. 14D). Under the microscope, tabular phlogopite crystals show sizes up to 0.3 cm and exhibit common resorption textures (Fig. 18A-B). Anhedral K-feldspar crystals up to 0.2 cm in size fill spaces between phlogopite and pyroxene (Fig. 18A-C). Pyroxenes are only preserved as relicts up to 500 μm in size. The groundmass is composed of a wide range of mafic minerals, including biotite and pyroxene, as well as K-feldspar (Fig. 18C). The visually estimated primary mineral composition is as follows: phlogopite (55%), K-feldspar (40%), and pyroxene (5%). Carbonates occur filling interstitial spaces and often as patches that are up to 0.5 cm in size, flooding the groundmass and partly replacing feldspars and pyroxene (Fig. 18D-E). Finally, local acicular aggregates of possible zeolites that fill interstitial spaces (Fig. 18F). Alteration features include partial alteration of phlogopite crystals to chlorite (Fig. 18B) and partial albitization of K-feldspar grains. In addition, pyroxenes have been pervasively replaced by carbonates, resulting in serrated textures at the edges (Fig. 18C).

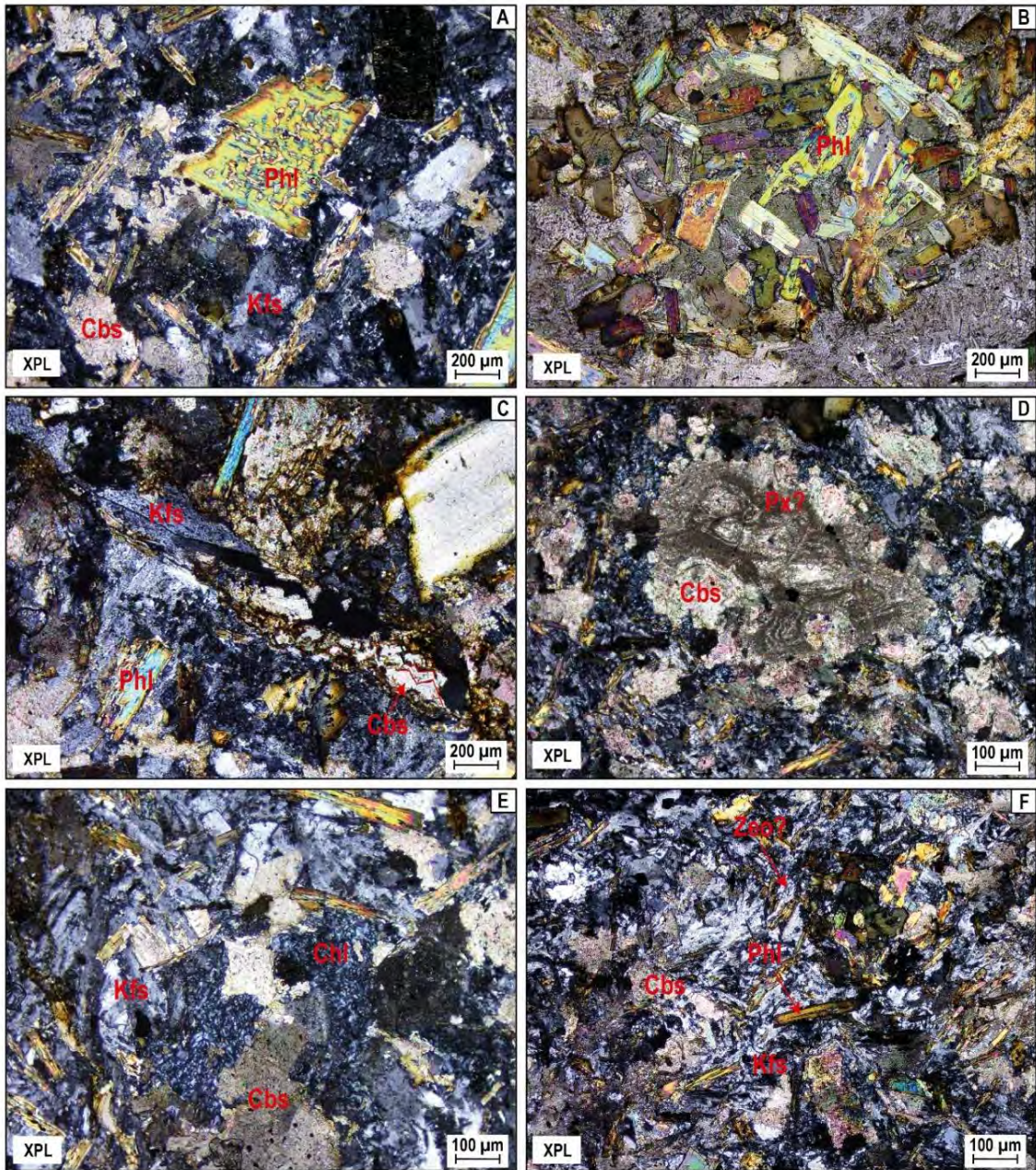


Figure 18. Representative transmitted-light images of minette (sample TC-23-03). (A) Phlogopite grain showing conspicuous resorption texture; (B) Phlogopite phenocrysts with resorption features and partly altered to chlorite within a K-feldspar-dominated groundmass; (C) Detail of K-feldspar partially altered to carbonates, with development of serrated texture at the edges; (D) Carbonate patches with remnant mold of possible pyroxene; (E) Abundant chlorite together with carbonates as open space and cavity fillers; (F) Acicular grains, possibly of zeolite, throughout the sample, in contact with feldspars, carbonates, and phlogopites. Abbreviations: Cbs—Carbonates, Chl—Chlorite, Kfs—K-feldspar, Phl—Phlogopite, Px—Pyroxene, XPL—Cross polarized light, Zeo—Zeolites

4.1.2. Ore samples

This investigation focused on the main mineralized bodies of the Kelly and Lorena systems. Since the ore mineralogy and alteration assemblages are similar for both mantos and veins within each system, they are described together below, with noted differences highlighted.

4.1.2.1. Kelly System

The Kelly mantos and veins contain a variety of metallic minerals, including pyrrhotite, pyrite, marcasite, cassiterite, sphalerite, chalcopyrite, stannite, and lesser amounts of arsenopyrite, franckeite, boulangierite, Ag-tetrahedrite-(Fe), galena, and native bismuth. Mantos are distinguished from veins by a distinctive skarn-like assemblage of green garnet (grossular and andradite), pyroxene (hedenbergite), and small amounts of quartz. In veins, pyrite is by far the predominant sulfide. In contrast, pyrrhotite is the most abundant sulfide in mantos. Cassiterite is present as anhedral aggregates of needle-like crystals (*var.* needle-tin), which are mostly found in secondary porosity within and interstitial space between pyrrhotite grains (Fig. 19A, F). Locally, pyrrhotite cuts across cassiterite aggregates (Fig. 19A), thus suggesting that both minerals could have been deposited during the same paragenetic episode. In general, pyrrhotite forms irregular and cariated grains that are partially replaced by pyrite, marcasite, chalcopyrite, stannite, and sphalerite. Fine intergrowths of pyrite, marcasite, and intermediate product formed as products of pyrrhotite replacement (Fig. 19A-B). This replacement is variable and includes pervasive cases in some vein samples in which only isolated islands of pyrrhotite within pyrite are preserved. Two generations of sphalerite and chalcopyrite have been identified. The first generation of chalcopyrite is characterized by anhedral grains with sizes reaching up to 250 μm , which have replaced pyrrhotite (Fig. 19C). The first generation of sphalerite is Fe-rich (7.5-12 wt.% Fe), hosts fine disseminations of

chalcopyrite (2nd generation), and has been partially replaced by pyrite and stannite (Fig. 19D). The second generation of sphalerite is Fe-poor (<1 wt.% Fe), characterized by its anhedral grains with sizes reaching up to 100 μm , and remarkably clean surfaces, and has also been partially replaced by pyrite (Fig. 19E). Scarce arsenopyrite appears as anhedral crystals or islands that have been replaced along their edges by pyrite (Fig. 19E). Galena and Ag-tetrahedrite-Fe occur as anhedral aggregates and are often intergrown with each other and appear in porosity in corroded pyrrhotite and in interstitial space between cassiterite crystals that are also found in this textural position (Fig. 19F). Lamellar aggregates of franckeite and boulangerite primarily occur within fractures, porosity, and interstices of pyrrhotite and pyrite (Fig. 19G). Native bismuth occurs as fine inclusions within galena and boulangerite (Fig. 19H). In the oxidation zone, minerals such as barite, anglesite, goethite, and hematite formed (Fig. 19I). The paragenetic sequence can be divided into four main stages (Fig. 20). Stage 0 is only observed in mantos and is characterized by a skarn-like assemblage of green garnet (grossular-andradite), pyroxene (hedenbergite), and lesser amounts of quartz. Stage I consists of a low-sulfidation assemblage that includes pyrrhotite, needle tin cassiterite, arsenopyrite, chalcopyrite (1st and 2nd generations), Fe-rich sphalerite (1st generation), and stannite. Subsequently, the minerals from this first stage were overprinted by intermediate-sulfidation assemblages of Stage II, which is divided into two sub-stages. During Stage IIa, subhedral to coarse anhedral pyrite \pm marcasite \pm intermediate product formed mostly as replacements of pyrrhotite. While this replacement was partial in mantos, it was more pervasive in veins. Stage IIb consists mainly of pyrite, Fe-poor sphalerite (2nd generation), galena, and minor amounts of Ag-tetrahedrite-(Fe), franckeite, boulangerite, and native bismuth. Finally, a supergene mineralization stage comprised the crystallization of goethite, hematite, barite, and anglesite.

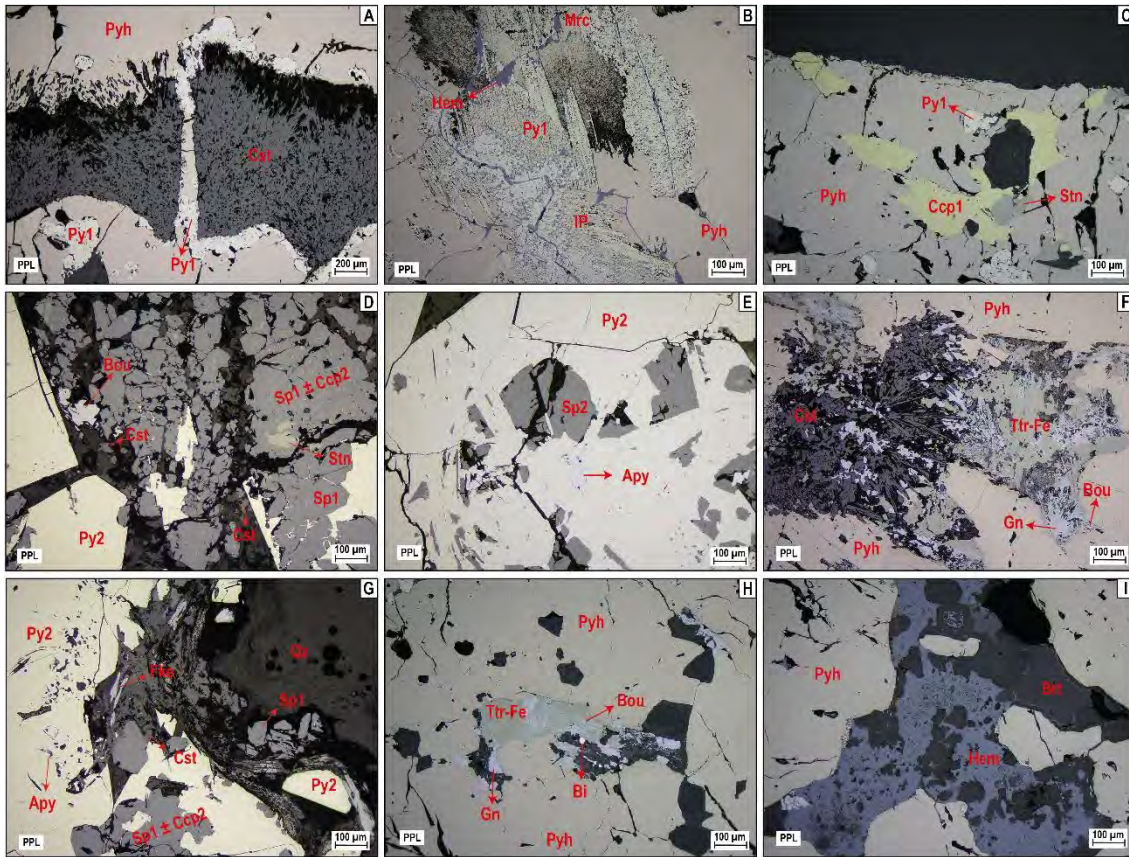


Figure 19. Photomicrographs of polymetallic mineralization in veins and mantos from the Kelly system. (A) Needle-tin cassiterite fills secondary porosity in corroded pyrrhotite, which has been partly replaced by pyrite + marcasite along grain boundaries; (B) Subhedral to coarse anhedral pyrite, marcasite, and intermediate product formed mainly as a replacement of pyrrhotite; (C) Pyrrhotite partly replaced from open spaces and cavities by chalcopyrite (1st generation) and stannite; (D) Isolated boulangerite crystal with sphalerite (1st generation) and fine disseminations of chalcopyrite (2nd generation) and pyrite as subhedral crystals; (E) Anhedral arsenopyrite and sphalerite grains replaced along their edges by pyrite; (F) Assemblage of galena, Ag-tetrahedrite-Fe and boulangerite crystals occupy interstitial space between cassiterite needles within open spaces in corroded pyrrhotite; (G) Isolated franckeite aggregates as infilling of cavities and open spaces of corroded pyrite along with quartz; (H) Galena with Ag-tetrahedrite-Fe finely intergrown with boulangerite and minute native bismuth grain in corroded pyrrhotite; (I) Anhedral aggregates of hematite as replacement of sulfides (mainly pyrrhotite, which is partly preserved in this sample) in the oxidation zone. Abbreviations: Ang—Anglesite, Apy—Arsenopyrite, Bi—Native bismuth, Bou—Boulangerite, Brt—Baryte, Ccp—Chalcopyrite, Cst—Cassiterite, Fke—Franckeite, Gn—Galena, Hem—Hematite, IP—Intermediate product, Mrc—Marcasite, Py—Pyrite, Pyh—Pyrrhotite, Qtz—Quartz, Sp—Sphalerite, Stn—Stannite, Ttr-Fe—Ag-Tetrahedrite-Fe, PPL—Plane Polarized Light

		Stage 0	Stage I (LS)	Stage II (IS)		Supergene
				Stage IIa (IS)	Stage IIb (IS)	
Garnet	$\text{Ca}_3\text{Al}_2(\text{SiO}_4)_3$	—				
Pyroxene	$\text{CaFeSi}_2\text{O}_6$	—				
Quartz	SiO_2	—	-----	-----	-----	
Pyrrhotite	Fe_{1-x}S		=====			
Cassiterite (<i>needle tin</i>)	SnO_2		—			
Arsenopyrite	FeAsS		—			
Fe-rich sphalerite	$(\text{Zn},\text{Fe})\text{S}$		—			
Chalcopyrite	CuFeS_2		-----			
Stannite	$\text{Cu}_2\text{FeSnS}_4$		—			
Pyrite	FeS_2			=====	-----	
Marcasite	FeS_2			=====		
Intermediate product	FeS_2			=====		
Fe-poor sphalerite	ZnS				—	
Ag-tetrahedrite-(Fe)	$(\text{Cu},\text{Ag})_{12}\text{Fe}_2\text{Sb}_4\text{S}_{13}$				—	
Galena	PbS				—	
Franckeite	$\text{Pb}_3\text{Sn}_3\text{Sb}_2\text{S}_{14}$				-----	
Boulangerite	$\text{Pb}_5\text{Sb}_4\text{S}_{11}$				-----	
Native bismuth	Bi				-----	
Baryte	BaSO_4					—
Anglesite	PbSO_4					—
Hematite	Fe_2O_3					—
Goethite	$\text{FeO}(\text{OH})$					—

Figure 20. Generalized paragenetic sequence for orebodies in the Kelly System. Bars indicate greater abundances, and dashed lines, lesser abundances

4.1.2.2. Lorena System

The Lorena mantos and veins contain a variety of metallic minerals, including pyrite, sphalerite, cassiterite, and lesser amounts of pyrrhotite, Ag-tetrahedrite-(Fe), galena, acanthite, boulangerite, and bournonite. Cassiterite is observed as anhedral to subhedral acicular grains (var. needle-tin) forming porous aggregates that may reach up to 1 mm in size. Cassiterite aggregates fill secondary porosity on and interstitial space between cariated pyrrhotite grains, which in most cases have been pervasively replaced by pyrite (Fig. 21A), as evidenced by remnants of the former occluded within the latter (Fig. 21B). Sphalerite is Fe-poor and forms anhedral aggregates with clean surfaces and yellow-orange internal reflections (Fig. 21C). Galena occurs as anhedral grains replacing, or in interstitial space between, sphalerite (Fig. 21C) and pyrite grains, often in the matrix

assemblage also including quartz and baryte in brecciated samples (Fig. 21D). Ag-tetrahedrite-(Fe) occurs as anhedral aggregates that replaced and cemented pyrite grains in the matrix of breccia samples (Fig. 21E), similar to bournonite aggregates with their characteristic wheel-like twinning and boulangerite, which have also replaced chalcopyrite and Ag-tetrahedrite-Fe (Fig. 21F-G). In the oxidation zone, minerals such as goethite, hematite, and barite, minor anglesite, and traces of acanthite formed (Fig. 21H-I). According to these observations, the paragenetic sequence can be divided into three main stages (Fig. 22). Stage I corresponds to a low-sulfidation assemblage of pyrrhotite and cassiterite. Subsequently, the minerals from this first stage were overprinted by later intermediate-sulfidation assemblages of Stage II. During Stage IIa, anhedral to subhedral pyrite formed as a replacement of pyrrhotite, a very dominant phenomenon in the Lorena system. Stage IIb is primarily composed of pyrite, Fe-poor sphalerite, galena, Ag-tetrahedrite-(Fe), boulangerite, and bournonite. Finally, a supergene stage comprised the deposition of goethite, hematite, anglesite, and acanthite.

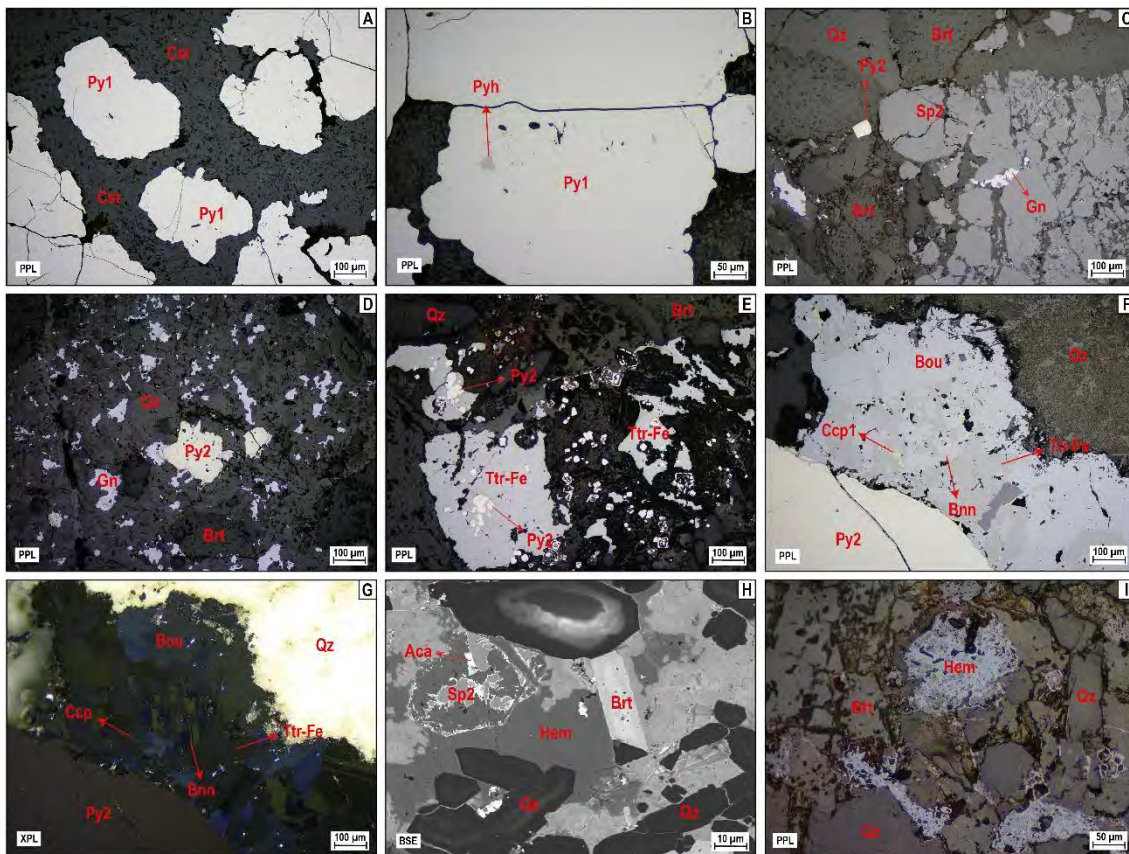


Figure 21. Photomicrographs of the polymetallic mineralization in veins and mantos from the Lorena System. (A) Cassiterite (var. needle tin) form porous aggregates that fill secondary porosity and spaces left by cariated pyrite formed through pervasive replacement of pyrrhotite; (B) Pyrrhotite occlusions within pyrite; (C) Anhedral aggregates of sphalerite with interstitial space filled with galena and quartz; (D) Anhedral galena grains occupying secondary porosity and interstitial space between anhedral quartz and pyrite; galena has also incipiently replaced pyrite along grain boundaries; (E) Anhedral Ag-tetraehedrite-Fe that has pervasively replaced pyrite, which is only preserved as minute, roundish grains; (F) Finely intergrown boulangerite and bournonite as a replacement of Ag-tetraehedrite-Fe and chalcopyrite interstitial to pyrite and quartz; (G) Same area as F in crossed polars; note the bournonite crystals with their characteristic wheel-like twins; (H) Brecciated texture in superficial sample with sphalerite remnants and quartz fragments cemented by a supergene assemblage of barite, hematite, and acanthite; (I) Brecciated sample with remnants of sphalerite and fragments of quartz cemented by a supergene assemblage of hematite, barite, and local acanthite in the surface oxidation zone. Abbreviations: Aca—Acanthite, Bnn—Bournonite, Bou—Boulangerite, Brt—Barite, Ccp—Chalcopyrite, Cst—Cassiterite, Gn—Galena, Hem—Hematite, Py—Pyrite, Pyh—Pyrrhotite, Qz—Quartz, Sp—Sphalerite, Ttr-Fe—Ag-Tetraehedrite-Fe, PPL—Plane Polarized Light, XPL—Cross Polarized Light, BSE—Backscattered electron image

		Stage II (IS)			
		Stage I (LS)	Stage IIa (IS)	Stage IIb (IS)	Supergene
Quartz	SiO ₂	-----	-----	-----	-----
Pyrrhotite	Fe _{1-x} S	-----			
Cassiterite	SnO ₂	_____			
Pyrite	FeS ₂		_____	-----	
Fe-poor sphalerite	ZnS			_____	
Ag-tetrahedrite-(Fe)	(Cu, Ag) ₁₂ Fe ₂ Sb ₄ S ₁₃			_____	
Galena	PbS			_____	
Boulangerite	Pb ₅ Sb ₄ S ₁₁			-----	
Bournonite	PbCuSbS ₃			-----	
Acanthite	Ag ₂ S				-----
Baryte	BaSO ₄				_____
Anglesite	PbSO ₄				_____
Hematite	Fe ₂ O ₃				_____
Goethite	FeO(OH)				_____

Figure 22. Generalized paragenetic sequence for orebodies in the Lorena System. Bars indicate greater abundances, and dashed lines, lesser abundances

4.2. Whole-rock element geochemistry

Analyzed intrusive samples from Taucane include granitoids (TC-23-01, TC-23-02, TC-23-04) and minette (TC-23-03). The litho-geochemistry of the minette will be addressed separately, but it is included in the general diagrams for granitoids as a reference to illustrate the compositional contrast. The whole-rock composition of the intrusive rocks is plotted in diagrams shown in Figures 23–27, and the dataset is presented in Table 2.

Granitoids show LOI values between 2.1 (Quartz-monzodiorite) and 4.2 wt.% (monzodiorite), and SiO₂ between 65.4 and 71.2 wt.%. They yield similar alkali (K₂O + Na₂O = 9.05–9.50 wt.%), Al₂O₃ (14.8–15.4 wt.%), and MgO (1.20–2.46 wt.%) contents. Harker's diagrams reveal decreasing contents of MgO, Fe₂O₃, and CaO with increasing SiO₂ (Fig. 23A-C). The chemical composition of the monzodiorite sample is intermediate between the most mafic and most felsic samples. CaO contents are contrasting between the samples, in the range between 0.46 wt.% (monzogranite) and 3.13 wt.%

(monzodiorite; Fig. 23C). A similar situation occurs with Na₂O contents, ranging between 3.2 wt.% (monzogranite) and 8 wt.% (monzodiorite; Fig. 23D). The K₂O content of the monzodiorite is extremely low (1.1 wt.%) compared to the other samples (Fig. 23E). Other elements, such as TiO₂ (0.26–0.46 wt.%), MnO (0.04–0.06 wt.%), and P₂O₅ (0.26–0.41 wt.%) are present in smaller amounts.

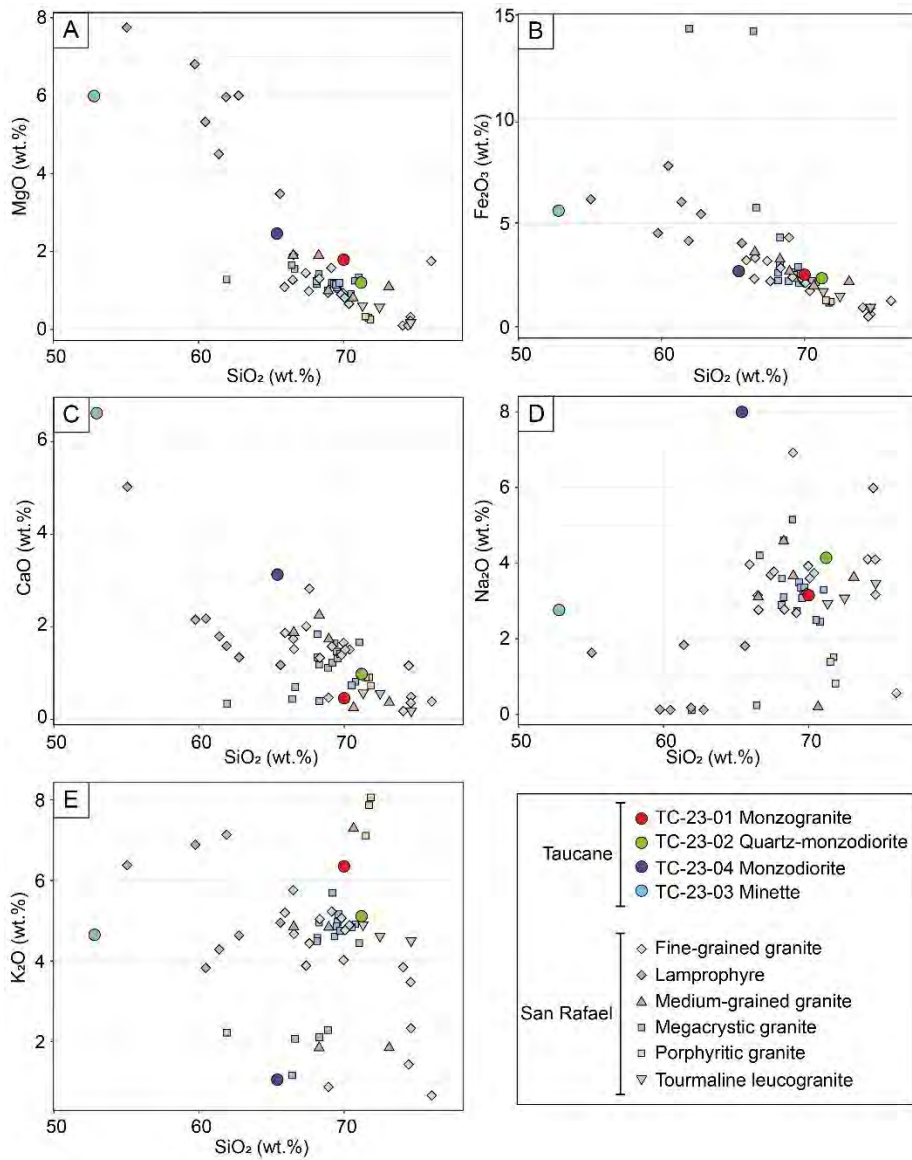


Figure 23. Harker diagrams of major and minor oxides from Taucane

Table 2: Major and trace element contents

Sample	TC-23-01	TC-23-02	TC-23-04	TC-23-03
Lithology	Monzogranite	Quartz-monzodiorite	Monzodiorite	Minette
Major oxides (wt.%)				
SiO ₂	70.0	71.2	65.4	52.8
Al ₂ O ₃	15.4	15.3	14.8	12.5
K ₂ O	6.4	5.1	1.1	4.7
Na ₂ O	3.2	4.1	8.0	2.8
Fe ₂ O ₃	2.5	2.3	2.7	5.6
MgO	1.8	1.2	2.5	6.0
CaO	0.5	1.0	3.1	6.6
TiO ₂	0.4	0.3	0.5	0.9
P ₂ O ₅	0.3	0.3	0.4	0.8
MnO	0.0	0.1	0.0	0.2
LOI	2.4	2.1	4.2	9.1
Total	100.4	102.9	98.4	92.8
Trace elements (ppm)				
Li	b.d.l.	b.d.l.	b.d.l.	b.d.l.
Be	21.7	22.4	17.5	10.1
Sc	9.1	7.4	12.6	19.3
Ti	2132	1466	2675	4903
V	40.6	32.7	73.9	132
Cr	93.0	63.0	106	461
Mn	281	450	305	1352
Co	4.3	6.4	6.1	26.6
Ni	14.4	17.8	19.0	54.7
Cu	4.6	1.9	1.8	3.0
Zn	22.2	39.4	16.6	207
Ga	18.3	18.9	17.6	17.0
Ge	2.3	2.6	1.8	2.8
As	41.6	8.6	4.1	39.8
Se	b.d.l.	b.d.l.	b.d.l.	b.d.l.
Rb	321	304	73.3	175
Sr	300	214	168	205
Y	13.4	16.0	16.9	22.3
Zr	222	132	177	308
Nb	17.8	16.5	16.2	22.3
Mo	3.6	2.5	4.2	3.3
Sn	18.4	21.8	8.3	4.6
Sb	1.3	0.7	2.2	5.7
Te	b.d.l.	b.d.l.	b.d.l.	b.d.l.
Cs	5.5	20.3	5.9	8.4
Ba	1838	1440	1257	4111
La	21.0	26.2	66.0	73.3
Ce	46.8	48.8	98.4	145
Pr	5.7	5.5	9.9	17.3
Nd	23.3	20.5	35.2	66.9
Sm	4.7	4.1	6.2	11.8
Eu	0.9	1.2	1.0	2.8
Gd	3.3	3.3	4.5	7.9
Tb	0.5	0.5	0.6	0.9
Dy	2.7	2.8	3.1	4.7
Ho	0.5	0.5	0.6	0.9
Er	1.5	1.5	1.7	2.0
Tm	0.2	0.2	0.2	0.3
Yb	1.5	1.6	1.5	1.8
Lu	0.2	0.2	0.2	0.3

Sample	TC-23-01	TC-23-02	TC-23-04	TC-23-03
Lithology	Monzogranite	Quartz-monzodiorite	Monzodiorite	Minette
Hf	6.6	4.1	4.9	8.2
Ta	2.4	3.0	2.4	1.4
W	9.2	6.8	2.4	4.8
Tl	1.7	1.4	0.2	0.4
Pb	55.7	89.9	1.7	20.6
Bi	0.3	0.2	0.0	0.3
Th	36.8	13.7	20.9	29.2
U	9.1	6.5	9.1	6.7
ΣREE	113	117	229	336
(La/Yb)CN	9.4	11.0	29.2	27.8
(Eu/Eu*)CN	0.7	1.0	0.6	0.9
Nb/Ta	7.4	5.5	6.8	15.7
Zr/Hf	33.5	32.1	36.0	37.7
Mineral-chemical parameters				
A/NK	1.3	1.2	1.0	1.3
A/CNK	1.2	1.1	0.7	0.6
A=Al-(K+Na+2Ca)	49.3	23.1	-102	-179
B=Fe+Mg+Ti	80.8	62.3	100	230
Q=Si/3-(K+Na+2Ca/3)	147	141	45.2	26.5
P=K-(Na+Ca)	25.0	-42.6	-292	-108

b.d.l. = below detection limit

ΣREE = sum of lanthanides (La to Lu)

The values of A/NK, A/CNK, A, B, Q, and P were calculated based on the major oxides

In the total alkalis vs silica (TAS) diagram, the monzogranite and quartz-monzodiorite samples appear in the granite field, and the monzodiorite sample fall into the quartz-monzodiorite field (Fig. 24A). The granitoids yield molar A/CNK $[Al_2O_3/(CaO+Na_2O+K_2O)]$ of 0.74-1.20 and A/NK $[Al_2O_3/(Na_2O+K_2O)]$ of 1.04-1.28. In the A/CNK vs A/NK diagram (Fig. 24B), the monzogranite and quartz-monzodiorite samples belong to the peraluminous field, whereas the monzodiorite sample is situated in the metaluminous domain. This is supported by diagrams B-A (Fig. 24C) and P-Q (Fig. 24D), the monzogranite and quartz-monzodiorite samples fall into the granite field and exhibit slightly to moderately peraluminous compositions, whereas the monzodiorite sample matches the quartz-diorite field and exhibits a metaluminous composition. The monzogranite and quartz-monzodiorite samples from Taucane have similar compositions to most granitoids from San Rafael. In contrast, the monzodiorite sample from Taucane yielded higher Na_2O , and CaO , and lower Al_2O_3 than most granitoids from San Rafael.

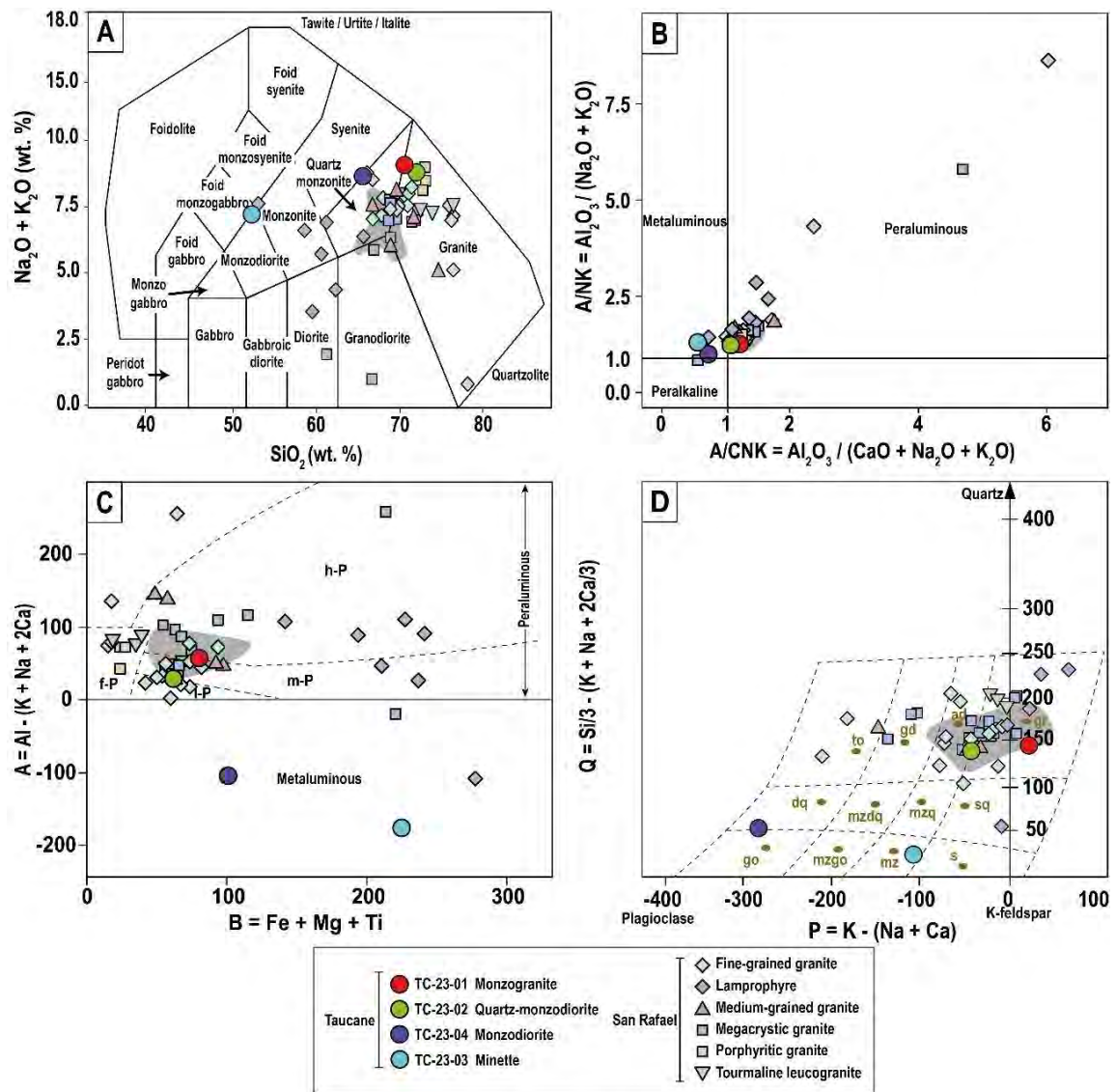


Figure 24. Geochemical diagrams for intrusive rocks from the Taucane Project. (A) Total alkali-silica (TAS) diagram after Middlemost (1994), representing the $\text{Na}_2\text{O} + \text{K}_2\text{O}$ vs SiO_2 contents; (B) Alumina saturation diagram representing the molar ratio $\text{A/NK} = \text{Al}_2\text{O}_3 / (\text{Na}_2\text{O} + \text{K}_2\text{O})$ as function of the molar ratio $\text{A/CNK} = \text{Al}_2\text{O}_3 / (\text{CaO} + \text{Na}_2\text{O} + \text{K}_2\text{O})$ after Shand (1943); (C) B-A diagram representing the differentiation index $B = \text{Fe} + \text{Mg} + \text{Ti}$ as function of the peraluminous index $A = \text{Al} - (\text{Na} + \text{K} + 2\text{Ca})$ expressed in millications. The subdivision of the peraluminous domains corresponds to: low peraluminous (l-P), moderately peraluminous (m-P), highly peraluminous (h-P), and felsic peraluminous (f-P), after Villaseca et al. (1998); (D) P-Q diagram, after Bonin et al. (2020), representing the relative proportion of feldspars ($P = \text{K} - (\text{Na} + \text{Ca})$) as function of the quartz content ($Q = \text{Si}/3 - (\text{Na} + \text{K} + 2\text{Ca}/3)$) expressed in millications. Millications represent 10^3 gram-atoms for 100 g of rock and are obtained by dividing the concentration of each oxide (in wt.%) by a factor obtained by dividing the molecular weight by the number of metallic atoms (cations) in the oxide formula, and then multiplied by 10^3 (Debon and Le Fort 1988). Bibliographic data on the San Rafael Intrusive Complex is shown for comparison (symbols identify different lithologies analyzed by Harlaux et al. 2021 and light grey fields represent data for the “least altered San Rafael megacrystic granite” from Kontak and Clark 2002 and Mlynarczyk 2005)

Compared to the upper continental crust (UCC), all granitoids exhibit strong enrichment in Be, Sn, Ta, Th, and U (Fig. 25A), ranging from five to ten times UCC values. Additionally, the monzogranite and quartz-monzodiorite samples show enrichment in Rb, Ba, Ta, W, and Pb, up to five times compared to the UCC. Enrichment in Cs and Sb has been observed in the quartz-monzodiorite and monzodiorite samples, up to five times compared to the UCC. In contrast, all granitoids are depleted in Cu, Y, Zn, and Sr relative to the UCC, and the monzodiorite sample is also depleted in Pb and Bi compared to the UCC. Compared with granitoids from San Rafael, the Taucane granitoids have similar contents of Be, Rb, Nb, Sn, Pb, Ta, W, and U.

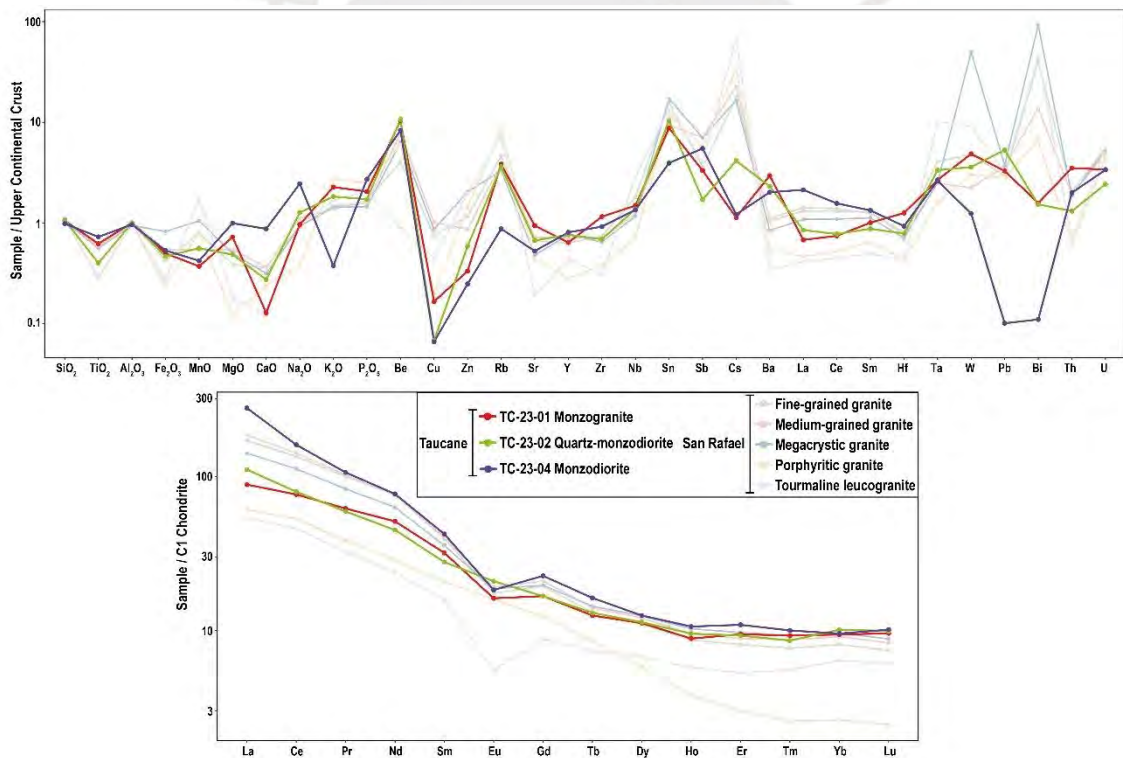


Figure 25. Normalized multi-element diagrams of major and trace elements in intrusive rocks from Taucane. (A) Major and trace elements contents normalized to upper continental crust values of Rudnick and Gao (2014); (B) Rare earth element contents normalized to C1 chondrite values of McDonough and Sun (1995). Bibliographic data of granitoids from the San Rafael intrusive complex (Harlaux et al. 2021) are shown for comparison

Granitoids yield individual rare earth element (REE) values that are ~10 to 300 times enriched relative to C1 chondrite values (Fig. 25B). Chondrite-normalized (CN) REE patterns show a negative slope from light (LREE) to heavy REE (HREE) [(La/Sm)_{CN} = 2.78 - 6.59, (Sm/Yb)_{CN} = 2.76 - 4.43] and moderate to subtle negative Eu anomalies [(Eu/Eu*)_{CN} = 0.59 - 0.97]. In general, the monzogranite and quartz monzodiorite show total REE contents (ΣREE = 113-117 ppm) similar to most granitoids from San Rafael, whereas the monzodiorite has higher ΣREE (229 ppm).

As expected, the minette sample yielded lower SiO₂ (52.80 wt.%) and alkalis (7.41 wt.%; K₂O/Na₂O = 1.69) and higher MgO (5.99 wt.%), CaO (6.62 wt.%), and TiO₂ (0.89 wt.%) compared to granitoids, reflecting its mafic affinity. In the MgO vs K₂O plot, the minette falls in the field of ultrapotassic rocks with both K₂O and MgO values exceeding 3 wt.% (Fig. 26A). In the Na₂O vs K₂O plot, however, the sample matches the shoshonitic domain, close to its boundary with the ultrapotassic field, due to its K₂O/Na₂O < 2 (Fig. 26B). This fact contrasts with lamprophyres from San Rafael, which systematically classify as ultrapotassic (Fig. 26).

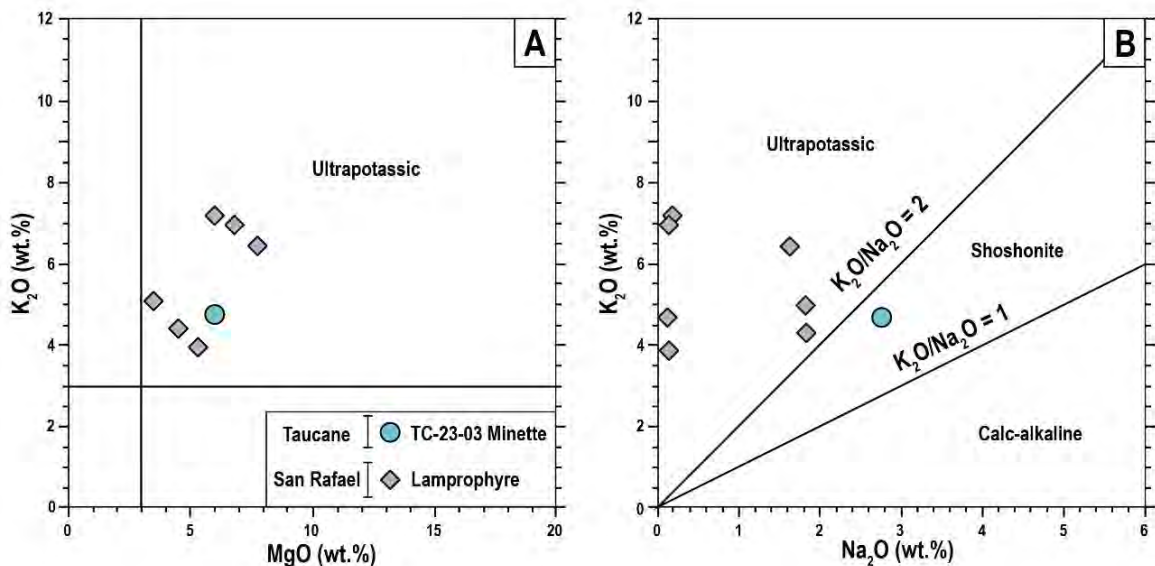


Figure 26. Binary diagrams of major element oxides for the Taucane minette after Foley et al. (1987).

(A) K₂O vs MgO; (B) K₂O vs Na₂O plot

Compared to the primitive mantle (PM), the minette exhibits strong enrichment in large-ion lithophile elements (LILE; Rb, Ba, Th, U, Pb) and high-field-strength elements (HFSE; Nb, Ta, Zr, Hf, Ti). LILE are enriched to almost 1,000 times the PM values, and HFSE are enriched between 10 and 100 times the PM values (Fig. 27A).

Individual REE values are 10 to 300 times enriched relative to C1 chondrite values (Fig. 27B). The CN REE pattern shows a steep negative slope $[(La/Sm)_{CN} = 3.87, (Sm/Yb)_{CN} = 7.17]$ that tends to be asymptotic for HREE. In general, trace element contents and patterns of the Taucane minette are similar to those of lamprophyres from San Rafael with the prominent exception of Pb. Lead exhibits a wide range of contents in the San Rafael lamprophyres—both lower and higher than Pb contents in the Taucane minette (Fig. 27A).

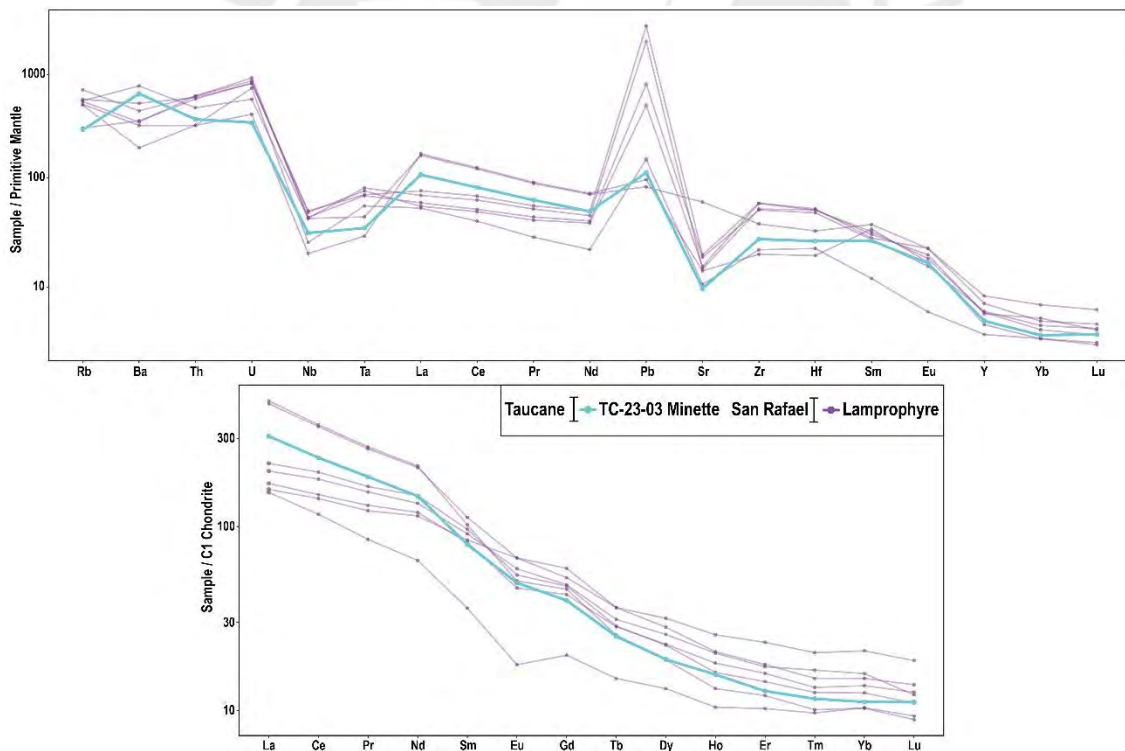


Figure 27. Normalized multi-element diagrams of major and trace elements in minette from Taucane. (A) Trace element contents normalized to primitive mantle values of Sun and McDonough (1989); (B) Rare earth element contents normalized to chondrite values of McDonough and Sun (1995). Bibliographic data of lamprophyres from the San Rafael intrusive complex (Harlaux et al. 2021) are shown for comparison

4.3. Cassiterite mineral geochemistry

4.3.1. Major and minor elements

Point analyses in the cassiterite grains reveal SnO₂ contents in the range between 96.47 and 100.61 wt.% (mean value $\pm 2\sigma = 98.06 \pm 1.79$; Table 3). Other measured elements that generally exceed their lower limit of detection with EPMA are FeO (<d.l. to 2.41 wt.%) and TiO₂ (<d.l. to 1.13 wt.%). The other elements measured by EMPA are systematically below their respective detection limits, including ZrO₂, Nb₂O₅, Ta₂O₅, and MnO. In general, cassiterite from the Kelly system shows higher FeO (1.29 ± 0.98 wt.%) compared to cassiterite from the Lorena system (0.14 ± 0.54 wt.% FeO; Fig. 28). A negative correlation is observed between SnO₂ and FeO for cassiterite from Kelly ($R^2 = 1$).

4.3.2. Trace elements

Cassiterite trace element data are illustrated in Figures 29 to 32. A complete set of box plots showing the contents of all elements analyzed by LA-ICP-MS is provided in Appendix J, and a selection of these is presented in Figure 29. Table 4 presents the statistical data for all elements analyzed. Trace element contents in this section will be expressed as interquartile ranges (IQR) unless otherwise indicated.

Cassiterite from Taucane yielded a broad spectrum of trace element contents. High contents (more than hundreds of ppm) were found for W (324—95.1 ppm), Ti (287—93.4 ppm), Sb (219—85.5 ppm), and V (199—62.8 ppm). Moderate contents (from hundreds to tens of ppm) were detected for Ni (96.11—35.61 ppm), In (38.2—9.30 ppm), Mn (22.07—8.99 ppm), Ga (19.03—4.98 ppm), Pb (17.6—1.39 ppm), As (17.49—1.80 ppm), Co (15.7—6.08 ppm), and Zr (10.66—2.80 ppm). Low contents (mostly from tens to a few ppm) were found for Zn (6.68—1.13 ppm), U (4.70—1.51 ppm), Sc (4.31—1.28

ppm), Cu (2.47—0.17 ppm), Nb (2.33—0.70 ppm), Ce (1.56—0.38 ppm), and Th (1.53—0.31 ppm). The other analyzed elements yielded very low contents (less than units of ppm), including Ge, Se, Y, Mo, Ag, Cd, La, Pr, Nd, Sm, Eu, Dy, Ho, Er, Tm, Yb, Lu, Hf, Ta, and Bi (Table 4).

Table 3. Major and minor element contents of cassiterite from Taucane (EPMA data)

	Min	Max	GM	2 σ	IQR
All data					
SnO ₂	96.47	100.61	98.06	1.79	98.69-97.35
ZrO ₂	b.d.l.	b.d.l.	-	-	-
Nb ₂ O ₅	b.d.l.	b.d.l.	-	-	-
FeO	b.d.l.	2.41	0.79	1.35	1.66-0.50
MnO	b.d.l.	b.d.l.	-	-	-
TiO ₂	b.d.l.	1.13	0.06	0.24	0.09-0.08
Ta ₂ O ₅	b.d.l.	b.d.l.	-	-	-
Kelly					
SnO ₂	96.47	100.61	97.84	1.63	98.31-97.28
ZrO ₂	b.d.l.	b.d.l.	-	-	-
Nb ₂ O ₅	b.d.l.	b.d.l.	-	-	-
FeO	b.d.l.	2.41	1.29	0.98	1.69-1.25
MnO	b.d.l.	b.d.l.	-	-	-
TiO ₂	b.d.l.	0.11	0.05	0.01	0.06-0.05
Ta ₂ O ₅	b.d.l.	b.d.l.	-	-	-
Lorena					
SnO ₂	97.18	100.38	98.84	1.44	99.43-98.57
ZrO ₂	b.d.l.	b.d.l.	-	-	-
Nb ₂ O ₅	b.d.l.	b.d.l.	-	-	-
FeO	b.d.l.	1.29	0.14	0.54	0.50-0.28
MnO	b.d.l.	b.d.l.	-	-	-
TiO ₂	b.d.l.	1.13	0.11	0.45	0.22-0.05
Ta ₂ O ₅	b.d.l.	b.d.l.	-	-	-

Min—minimum; Max—maximum; GM—Geometric mean; IQR—Interquartile range

b.d.l.—below detection limit

For GM, 2 σ , and IQR calculation, data below the detection limit (b.d.l.) were replaced by half the limit for the statistics calculation

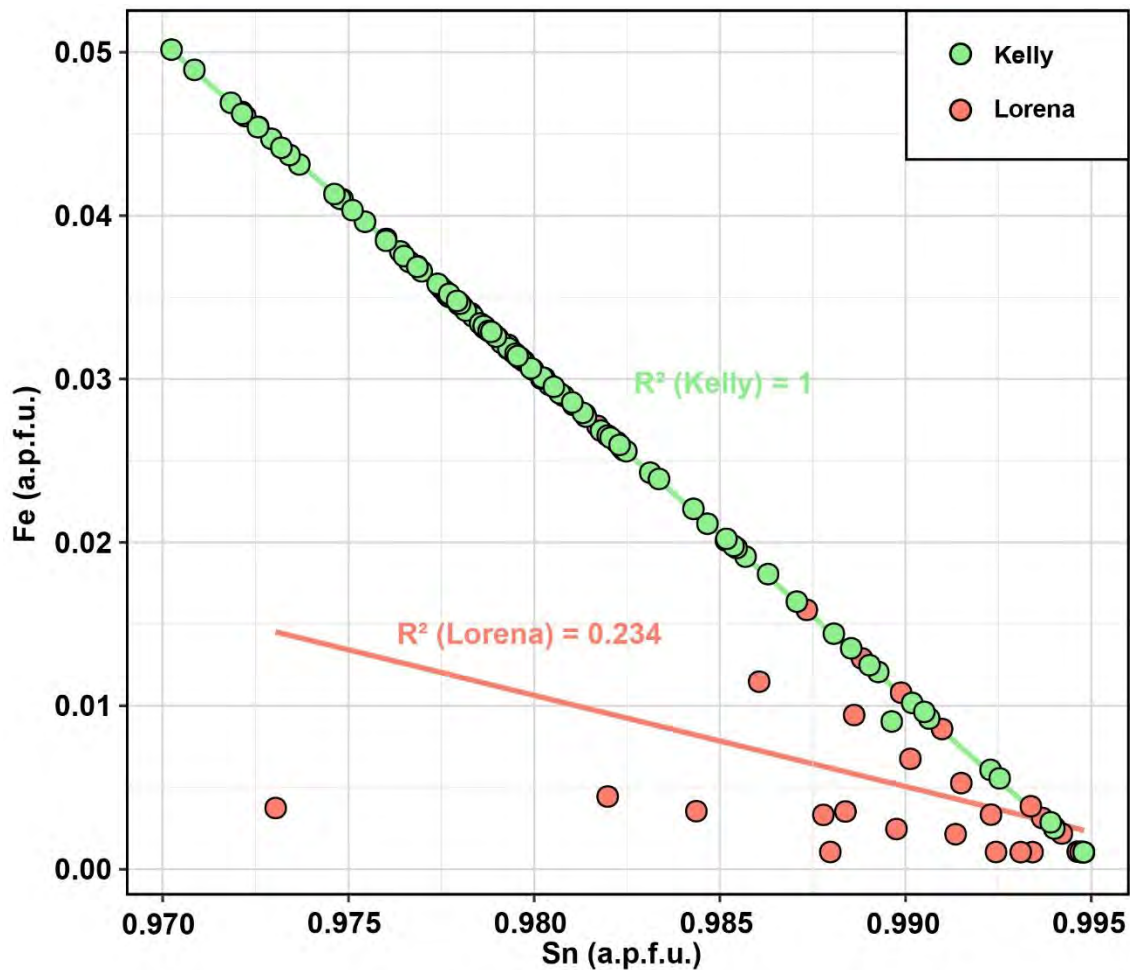


Figure 28. Binary SnO_2 vs FeO correlation diagram for cassiterite from Taucane (EMPA data)

To validate the consistency between the results obtained by EPMA and LA-ICP-MS, the Ti values were compared. The Ti contents expressed in wt.% were converted to Ti (ppm) using the stoichiometric ratio between TiO_2 and Ti. The Ti content obtained by EPMA ranged from <d.l. to 6,764 ppm, which is broadly equivalent to the Ti content obtained by LA-ICP-MS, ranging from 4.86 to 6,334 ppm. Likewise, EPMA values for cassiterite from Kelly ranged from <d.l. to 658 ppm, and LA-ICP-MS values ranged from 4.86 to 552 ppm. EPMA values for Lorena ranged from <d.l. to 6,764 ppm, and LA-ICP-MS values ranged from 24.3 to 6,334 ppm.

Table 4. Trace element contents of cassiterite from Taucane (LA-ICP-MS data)

	ppm	Sc	Ti	V	Mn	Co	Ni	Cu	Zn	Ga	Ge	As
All data	Min	0.08	4.86	3.24	0.25	0.22	1.29	0.001	0.05	0.14	0.01	0.06
	Max	81.7	6334	1520	274	104	628	15220	275	235	17.4	1392
	GM	2.5	183	110	13.71	9.61	57	0.63	2.63	9.78	0.30	5.19
	2σ	26.4	2011	429	84.8	31.1	190	2315	43.5	56	4.83	251
	IQR	4.31—1.28	287—93.4	199—62.8	22.07—8.99	15.7—6.08	96.11—35.61	2.47—0.17	6.68—1.13	19.03—4.98	0.52—0.13	17.49—1.80
Kelly	Min	0.08	4.86	3.24	0.51	0.37	2.25	0.001	0.05	0.23	0.01	0.06
	Max	21.7	552	278	274	28.4	176	15220	275	23.4	1.53	252
	GM	1.60	116	88.9	12.0	7.90	46.6	0.36	2.17	7.33	0.17	2.40
	2σ	5.01	208	145	82.2	11.9	73.8	2593	48.2	13.5	0.47	44.6
	IQR	3.21—1.02	207—72.91	185—52.7	15.4—8.25	13.4—4.63	81.9—25.7	0.76—0.14	5.31—0.95	16.6—4.03	0.26—0.11	3.32—1.39
Lorena	Min	0.35	24.32	3.59	0.25	0.22	1.29	0.11	0.07	0.14	0.04	2.67
	Max	81.7	6334	1520	218	104	628	34.2	28.91	235	17.4	1392
	GM	14.4	1051	254	23.2	20.6	125	5.39	5.53	30.0	2.72	105
	2σ	43.8	3354	738	89.7	53.19	323	15.8	15.0	100	7.95	449
	IQR	31—8.26	2888—658	610—162	52.0—18.1	38.2—14.5	234—88.7	10.07—3.42	12.7—3.5	50.7—17.5	5.6—1.9	222—69.1

	ppm	Se	Y	Zr	Nb	Mo	Ag	Cd	In	Sb	La
All data	Min	0.002	0.01	0.21	0.03	0.0002	0.0001	0.0021	0.11	3.52	0.01
	Max	12.5	38.5	102	90.2	1.28	483	3.19	128	2172	19.2
	GM	0.14	0.54	5.30	1.48	0.01	0.02	0.13	18.7	132	0.34
	2σ	1.92	9.08	30.3	26.1	0.36	77.1	0.62	43.2	619	3.97
	IQR	0.32—0.059	0.78—0.27	10.66—2.80	2.33—0.70	0.013—0.00	0.18—0.002	0.22—0.091	38.2—9.30	219—85.5	0.69—0.18
Kelly	Min	0.003	0.01	0.21	0.03	0.0002	0.0001	0.005	1.05	4.95	0.01
	Max	4.38	1.72	39.3	4.52	0.04	483	3.19	88.0	2172	1.36
	GM	0.12	0.32	3.94	0.89	0.00	0.01	0.11	20.9	111	0.23
	2σ	0.78	0.60	11.0	1.59	0.01	86.2	0.62	35.2	512	0.49
	IQR	0.27—0.05	0.49—0.23	6.96—2.65	1.64—0.61	0.01—0.00	0.02—0.00	0.18—0.07	38.3—12.6	187—73.7	0.36—0.16
Lorena	Min	0.00	0.06	0.36	0.29	0.00	0.01	0.00	0.11	3.52	0.02
	Max	12.5	38.5	102	90.2	1.28	2.05	1.11	128	2165	19.2
	GM	0.33	4.35	16.7	10.6	0.11	0.22	0.22	12.2	256	1.55
	2σ	3.79	15.9	50.6	45.8	0.67	0.85	0.56	66.0	841	7.54
	IQR	0.9—0.2	10.1—3.0	44.7—10.4	29.4—5.4	0.3—0.0	0.5—0.2	0.4—0.1	37.8—5.9	574—193	3.5—0.9

	ppm	Ce	Pr	Nd	Sm	Eu	Dy	Ho	Er	Tm
All data	Min	0.02	0.002	0.01	0.001	0.002	0.001	0.0003	0.001	0.0002
	Max	52.5	7.57	34.6	11.1	7.13	10.3	1.81	5.21	0.81
	GM	0.75	0.09	0.39	0.09	0.07	0.09	0.02	0.08	0.02
	2σ	10.86	1.58	7.26	2.42	1.54	2.43	0.44	1.29	0.21
	IQR	1.56—0.38	0.18—0.047	0.71—0.19	0.15—0.039	0.21—0.026	0.16—0.035	0.036—0.009	0.12—0.037	0.024—0.009
Kelly	Min	0.02	0.002	0.01	0.001	0.002	0.001	0.0003	0.001	0.0002
	Max	2.67	0.32	1.24	0.37	0.59	0.39	0.08	0.27	0.05
	GM	0.49	0.06	0.23	0.05	0.04	0.05	0.01	0.05	0.01
	2σ	1.04	0.12	0.47	0.11	0.20	0.13	0.03	0.09	0.02
	IQR	0.73—0.36	0.09—0.04	0.33—0.18	0.07—0.04	0.05—0.02	0.07—0.03	0.02—0.01	0.07—0.03	0.02—0.01
Lorena	Min	0.04	0.01	0.03	0.01	0.01	0.02	0.00	0.01	0.00
	Max	52.5	7.57	34.6	11.1	7.13	10.3	1.81	5.21	0.81
	GM	4.07	0.60	2.77	0.99	0.66	1.15	0.21	0.66	0.11
	2σ	20.6	3.00	13.6	4.45	2.79	4.24	0.76	2.21	0.35
	IQR	9.5—2.3	1.37—0.34	6.64—1.63	2.27—0.65	1.48—0.42	2.73—0.83	0.51—0.16	1.56—0.50	0.27—0.08

	ppm	Yb	Lu	Hf	Ta	W	Pb	Bi	Th	U
All data	Min	0.003	0.001	0.005	0.0003	2.37	0.03	0.0002	0.01	0.08
	Max	6.08	0.77	3.08	0.48	14807	188398	1766	6.11	51.2
	GM	0.21	0.05	0.13	0.02	194	8.35	0.04	0.56	2.61
	2σ	1.64	0.21	0.92	0.15	3204	31062	274	2.05	14.8
	IQR	0.33—0.12	0.10—0.027	0.30—0.067	0.036—0.009	324—95.1	17.6—1.39	0.23—0.005	1.53—0.31	4.70—1.51
Kelly	Min	0.003	0.001	0.005	0.0003	2.37	0.03	0.0002	0.01	0.08
	Max	0.53	0.12	1.11	0.20	894	188398	1766	4.52	11.0
	GM	0.14	0.04	0.10	0.01	113	7.34	0.03	0.48	1.87
	2σ	0.23	0.07	0.30	0.04	288	34691	306	1.54	3.87
	IQR	0.29—0.09	0.08—0.02	0.19—0.06	0.02—0.01	198—78.2	10.4—1.06	0.07—0.00	1.34—0.29	3.37—1.15
Lorena	Min	0.01	0.00	0.01	0.00	15.12	0.49	0.01	0.01	0.11
	Max	6.08	0.77	3.08	0.48	14807	108	2.47	6.11	51.2
	GM	0.96	0.13	0.48	0.07	1567	13.7	0.25	1.02	9.46
	2σ	2.74	0.35	1.56	0.26	5586	42.3	0.79	3.08	23.8
	IQR	2.23—0.74	0.29—0.10	1.15—0.31	0.18—0.03	3236—1036	29.7—7.33	0.47—0.16	2.35—0.45	19.2—6.28

Data below the detection limit (b.d.l.) were replaced by half the limit for the statistics calculation
Min—minimum; Max—maximum; GM—Geometric mean; IQR—Interquartile range

Cassiterite from the Kelly and Lorena systems shows partially overlapping IQR values for some elements, such as In, Th, Pb, and Zn. However, cassiterite from Kelly tends to be depleted in the remaining elements compared to cassiterite from Lorena (Fig. 29).

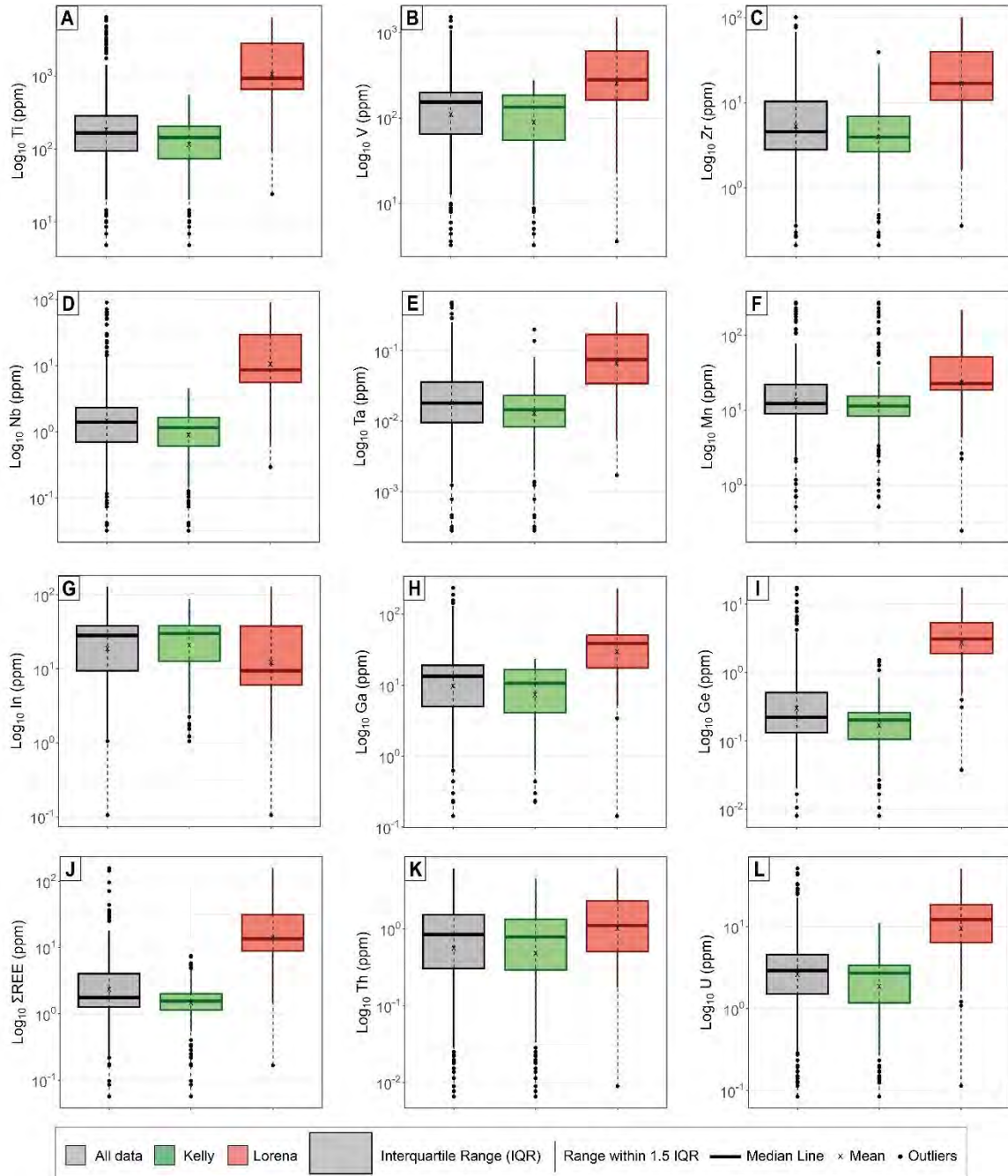


Figure 29. Selected box plots showing element contents in cassiterite from Taucane (LA-ICP-SF-MS data). The values for Gd and Tb were not included in the Σ REE since they are affected by polyatomic interference from tin oxides (see Yang et al. 2024)

Zirconium and Hf show an almost perfect linear correlation for cassiterite from both the Kelly ($R^2 = 0.97$) and Lorena systems ($R^2 = 0.99$; Fig. 30A). The datapoints draw a trend that is parallel to the Zr:Hf = 1:1 ratio line. Niobium and Ta also yielded good positive correlations for cassiterite from Kelly ($R^2 = 0.69$) and Lorena ($R^2 = 0.96$; Fig. 30B), with datapoints clustering along a parallel trend of the Nb:Ta = 1:1 ratio line. Zr/Hf (between 28 and 71; mean = 41; Fig. 30A) and Nb/Ta (between 19 and 320; mean = 100; Fig. 30B) are highly variable, with broadly equivalent Zr/Hf in cassiterite from both localities and slightly higher Nb/Ta in cassiterite from Lorena regarding cassiterite from Kelly (Fig. 30C). A fair positive correlation between Nb/Ta and Zr/Hf is observed in cassiterite from Kelly ($R^2 = 0.51$) but not in cassiterite from Lorena ($R^2 = 0.01$). Manganese shows a good correlation with Nb + Ta in cassiterite from Lorena ($R^2 = 0.81$) at Mn:(Nb + Ta) ratios close to 1:1 ratio line; in contrast, these elements do not show correlation in cassiterite from Kelly ($R^2 = 0.02$; Fig. 30D).

Titanium is positively correlated with Zr (Kelly: $R^2 = 0.68$; Lorena: $R^2 = 0.98$; Fig. 30E), U (Kelly: $R^2 = 0.84$; Lorena: $R^2 = 0.90$; Fig. 30F), and Sc (Kelly: $R^2 = 0.89$; Lorena: $R^2 = 0.91$; Fig. 30G) with datapoints in the three diagrams being located parallel and above the 1:1 ratio line. Scandium shows a strong positive correlation with V in cassiterite from Kelly ($R^2 = 0.80$) and Lorena ($R^2 = 0.94$; Fig. 30H), with datapoints from both systems drawing a trend that is parallel the 1:1 ratio line.

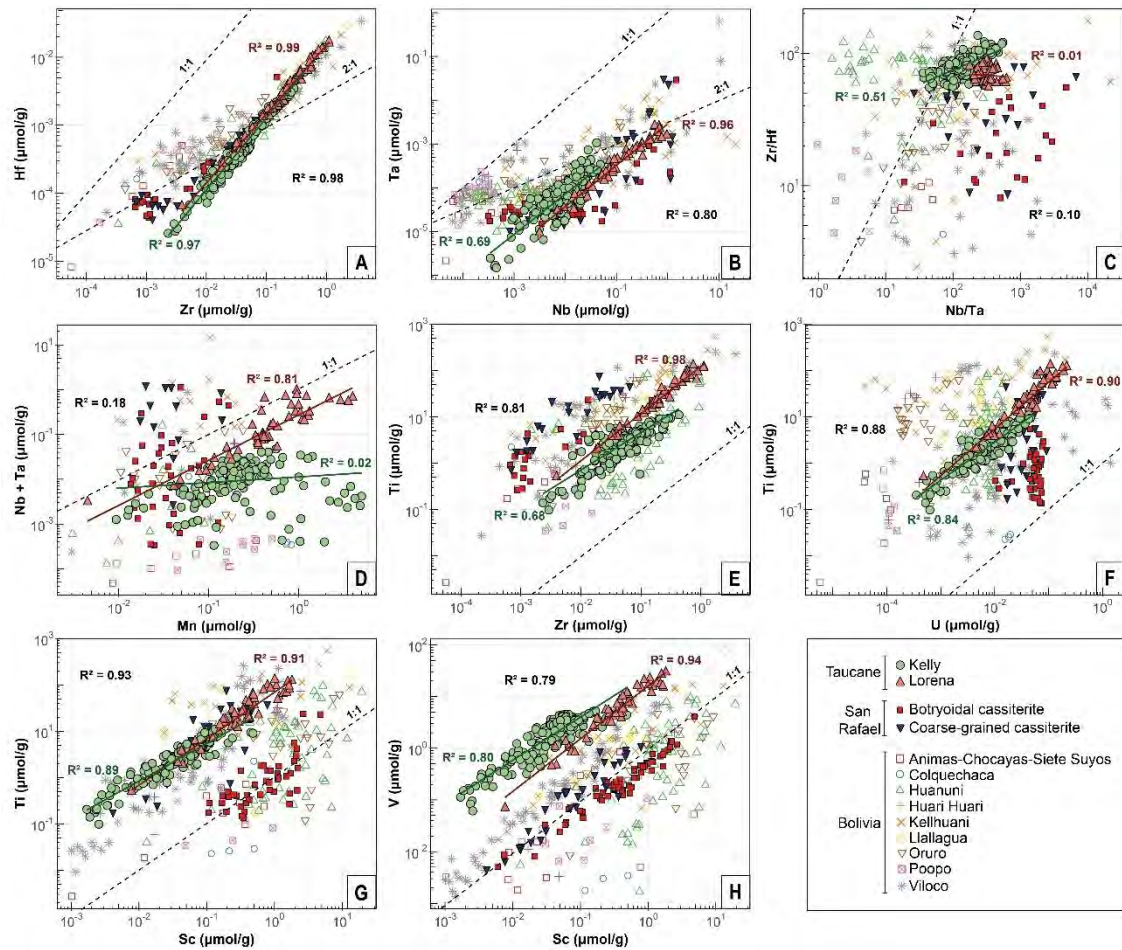


Figure 30. Correlation binary plots for cassiterite from Taucane. Bibliographic data is shown for comparison: Bolivian deposits (Gemrich et al. 2021); San Rafael (Harlaux et al. 2023)

In general, cassiterite from the Lorena system yielded higher REE contents ($\Sigma\text{REE} = 0.17$ - 157 ppm) than cassiterite from the Kelly system ($\Sigma\text{REE} = 0.06$ - 7.48 ppm; The values for Gd and Tb were not included in the ΣREE since they are affected by polyatomic interference from tin oxides). Cassiterite from the Kelly system shows variable enrichment/depletion of LREE with respect to HREE [$(\text{La}/\text{Sm})_{\text{CN}} = 0.32$ - 24.41, $(\text{Sm}/\text{Yb})_{\text{CN}} = 0.125$ - 4.89] and systematic positive Eu enrichment relative to Sm (Fig. 31A). The positive slope from Dy to Lu is a differential fact of cassiterite from Kelly [$(\text{Lu}/\text{Dy})_{\text{CN}} = 0.96$ - 22.1], which is not observed in cassiterite from Lorena [$(\text{Lu}/\text{Dy})_{\text{CN}} = 0.65$ - 1.67]. Cassiterite from the Lorena system exhibits flat CN REE patterns without significant fractionation between LREE and HREE [$(\text{La}/\text{Sm})_{\text{CN}} = 0.56$ - 2.55, $(\text{Sm}/\text{Yb})_{\text{CN}}$

= 0.71 – 2.29], except for Eu, which shows a slight positive anomaly relative to Sm (Fig. 31B).

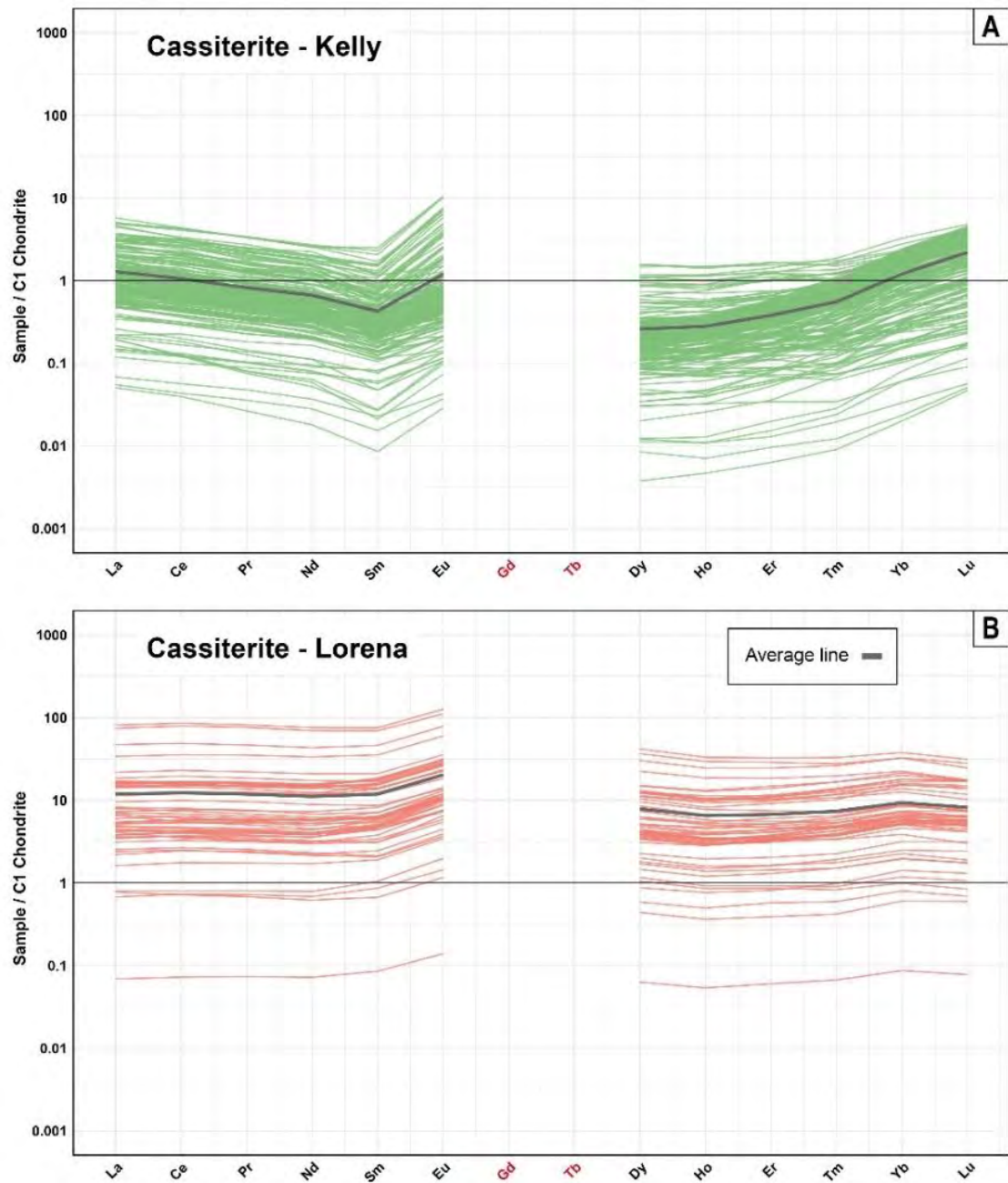


Figure 31. REE spider diagrams normalized to C1 chondrite values from McDonough and Sun (1995), represented as individual analyses and average values for Taucane cassiterite from (A) Kelly and (B) Lorena. The values for Gd and Tb were not included in the graph because they are affected by polyatomic interference from tin oxides (see Yang et al. 2024)

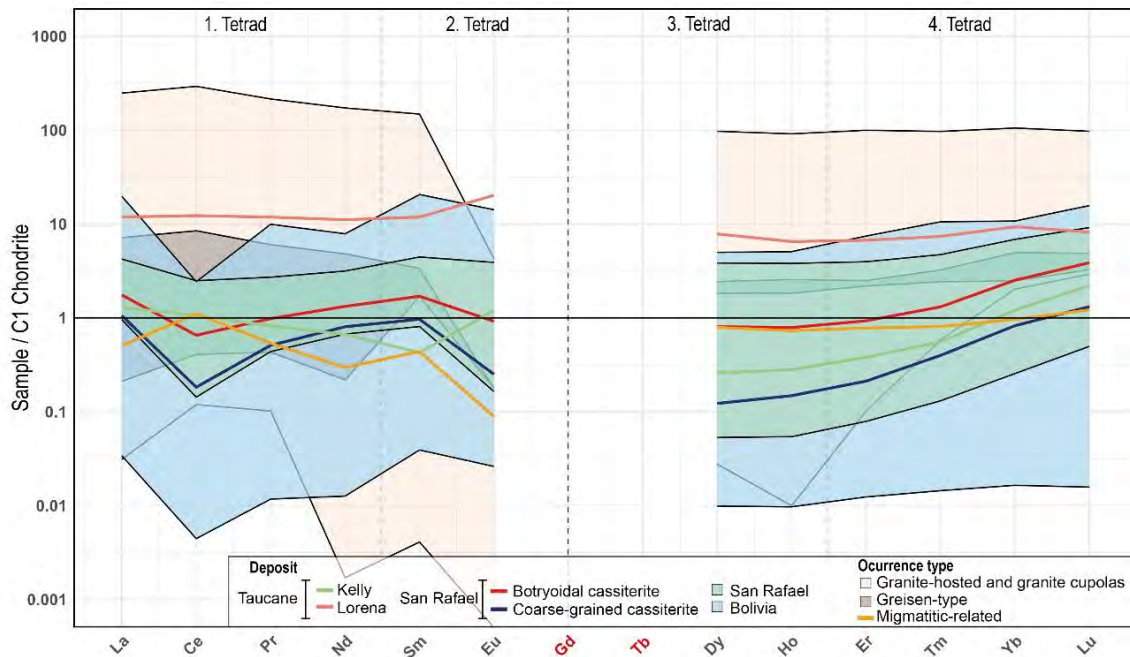


Figure 32. Rare earth element contents normalized to C1 chondrite values of McDonough and Sun (1995), for Taucane cassiterite represented as average values for Kelly and Lorena systems. Bibliographic data are shown for comparison. Granite-hosted and granite cupolas: Plimer et al. (1991) and Zoheir et al. (2020). Greisen-type: Plimer et al. (1991). Migmatitic-related: Jiang et al. (2004). Bolivian deposits: Gemrich et al. (2021). San Rafael: Harlaux et al. (2023). The values for Gd and Tb were not included in the graph because they are affected by polyatomic interference from tin oxides (see Yang et al. 2024)

4.3.3. Cassiterite U-Pb dating

A total of 254 in situ U-Pb analyses were performed on cassiterite grains from samples 2024-TAU-06 (Lorena), 2024-TAU-21 (Kelly), and 2024-TAU-22 (Kelly). From the measured $^{207}\text{Pb}/^{206}\text{Pb}$ and $^{238}\text{U}/^{206}\text{Pb}$ ratios, the samples form Tera-Wasserburg isochrons defining lower-intercept dates of 20.7 ± 4.3 Ma (2024-TAU-06; Fig. 33A), 23.0 ± 2.4 Ma (2024-TAU-21; Fig. 33B), and 22.1 ± 5.2 Ma (2024-TAU-22; Fig. 33C). Therefore, the three dates overlap within analytical errors.

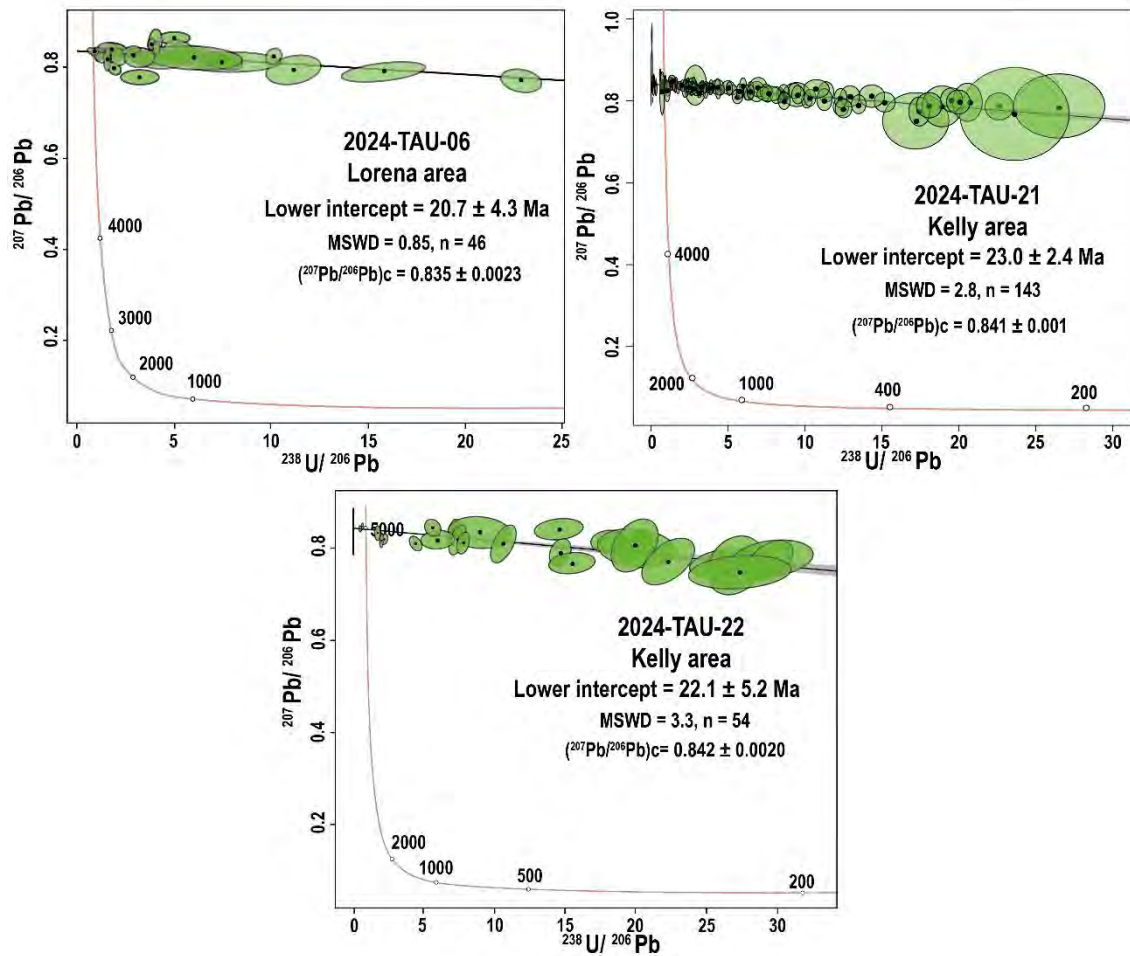


Figure 33. Results of in situ U-Pb isotope analyses of cassiterite from (A) 2024-TAU-06, Lorena area; (B) 2024-TAU-21, Kelly area; (C) 2024-TAU-22, Kelly area. The orange line is the concordia curve representing the expected U-Pb isotopic ratios for an unaltered system

4.4. Zircon geochronology and mineral geochemistry

4.4.1. Zircon U-Pb dating

In situ U-Pb isotope analyses were carried out on zircon grains from monzogranite (sample TC-23-01), quartz-monzodiorite (TC-23-02), and monzodiorite (TC-23-04). Zircon grains exhibit oscillatory growth zoning observed by CL-SEM. A representative selection of CL-SEM images of zircon grains is shown in Figure 34. 378 isotopic analyses were analyzed on 201 zircon grains, targeting both crystal cores and rims (Appendix H). The analyses were classified according to their analytical quality on a scale of 0 = worst to 3 = best, based on the degree of U-Pb concordance, precision, and signal stability. The

U-Pb dates of this group of zircons range from ca. 22 to 26 Ma. Some analyses with a score < 2 yielded significantly older dates, up to 2,686 Ma, which have been classified as xenocrystic zircon. Only analyses with a score ≥ 2 were considered for date calculations. These analyses cluster closely on the concordia curve, yielding $^{206}\text{Pb}/^{238}\text{U}$ weighted mean dates of 23.79 ± 0.57 Ma (TC-23-01; Fig. 35A), 24.16 ± 0.37 Ma (TC-23-02; Fig. 35B), and 24.06 ± 0.58 Ma (TC-23-04; Fig. 35C).



Figure 34. CL images of representative zircon grains from granitoids in the Taucane Project

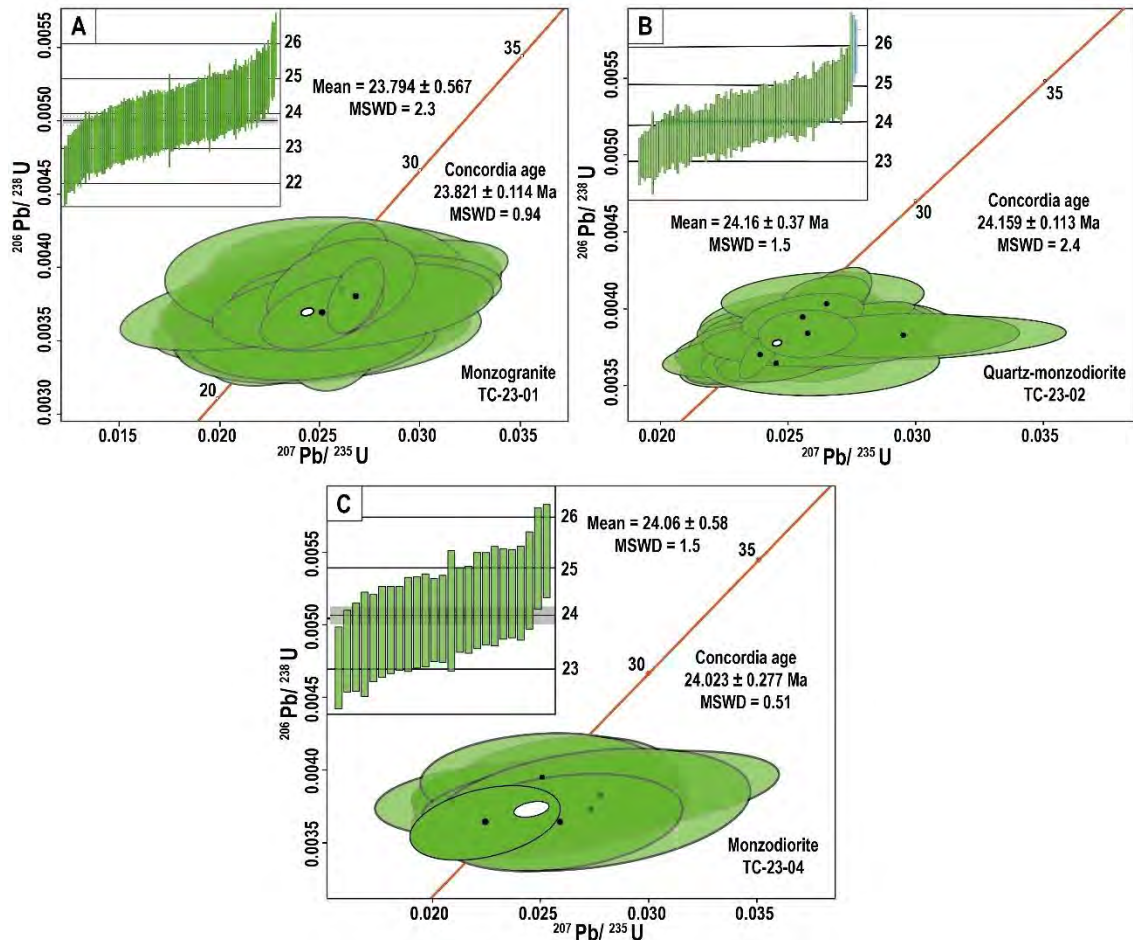


Figure 35. Zircon U–Pb concordia diagrams and weighted mean model ages for Taucane granitoids, including A) monzogranite; B) quartz-monzodiorite; and C) monzodiorite. The orange line is the concordia curve representing the expected U–Pb isotopic ratios for an unaltered system

4.4.2. Trace elements

Diagrams with the measured zircon trace element contents are presented in Figures 36 to 37. Xenocrystic zircon data will not be included in this section. Element contents will be expressed as interquartile ranges (IQR) in this section, unless otherwise indicated. The zircon grains from Taucane granitoids have high to very high contents of Hf (10,781–8,608 ppm), Y (2,391–1,044 ppm), U (1,866–616 ppm), Th (1,202–368 ppm), and P (305–175 ppm). Much lower contents were found for Al (11.8–2.74), Nb (7.71–2.05), Ti (5.97–2.98), Ta (3.42–1.00), and Pb (2.65–0.88). In terms of REE, the zircon grains from the three granitoid samples exhibit moderate-high Σ REE (1,632–746 ppm), and identical chondrite-normalized patterns, with enrichment in HREE relative to LREE [(La/Yb)_{CN}

<0.01, IQR = 0.00011–0.0003 ppm], positive Ce anomalies $[(Ce/Ce^*)_{CN} = 0.73–130]$, IQR = 31.4–9.35], and negative Eu anomalies $[(Eu/Eu^*)_{CN} = 0.06–0.82]$, IQR = 0.47–0.23].

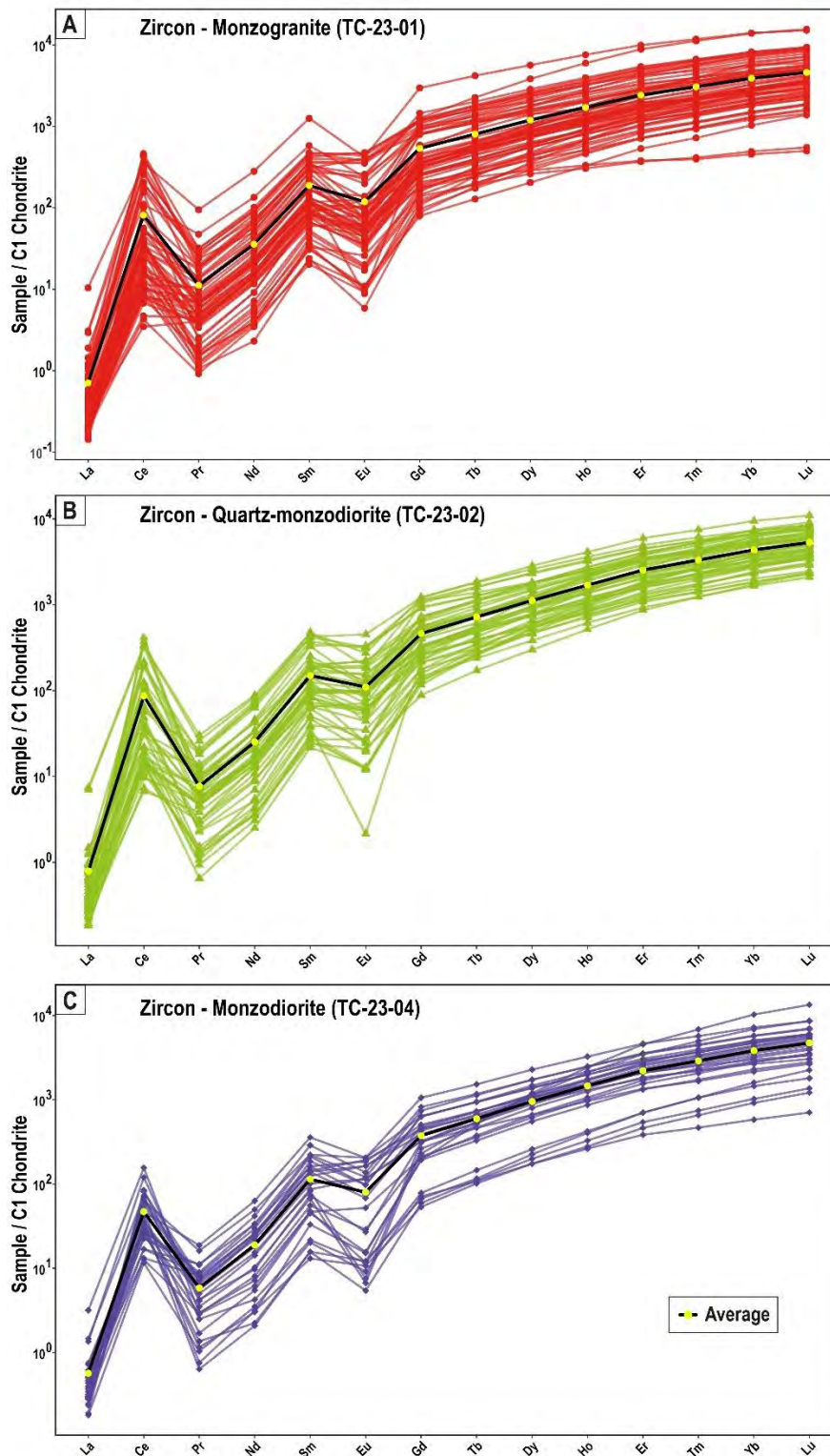


Figure 36. REE contents of zircon from Taucane normalized to Chondrite C1 values from McDonough and Sun (1995). A) Monzogranite (TC-23-01); B) Quartz-monzodiorite (TC-23-02); C) Monzodiorite (TC-23-04)

In the $(\text{Sm}/\text{La})_{\text{CN}}$ vs $(\text{Ce}/\text{Ce}^*)_{\text{CN}}$ diagram, most zircon datapoints plot in the magmatic field, with a few zircon rim datapoints deviating to compositions that are more typical of hydrothermal zircon (Fig. 37A). The vast majority of zircon analyses yielded U/Yb mostly above 1 (IQR = 4.24–1.62) and Hf > 7,000 ppm, hence plotting within the continental zircon field (Fig. 37B). The Hf vs Ti diagram reveals an inverse correlation between these elements (Fig. 37C). Although mostly overlapping, the highest $(\text{Yb}/\text{Gd})_{\text{CN}}$ ratios are associated with zircon rims (5.63–44.1 ppm; IQR = 16.6–9.57) compared to zircon cores (3.98–29.80 ppm; IQR = 12.2 – 7.02). An inverse correlation trend is observed for Th/U (0.95–0.46), Nb/Ta (2.64–1.69), $(\text{Sm}/\text{La})_{\text{CN}}$ (699–274), and Ti (5.97–2.98) when plotted against $(\text{Yb}/\text{Gd})_{\text{CN}}$ (Fig. 37D-G). The calculated crystallization temperatures for zircon grains from the three samples are extremely similar (monzogranite: IQR = 735–669°C; quartz-monzodiorite: IQR = 724–667°C; monzodiorite: IQR = 726–693°C), with a total range variation between 577 °C and 820 °C (GM = 670 ± 88.6 °C; Fig. 37G). The calculated $\log f\text{O}_2$ values range from -22.8 to -11.6, plotting between the HM (Hematite-Magnetite) and IW (Iron-Wustite) buffers and predominantly grouping below the NNO (Nickel-Nickel Oxide) fugacity curve (Fig. 37H). The ΔFMQ values range from -3.79 to 4.51. Zircon rims and cores yielded largely overlapping crystallization temperatures and oxygen fugacities.

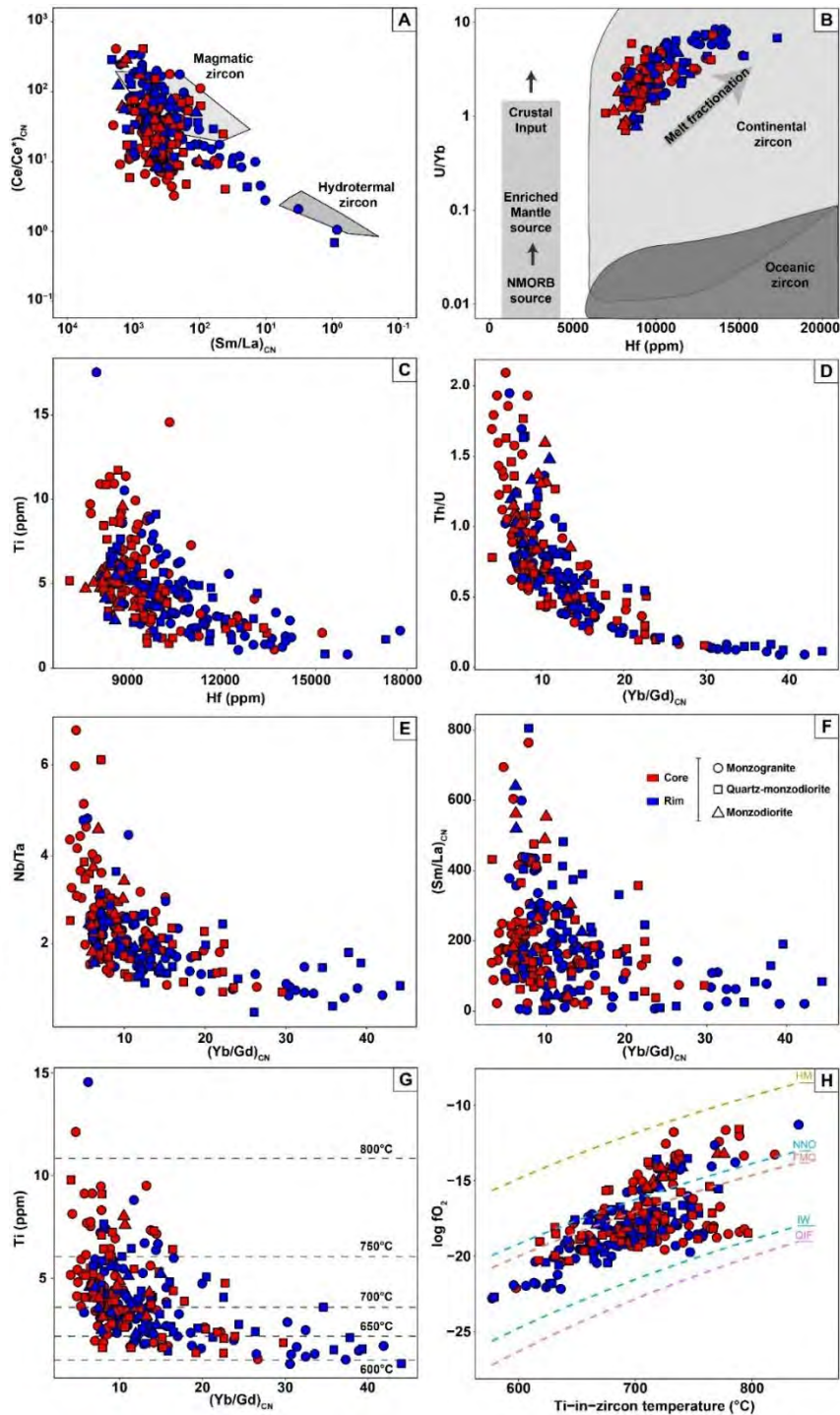


Figure 37. Binary diagrams of trace elements and derived parameters for zircon grains from Taucane. (A) $(Sm/La)_{CN}$ vs $(Ce/Ce^*)_{CN}$, with compositional fields after Hoskin (2005); (B) Hf vs U/Yb, with compositional fields after Grimes et al. (2015); (C) Hf vs Ti; (D) $(Yb/Gd)_{CN}$ vs Th/U; (E) $(Yb/Gd)_{CN}$ vs Nb/Ta; (F) $(Yb/Gd)_{CN}$ vs $(Sm/La)_{CN}$; (G) $(Yb/Gd)_{CN}$ vs Ti-in-zircon temperature; (H) Ti-in-zircon temperature vs $\log fO_2$ with buffers calculated according to Frost (1991). $(Ce/Ce^*)_{CN}$, $(Sm/La)_{CN}$, and $(Yb/Gd)_{CN}$ values are normalized to chondrite C1 values of McDonough and Sun (1995). Temperatures are calculated using the Ti-in-zircon thermometer of Ferry and Watson (2007). Abbreviations: FMQ–Fayalite-Magnetite-Quartz; HM–Hematite-Magnetite; IW–Iron-Wustite; NNO–Nickel-Nickel Oxide; QIF–Quartz-Iron-Fayalite

5. DISCUSSION

5.1. Kelly vs Lorena systems: exploration constraints

The mineralization in both the Kelly and Lorena systems embraces volumetrically dominant manto-type orebodies and, to a lesser extent, veins. They also share broadly similar ore mineralogy (Figs. 19, 21) and paragenetic sequences (Figs. 20, 22). In approximate order of abundance, the identified hypogene ore minerals in both mantos and veins are Fe sulfides (pyrrhotite and pyrite \pm marcasite \pm intermediate product), sphalerite, cassiterite, chalcopyrite, stannite, galena, Ag-tetrahedrite-(Fe) and Pb-Sb sulfosalts (franckeite, boulangerite, bournonite), arsenopyrite, and native Bi (Fig. 38). In general, orebodies from both areas comprise a Stage I that is composed of a low-sulfidation assemblage of pyrrhotite, needle tin cassiterite, chalcopyrite (1st and 2nd generations), Fe-rich sphalerite (1st generation; 7.5-12 wt.% Fe), and stannite. Stage I assemblages are overprinted by the Stage II mineral assemblage, defining by an intermediate-sulfidation assemblage of coarse anhedral pyrite \pm marcasite \pm intermediate product—formed mostly as replacements of pyrrhotite—as well as volumetrically more restricted Fe-poor sphalerite (2nd generation; < 1 wt.% Fe), galena, and minor amounts of Ag-tetrahedrite-(Fe), franckeite, boulangerite, and native bismuth. The decrease in Fe content from first- to second-generation sphalerite indicates an increase in fS_2 and fO_2 in the system, which is consonant with the observed transition from low- to intermediate-sulfidation conditions (Scott and Barnes 1971; Czamanske 1974; Fig. 38).

		Stage 0	Stage I (LS)	Stage II (IS)			Supergene
				Stage IIa (IS)	Stage IIb (IS)		
Garnet	$\text{Ca}_3\text{Al}_2(\text{SiO}_4)_3$	—					
Pyroxene	$\text{CaFeSi}_2\text{O}_6$	—					
Quartz	SiO_2	—	—	—	—	—	
Pyrrhotite	Fe_{1-x}S		—				
Cassiterite (needle tin)	SnO_2		—				
Arsenopyrite	FeAsS		—				
Fe-rich sphalerite	$(\text{Zn},\text{Fe})\text{S}$		—				
Chalcopyrite	CuFeS_2		—				
Stannite	$\text{Cu}_2\text{FeSnS}_4$		—				
Pyrite	FeS_2			—	—	—	
Marcasite	FeS_2			—	—	—	
Intermediate product	FeS_2			—	—	—	
Fe-poor sphalerite	ZnS				—	—	
Ag-tetrahedrite-(Fe)	$(\text{Cu},\text{Ag})_{12}\text{Fe}_2\text{Sb}_4\text{S}_{13}$				—	—	
Galena	PbS				—	—	
Franckeite	$\text{Pb}_5\text{Sn}_3\text{Sb}_2\text{S}_{14}$				—	—	
Boulangerite	$\text{Pb}_5\text{Sb}_4\text{S}_{11}$				—	—	
Bournonite	PbCuSbS_3				—	—	
Native bismuth	Bi				—	—	
Acanthite	Ag_2S						—
Baryte	BaSO_4						—
Anglesite	PbSO_4						—
Hematite	Fe_2O_3						—
Goethite	$\text{FeO}(\text{OH})$						—

Figure 38. Generalized paragenetic sequence for mantos and veins from the Kelly and Lorena systems.

Bars indicate greater abundances, and dashed lines, lesser abundances. Black bars indicate mineralization shared by mantos and veins. Green bars indicate manto-type-only mineralization. Beige bars indicate vein-type-only mineralization

Despite these similarities, the Kelly and Lorena systems differ in significant ways. Mantos from Kelly host a skarn-like alteration assemblage (grossular-andradite, hedenbergite; Stage 0), which has not been observed in mantos from Lorena. These skarn phases were generated by the interaction of monzogranite with calcareous sandstone of the Muni Formation (Fig. 11D). This difference may indicate that the Kelly mineralization is located more proximally to the causative intrusions, relative to Lorena, within a skarn–carbonate-replacement (CRD) mineralization continuum (Einaudi et al. 1981; Meinert 1992; Meinert et al. 2005; Bendezú and Fontboté 2009; Catchpole et al. 2015; Benites et al. 2021). Besides, while pyrrhotite is more abundant in mantos from the

Kelly area, pyrite is dominant in mantos from the Lorena area and in veins from both areas. Furthermore, Fe-rich sphalerite has only been found in mantos from Kelly, while Fe-poor sphalerite is observed in veins from both areas. Therefore, the low-sulfidation assemblages are more conspicuous in the Kelly system, particularly in the mantos, while the intermediate-sulfidation overprinting is more pervasive in the Lorena system and dominates veins. The observed differences in the sulfidation state can be attributed to a proximal-distal temperature gradient (Einaudi et al. 1981; Meinert et al. 2005). Therefore, the Kelly system could represent a more proximal, transitional skarn-carbonate replacement deposit (CRD), whereas the Lorena system corresponds to the distal skarn-free carbonate replacement deposit (Meinert et al. 2005).

Beyond differences in ore mineralogy and paragenesis, cassiterite from Kelly and Lorena also reflects some compositional differences. Cassiterite from Kelly generally has higher FeO contents (Fig. 28). According to Cheng et al. (2019), an increase in Fe contents in cassiterite can occur towards more oxidized distal zones through the entry of Fe³⁺. However, this contradicts our paragenetic constraints and could instead respond to high activity of Fe²⁺ inherited from the previous skarn phase and higher temperatures (Patterson et al. 1981; Wright and Kwak 1989; Halley and Walshe 1995) and its incorporation through substitutions of the type $2(Ta, Nb)^{5+} + (Fe, Mn)^{2+} = 3 Sn^{4+}$ (Möller et al. 1988). Furthermore, cassiterite from Lorena exhibits higher values for Mn, Nb, Ta, Zr, Hf, Ti, U, Sc, and V compared to cassiterite from Kelly (Fig. 29). This enrichment in Lorena is characteristic of cassiterite precipitated in later hydrothermal stages, in which progressive fractionation allows incompatible elements to accumulate in the residual fluid (Lehmann 2021).

On the other hand, both systems have Zr/Hf ratios in cassiterite between 28 and 70 (Fig. 30A), which exceed chondritic values (~35 and 40; Hoskin and Schaltegger 2003). A

comparable trend is evident for Nb/Ta ratios, which range from 18.5 to 320 (Fig. 30B), and are mostly well above chondritic values (19.9 ± 0.6 ; Münker et al. 2003). This typically occurs in hydrothermal environments, particularly at high activities of fluorinated ligands, and in highly differentiated igneous rocks (Bau 1996; Cheng et al. 2019). The broadly similar Zr/Hf and Nb/Ta ratios for cassiterite from both Kelly and Lorena do not allow clear constraints regarding differences in the formation conditions. Likewise, cassiterite from the Kelly system has similar Ti/Zr (IQR = 39.55–21.16) and Ti/Sc (IQR = 85.69–62.84) to cassiterite from the Lorena system (Ti/Zr, IQR = 67.97–57.31; Ti/Sc, IQR = 97.47–51.26; Fig. 30E, G). Therefore, these ratios do not indicate any differences in the physicochemical characteristics of the hydrothermal fluids in our study case either (Taylor 1979; Cheng et al. 2019) and suggest that cassiterite from both areas crystallized under similar conditions during the low-sulfidation paragenetic stage.

5.2. Mineralization style and comparison with other Sn(-polymetallic) deposits

This research highlights the atypical nature of Taucane relative to other Sn deposits in the Central Andean Tin Belt. A significant difference of Taucane is the mineralization style, comprising volumetrically dominant mantos and more restricted veins. This contrasts with traditional stanniferous deposits along the Central Andean Tin Belt, which typically occur as quartz-cassiterite veins and lodes (Turneure 1971; Corthay et al. 2014; Heuschmidt et al. 2002; Mlynarczyk and Williams-Jones 2005; Torró et al. 2019a, b, 2024; Gemmrich et al. 2021; Harlaux et al. 2021). Mantos in Taucane developed within limestone and calcareous sandstone horizons of the Muni Formation and the Moho Group, with massive sulfides mineralization and minor proportions of needle-tin cassiterite. The stratigraphic and lithological controls are probably a consequence of the nature of the host rocks, which in Taucane include highly reactive carbonated rocks, unlike traditional Sn(W) deposits from the Central Andean Tin Belt, which are largely

hosted by detrital (meta)sedimentary rocks or felsic igneous rocks (Heuschmidt et al., 2002; Arce Burgoa, 2007; Harlaux et al. 2023; Torr o et al. 2024). The carbonated nature of the host in Taucane is also connected with the formation of skarn-like alteration assemblages, which are not described in other Sn deposits from the Central Andean Tin Belt (Fig. 39). These characteristics indicate that there was greater stratigraphic and lithological control than in traditional deposits in the Central Andean Tin Belt, where structural controls were dominant during orebody formation (Heuschmidt et al. 2002).

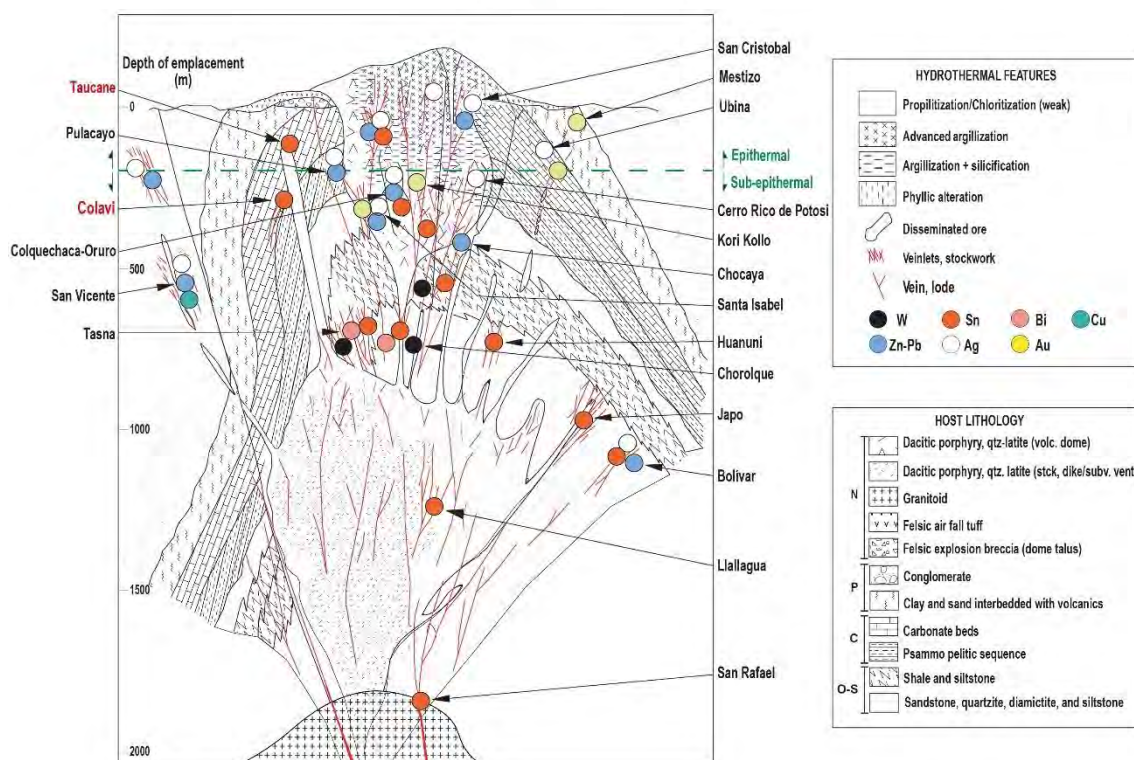


Figure 39. Conceptual model of veiniform Sn(W) deposit in the Central Andean Tin Belt in Bolivia (modified from Heuschmidt 2002) with the tentative incorporation of the San Rafael deposit and the Taucane Project in Peru

Within the Central Andean Tin Belt, Colavi is the only known deposit exhibiting a mineralization style, in part, similar to that of Taucane. Colavi is located 812 km southeast of La Paz and 35 km northeast of Potos ı in Bolivia. The mineralization in Colavi is mainly hosted in Upper Ordovician shale and sandstone, Lower Silurian diamictite, and in discordantly overlying Cretaceous conglomerate, quartz sandstone, limestone, and claystone of the La Puerta, Miraflores, and Aroifilla formations (Sugaki et al. 1983; Arce-

Burgoa 2007). The sedimentary sequence in Colavi was intruded by a series of Tertiary stocks, domes, dykes, and sills of dacitic composition that are closely related to the mineralization (Arce-Burgoa 2007; Arce-Burgoa and Goldfarb 2009). The Sn mineralization is mainly associated with quartz and calcareous sandstone, which are weakly to moderately sericitized and silicified. Mineralization occurs as fault and fracture fillings (vein-type) with sphalerite, pyrite, cassiterite (*var.* wood tin), and Fe oxides, and in mantos within La Puerta Formation comprising cassiterite, pyrite, sphalerite, and Ag sulfosalts (Arce-Burgoa 2007). Mantos reach thicknesses of 0.8-1 m (Sugaki et al. 1983). In general, the polymetallic sulfide-sulfosalt mineralization at Colavi is volumetrically scarce compared to other tin deposits in the Oruro and Potosí districts (Sugaki et al. 1983). This is distinct from Taucane, which is predominantly composed of polymetallic sulfides and sulfosalts and lesser proportions of needle-tin cassiterite.

In the search for deposits with comparable mineralization styles and located outside of the Central Andean Tin Belt, polymetallic tin deposits such as Renison Bell, Mount Bischoff, Cleveland (Australia), Dafulou, Huile (China), and Ayawilca (Peru) are presented. Tasmania leads Australia in tin production and hosts deposits such as Renison Bell, Mount Bischoff, and Cleveland (Denholm et al. 2021). The mineralization of the Renison Bell deposit is hosted in dolomite beds of the Late Precambrian Success Creek and Early Cambrian Crimson Creek formations (Patterson et al. 1981; Denholm et al. 2021) and is mainly of two types: stratabound massive sulfide orebodies (5-15 m in thickness) and “stratafault” replacement ores (Patterson et al. 1981). In the former, massive pyrrhotite with minor amounts of cassiterite, arsenopyrite, and other sulfides occurs within dolostone horizons in the Success Creek Group and the Red Rock sequence; in the latter, large blocks of dolomite have been dragged into faults and replaced by a talc-pyrrhotite-cassiterite assemblage (Denholm et al. 2021). The Mount Bischoff

deposit, which is located 38 km north of Renison Bell, lies within a core of Precambrian sedimentary rocks surrounded by Lower Paleozoic and Tertiary sedimentary and volcanic rocks (Wright and Kwak 1989). Mineralization occurs mainly as dolomite replacement in lenses up to 30 m thick, composed of cassiterite, pyrrhotite, carbonates, and a variety of silicate phases, and to a lesser extent as polymetallic cassiterite veins (Halley and Walshe 1995). The Cleveland deposit is located 35 km north of Renison Bell and 15 km west of Mt. Bischoff (Collins 1981). This deposit contains 11 stratiform lenses of near-vertical massive sulfide bodies with a maximum thickness of 30 m within the Halls Formation. It is composed largely of fine to medium-grained quartz, tourmaline, fluorite, chlorite, pyrrhotite, chalcopyrite, stannite, wolframite, and cassiterite that replaced limestone (Collins 1981; Denholm et al. 2021). The Tasmanian deposits are mainly composed of Sn mineralization (Denholm et al. 2021), unlike the significant polymetallic factor present in Taucane.

The Chinese Dafulou and Huile Sn-Zn deposits are located in the eastern part of the Dachang tin field, on the eastern limb of the Longxianggai anticline, and are hosted by a thick sequence of Lower-Middle Devonian calcareous black shale (Pašava et al. 2003; Guo et al. 2018). The Dafulou Sn–Zn deposit has two types of Sn-Zn ores: stratiform orebodies in the deeper part, with thicknesses of up to 2.5 m, and fault-controlled veins/stockworks in the upper part (Guo et al. 2018). The Huile deposit, which is about 1.5 km southeast of the Dafulou deposit, presents similar ore types to Dafulou, with cassiterite-bearing quartz veins at shallow levels and gently dipping stratiform orebodies in the deeper part (Pašava et al. 2003; Guo et al. 2018).

In Peruvian territory, but ~800 km to the north of the northernmost tip of the Central Andean Tin Belt, the Ayawilca Zn-Pb-Ag-In-Sn-Cu deposit shares many similarities with Taucane. Their current indicated mineral resources are 28.3 million tons at a grade of

5.82% Zn, 16.4 g/t Ag, 91 g/t In, and 1.4 Mt at a grade of 0.72% Sn (Tinka Resources Ltd 2024). Benites et al. (2022) provide a detailed description of the Ayawilca deposit. Mineralization style is primarily observed as replacement mantos, ranging in thickness from 10 to 70 m, and, to a lesser extent, as veins. These are mainly hosted in carbonate rocks of the Pucara Group (Late Triassic to Early Jurassic), with subordinate mineralization in sandstone-siltites of the Goyllarisquizga Group (Cretaceous) and phyllites of the Excelsior Group (Devonian). The mineralization sequence comprises four stages. The Pre-A stage is composed of Mg-siderite, talc, magnetite, chlorite, and minor amounts of actinolite-tremolite, along with cassiterite (relics of a distal magnesian retrograde skarn). Stage A (low-sulfidation) is composed of quartz, pyrrhotite, arsenopyrite, chalcopyrite, Fe-rich sphalerite, stannite, herzenbergite (SnS), and minor amounts of mackinawite. Stage B (intermediate-sulfidation) is composed of pyrite, marcasite, quartz, and intermediate product (transition from pyrrhotite to pyrite/marcasite). Stage C (intermediate-sulfidation) is characterized by the presence of Fe-poor sphalerite, galena, chalcopyrite, Cu-Ag sulfosalts, native bismuth, bismuthiferous galena, siderite, Mn-Fe carbonates, kaolinite, dickite, and sericite. Interestingly, Ayawilca shares mineralization age (23 Ma, i.e., early Miocene) with deposits in the Central Andean Tin Belt in Bolivia (Gemrich et al. 2021), and San Rafael (Harlaux et al. 2020, 2021, 2023; Markovic et al. 2025), Santo Domingo (Clark et al. 1990), and Taucane (this thesis) in Peru. Despite these similarities, no granitic intrusions with the characteristics of those typically associate with tin mineralization have yet been identified in the area where Ayawilca is located. It is also important to highlight the effect of the organic matter-rich Excelsior Group phyllites, which could have behaved as a strong redox buffer promoting highly reducing conditions that favored tin transport at Ayawilca (Benites et al. 2022).

5.3. Age of the mineralization and relationship with intrusive rocks

U-Pb cassiterite geochronology from the Kelly (23.0 ± 2.4 to 22.1 ± 5.2 Ma) and Lorena (20.7 ± 4.3 Ma) systems in Taucane clearly constrain mineralization to the latest Oligocene-Early Miocene metallogenic event of the Central Andean Tin Belt (Mlynarczyk and Williams-Jones 2005; Fig. 40). Furthermore, the obtained dates overlap within error with U-Pb cassiterite dates for other deposits in the Peruvian (San Rafael: 24.10 ± 0.37 to 23.47 ± 0.53 Ma; Harlaux et al. 2023; Markovic et al. 2025) and Bolivian (Viloco: 24.4 ± 0.4 Ma; Huanuni: 24.0 ± 2.4 Ma; Llallagua: 24.0 ± 5.1 Ma; Gemmrich et al. 2021) segments of the Central Andean Tin Belt. On the other hand, zircon U-Pb dates for Taucane granitoids yielded more precise average dates between 24.16 ± 0.37 Ma and 23.79 ± 0.57 Ma, which overlap within error with the obtained U-Pb cassiterite dates from the same project. These new zircon U-Pb dates coincide with zircon U-Pb dates for intrusive rocks in San Rafael that yields values between 24.26 ± 0.26 Ma and 24.02 ± 0.25 Ma (Harlaux et al. 2021), further refined through high-precision zircon U-Pb ID-TIMS, indicating that the emplacement took place from 24.402 ± 0.019 Ma to 24.027 ± 0.028 Ma (Markovic et al. 2025). In Santo Domingo, K-Ar dating of magmatic biotite from a monzogranite dike yielded 24.3 ± 0.6 Ma (Clark et al. 1983). This suggests synchronicity between magmatism and hydrothermal activity not only within the Macusani Structural Zone, where all Peruvian Sn deposits belonging to the Central Andean Tin Belt are located, but also along its boundary with the Central Andean Backthrust Belt, where the Taucane Project is located (Figs. 7-9).

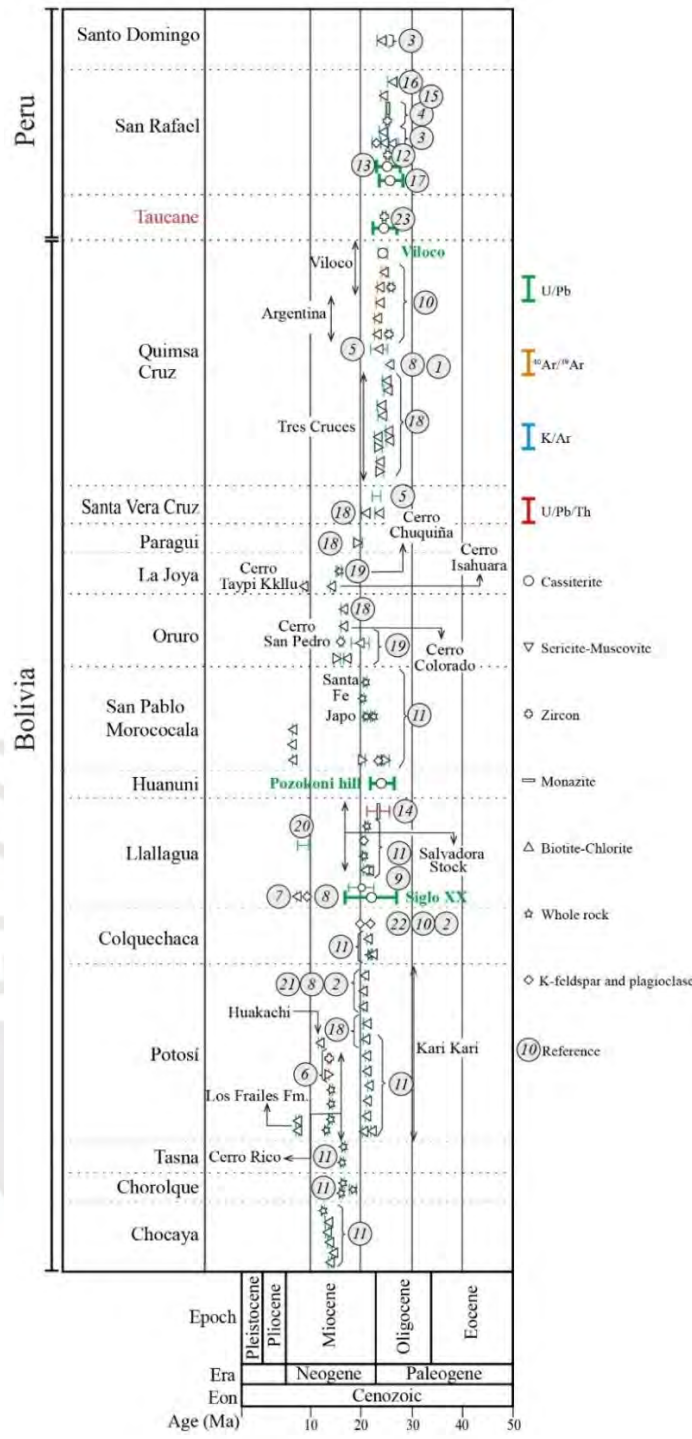


Figure 40. Oligocene to recent geochronologic chart of the Central Andean Tin Belt, including the new U-Pb cassiterite data presented here. Data are ordered from north to south of the Central Andean Tin Belt. Circled numbers correspond to the following references: (1) Ahfeld and Brainsa (1960); (2) Ahfeld and Schneider-Scherbina (1964); (3) Clark et al. (1983); (4) Clark et al. (2000); (5) Cordani (1967); (6) Cunningham et al. (1996); (7) Everden (1961); (8) Evernden et al. (1977); (9) Farrar et al. (1990); (10) Gillis et al. (2006); (11) Grant et al. (1979); (12) Harlaux et al. (2021); (13) Harlaux et al. (2023); (14) Kempe et al. (2008); (15) Kontak and Clark (2002); (16) Kontak et al. (1987); (17) Markovic et al. (2025); (18) McBride et al. (1983); (19) Redwood and Macintyre (1989); (20) Revollo (1967); (21) Rivas and Carrasco (1968); (22) Thormann (1966); (23) this thesis.

The Taucane granitoids show discrepancies between the petrographic and the different geochemical classifications could be due to hydrothermal alteration of the studied granitoids leading to the mobilization of some major elements. Taucane granitoids (monzogranite, quartz-monzodiorite, monzodiorite) are generally characterized by similar mineralogical and geochemical compositions. All are composed of primary igneous minerals, including abundant K-feldspar, plagioclase, quartz, and biotite (Fig. 15-17), and variable proportions of aluminous mineral phases such as muscovite, cordierite, and tourmaline (Figs. 15-16). The Taucane granitoids have peraluminous (monzogranite, quartz-monzodiorite) and metaluminous (monzodiorite) compositions (Fig. 24A-B). The monzodiorite is interpreted as a mixture of peraluminous monzogranitic magmas and minette-type lamprophyre magmas, denoting its intermediate composition (Fig. 23A-E; Vallance 2015; Alayza 2016). This explains the absence of cordierite in monzodiorite, since this mineral is only stable in peraluminous magmas, meaning that mixing would cause it to redissolve (Fig. 17; Vallance 2015). Similar evidence of magmatic mixing has been observed in the San Rafael intrusive complex, which formed through multiple injections and mixing of coexisting felsic and mafic magmas (Harlaux et al. 2021). It is noteworthy that it is in the Eastern Cordillera of southern Peru (Cayconi Volcanic Field) where seminal work on mixing between peraluminous granitic and ultrapotassic basaltic magmas (Sandeman et al., 1997; Sandeman and Clark 2004). These ultrapotassic basaltic magmas would have derived from a metasomatized subcontinental lithospheric mantle (Carlier et al. 1997, 2005). Importantly, the age of the mixed and commingled rocks in Cayconi is late Oligocene to early Miocene (ca. 23-25 Ma), coeval with the Taucane granitoids and the San Rafael Intrusive Complex (Sandeman and Clark 2004). These observations support the idea that

mixing and comingling of ultrapotassic mafic and peraluminous granitic magmas was a widespread phenomenon in the region during Sn deposit formation.

The moderate-high enrichment in incompatible lithophile elements (Sn, Ta, Rb, Ba, Cs, Th, and U; Fig. 25A), high Zr/Hf ratios (32.1–36.00) and moderate Nb/Ta ratios (5.48–7.41) indicate that the granitoids were moderately fractionated (Breiter et al. 2014; Grimes et al. 2015). According to Breiter et al. 2014, this may represent early pulses within complex magmatic systems. This is consistent with the diagram by Ballouard et al. 2016, as the Zr/Hf and Nb/Ta ratios situate the Taucane granitoids within the “barren granite” field of Ballouard et al. (2016), very close to the boundary with the “Sn-W-related granite” field (Fig. 41). The Nb/Ta ratios were probably lowered by fractional crystallization of micas, as these typically fractionate Nb more than Ta (Ballouard et al. 2016). Biotite and muscovite are present in significant contents as primary phases in the Taucane granitoids (Figs. 15-17).

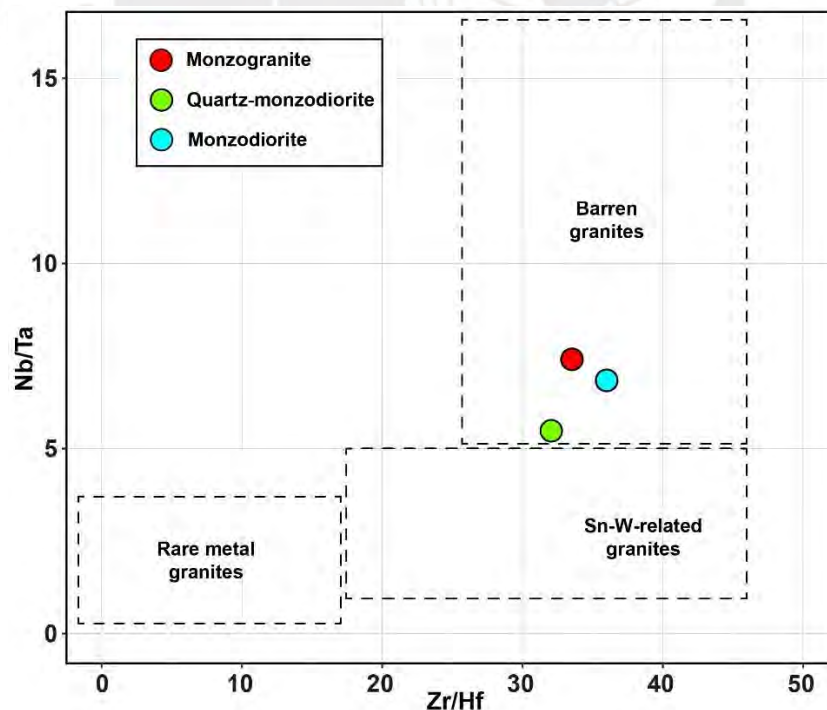


Figure 41. Whole-rock compositions of the granitoids from Taucane plotted in the Zr/Hf vs Nb/Ta granitoid classification diagram of Ballouard et al. (2016)

Chondrite-normalized REE patterns show a negative slope from light to heavy REE (Fig. 25B), which could indicate the presence of MREE- and HREE-fractionating minerals such as garnet and amphibole in the lower/intermediate crust (Rubatto and Hermann 2007; Moyen 2009; Tang et al. 2021). On the other hand, the negative $(Eu/Eu^*)_{CN}$ anomalies exhibited by the granitoids reflect plagioclase fractionation (Rudnick 1992). However, the coexistence of garnet and plagioclase is not possible, as they are not stable together (Tang et al. 2021). Therefore, the possibility of a transition from high- to medium-pressure conditions is hence considered, which will be contrasted with petrogenetic constraints based on zircon compositions.

Zircon grains from the Taucane granitoids exhibit mostly overlapping age and compositions, suggesting co-magmatic petrogenesis. They exhibit similar Chondrite normalized REE patterns, with enrichment in HREE relative to LREE, positive Ce anomalies, and negative Eu anomalies (Fig. 36). The results suggest that magmas forming these rocks were reduced (up to $\Delta FMQ - 3$), triggering an Eu valence of +2, which is not easily accepted in the zircon lattice, and therefore, being incorporated in plagioclase, producing the negative Eu anomaly in zircon chemistry (Fig. 36; Trail et al. 2012; Tang et al., 2021). Most zircon grains have $(Sm/La)_{CN}$ vs $(Ce/Ce^*)_{CN}$ typical of magmatic zircon with a few rims that have compositions that are typical of hydrothermal zircon and could indicate transition from magmatic to magmatic-hydrothermal conditions during granitoids emplacement and cooling (Hoskin, 2005; Fig. 37A). Magmatic zircons from Taucane granitoids are indisputably of continental origin, as demonstrated in the Hf vs. U/Yb diagram (Fig. 37B), where elements like U are significantly enriched in the continental crust compared to the mantle, and whereby heavy rare earth elements like Yb exhibit more conservative behavior, resulting in pronounced U/Yb fractionation (Rudnick and Gao 2003). A comparable situation is evident in the case of Hf, which is

predominantly partitioned into zircon, resulting in zircon becoming the predominant host of Hf within the continental crust (Rudnick and Gao 2003; Pearce 2008). Likewise, a trend toward higher values for zircon rims suggesting some degree of melt fractionation from zircon core to rim formation. As Ti decreases, Hf increases, indicating a continuous process of magmatic differentiation and cooling (Fig. 37C). Similar trends in the Th/U, Nb/Ta, and $(\text{Sm/La})_{\text{CN}}$ vs $(\text{Yb/Gd})_{\text{CN}}$ (Fig. 37D-F) indicate progressive crystal fractionation of the granitic melt (Buret et al. 2016; Chelle-Michou et al. 2014; Wotzlaw et al. 2013). A different version of Figure 36, in which zircon trace elements are presented as a function of their age, is shown in Appendix K. Compositional trends cannot be correlated with zircon age, probably because of overlapping dates within analytical errors. Garnet fractionates HREE, resulting in low $(\text{Yb/Gd})_{\text{CN}}$ values of the magmas in equilibrium with this mineral. Garnet crystallization preferentially incorporates Fe^{2+} and probably induces melt oxidation, whereby Eu^{3+} is incorporated into zircon and Eu anomalies are observed (Yakymchuck et al. 2023; Yakymchuck and Kirkland 2025). Therefore, in peraluminous magmas, Eu is divided into multiple phases (plagioclase, zircon), resulting in a soft Eu anomaly. Likewise, stable garnet requires high crystallization pressure and hence thick crustal environments (Tang et al. 2021). Consequently, as the pressure decreases, plagioclase stabilizes, fractionating Eu in the middle and upper crust during magmatic differentiation. This is consistent with the $(\text{Yb/Gd})_{\text{CN}}$ vs Ti diagram (Fig. 37G), where minimum values of $(\text{Yb/Gd})_{\text{CN}}$ are observed at high temperatures, which would indicate that garnet was present from early stages. In the Ti-in-zircon temperature vs $\log f\text{O}_2$ diagram (Fig. 37H), the values lie between the HM and IW buffers, although most of the data are found in the $\Delta\text{FMQ} - 2$ range. These values indicate highly reduced conditions that are favorable for Sn mobility. Based on the

evidence provided, it is concluded that the peraluminous intrusions of Taucane are the most plausible source of Sn.

5.4. Tin: new horizons for exploration in southern Peru

The Taucane Project, located in the Central Andean Backthrust Belt (Mesozoic block) in the southwestern end of the Eastern Cordillera of Peru (Figs. 7-8), represents the first recorded tin discovery in this morphostructural province. This discovery ushers in the metallogenic potential of the area, which was previously disregarded for Sn deposits. The occurrence of the Taucane Project demonstrates favorable conditions for the emplacement of Sn mineralization outside the areas traditionally recognized in Peru (i.e., the Macusani Structural Zone, the Paleozoic block, hosting the world-class San Rafael deposit and all its satellite deposits).

The mineralization present in the Taucane Project is, in volumetric terms, mainly of the manto-type, contrasting with the typical vein and lode Sn(W) deposits in Peru (e.g., Harlaux et al. 2023), and other deposits of the Central Andean Tin Belt in Bolivia (Jiménez-Franco et al. 2018; Torró et al. 2019a, b; Gemmrich et al. 2021; Torró et al. 2025) and Argentina (Desanois et al. 2019; Passamani et al. 2020). In contrast, it resembles the Colavi Sn ± Ag deposit near Potosí in Bolivia, where mantos hosted in the Cretaceous La Puerta Formation are volumetrically important (Ahlfeld and Schneider-Scherbina 1964; Arce-Burgoa 2007).

The occurrence of Taucane and Colavi in Cretaceous carbonated rocks outside the “Paleozoic block” along the Central Andean Tin Belt suggests that the generation of Sn-fertile magmas may have extended further than previously thought and probably concentrated along structural boundaries such as the one represented by the structural zone between the Macusani Structural Zone and the Central Andean Backthrust Belt.

Also, that Sn-bearing manto-type orebodies can be locally important near the Central Andean Tin Belt, where peraluminous magmas intersect carbonated sequences.

As demonstrated above, the discovery of Taucane marks a significant shift in tin exploration in southern Peru, addressing the historical uncertainty surrounding the northern extension of the Central Andes tin belt as discussed by Petersen (1972). As the San Rafael deposit previously demonstrated the economic potential of the region, Taucane's location outside the traditionally prospective Paleozoic block marks a critical departure from established exploration models and extends the known boundaries of the Central Andean Tin Belt southwestward.

6. CONCLUSIONS

The Taucane deposit is an anomalous discovery within the region, making it an exceptional case study for Sn-deposits. Within Taucane, the Lorena and Kelly systems are the most volumetrically significant. Orebodies in both systems are dominantly of manto-type and, to a lesser extent, veins. Intrusive rocks in the deposit include peraluminous and metaluminous granitoids and lamprophyres (minette). The hypogene mineralization comprised three main paragenetic stages recording a transition from low- to intermediate-sulfidation conditions.

Differences in mineralogy, paragenesis, and mineral compositions suggest that the Kelly system represents a more proximal position than the Lorena system within a continuum skarn-carbonate replacement deposit (CRD).

Taucane is the first polymetallic-Sn deposit in the region that is volumetrically dominated by manto-type orebodies and, to a lesser extent, vein-type orebodies. This contrasts with traditional tin deposits along the Central Andean Tin Belt, which typically occur as quartz-cassiterite veins and lodes. The exception is the Bolivian Colavi deposit, which has a mineralization style similar to that of Taucane, but with a lower volumetric

component of polymetallic sulfides and sulfosalts. In addition, there are a few deposits worldwide with mineralization styles comparable to Taucane, such as Renisson Bell, Mount Bischoff, and Cleveland in Australia, Dafulou and Huile in China, and Ayawilca in Peru.

Robust U-Pb cassiterite and zircon geochronology confirms that mineralization and granitoid emplacement were contemporaneous at ca. 24 Ma. In addition, the U-Pb cassiterite geochronology confirms the formation of Taucane during the most recent metalliferous event recorded in the Central Andean Tin Belt, spanning from the latest Oligocene to the Miocene. This demonstrates temporal synchronicity with the main Sn deposits along the Central Andean Tin Belt, including the giant San Rafael deposit in Peru and other world-class deposits in Bolivia, suggesting a regional-scale mineralizing event.

The discovery of Taucane, in an area previously ruled out as prospective for Sn, such as the Central Andean Backthrust Belt, represents a significant change in the Sn exploration strategy in Peru. This strategic change allows for the exploration of new areas with potential in the southern part of the country.

7. REFERENCES

- Acosta J, Rodríguez I, Valencia M, Flores A (2011) Memoria sobre la geología económica de la Región Puno. INGEMMET, Lima, p 50
- Ahlfeld F, Branisa L (1960) Geología de Bolivia. Editorial Don Bosco, p 245
- Ahlfeld F, Schneider-Scherbina A (1964) Los yacimientos minerales y de hidrocarburos de Bolivia. Bolivia Departamento Nac Geol 5:1–388
- Ahlfeld F (1967) Metallogenetic epochs and provinces of Bolivia. *Miner Deposita* 2:291–311. <https://doi.org/10.1007/BF00207022>
- Alayza D (2016) Generación de un modelo exploratorio local mediante la caracterización de la ocurrencia polimetálica del prospecto Taucane en la pre cordillera de Carabaya-Puno. Undergraduated thesis, Universidad Nacional de Ingeniería, Lima, p 324
- Alayza D, Chavez N, La Torre W, Kalinaj M (2017) Proyecto de exploración Taucane: Geología de un nuevo depósito polimetálico – Sn en el Sur del Perú. ProExplo: X Congreso Internacional de prospectores y exploradores, Lima, Perú, p 6
- Arce-Burgoa O (2007) Guía a los yacimientos metalíferos de Bolivia. SPC Impresores S.A., La Paz, p 346, ISBN 978-99954-0-143-6
- Arce-Burgoa O, Goldfarb R (2009) Metallogeny of Bolivia. *SEG NewsL.* 79:8–15. <https://doi.org/10.5382/SEGnews.2009-79.fea>
- Arenas M (1999) Exploración y geología de la mina San Rafael, Puno. *Minería* 260:10–31
- Arias T (2023) Estudio geológico y análisis del comportamiento mineralógico de SN en Veta Lorena–Proyecto Taucane, Distrito de San José–Azángaro–Puno. Universidad Nacional del Atiplano de Puno, Puno, p 134
- Aydın E, Sezgintürk M (2017) Indium tin oxide (ITO): a promising material in biosensing technology. *TrAC, Trends Anal Chem* 97:309–315. <https://doi.org/10.1016/j.trac.2017.09.021>
- Bahlburg H, Carlotto V, and Cardenas J (2006) Evidence of Early to Middle Ordovician arc volcanism in the Cordillera Oriental and Altiplano of southern Peru, Ollantaytambo formation and Umachiri beds: *J South Am Earth Sci* 22:52–65
- Ballouard C, Poujol M, Boulvais P, Branquet Y, Tartèse R, Vigneresse J (2016) Nb-Ta fractionation in peraluminous granites: a marker of the magmatic-hydrothermal transition. *Geology* 44:231–234. <https://doi.org/10.1130/G37475.1>
- Barbarin B (1999) A review of the relationships between granitoid types, their origins and their geodynamic environments. *Lithos* 46:605–626. [https://doi.org/10.1016/S0024-4937\(98\)00085-1](https://doi.org/10.1016/S0024-4937(98)00085-1)
- Bashar S (1998) Study of Indium Tin Oxide (ITO) for Novel Optoelectronic Devices. University of Manchester Institute of Science and Technology, Manchester, p 278
- Bau M (1996) Controls on the fractionation of isovalent trace elements in magmatic and aqueous systems: evidence from Y/Ho, Zr/Hf, and lanthanide tetrad effect. *Contrib Mineral Petrol* 123:323–333. <https://doi.org/10.1007/s004100050159>

- Benavides-Cáceres V (1999) Orogenic evolution of the Peruvian Andes: The Andean cycle. In: *Geology and Ore Deposits of the Central Andes*. *Econ. Geol. Bull. Soc. Econ Geol* 7:61–107. <https://doi.org/10.5382/SP.07.03>
- Bendezú R, Fontboté L (2009) Cordilleran epithermal Cu-Zn-Pb-(Au-Ag) mineralization in the colquijirca district, central Peru: deposit-scale mineralogical patterns. *Econ Geol* 104:905–944. <https://doi.org/10.2113/econgeo.104.7.905>
- Benites D, Torró L, Vallance J, Laurent O, Valverde P, Kouzmanov K, Chelle-Michou C, Fontboté L (2021) Distribution of indium, germanium, gallium and other minor and trace elements in polymetallic ores from a porphyry system: the Morococha district, Peru. *Ore Geol Rev* 136:1–25. <https://doi.org/10.1016/j.oregeorev.2021>.
- Benites D, Torró L, Vallance J, Laurent O, Quispe P, Rosas S, Uzieda M, Holm- Denoma C, Pianowski L, Camprubí A, Colás V, Fernández-Baca A, Giraldo L, Chelle-Michou C, Sáez J, Kouzmanov K, Fontboté L (2022) Geology, mineralogy, and cassiterite geochronology of the Ayawilca Zn-Pb-Ag-In-Sn- Cu deposit, Pasco, Peru. *Miner Deposita* 57 (3):481–507. <https://doi.org/10.1007/s00126-021-01066-z>
- Benjamin M, Johnson N, Naeser C (1987) Recent rapid uplift in the Bolivian Andes: evidence from fission-track dating. *Geology* 15 (7):680–683. [https://doi.org/10.1130/0091-7613\(1987\)15<680:RRUITB>2.0.CO;2](https://doi.org/10.1130/0091-7613(1987)15<680:RRUITB>2.0.CO;2)
- Bennett J, Kemp A, Hagemann S, Fiorentini M, Roberts M (2024) Systematic trends in the substitution mechanisms of minor elements in cassiterite. *Aust J Earth Sci* 71:1-27. <https://doi.org/10.1080/08120099.2024.2325396>
- Blake D, Smith J (1970) Mineralogical zoning in the Herberton tinfield, north Queensland, Australia. *Econ Geol* 65:993–997. <https://doi.org/10.2113/gsecongeo.65.8.993>
- Boekhout F, Reitsma M, Spikings R, Rodriguez R, Ulianov A, Gerdes A, Schaltegger U (2018) New age constraints on the palaeoenvironmental evolution of the late Paleozoic back-arc basin along the western Gondwana margin of southern Peru. *J S Am Earth Sci* 82:165–180. <https://doi.org/10.1016/j>.
- Bonin B, Janoušek V, Moyen J (2020) Chemical variation, modal composition and classification of granitoids. *Geol. Soc. Lond. Spec. Publ.* 491:9–51. <https://doi.org/10.1144/SP491-2019-138>
- Bowles J (2021) Oxides. In: Elias S, Alderton D (eds) *Encyclopedia of Geology*, 2nd edn. Elsevier, Amsterdam, pp 428–441. <https://doi.org/10.1016/B978-0-08-102908-4.00185-5>
- Breiter K, Lamarão C, Borges R, Dall'Agnol R (2014) Chemical characteristics of zircon from A-type granites and comparison to zircon of S-type granites. *Lithos* 192, 208–225. <https://doi.org/10.1016/j.lithos.2014.02.004>
- Buret Y, von Quadt A, Heinrich C, Selby D, Wälle M, Peytcheva I (2016) From a long-lived upper-crustal magma chamber to rapid porphyry copper emplacement: Reading the geochemistry of zircon crystals at Bajo de la Alumbrera (NW Argentina). *Earth Planet Sci Lett* 450:120–131. <https://doi.org/10.1016/j.epsl.2016.06.017>
- Cacho A, Melgarejo J, Camprubí A, Torró L, Castillo-Oliver M, Torres B, Artiaga D, Tauler E, Martínez A, Campeny M, Alfonso P, Arce-Burgoa O (2019) Mineralogy and distribution

of critical elements in the Sn–S–Pb–Ag–Zn Huanuni deposit, Bolivia. *Minerals* 9 (12):753. <https://doi.org/10.3390/min9120753>.

- Canaza M (2018) Estilo estructural y evolución tectónica sedimentaria de la faja plegada y corrida, del norte de la cuenca Titicaca, ubicado entre Azángaro y Putina. Undergraduated thesis, Universidad Nacional del Altiplano, Puno, p 195
- Cao H, Zhang Y, Pei Q, Zhang R, Tang L, Lin B, Cai G (2017) U–Pb dating of zircon and cassiterite from the Early Cretaceous Jiaojiguan iron-tin polymetallic deposit, implications for magmatism and metallogeny of the Tengchong area, western Yunnan, China. *Int Geol Rev* 59:234–238. <https://doi.org/10.1080/00206814.2016.1220842>
- Capitanio F, Faccenna C, Zlotnik S, Stegman D (2011) Subduction dynamics and the origin of Andean orogeny and the Bolivian orocline. *Nature* 480:83–86. <https://doi.org/10.1038/nature10596>
- Carlotto V, Quispe J, Acosta H, Rodriguez R, Romero D, Cerpa L, Mamani M, Velarde T, Lu S, Cueva E (2009) Dominios geotectónicos y metalogénesis del Perú. *Bol Soc Geol Perú* 103:1–89
- Carlotto V (2013) Paleogeographic and tectonic controls on the evolution of Cenozoic basins in the Altiplano and Western Cordillera of southern Peru. *Tectonophysics* 589:195–219. <https://doi.org/10.1016/j.earscirev.2017.11.025>
- Carr P, Zink S, Bennett V, Norman M, Amelin Y, Blevin P (2020) A new method for U-Pb geochronology of cassiterite by ID-TIMS applied to the Mole Granite polymetallic system, eastern Australia. *Chem Geol* 539:119539. <https://doi.org/10.1016/j.chemgeo.2020.119539>
- Carlier G, Lorand J, Audebaud E, Kienast J (1997) Petrology of an unusual orthopyroxene-bearing minette suite from southeastern Peru, Eastern Andean Cordillera: Al-rich lamproites contaminated by peraluminous granites. *J Volcanol Geotherm Res* 75:59–87. [https://doi.org/10.1016/S0377-0273\(96\)00035-2](https://doi.org/10.1016/S0377-0273(96)00035-2)
- Carlier G, Lorand J, Liégeois J, Fornari M, Soler P, Carlotto V, Cardenas J (2005) Potassic-ultrapotassic mafic rocks delineate two lithospheric mantle blocks beneath the southern Peruvian Altiplano. *Geology* 33:601–604. <https://doi.org/10.1130/G21643.1>
- Catchpole H, Kouzmanov K, Putlitz B, Seo J, Fontboté L (2015) Zoned base metal mineralization in a porphyry system: origin and evolution of mineralizing fluids in the Morococha district, Peru. *Econ Geol* 110:39–71. <https://doi.org/10.2113/econgeo.110.1.39>
- Chappell B, White A (1992) I- and S-type granites in the Lachlan Fold Belt. *Trans R Soc Edinb Earth Sci* 83:1–26. <https://doi.org/10.1017/S0263593300007720>
- Chelle-Michou C, Chiaradia M, Ovtcharova M, Ulianov A, Wotzlav J (2014) Zircon petrochronology reveals the temporal link between porphyry systems and the magmatic evolution of their hidden plutonic roots (the Eocene Corocochuayco deposit, Peru). *Lithos* 198:129–140. <https://doi.org/10.1016/j.lithos.2014.03.017>
- Cheng Y, Spandler C, Kemp A, Mao J, Rusk B, Hu Y, Blake K (2019) Controls on cassiterite (SnO₂) crystallization: Evidence from cathodoluminescence, trace- element chemistry, and geochronology at the Gejiu tin district. *Am Mineral* 104:118–129. <https://doi.org/10.2138/am-2019-6466>

- Chew D, Schaltegger U, Košler J, Whitehouse M, Gutjahr M, Spikings R and Mišković A (2007) U-Pb geochronologic evidence for the evolution of the Gondwanan margin of the north Central Andes: *Geol Soc Am Bull* 119 (5–6):697–711
- Chew D, Magna T, Kirkland C, Mišković A, Cardona A, Schaltegger U, Spikings R (2008) Detrital zircon fingerprint of the Proto-Andes: Evidences for a Neoproterozoic active margin? *Precambrian Res* 167:186–200. <https://doi.org/10.1016/j.precamres.2008.08.002>
- Chew D, Pedemonte G, Corbett E (2016) Proto-Andean evolution of the Eastern Cordillera of Peru. *Gondwana Res* 35:59–78. <https://doi.org/10.1016/j.gr.2016.03.016>
- Claiborne L, Miller C, Wooden J (2010) Trace element composition of igneous zircon: a thermal and compositional record of the accumulation and evolution of a large silicic batholith, Spirit Mountain, Nevada. *Contrib Mineral Petrol* 160:511–531
- Claire T (1986) Bolivia: La maldición del estaño. *Nueva Soc.* 81: 4-7
- Clark A, Palma V, Archibald D, Farrar E, Arenas F, Robertson R (1983) Occurrence and age of tin mineralization in the Cordillera Oriental, southern Peru. *Econ Geol* 78:514–520. <https://doi.org/10.2113/gsecongeo.78.3.514>
- Clark A, Farrar E, Kontak D, Langridge R, Arenas M, France L, McBride S, Woodman P, Wasteneys H, Sandeman H (1990) Geologic and geochronological constraints on the metallogenic evolution of the Andes of southeastern Peru. *Econ Geol* 85:1520–1583. <https://doi.org/10.2113/gsecongeo.85.7.1520>
- Clark A, Chen Y, Grant J, Kontak D, Wasteneys H, Sandeman H, Farrar E, Archibald D (2000) Delayed inception of ore deposition in major lithophile-metal vein systems: the San Rafael tin and Pasto Bueno tungsten deposits, Peru. *Geol Soc Am S* 32:279
- Collins P (1981) The geology and genesis of the Cleveland tin deposit, western Tasmania; fluid inclusion and stable isotope studies. *Econ Geol* 76:365–392. <https://doi.org/10.2113/gsecongeo.76.2.365>
- Cooke C, Abbott M, Wolfe P (2008) Metallurgy in Southern South America, in *Encyclopedia of the History of Science, Technology, and Medicine in Non-Western Cultures*, ed. H. Selin. Springer, Cham, pp 1658–1662. https://doi.org/10.1007/978-1-4020-4425-0_9628
- Cooke D, Hollings P, Wilkinson J, Tosdal R (2014) Geochemistry of porphyry deposits. In: Turekian HDHK (ed) *Treatise on geochemistry*, 2nd Edition. Elsevier, Oxford, pp 357–381
- Cordani U G (1967) Unpublished letter in library of Servicio Geológico de Bolivia, La Paz
- Cunningham C, Zartman R, McKee E, Rye R, Naeser C, Sanjinés V, Erickson G, Tavera V (1996) The age and thermal history of Cerro Rico de Potosí, Bolivia. *Miner Deposita* 31: 374–385. <https://doi.org/10.1007/BF00189185>
- Czamanske G (1974) The FeS content of sphalerite along the chalcopyrite-pyrite-bornite sulfur fugacity buffer. *Econ Geol* 69:1328–1334. <https://doi.org/10.2113/gsecongeo.69.8.1328>
- Dalmayrac B, Laubacher G, Marocco R (1980) Caractères gé é aux de l'évolution géologique des Andes Péruviennes. *Géol. Andes Péruviennes* 122. BRGM, Paris, p 501

- De La Cruz N (1995) Estudio geológico de los cuadrángulos de Velille, Yauri y Azángaro. INGEMMET, Bol 58 (A), p 150
- De Silva S, Kay M (2018) Turning up the heat: high-flux magmatism in the Central Andes. *Elements* 14:245-250. <https://doi.org/10.2138/gselements.14.4.245>
- Debon F, Le Fort P (1988) A cationic classification of common plutonic rocks and their magmatic associations: principles, method, applications. *Bull Mineral* 111(5):493–510. <https://doi.org/10.3406/bulmi.1988.8096>
- Denholm J, Stepanov A, Meffre S, Bottrill R, Thompson J (2021) The Geochronology of Tasmanian tin deposits using LA-ICP-MS U-Pb cassiterite dating. *Econ Geol* 116:1387–1407. <https://doi.org/10.5382/econgeo.4837>
- Dietrich A, Lehmann B, Wallianos A (2000) Bulk rock and melt inclusion geochemistry of Bolivian tin porphyry systems. *Econ Geol* 95:313-326. <https://doi.org/10.2113/gsecongeo.95.2.313>
- Dines H (1956) *The Metalliferous Mining Region of South-West England*. HMSO publications (2), p 526
- Desanois L, Lüders V, Niedermann S, Trumbull R (2019) Formation of epithermal Sn-Ag-(Zn) vein-type mineralisation at the Pirquitas deposit, NW Argentina: Fluid inclusion and noble gas isotopic constraints. *Chem Geol* 508:78–91. <https://doi.org/10.1016/j.chemgeo.2018.04.024>
- Egeler C and De Booy T (1961) Preliminary note on the geology of the Cordillera Vilcabamba (SE Peru), with emphasis on the essentially pre-Andean origin of the structure: *Geologie en Mijnbouw, Jaargang* 40:319–325
- Eichelberger N, McQuarrie N, Ehlers T, Enkelmann E, Barnes J, Lease R (2013) New constraints on the chronology, magnitude, and distribution of deformation within the central Andean orocline. *Tectonics* 32:1432–1453. <https://doi.org/10.1002/tect.20073>.
- Eichelberger N, McQuarrie N, Ryan J, Karimi B, Beck S, Zandt G (2015) Evolution of crustal thickening in the central Andes, Bolivia. *Earth Planet Sci Lett* 426:191–203. <https://doi.org/10.1016/j.epsl.2015.06.035>.
- Einaudi M, Meinert L, Newberry R (1981) Skarn deposits. *Economic Geology* 75th Anniversary Volume 317–391. <https://doi.org/10.5382/AV75.11>
- Everden J (1961) Edades absolutas de algunas rocas ígneas en Bolivia por el método potasio-argón. *Soc Geol Bol Not* 2:3
- Evernden J, Kriz S, Cherroni C (1977) Potassium-argon ages of some Bolivian rocks. *Econ Geol* 72:1042–1061. <https://doi.org/10.2113/gsecongeo.72.6.1042>
- Farrar E, Clark A, Kontak D, Archibald D (1988) Zongo-San Gaban zone: Eocene foreland boundary of the Central Andean orogen, northwest Bolivia and southeast Peru. *Geology* 16:55-58. [https://doi.org/10.1130/0091-7613\(1988\)016<0055:ZSGNZE>2.3.CO;2](https://doi.org/10.1130/0091-7613(1988)016<0055:ZSGNZE>2.3.CO;2)
- Farrar E, Clark A, Heinrich S (1990) The age of the Zongo pluton and the tectonothermal evolution of the Zongo-San Gabán Zone in the Cordillera Real, Bolivia. *Extended abstracts, 1st International Symposium on Andean Geodynamics, Grenoble*, pp 171–174

- Farmer C, Searl A, Halls C (1991) Cathodoluminescence and growth of cassiterite in the composite lodes at South Crofty mine. Cornwall, England, *Miner Mag* 55:447–458. <https://doi.org/10.1180/minmag.1991.055.380.14>
- Ferry J, Watson E (2007) New thermodynamic models and revised calibrations for the Ti-in-zircon and Zr-in-rutile thermometers. *Contrib Mineral Petrol* 154:429–437.
- Foley S, Venturelli G, Green D, Toscani L (1987) The ultrapotassic rocks: characteristics, classification, and constraints for petrogenetic models. *Earth Sci Rev* 24 (2):81–134. [https://doi.org/10.1016/0012-8252\(87\)90001-8](https://doi.org/10.1016/0012-8252(87)90001-8)
- Fontboté L (2018) Ore deposits of the Central Andes. *Elements* 14:257–261. <https://doi.org/10.2138/gselements.14.4.257>
- Frost B (1991) Introduction to oxygen fugacity and its petrologic importance. In: Lindsley, D.H. (Ed.), *Oxide Minerals: Petrologic and Magnetic Significance*. *Rev Mineral* 25:1–8.
- Gemrich L, Torró L, Melgarejo J, Laurent O, Vallance J, Chelle-Michou C, Sempere T (2021) Trace element composition and U-Pb ages of cassiterite from the Bolivian tin belt. *Miner Deposita* 56:1491–1520. <https://doi.org/10.1007/s00126-020-01030-3>
- Gillis R, Horton B, Grove M (2006) Thermochronology, geochronology, and upper crustal structure of the Cordillera Real: implications for Cenozoic exhumation of the central Andean plateau. *Tectonics* 25:1–22. <https://doi.org/10.1029/2005TC001887>
- Grant N, Halls C, Avila W, Snelling N (1979) K-Ar Ages of Igneous Rocks and Mineralization in Part of the Bolivian Tin Belt. *Econ Geol* 74:838–851. <https://doi.org/10.2113/gsecongeo.74.4.838>
- Grimes C, Wooden J, Cheadle M, John B (2015) Fingerprinting” tectonomagmatic provenance using trace elements in igneous zircon. *Contrib Mineral Petrol* 170:1–26. <https://doi.org/10.1007/s00410-015-1199-3>
- Guillong M, Hametner K, et al. (2005) Preliminary characterisation of new glass reference materials (GSA-1G, GSC-1G, GSD-1G and GSE-1G) by Laser Ablation-Inductively Coupled Plasma-Mass Spectrometry using 193 nm, 213 nm and 266 nm wavelengths. *Geostand Geoanal Res* 29:315-331. <https://doi.org/10.1111/j.1751-908X.2005.tb00903.x>
- Guillong M, Meier D, Allan M, Heinrich C, Yardley B (2008) SILLIS: A MATLAB-based program for the reduction of laser ablation ICP-MS data of homogeneous materials and inclusions. In: Sylvester P, (ed) *Laser Ablation ICP-MS in the Earth Sciences: Current Practices and Outstanding Issues*. *Miner. Assoc. Can Short Course* 40, Vancouver, pp 328-33
- Guillong M, Von-Quadt A, Sakata S, Peytcheva I, Bachmann O (2014) LA-ICP-MS Pb–U dating of young zircons from the Kos–Nisyros volcanic centre, SE Aegean arc. *J Anal At Spectrom* 29:963-970. <https://doi.org/10.1039/C4JA00009A>
- Guo J, Zhang R, Sun W, Ling M, Hu Y, Wu K, Luo M, Zhang L (2018) Genesis of tin-dominant polymetallic deposits in the Dachang district, South China: Insights from cassiterite U-Pb ages and trace element compositions. *Ore Geol Rev* 95:863–879. <https://doi.org/10.1016/j.oregeorev.2018.03.023>
- Grimes C, Wooden J, Cheadle M, John B (2015) Fingerprinting” tectono- magmatic provenance using trace elements in igneous zircon. *Contrib Mineral Petrol* 170:1–26.

- Haldar S (2020) Introduction to mineralogy and petrology, 2nd edition. Elsevier, Oxford, pp 1-51. <https://doi.org/10.1016/C2012-0-03337-6>
- Halley S, Walshe J (1995) A reexamination of the Mount Bischoff cassiterite sulfide skarn, western Tasmania. *Econ Geol* 90:1676–1693. <https://doi.org/10.2113/gsecongeo.90.6.1676>
- Harlaux M, Kouzmanov K, Gialli S, Laurent O, Rielli A, Dini A, Chauvet A, Menzies A, Kalinaj M, Fontboté L (2020) Tourmaline as a tracer of late-magmatic to hydrothermal fluid evolution: the world-class San Rafael tin (-copper) deposit. Peru. *Econ Geol* 115:1665–1697. <https://doi.org/10.5382/econgeo.4762>
- Harlaux M, Kouzmanov K, Gialli S, Clark A, Laurent O, Corthay G, Flores E, Dini A, Chauvet A, Ulianov A, Chiaradia M, Menzies A, Durand G, Kalinaj M, Fontboté L (2021) The upper Oligocene San Rafael intrusive complex (Eastern Cordillera, southeast Peru), host of the largest-known high-grade tin deposit. *Lithos* 400:106409. <https://doi.org/10.1016/j.lithos.2021.106409>
- Harlaux M, Kontak D, Clark A, Kouzmanov K, Holm-Denoma C, Gialli S, Fontboté L (2023) Depositing >1.5 Mt of tin within < 1 m.y. of initial granitic intrusion in the San Rafael tin (-copper) Deposit, Southeastern Peru. *Econ Geol* 118(6):1371-1396. <https://doi.org/10.5382/econgeo.5021>
- Hayden L, Watson E (2007) Rutile saturation in hydrous siliceous melts and its bearing on Ti-thermometry of quartz and zircon. *Earth Planet Sci Lett* 258:561–568.
- Hellstrom J, Paton C, et al. (2008) Iolite: Software for spatially resolved LA-(quad and MC) ICP-MS analysis. In: Sylvester P (ed) *Laser ablation ICP-MS in the Earth sciences: Current practices and outstanding issues*. *Miner Assoc Can* 40:343–348.
- Heuschmidt B, La Torre J, Angels V, Zapata M (2002) Las áreas prospectivas de Bolivia para yacimientos metalíferos. *Bol Serv Nac Geol Min* 30. ISSN 1023 -7674.
- Horstwood M, Košler J, et al. (2016) Community-derived standards for LA-ICP-MS U-(Th)Pb geochronology – uncertainty propagation, age interpretation and data reporting. *Geostand Geoanal Res* 40:311-332. <https://doi.org/10.1111/j.1751-908X.2016.00379.x>
- Horton B (2018) Sedimentary record of Andean Mountain building. *Earth-Sci Rev* 178:279–309. <https://doi.org/10.1016/j.earscirev.2017.11.025>
- Hou Z, Zaw K, Pan G, Mo X, Xu Q, Hu Y, Li X (2007) Sanjiang Tethyan metallogenesis in S.W. China: Tectonic setting, metallogenic epochs and deposit types. *Ore Geol Rev* 31:48–87. <https://doi.org/10.1016/j.oregeorev.2004.12.007>
- Hoskin P (2005) Trace-element composition of hydrothermal zircon and the alteration of Hadean zircon from the Jack Hills, Australia. *Geochim Cosmochim Acta* 69:637–648. <https://doi.org/10.1016/j.gca.2004.07.006>
- Huberty J, Kita N, Kozdon R, Heck P, Fournelle J, Spicuzza M, Xu H, Valley J (2010) Crystal orientation effects in $\delta^{18}\text{O}$ for magnetite and hematite by SIMS. *Chem Geol* 276:269–283. <https://doi.org/10.1016/j.chemgeo.2010.06.012>
- Ingham F, Bradford E (1960) The geology and mineral resources of the Kinta Valley, Perak. *Geol. Surv. Malaysia, District Mem* 9:1–347.

- Instituto Geológico, Minero y Metalúrgico (2023) Carta Geológica Nacional - Escala 1:50,000. Ministerio de Energía y Minas, Repositorio Institucional INGEMMET
- Ishihara S (1981) The granitoid series and mineralization. *Econ Geol* (75):458–484. <https://doi.org/10.5382/AV75.14>
- Ishihara S, Murakami H, Márquez-Zavalía M (2011) Inferred indium resources of the Bolivian tin-polymetallic deposits. *Resour Geol* 61:174–191. <https://doi.org/10.1111/j.1751-3928.2011.00157.x>
- Jiang S, Yu J, Lu J (2004) Trace and rare-earth element geochemistry in tourmaline and cassiterite from the Yunlong tin deposit, Yunnan, China: implication for migmatitic-hydrothermal fluid evolution and ore genesis. *Chem Geol* 209:193–213. <https://doi.org/10.1016/j.chemgeo.2004.04.021>
- Jiménez N, López-Velásquez S (2008) Magmatism in the Huarina belt, Bolivia, and its geotectonic implications. *Tectonophysics* 459(1):85–106. <https://doi.org/10.1016/j.tecto.2007.10.012>
- Jiménez-Franco A, Alfonso P, Canet C, Trujillo J (2018) Mineral chemistry of In-bearing minerals in the Santa Fe mining district, Bolivia. *Andean Geol* 45(3):410–432. <https://doi.org/10.5027/andgeoV45n3-3052>
- Kamilli, R.J., and Criss, R.E., 1996, Genesis of the Silsilah tin deposit, Kingdom of Saudi Arabia. *Econ Geol* 91:1414–1434. <https://doi.org/10.2113/gsecongeo.91.8.1414>
- Kamilli R, Kimball B, Carlin Jr (2017) Tin, In: Schulz K, DeYoung J, Seal II R, Bradley D (Eds.) Chapter 5 of Critical mineral resources of the United States-Economic and environmental geology and prospects for future supply. USGS Professional Paper 1802, pp. S1–S53
- Kay S, Coira B, Caffè P, Chen C (2010) Regional chemical diversity, crustal and mantle sources and evolution of central Andean Puna plateau ignimbrites. *J. Volcanol. Geotherm. Res.* 198(1-2):81-111. <https://doi.org/10.1016/j.jvolgeores.2010.08.013>
- Kay S, Mpodozis C (2020) The Andes. *Encycl Geol* 80:41–72. <https://doi.org/10.1016/B978-0-08-102908-4.00173-9>
- Kelly W, Turneure F (1970) Mineralogy, paragenesis and geothermometry of the tin and tungsten deposits of the Eastern Andes, Bolivian. *Econ Geol* 65:609–680. <https://doi.org/10.2113/gsecongeo.65.6.609>
- Kempe U, Lehmann B, Wolf D, Rodionov N, Bombach K, Schwengfelder U, Dietrich A (2008) U–Pb SHRIMP geochronology of Th-poor, hydrothermal monazite: An example from the Llallagua tin-porphyry deposit, Bolivia. *Geochim Cosmochim Acta* 72:4352–4366. <https://doi.org/10.1016/j.gca.2008.05.059>
- Kendall-Langley L, Kemp A, Grigson J, Hammerli J (2019) U-Pb and reconnaissance Lu-Hf isotope analysis of cassiterite and columbite group minerals from Archean Li- Cs-Ta type pegmatites of Western Australia. *Lithos* (352–353):105231. <https://doi.org/10.1016/j.lithos.2019.105231>
- Kontak D, Clark A (2002) Genesis of the giant, bonanza San Rafael lode tin deposit, Peru: origin and significance of pervasive alteration. *Econ Geol* 97:1741–1777. <https://doi.org/10.2113/gsecongeo.97.8.1741>

- Kontak D, Clark A, Farrar E (1984) The Magmatic Evolution of the Cordillera Oriental, Southeastern Peru. In: Harmon R, Barreiro B (Eds.), *Andean Magmatism-Chemical and Isotopic Constraints*. Shiva, London, pp. 203–219. https://doi.org/10.1007/978-1-4684-7335-3_15
- Kontak D, Clark A, Farrar E, Archibald D, Baadsgaard H (1987) Geochronological data for tertiary granites of the Southeast Peru segment of the central Andean tin belt. *Econ Geol* 82:1711–1618. <https://doi.org/10.2113/gsecongeo.82.6.1611>
- Kley J, Müller J, Tawackoli S, Jacobshagen V, Manutsoglu E (1997) Pre-Andean and Andean-age deformation in the Eastern Cordillera of southern Bolivia. *J S Am Earth Sci* 10:1–19. [https://doi.org/10.1016/S0895-9811\(97\)00001-1](https://doi.org/10.1016/S0895-9811(97)00001-1).
- Kley J (1999) Geologic and geometric constraints on a kinematic model of the Bolivian orocline. *J S Am Earth Sci* 12:221–235. [https://doi.org/10.1016/S0895-9811\(99\)00015-2](https://doi.org/10.1016/S0895-9811(99)00015-2)
- Kontak D, Clark A, Farrar E, Strong D (1985) The rift associated Permo-Triassic magmatism of the Eastern Cordillera: a precursor to the Andean orogeny. In: Pitcher W, Atherton M, Cobbing J, and Beckinsale R (Eds.), *Magmatism at a plate edge: The Peruvian Andes*. Blackie, Glasgow, and Halsted Press, New York, pp. 36–44
- Kontak D, Clark A, Farrar E, Archibald A (1987) Geochronological data for Tertiary granites of the southeast Peru segment of the central andean tin belt. *Econ Geol* 82:1611–1618. <https://doi.org/10.2113/gsecongeo.82.6.1611>
- Kontak D, Clark A, Farrar E, Archibald D, Baadsgaard H (1990a) Late Paleozoic-Early Mesozoic magmatism in the Cordillera de Carabaya, Puno, southeastern Peru: geochronology and petrochemistry. *J S Am Earth Sci* 3:213–230. [https://doi.org/10.1016/0895-9811\(90\)90004-K](https://doi.org/10.1016/0895-9811(90)90004-K)
- Kontak D, Farrar E, Clark A, Archibald D (1990b) Eocene tectono-thermal rejuvenation of an upper Paleozoic-lower Mesozoic terrane in the Cordillera de Carabaya, Puno, southeastern Peru, revealed by K–Ar and ⁴⁰Ar/³⁹Ar dating. *J S Am Earth Sci* 3:231–246. [https://doi.org/10.1016/0895-9811\(90\)90005-L](https://doi.org/10.1016/0895-9811(90)90005-L)
- Kontak D, Clark A (2002) Genesis of the giant, Bonanza San Rafael lode tin deposit, Peru: Origin and significance of pervasive alteration. *Econ Geol* 97 (8):1741–1777. <https://doi.org/10.2113/gsecongeo.97.8.1741>
- Lanari P, Vidal O, De Andrade V, Dubacq B, Lewin E, Grosch E, Schwartz S (2014) XMapTools: a MATLAB©-based program for electron microprobe X-ray image processing and geothermobarometry. *Comput Geosci* 62:227–240. <https://doi.org/10.1016/j.cageo.2013.08.010>
- Lanari P, Vho A, Bovay T, Airaghi L, Centrella S (2019) Quantitative compositional mapping of mineral phases by electron probe micro-analyser. *Geol Soc Lond, Spec Publ* 478:39–63. <https://doi.org/10.1144/SP478.4>
- Laubacher G (1978) Géologie de la Cordillère Orientale et de l'Altiplano au nord et au nord-ouest du Lac Titicaca (Pérou). *Trav Doc ORSTOM* 95, p 217
- Le Maitre R, Streckeisen A, Zanettin B, Le Bas M, Bonin B, Bateman P, Bellieni G, Dudek A, Efremova S, Keller J, Lameyre J, Sabine P, Schmid R, Sørensen H, Woolley A (2002) *Igneous rocks - A Classification and Glossary of Terms*, Cambridge, University Press 2nd edition, p 256

- Lehmann B (1985) Formation of the strata-bound Kellhuani tin deposits, Bolivia. *Miner Deposita* 20:169–176. <https://doi.org/10.1007/BF00204561>
- Lehmann B (1987) Tin granites, geochemical heritage, magmatic differentiation. *Geol Rundsch* 76:177-185. <https://doi.org/10.1007/BF01820581>
- Lehmann B (1990a) Metallogeny of tin. In Bhattacharji S, Friedman G, Neugebauer H, Seilacher A (Eds) *Lecture Notes in Earth Sciences* (32). Berlin, Springer-Verlag, p 211. <https://doi.org/10.1007/BFb0010922>
- Lehmann B (1990b) The stratabound Kellhuani tin deposits, Bolivia. In: Fontboté, L., Amstutz, G.C., Cardozo, M., Cedillo, E., Frutos, J. (eds) *Stratabound Ore Deposits in the Andes. Soc. Geol. Appl. Miner. Depos., Spec. Publ. 8*. Springer, Berlin, pp.147-160. https://doi.org/10.1007/978-3-642-88282-1_9
- Lehmann B, Ishihara S, Michel H, Miller J, Rapela C, Sanchez A, Tisl M, Winkelmann L (1990) The Bolivian tin province and regional tin distribution in the Central Andes: a reassessment. *Econ Geol* 85:1044–1058. <https://doi.org/10.2113/gsecongeo.85.5.1044>
- Lehmann B (2021) Formation of tin ore deposits: A reassessment. *Lithos* 402:105756. <https://doi.org/10.1016/j.lithos.2020.105756>
- Leopardi D, Gerdes A, Albert R, Gutzmer J, Lehmann B, Burisch M (2024) LA-ICP-MS U-Pb cassiterite age data of the Sadisdorf deposit link Sn-Li-(W-Cu) mineralization in the eastern Erzgebirge to the collapse of the Altenberg-Teplice Caldera. *Geochem* 84(1):126038. <https://doi.org/10.1016/j.chemer.2023.126038>
- Li Y, He S, Zhang R, Bi X, Feng J, Teng G, Wang W, Huang F, Li X (2022) Cassiterite oxygen isotopes in magmatic-hydrothermal systems: in situ microanalysis, fractionation factor, and applications. *Miner Deposita* 57:643–661. <https://doi.org/10.1007/s00126-021-01068-x>.
- Loucks R, Fiorentini M, Henríquez G (2020) New magmatic oxybarometer using trace elements in zircon. *J Petrol* 61:egaa034.
- Maffione M, Speranza F, Faccenna C (2009) Bending of the Bolivian orocline and growth of the central Andean plateau: Paleomagnetic and structural constraints from the Eastern Cordillera (22–24°S, NW Argentina). *Tectonics* 28:TC4006. <https://doi.org/10.1029/2008TC002402>
- Mamani M, Wörner G, Sempere T (2010) Geochemical variations in igneous rocks of the central Andean orocline (13°S to 18°S): tracing crustal thickening and magma generation through time and space. *Geol Soc Am Bull* 122:162–182. <https://doi.org/10.1130/B26538.1>
- Mao W, Zhong H, Yang J, Tang Y, Liu L, Fu Y, Zhang X, Sein K, Aung S, Zhang L (2020) Combined zircon, molybdenite, and cassiterite geochronology and cassiterite geochemistry of the Kuntabin tin-tungsten deposit in Myanmar. *Econ Geol* 115:603–625. <https://doi.org/10.5382/econgeo.4713>
- Markovic S, Szymanowski D, Tavazzani L, Torró L, Kouzmanov K, Kalinaj M, Chelle-Michou C (2025) Timescales of magmatic-hydrothermal activity at the giant San Rafael tin deposit (Peru). *Earth Planet Sci Lett* 671:119624. <https://doi.org/10.1016/j.epsl.2025.119624>

- Marocco R (1978) Un segment E-W de la chaîne des Andes péruviennes: la déflexion d'Abancay. Etude géologique de la Cordillère orientale et des hauts plateaux entre Cuzco et San Miguel, sud du Pérou (12°30'S–14°00'S): Géologie des Andes péruviennes, Travaux et documents de l'O.R.S.T.O.M., Paris, v. 94, p 196
- Mathur R, Powell W, Mason A, Godfrey L, Yao J, Baker M (2017) Preparation and measurement of cassiterite for Sn isotope analysis. *Geostand Geoanal Res* 41(4):701-707. <http://dx.doi.org/10.1111/ggr.12174>
- McBride S, Robertson R, Clark A, Farrar E (1983) Magmatic and metallogenetic episodes in the northern tin belt, Cordillera Real, Bolivia. *Geol Rundsch* 72:685–671. <https://doi.org/10.1007/BF01822089>
- McDonough W, Sun S (1995) Composition of the Earth. *Chem Geol* 120(3-4):223-253. [https://doi.org/10.1016/0009-2541\(94\)00140-4](https://doi.org/10.1016/0009-2541(94)00140-4)
- McQuarrie N, DeCelles P (2001) Geometry and structural evolution of the central Andean. *Tectonics* 20:669–692. <https://doi.org/10.1029/2000TC001232>
- Meinert L (1992) Skarns and skarn deposits. *Geosci Can* 19 (4):145–162
- Meinert L, Dipple G, Nicolescu S (2005) World skarn deposits. *Economic Geology* 100th Anniversary Volume 299–336. <https://doi.org/10.5382/AV100.11>
- Meyer N, Markl G, Gerdes A, Gutzmer J, Burisch M (2024) Timing and origin of skarn-, greisen-, and vein-hosted tin mineralization at Geyer, Erzgebirge (Germany). *Miner Deposita* 59:1–22. <https://doi.org/10.1007/s00126-023-01194-8>
- Middlemost E (1994) Naming Materials in the Magma/Igneous Rock System. *Earth-Sci Rev* 37:215-224. [https://doi.org/10.1016/0012-8252\(94\)90029-9](https://doi.org/10.1016/0012-8252(94)90029-9)
- Mišković A, Spikings R, Chew D (2009) Tectonomagmatic evolution of Western Amazonia: Geochemical characterization and zircon U-Pb geochronologic constraints from the Peruvian Eastern Cordillera. *Geol Soc Am Bull* 121 (9–10):1298–1324. <https://doi.org/10.1130/B26488.1>
- Młynarczyk M, Sherlock R, Williams-Jones A (2003) San Rafael, Peru: geology and structure of the world's richest tin lode. *Miner Deposita* 38:555–567. <https://doi.org/10.1007/s00126-002-0334-z>
- Młynarczyk M, Williams-Jones A (2005) The role of collisional tectonics in the metallogeny of the Central Andean tin belt. *Earth Planet. Sci Lett* 240:656–667. <https://doi.org/10.1016/j.epsl.2005.09.047>
- Moyen J (2009) High Sr/Y and La/Yb ratios: the meaning of the “adakitic signature”. *Lithos* 112:556–574. <https://doi.org/10.1016/j.lithos.2009.04.001>
- Möller P, Dulski P, Szacki W, Malow G, Riedel E (1988) Substitution of tin in cassiterite by tantalum, niobium, tungsten, iron and manganese. *Geochim Cosmochim Acta* 52:1497–1503. [https://doi.org/10.1016/0016-7037\(88\)90220-7](https://doi.org/10.1016/0016-7037(88)90220-7)
- Münker C, Pfänder J, Weyer S, Büchl A, Kleine T, Mezger K (2003) Evolution of planetary cores and the Earth–Moon system from Nb/Ta systematics. *Science* 301:84–87
- Neymark L, Holm-Denoma C, Moscatti R (2018) In situ LA-ICPMS U–Pb dating of cassiterite without a known-age matrix-matched reference material: examples from worldwide tin

- deposits spanning the Proterozoic to the tertiary. *Chem Geol* 483:410–425. <https://doi.org/10.1016/j.chemgeo.2018.03.008>
- Paar W, de Brodtkorb M, Sureda R, Topa D (1998) A microprobe study of complex Ag-Sn ores from Pirquitas, Jujuy province, Argentina. In Proceedings of the Abstracts for the Plenary Lectures, Symposia, and Special Sessions of the 17th General Meeting of the International Mineralogical Association, Toronto, Japan, 7–19 August; p. A118.
- Passamani F, Bongiolio E, Nepomuceno de Oliveira F, Neumann R (2020) Geology and structural controls of the Ag–Sn–Zn Pirquitas deposit, northwestern Argentina. *J S Am Earth Sci* 100:1–15. <https://doi.org/10.1016/j.jsames.2020.102537>
- Pašava J, Kříbek B, Dobeš P, Vavřín I, Žák K, Fan D, Zhang T, Boiron M (2003) Tin-polymetallic sulfide deposits in the eastern part of the Dachang tin field (South China) and the role of black shales in their origin. *Miner Deposita* 38:39–66. <https://doi.org/10.1007/s00126-002-0269-4>
- Patterson D, Ohmoto H, Solomon M (1981) Geologic setting and genesis of cassiterite-sulfide mineralization at Renison Bell, western Tasmania. *Econ Geol* 76:393–438. <https://doi.org/10.2113/gsecongeo.76.2.393>
- Paton C, Woodhead J, et al. (2010) Improved laser ablation U-Pb zircon geochronology through robust downhole fractionation correction. *Geochem Geophys Geosyst* 11:1–36. <https://doi.org/10.1029/2009GC002618>
- Perez N, Horton B (2014) Oligocene-Miocene deformational and depositional history of the Andean hinterland basin in the northern Altiplano plateau, southern Peru. *Tectonics* 33:1819–1847. <https://doi.org/10.1002/2014TC003647>
- Perez N, Horton B, Carlotto V (2016a) Structural inheritance and selective reactivation in the central Andes: Cenozoic deformation guided by pre-Andean structures in southern Peru. *Tectonophysics* 671:264–280. <https://doi.org/10.1016/j.tecto.2015.12.031>
- Perez N, Horton B, McQuarrie N, Stübner K, Ehlers T (2016b) Andean shortening, inversion, and exhumation associated with thin- and thick-skinned deformation in southern Peru. *Geol Mag* 153(5-6):1013–1041. <https://doi.org/10.1017/S0016756816000121>
- Petrus J, Kamber B (2012) VizualAge: A novel approach to Laser Ablation ICP-MS U-Pb geochronology data reduction. *Geostand Geoanal Res* 36:247–270. <https://doi.org/10.1111/j.1751-908X.2012.00158.x>
- Petersen U (1972) Geochemical and tectonic implications of South American metallogenic provinces. *New York Acad. Sci Ann* 196:3–38
- Pfiffner O, Gonzalez L (2013) Mesozoic–Cenozoic evolution of the western margin of South America: Case study of the Peruvian Andes. *Geosci* 3:262–310. <https://doi.org/10.3390/geosciences3020262>
- Pichavant M, Erdmann S, Kontak D, Michaud J, Villaros A (2024) Trace element partitioning in strongly peraluminous rare-metal silicic magmas – Implications for fractionation processes and for the origin of the Macusani Volcanics (SE Peru). *Geochim Cosmochim Acta* 365:229–252. <https://doi.org/10.1016/j.gca.2023.11.021>
- Pitcher W, Atherton M, Cobbing E, and Beckinsale R (1985) Magmatism at a plate edge: The Peruvian Andes: Glasgow, Blackie, p 328

- Ramirez-Briones, JS (2024) Elemental and isotope characterization of the Lithium-rich tuff from the Macusani volcanic field, Puno, Peru. M.S. thesis, Pontificia Universidad Católica del Peru, p 195
- Ramirez-Briones JS, Torró L, Chiaradia M, Laurent O, Mandrou S, Tavazzani L, Chelle-Michou C, Vallance J, Baby P (2025) Petrogenesis of volcanogenic sedimentary lithium ore in the Neogene Macusani Volcanic Field, Puno, Peru. *J Petrol* 66(5):egaf041. <https://doi.org/10.1093/petrology/egaf041>
- Ramos V (1988) Late Proterozoic-Early Paleozoic of South America a collisional history. *Episodes* 11:168-174. <https://doi.org/10.18814/epiiugs/1988/v11i3/003>
- Ramos V (2008) The basement of the central Andes: the Arequipa and related terranes. *Annu. Rev. Earth Planet Sci* 36:289–324. <https://doi.org/10.1146/annurev.earth.36.031207.124304>
- Ramos V (2018) Tectonic evolution of the Central Andes: from terrane accretion to crustal delamination. In: Zamora G, McClay K, Ramos V (Eds.), *Petroleum Basins and Hydrocarbon Potential of the Andes of Peru and Bolivia*. *Am Assoc Pet Geol* pp. 1–34. <https://doi.org/10.1306/13622115M1172855>
- Ramos V, Jiménez N (2014) Extensión oriental del macizo de Arequipa en los Andes bolivianos: Sus implicancias tectónicas. In: *Simposio Tectónica preandina, Actas 19º Congreso Geológico Argentino, Córdoba, S21–50*, p 2
- Redwood S, MacIntyre R (1989) K-Ar dating of Miocene magmatism and related epithermal mineralization of the northeastern Altiplano of Bolivia. *Econ Geol* 84:618–630. <https://doi.org/10.2113/gsecongeo.84.3.618>
- Reitsma M (2012) Reconstructing the Late Paleozoic–Early Mesozoic Plutonic and Sedimentary Record of South-East Peru: Orphaned Back-arcs Along the Western Margin of Gondwana. Ph.D. thesis, University of Geneva, Switzerland, p. 226
- Revollo R (1967) *Geología de la Cordillera de Santa Vera Cruz: Tesis de Grado, Universidad Mayor San Andrés, La Paz*
- Rivas S, Carrasco R (1968) *Geología y yacimientos minerales de la Region de Potosi. Bol Geol Bol* 11
- Rodríguez R, Acosta H, Cueva E, Carlotto V (2010) Dominios y estilos estructurales en el Altiplano y borde oeste de la Cordillera Oriental del sur del Perú. In: *XV Congreso Peruano de Geología, resúmenes extendidos*. Lima: Sociedad Geológica del Perú, *Pub Esp* (9):810-813
- Rodríguez R, Choquehuanca S, Sánchez E, Fabián C, Del Castillo B (2021) Geología de los cuadrángulos de Macusani (hojas 29v1, 29v2, 29v3, 29v4) y Limbani (hojas 29x1, 29x2, 29x3, 29x4). Instituto Geológico, Minero y Metalúrgico, *Boletín Serie L4*, p 82
- Rubatto D, Hermann J (2007) Experimental zircon/melt and zircon/garnet trace element partitioning and implications for the geochronology of crustal rocks. *Chem Geol* 241:38–61. <https://doi.org/10.1016/j.chemgeo.2007.01.02>
- Rudnick R, Gao S (2014) Composition of the Continental Crust. In: Holland HD, Turekian KK (eds) *Treatise on geochemistry*, 2nd edn, Amsterdam, Elsevier: p 51. <https://doi.org/10.1016/B978-0-08-095975-7.00301-6>

- Sánchez A, Zapata A (2003) Memoria descriptiva de la revisión y actualización de los cuadrángulos de Macusani (29-v) y Azángaro (30-v) —incluidos en: Sicuani (29-t), Nuñoa (29-u), Limbani (29-x), Sandia (29-y), San Ignacio (29-z), Yauri (30-t), Putina (30-x), La Rinconada (30-y), Condorama (31-t), Ocuwiri (31-u), Juliaca (31-v), Callalli (32-t), y Ácora (32-x)—, escala 1:100 000. Boletín Serie L: Actualización Carta Geológica Nacional, Instituto Geológico, Minero y Metalúrgico (INGEMMET), Lima, p 55
- Sánchez O (2016) Controles de mineralización en el sistema de vetas SN-(CU) Santo Domingo-proyecto Santo Domingo-Puno. Universidad Nacional Mayor de San Marcos, Lima, p 164
- Sandeman H, Clark A, Farrar E (1995) An integrated tectono-magmatic model for the evolution of the southern Peruvian Andes (13-20°S) since 55 Ma. *Int Geol Rev* 37:1039-1073. <https://doi.org/10.1080/00206819509465439>
- Sandeman H, Clark A, Farrar E, Arroyo G (1997) Lithostratigraphy petrology and ⁴⁰Ar-³⁹Ar geochronology of the Crucero Supergroup, Puno Department, SE Peru. *J S Am Earth Sci* 10(3):223–245. [https://doi.org/10.1016/S0895-9811\(97\)00023-0](https://doi.org/10.1016/S0895-9811(97)00023-0)
- Sandeman H, Clark A (2004) Commingling and mixing of S-type peraluminous, ultrapotassic and basaltic magmas in the Cayconi volcanic field, Cordillera de Carabaya, SE Peru. *Lithos* 73:187–213. <https://doi.org/10.1016/j.lithos.2003.12.005>
- Salisbury M, Jiménez N, Barfod D (2022) 40Ar/39Ar ages and geochemistry of the Intersalar Range of the Bolivian Altiplano: A volcanological transect spanning the arc and reararc of the Central Andean Plateau. *Front. Earth Sci* 10:23. <https://doi.org/10.3389/feart.2022.917488>
- Scherrenberg A, Jacay J, Holcombe R, Rosenbaum G (2012) Stratigraphic variations across the Marañon Fold-Thrust Belt, Peru: Implications for the basin architecture of the West Peruvian Trough. *J S Am Earth Sci* 38:147–158. <https://doi.org/10.1016/j.jsames.2012.06.006>
- Scott S, Barnes H (1971) Sphalerite geothermometry and geobarometry. *Econ Geol* 66:653–669. <https://doi.org/10.2113/gsecongeo.66.4.653>
- Schuiling R (1967) Tin belts on the continents around the Atlantic Ocean. *Econ Geol* 62:540-550. <https://doi.org/10.2113/gsecongeo.62.4.540>
- Sempere T, Herail G, Oller J, Bonhomme M (1990) Late Oligocene early Miocene major tectonic crisis and related basins in Bolivia. *Geology* 18(10):946-949. [https://doi.org/10.1130/0091-7613\(1990\)018<0946:LOEMMT>2.3.CO;2](https://doi.org/10.1130/0091-7613(1990)018<0946:LOEMMT>2.3.CO;2)
- Sempere T, Carlier G, Soler P, Fornari M, Carlotto V, Jacay J, Arispe O, Néraudeau D, Cárdenas J, Rosas S, Jiménez N (2002) Late Permian–Middle Jurassic lithospheric thinning in Peru and Bolivia, and its bearing on Andean-age tectonics. *Tectonophysics* 345:153–181. [https://doi.org/10.1016/S0040-1951\(01\)00211-6](https://doi.org/10.1016/S0040-1951(01)00211-6)
- Sempere T, Acosta H, Carlotto V (2004) Estratigrafía del Mesozoico y Paleógeno al norte del Lago Titicaca. *Publicación Especial Sociedad Geológica del Perú* 5: 81-103
- Sempere T, Folguera A, Gerbault M (2008) New insights into the Andean evolution: an introduction to contributions from the 6th ISAG symposium (Barcelona, 2005). *Tectonophysics* 459:1-13. <https://doi.org/10.1016/j.tecto.2008.03.011>

- Sempere T, Jacay J (2008) Anatomy of the Central Andes: Distinguishing between western, magmatic Andes and eastern, tectonic Andes. 7th International Symposium on Andean Geodynamics 504–507:1-5
- Shand S (1943) Eruptive rocks: their genesis, composition, and classification, with a chapter on meteorites. J. Wiley & sons. Incorporated.
- Sillitoe R, Halls C, Grant J (1975) Porphyry tin deposits in Bolivia. *Econ Geol* 70:913–927. <https://doi.org/10.2113/gsecongeo.70.5.913>
- Sillitoe R (1976) Andean Mineralization: a model for the metallogeny of convergent plate margins. *Spec Pap – Geol Assoc Can* 14:59-100
- Sillitoe R, Steele G, Thompson J, Lang J (1998) Advanced argillic lithocaps in the Bolivian tin-silver belt. *Miner Deposita* 33:539–546. <https://doi.org/10.1007/s001260050170>
- Sillitoe R, Lehmann B (2022) Copper-rich tin deposits. *Miner Deposita* 57:1–11. <https://doi.org/10.1007/s00126-021-01078-9>
- Shulaker D, Schmitt A, Zack T, Bindeman I (2015) In-situ oxygen isotope and trace element geothermometry of rutilated quartz from Alpine fissures. *Am Mineral* 100:915–925. <https://doi.org/10.2138/am-2015-4961>
- Spikings R, Reitsma M, Boekhout F, Mi A, Ulianov A, Chiaradia M, Gerdes A, Schaltegger U (2016) Characterisation of Triassic rifting in Peru and implications for the early disassembly of western Pangaea. *Gondwana Res* 35:124–143. <https://doi.org/10.1016/j.gr.2016.02.008>
- Sugaki A, Ueno H, Shimada N, Kusachi I, Kitakaze A, Hayashi K, Kojima S, Sanjines V (1983) Geological study on the polymetallic ore deposits in the Potosi district, Bolivia. *Sci Rep Tohoku Univ Series III* 15(3):409–460
- Sun S, McDonough W (1989) Chemical and isotopic systematics of oceanic basalts: implications for mantle composition and processes *Geol Soc Spec Publ* 42:313-345. <https://doi.org/10.1144/GSL.SP.1989.042.01.19>
- Sun K, She J, Du D, Li W, Deng J (2024) Extreme Sn isotope fractionation in highly evolved granites. *Chem Geol* 644:121843. <https://doi.org/10.1016/j.chemgeo.2023.121843>
- Sundell K, Saylor J, Lapen T, Styron R, Villarreal D, Usnayo P, Cárdenas J (2019) Peruvian Altiplano stratigraphy highlights along-strike variability in foreland basin evolution of the Cenozoic Central Andes. *Tectonics* 37(6):1876-1904. <https://doi.org/10.1029/2017TC004775>
- Tang M, Ji W, Chu X, Wu A, Chen C (2021) Reconstructing crustal thickness evolution from europium anomalies in detrital zircons. *Geology* 49:76–80. <https://doi.org/10.1130/G47745.1>
- Thouret J, Jicha B, Paquette J, Cubukcu E (2016) A 25Myr chronostratigraphy of ignimbrites in south Peru: implications for the volcanic history of the Central Andes. *J Geol Soc* 173(5):734–756. <https://doi.org/10.1144/jgs2015-162>
- Thormann W (1966) Investigaciones preliminares sobre la geotectónica y metalogénesis de la zona Challapata-Caxata. *Bol Serv Geol Bolivia* 7:118

- Tinka Resources Ltd. (2024) NI 43-101 technical report on a preliminary economic assessment of the Ayawilca polymetallic project, Peru. Prepared by SRK Consulting, effective date 28 February 2024. <https://www.tinkaresources.com>
- Torres B, Melgarejo J, Torró L, Camprubí A, Castillo-Oliver M, Artiaga D, Campeny M, Tauler E, Jiménez-Franco A, Alfonso P, Arce-Burgoa O (2019) The Poopó polymetallic epithermal deposit, Bolivia: mineralogy, genetic constraints, and distribution of critical elements. *Minerals* 9:472. <https://doi.org/10.3390/min9080472>
- Torró L, Melgarejo J, Gemmrich L, Mollinedo D, Cazorla M, Martínez Á, Pujol-Solà N, Farré de Pablo J, Camprubí A, Artiaga D, Torres B, Alfonso P, Arce-Burgoa O (2019a) Spatial and temporal controls on the distribution of indium in xenothermal vein deposits: the Huari Huari district, Potosí, Bolivia. *Minerals* 9:304. <https://doi.org/10.3390/min9050304>
- Torró L, Cazorla M, Melgarejo J, Camprubí A, Tarrés M, Gemmrich L, Campeny M, Castillo-Oliver M, Artiaga D, Torres B, Martínez A, Molliendo D, Alonso P, Arce-Burgoa O (2019b) Indium mineralization in the volcanic dome-hosted Ánimas-Chocaya-Siete Suyos polymetallic deposit, Potosí, Bolivia. *Minerals* 9:604. <https://doi.org/10.3390/min9100604>
- Trail D, Watson E, Tailby N (2012) Ce and Eu anomalies in zircon as proxies for the oxidation state of magmas. *Geochim Cosmochim Acta* 97:70–87. <https://doi.org/10.1016/j.gca.2012.08.032>
- Turneure F (1971) The Bolivian tin-silver province. *Econ Geol* 66:215–225. <https://doi.org/10.2113/gsecongeo.66.2.215>
- U.S. Geological Survey (2020) Mineral commodity summaries 2020. U.S. Geol Surv <https://pubs.usgs.gov/periodicals/mcs2020/mcs2020.pdf>. Accessed 30 April 2025
- U.S. Geological Survey (2025) Mineral commodity summaries 2025. U.S. Geol Surv <https://doi.org/10.3133/mcs2025>. Accessed 30 April 2025
- Vallance J (2013) Los cuerpos de brecha en intrusivos en el Cerro Santa Barbara, proyecto Taucane: observaciones de campo e interpretaciones tentativas. Internal report for Minsur S.A., p 15
- Vallance J (2015) Informe de estudio petrográfico y minerográfico de 19 láminas delgadas y 12 secciones pulidas del proyecto Taucane. Internal report for Minsur S.A., p 7
- Villaseca C, Barbero L, Herreros V (1998) A reexamination of the typology of peraluminous granite types in intracontinental orogenic belts. *Transactions of the Royal Society of Edinburgh: Earth Sciences* 89:113–119. <https://doi.org/10.1017/S0263593300007045>
- Villón G (2025) Desarrollo del Proyecto Nazareth (Sn – Cu), Región Puno, Sur del Perú. ProExplo: X Congreso Internacional de prospectores y exploradores, Lima, Perú, p 4
- Wagner T, Mlynarczyk M, Williams-Jones A, Boyce A (2009) Stable isotope constraints on ore formation at the San Rafael tin-copper deposit, southeast Peru. *Econ Geol* 104:223–248. <https://doi.org/10.2113/gsecongeo.104.2.223>
- Wang T, She J, Yin K, Wang K, Zhang Y, Lu X, Liu X, Li W (2021) Sn(II) chloride speciation and equilibrium Sn isotope fractionation under hydrothermal conditions: A first principles study. *Geochim Cosmochim Acta* 300:25–43. <https://doi.org/10.1016/j.gca.2021.02.023>

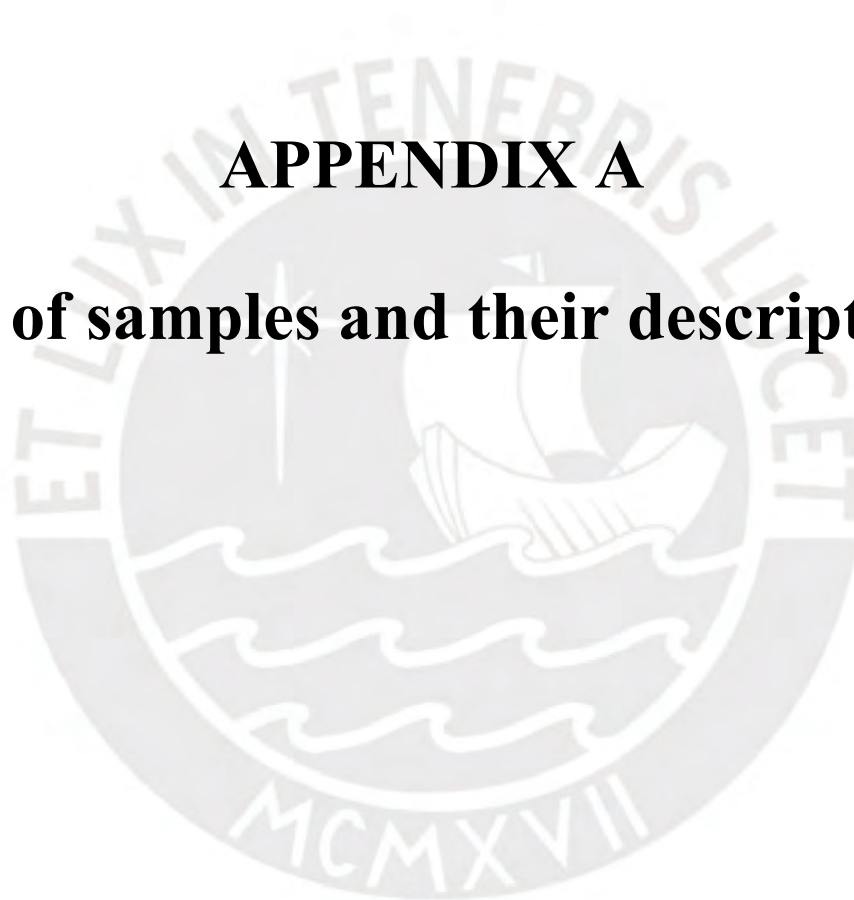
- Watson E, Wark D, Thomas J (2006) Crystallization thermometers for zircon and rutile. *Contrib Mineral Petrol* 151:413–433.
- Wilson J (1963) Cretaceous stratigraphy of Central Andes of Peru. *Am Assoc Pet Geol Bull* 47:1–34. <https://doi.org/10.1306/BC74396D-16BE-11D7-8645000102C1865D>
- Winter J (2014) *Principles of igneous and metamorphic petrology*. 2nd edn. Pearson Education, Boston, p 745
- Wipf M (2006) Evolution of the Western Cordillera and Coastal Margin of Peru: Evidence from low-temperature thermochronology and geomorphology. *Eidgenöss. Tech Hochsch, Zürich*, p 152. <https://doi.org/10.3929/ethz-a-005146374>
- Wörner G, Schildgen T, Reich M (2018a) The Central Andes: Elements of an extreme land. *Elements* 14:225–230. <https://doi.org/10.2138/gselements.14.4.225>
- Wörner G, Mamani M, Blum-Oeste M (2018b) Magmatism in the Central Andes. *Elements* 14:237–244. <https://doi.org/10.2138/gselements.14.4.237>
- Wotzlav J, Schaltegger U, Frick D, Dungan M, Gerdes A, Günther D (2013) Tracking the evolution of large-volume silicic magma reservoirs from assembly to supereruption. *Geology* 41:867–870. <https://doi.org/10.1130/G34366.1>
- Wright J, Kwak T (1989) Tin-bearing greisens of Mount Bischoff, northwestern Tasmania, Australia. *Econ Geol* 84:551–574. <https://doi.org/10.2113/gsecongeo.84.3.551>
- Wu J, Li H, Mathur R, Bouvier A, Powel W, Yonezu K, Zhu D (2023) Compositional variation and Sn isotope fractionation of cassiterite during magmatic- hydrothermal processes. *Earth Planet Sci Lett* 613:118186. <https://doi.org/10.1016/j.epsl.2023.118186>
- Yakymchuk C, Holder R, Kendrick J, Moyen J (2023) Europium anomalies in zircon: a signal of crustal depth? *Earth Planet Sci Lett* 622, 118405. <https://doi.org/10.1016/j.epsl.2023.118405>
- Yakymchuk C, and Kirkland C (2025) “Interpreting Europium Anomalies in Zircon: The Importance of Source Redox.” *Geochemistry, Geophysics, Geosystems* 26: e2025GC012505. <https://doi.org/10.1029/2025GC012505>
- Yamazaki E, Nakai S, Sahoo Y, Yokoyama T, Mifune H, Saito T, Chen J, Takagi N, Hokanishi N, Yasuda A (2014) Feasibility studies of Sn isotope composition for provenancing ancient bronzes. *J Archaeol Sci* 52:458–467
- Yang M, Romer R, Yang Y, Wu S, Wang H, Tu J, Zhou H, Xie L, Huang C, Xu L (2022) U-Pb isotopic dating of cassiterite: development of reference materials and in situ applications by LA-SF-ICP-MS. *Chem Geol* 593:120754. <https://doi.org/10.1016/j.chemgeo.2022.120754>
- Yang M, Yang Y, Romer R, Wu S, Wu T, Wang H (2023) In situ Hf isotope analysis of cassiterite by LA-MC-ICP-MS: protocol and applications. *J Anal At Spectrom* 38(2):437-448. <https://doi.org/10.1039/D2JA00340F>
- Yang M, Wei W, Yang Y, Romer R, Wu S, Wu T, Zhong L (2024) Accurate determination of ultra-trace rare earth elements by LA-ICP-MS/MS and its application to cassiterite for effective elimination of Gd and Tb false positive anomalies. *J Anal At Spectrom* 39:2992–2999. <https://doi.org/10.1039/D4JA00271G>

- Zappettini E, Miranda-Angles V, Rodríguez C, Palacios O, Cocking R, Godeas M, Uribe-Zeballos H, Vivallo W, Paz M, Seggiaro R, Heuschmidt B, Gardeweg M, Boulanger Rondoy E, Korzeniewski L, Mpodozis C, Carpio M, Rubiolo D (2001) Mapa metalogénico de la región fronteriza entre Argentina, Bolivia, Chile y Perú (14°S y 28°S). *Publicación Geológica Multinacional* 2, Santiago de Chile, p 222
- Zhao Y, Chen S, Huang Y, Zhao J, Xiang T, Chen X (2019) U-Pb ages, O isotope compositions, Raman spectrum, and geochemistry of cassiterite from the Xiao copper-tin polymetallic deposit in Gejiu District, Yunnan Province. *Minerals* 9:212. <https://doi.org/10.3390/min9040212>
- Zhang R, Lu J, Lehmann B, Li C, Li G, Zhang L, Guo J, Sun W (2017) Combined zircon and cassiterite U–Pb dating of the Piaotang granite-related tungsten–tin deposit, southern Jiangxi tungsten district, China. *Ore Geol Rev* 82:268–284. <https://doi.org/10.1016/j.oregeorev.2016.10.039>
- Zhou Z, Mao J, Zhao J, Gao X, Weyer S, Horn I, Holtz F, Sossi P, Wang D (2022) Tin isotopes as geochemical tracers of ore-forming processes with Sn mineralization. *Am Mineral* 107:2111–2127



APPENDIX A

List of samples and their descriptions



Sample	UTM E	UTM N	Latitude	Longitude	Elevation (m.a.s.l)	Sample type	Depth (m)	Mineralization Type	Description
TC23-1	375482	8393628	-24.30000°	-70.65000°	4836	surface			Tourmaline-quartz(qtz)-monzogranite (no Crd); very altered outcrop; Lorena vein system
TC23-2	375531	8394234	-24.29417°	-70.64972°	4863	surface			Qtz-monzodiorite = main intrusion; qtz-bt-Crd ± patchy Tourmaline (along cracks only?)
TC23-3	375453	8394536	-24.29139°	-70.65017°	4906	surface			Very fresh minette; crosscutting the monzodiorite (next sample, not the main intrusion) and the vallance breccia; since the breccia contains granitoid clasts and calcareous groundmass, minette may be post-ore
TC23-4	375415	8394574	-24.29103°	-70.65056°	4925	surface			Monzodiorite (no tourmaline) ± Crd, no qtz. Similar rock in SD-SR but here less altered
TC23-5	374622	8393654	-24.29961°	-70.65869°	4726	surface			Dyke of monzogranite (as sample TC23-1) cut by 2-5 cm vein containing cassiterite (≤ 1 % Sn) and pyrite; 0.25 m @ 110 ppm Ag, 5210 ppm As, 1010 ppm Cu, 129.5 ppm In, 42200 ppm Pb, 5130 ppm Sb, 25000 ppm Zn, 8190 ppm Sn
TAU-IF-001	374624	8393654	-24.29961°	-70.65867°	4700	surface		Kelly Vein	Veinlets Qtz-Apy-Stb-Br-Py (cubic crystals)-Cst (needle tin), veinlets 1-2cm width, cutting monzogranitic dyke, outcrop with 0.82% Sn, 4.2% Pb, 2.5% Zn, 0.1% Cu, 110ppm Ag, 0.51% Sb, Kelly Vein System
TAU-IF-002	374716	8393488	-24.30112°	-70.65768°	4730	surface		Kelly Vein	Huancané coarse grain sandstone with veinlets Py-FeOx-Br-Sp-Gn-silver-Cst (needle tin), veinlets 1-3mm width, outcrop with 0.20% Sn, 6.1% Pb, 0.3% Zn, <0.02% Cu, 103ppm Ag, 0.56% Sb, Kelly Vein System

Sample	UTM E	UTM N	Latitude	Longitude	Elevation (m.a.s.l)	Sample type	Depth (m)	Mineralization Type	Description
TAU-IF-003	374864	8393334	-24.30253°	-70.65621°	4834	surface		Kelly Vein	Vein breccia, boxwork FeOx (Gt, Lmn)-Py-Br (1%), clasts: sandstone, outcrop with 0.22% Sn, 0.69% Pb, 0.1% Zn, <0.02% Cu, 20ppm Ag, 0.1% Sb, Kelly Vein System.
TAU-IF-004	374962	8393177	-24.30398°	-70.65525°	4863	surface		Kelly Vein	Vein breccia, boxwork FeOx (Gt, Lmn)-Py-Br-Gn-silver, Huancané sandstone clasts. Kelly Vein System
TAU-IF-005	375721	8393542	-24.30030°	-70.64823°	4868	surface		Lorena Vein	Vein, Brt>Gn-silver + FeOx, vein in contact Huancané sandstone-monzogranitic dyke. 1.5% Pb, 0.54% Zn, 25.8ppm Ag, Lorena Vein System.
TAU-IF-006	375931	8393309	-24.30245°	-70.64624°	4960	surface		Lorena Vein	Vein breccia, boxwork FeOx (Gt, Lmn)-Py-Br-Gn-silver, cutting monzogranitic dyke. 25ppm Ag, >1% As, 1.56% Pb, Lorena Vein System
TAU-IF-007	376244	8393104	-24.30428°	-70.64327°	4928	surface		Lorena Vein	Vein breccia, boxwork FeOx (Gt, Lmn)-Py-Br-Gn-silver-Cu sulfosalts. Lorena Vein System. >3000ppm Mo, 287ppm Ag, >1% As, 0.2% Cu, 8.7%Pb, 0.65% Sb
TAU-24-01	376122	8393074	-24.30454°	-70.64447°	4903	DDH TAU-004-14	425.70-425.82	Lorena Vein	Brecciated sandstone with calcite clasts with strong alteration. Moderate chlorite in groundmass. Calcite in fractures and groundmass. Pyrite < 5% disseminated in breccia groundmass.
TAU-24-02	376122	8393074	-24.30454°	-70.64447°	4903	DDH TAU-004-14	456.5-456.76	Lorena Vein	Light brown sulfides and carbonates. Complex textures between sedimentary carbonate and hydrothermal carbonate.

Sample	UTM E	UTM N	Latitude	Longitude	Elevation (m.a.s.l)	Sample type	Depth (m)	Mineralization Type	Description
TAU-24-03	376122	8393074	-24.30454°	-70.64447°	4903	DDH TAU-004-14	459.30-459.42	Lorena Vein	Pyritized vein (pyrite < 75%), medium to coarse grained. Moderate calcite in fractures and groundmass. Chlorite is present in veinlets with weak intensity.
TAU-24-04	376122	8393074	-24.30454°	-70.64447°	4903	DDH TAU-004-14	460.90-461.00	Lorena Vein	Transition zone in monzogranite with calcic alteration of weak intensity. Presence of crackle breccia with weak calcite in fractures and veinlets. Weak chlorite in fractures. Pyrite < 5%.
TAU-24-05	376122	8393074	-24.30454°	-70.64447°	4903	DDH TAU-004-14	484.30-484.47	Lorena Vein	Crackle-type breccia with subangular calcareous sandstone clasts smaller than 5 cm. Calcareous groundmass with calcite, chlorite, and pyrite. Presence of tourmaline spots with rhyolite.
TAU-24-06	376122	8393074	-24.30454°	-70.64447°	4903	DDH TAU-004-14	525.70-525.75	Lorena Vein	Pyritized gouge-like vetiform breccia with pyrite content <80% (possibly related to vein fractures). Weak calcite and chlorite in the groundmass. Sn <2% in groundmass, associated with calcite.
TAU-24-07	376122	8393074	-24.30454°	-70.64447°	4903	DDH TAU-004-14	535.80-535.86	Lorena Vein	Pyritized vein (pyrite content <60%) with weak fracturing, cutting moderately silicified sandstone. Weak calcite in fractures and groundmass.
TAU-24-08	376122	8393074	-24.30454°	-70.64447°	4903	DDH TAU-004-14	536.50-536.59	Lorena Vein	Calcareous sandstone with moderate fracturing. Calcite, chlorite, and pyrite together < 4%, arsenopyrite < 1%. Very weak argillic alteration in fractures.
TAU-24-09	376122	8393074	-24.30454°	-70.64447°	4903	DDH TAU-004-14	540.35-540.53	Lorena Vein	Moderately silicified sandstone with replacement-type alteration and very weak fracturing. Very weak calcite in fractures and patches. Pyrite < 5% in patches and fractures. Sn <1% in patches.

Sample	UTM E	UTM N	Latitude	Longitude	Elevation (m.a.s.l)	Sample type	Depth (m)	Mineralization Type	Description
TAU-24-10	376122	8393074	-24.30454°	-70.64447°	4903	DDH TAU-004-14	541.75-541.85	Lorena Vein	Medium to coarse-grained pyritized vein (pyrite content <80%) with strong fracturing. Weak calcite and chlorite in the groundmass. Sn <5%, associated with calcite.
TAU-24-11	376122	8393074	-24.30454°	-70.64447°	4903	DDH TAU-004-14	549.80-549.86	Lorena Vein	
TAU-24-12	376122	8393074	-24.30454°	-70.64447°	4903	DDH TAU-004-14	572.00-572.10	Lorena Vein	Massive pyrite and barite. Gray sulfides <1% in fractures and patches. Calcite with strong replacement-type alteration. Weak chlorite in veinlets.
TAU-24-13	376122	8393074	-24.30454°	-70.64447°	4903	DDH TAU-004-14	575.60-575.70	Lorena Vein	Cubic massive pyrite <50%. Very weak chlorite in veinlets and edges of fragments. Calcite and cubic pyrite form druses smaller than 10 cm. Sn <1% in groundmass. Siderite is present as a mineral associated with calcite. Massive mantle with dark brown carbonate.
TAU-24-14	376122	8393074	-24.30454°	-70.64447°	4903	DDH TAU-004-14	576.00-576.10	Lorena Vein	
TAU-24-15	376122	8393074	-24.30454°	-70.64447°	4903	DDH TAU-004-14	576.50-576.55	Lorena Vein	
TAU-24-16	376122	8393074	-24.30454°	-70.64447°	4903	DDH TAU-004-14	583.00-583.06	Lorena Vein	Pyritized veinlets (pyrite content <30%). Calcite with high groundmass content. Weak chlorite in fractures. Cubic pyrite with drusiform texture. Galena <1% in fractures and fine veinlets.

Sample	UTM E	UTM N	Latitude	Longitude	Elevation (m.a.s.l)	Sample type	Depth (m)	Mineralization Type	Description
TAU-24-17	376122	8393074	-24.30454°	-70.64447°	4903	DDH TAU-004-14	584.80-584.91	Lorena Vein	Calcareous sandstone with strong fracturing. Strong argillic alteration of replacement type in fractures. Cubic pyrite in patchy and fractures, associated with calcite.
TAU-24-18	374642	8393405	-24.30179°	-70.65839°	4749	DDH TAU-011-14	340.40-340.55	Kelly Manto	Skarnized vein with pervasive alteration. Presence of green and brown garnets. Very weak chlorite in fractures. Carbonates with moderate pervasive replacement. Calcite in veinlets forming druses smaller than 5 cm. Pyrrhotite <15%, pyrite <8% in patches, and disseminated chalcopyrite 1%.
TAU-24-19	374642	8393405	-24.30179°	-70.65839°	4749	DDH TAU-011-14	349.15-349.26	Kelly Manto	Greenish biotitic monzodiorite dyke. Chlorite with weak replacement alteration. Weak calcite in veinlets. Green garnet as veinlets together with bands of pyrrhotite and pyrite <1%, disseminated. Presence of cassiterite in traces.
TAU-24-20	374642	8393405	-24.30179°	-70.65839°	4749	DDH TAU-011-14	353.00-353.12	Kelly Manto	Greenish-gray monzodiorite with the presence of weak calcite and chlorite in veinlets and fractures. Pyrrhotite <5% in patches, pyrite <3% in veinlets.
TAU-24-21	374642	8393405	-24.30179°	-70.65839°	4749	DDH TAU-011-14	371.00-371.13	Kelly Manto	Massive sulfides and moderate-strong fracturing. Massive pyrrhotite <70%, pyrite 8% in fractures and rims, galena 2% in patches, sphalerite and chalcopyrite 1% in veinlets and disseminated. Cassiterite <1% in fractures.
TAU-24-22	374642	8393405	-24.30179°	-70.65839°	4749	DDH TAU-011-14	372.80-372.89	Kelly Manto	
TAU-24-23	374642	8393405	-24.30179°	-70.65839°	4749	DDH TAU-011-14	408.00-408.13	Kelly Manto	Carbonates with strong, pervasive alteration. Weak calcite in veinlets. Moderate chlorite in patches and veinlets. Pyrite <8% in patches and veinlets, sphalerite 5%, galena 2% in veinlets, pyrrhotite <2% in patches, and disseminated chalcopyrite <1%. Trace cassiterite. Cauliflower forms.



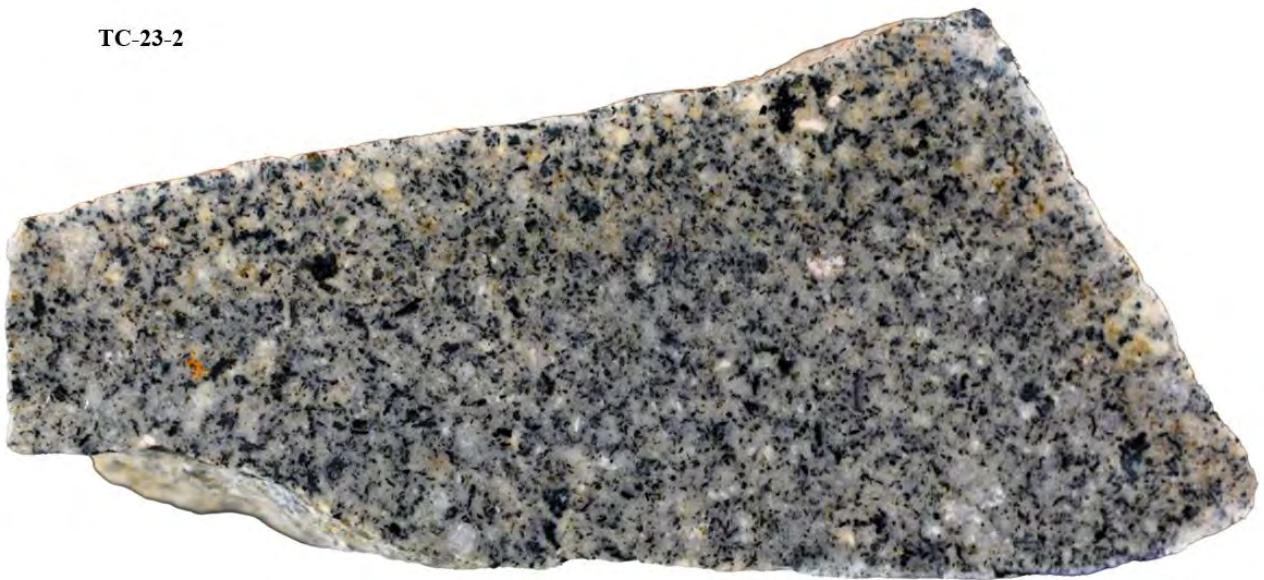
APPENDIX B

Hand sample pictures

TC-23-1



TC-23-2



TC-23-3



TC-23-4

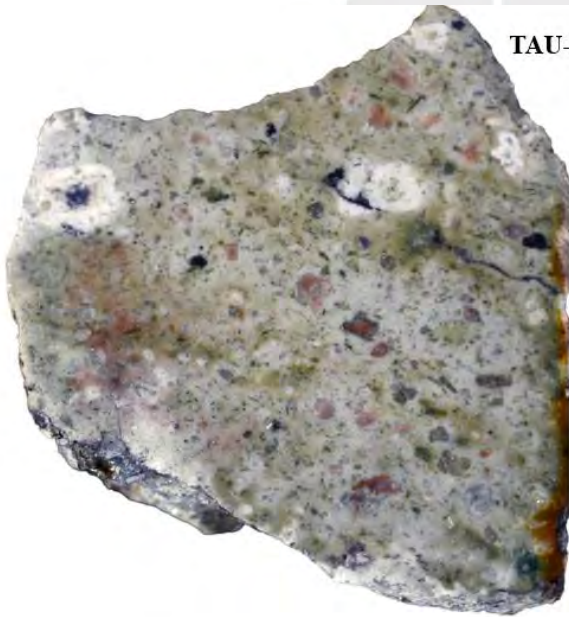


TC-23-5



4 cm

TAU-IF-001



4 cm



4 cm

TAU-IF-002



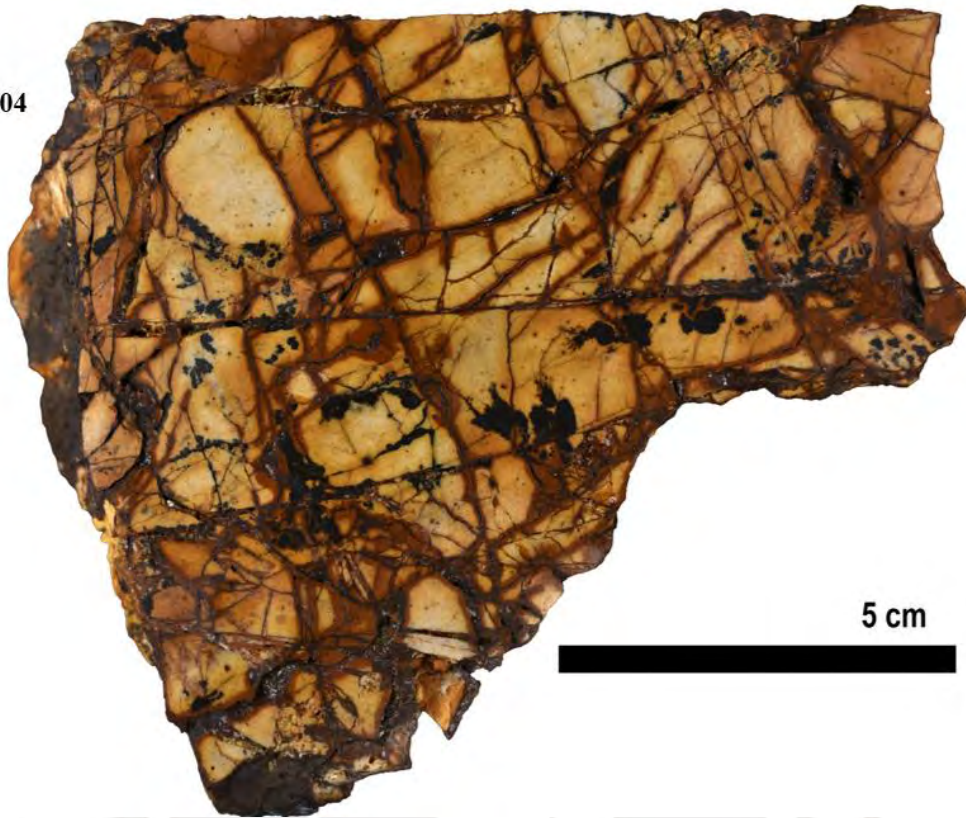
4 cm

TAU-IF-003

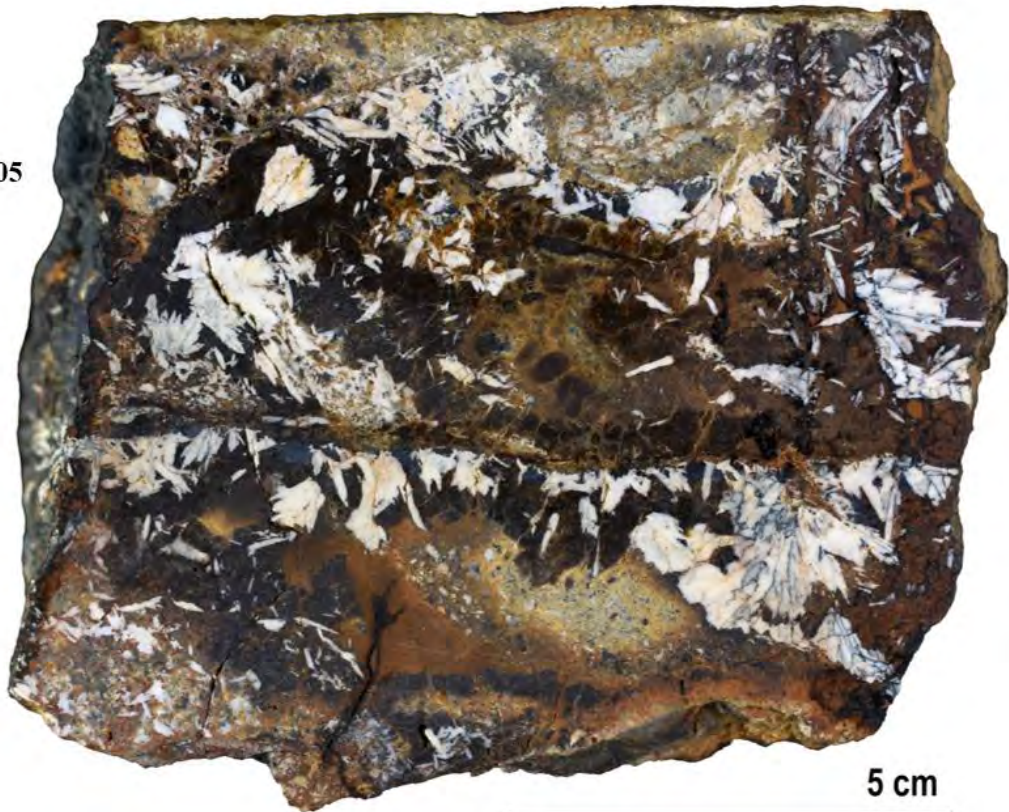


5 cm

TAU-IF-004



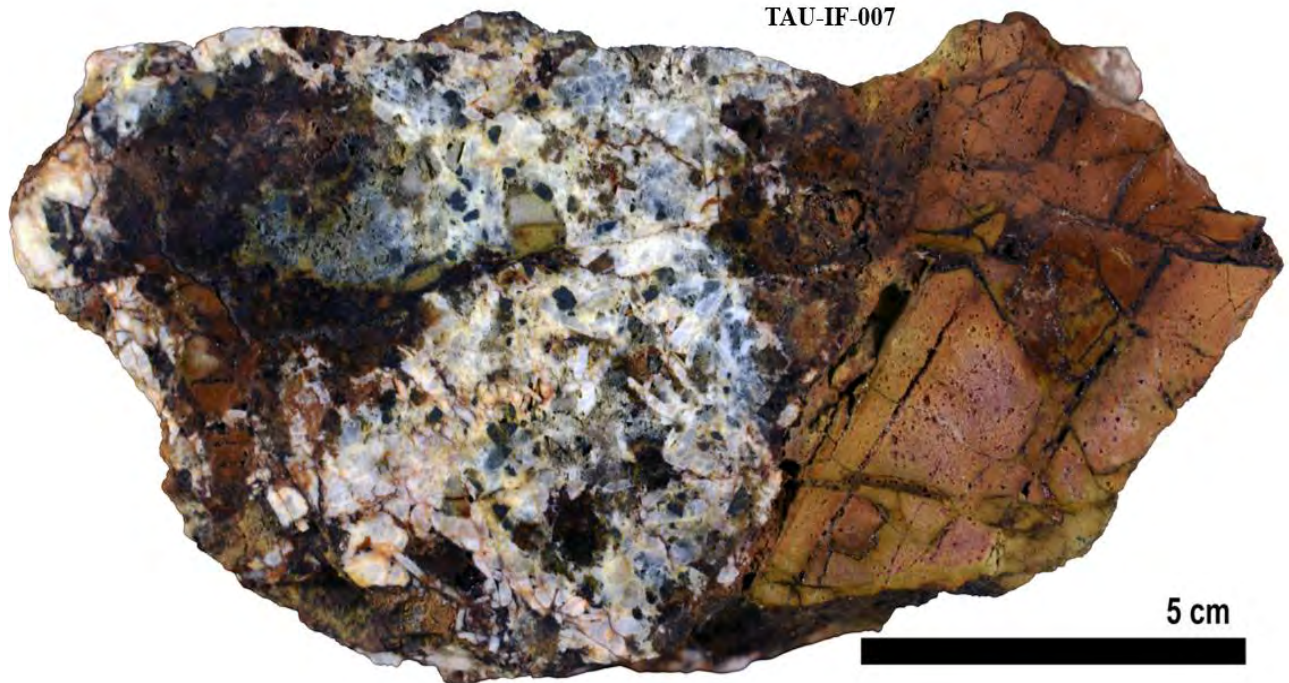
TAU-IF-005



TAU-IF-006



TAU-IF-007



TAU-24-01



TAU-24-02



TAU-24-03



5 cm



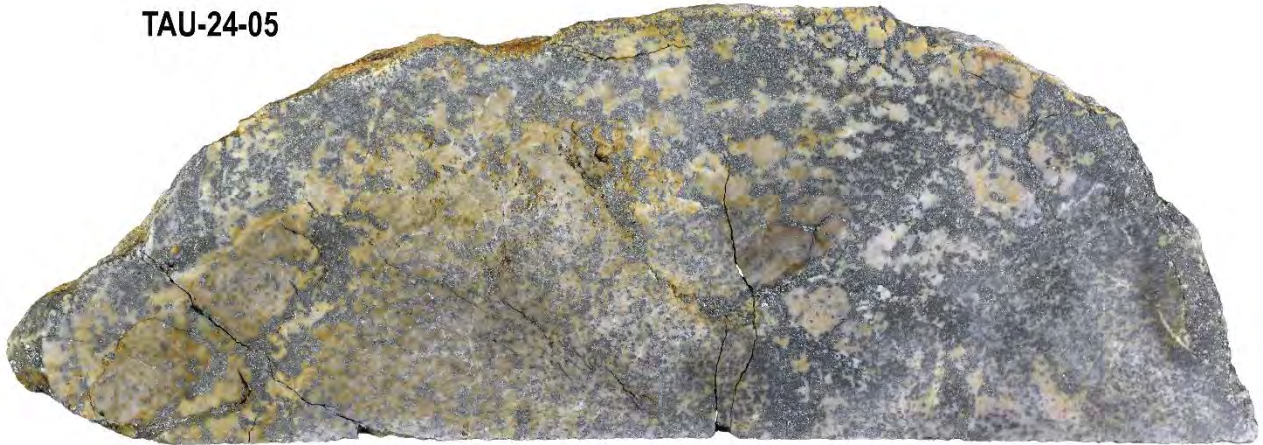
TAU-24-04



4 cm



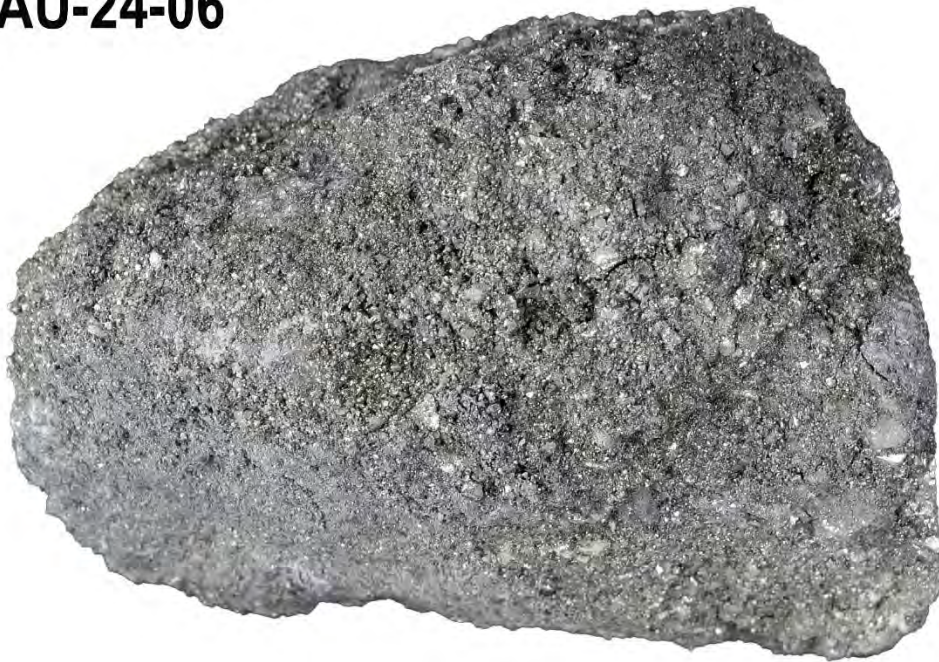
TAU-24-05



5 cm



TAU-24-06



3 cm



TAU-24-07



3 cm

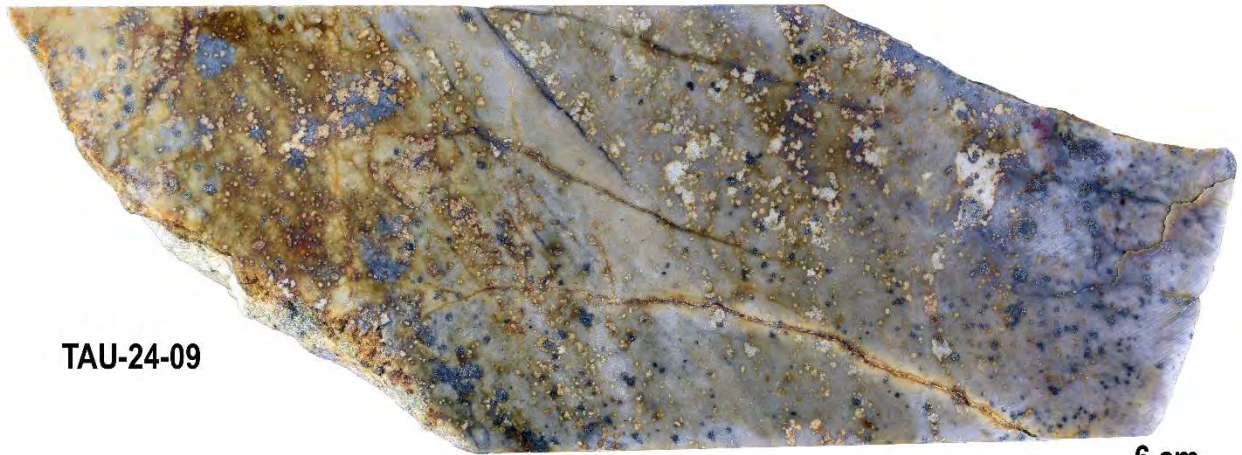


TAU-24-08



4 cm





TAU-24-09

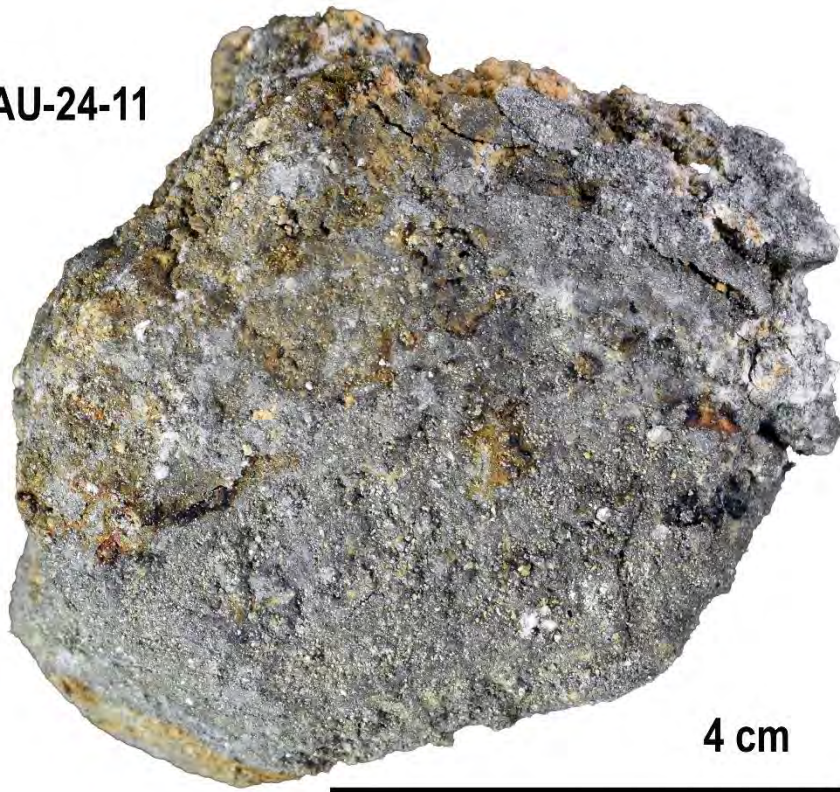
6 cm



TAU-24-10

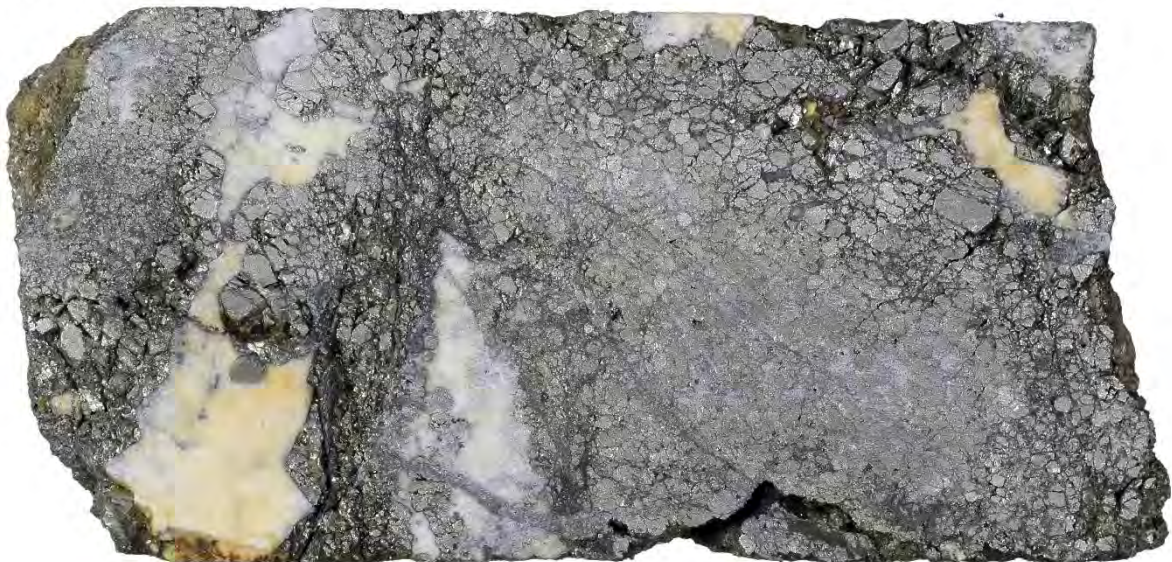
5 cm

TAU-24-11



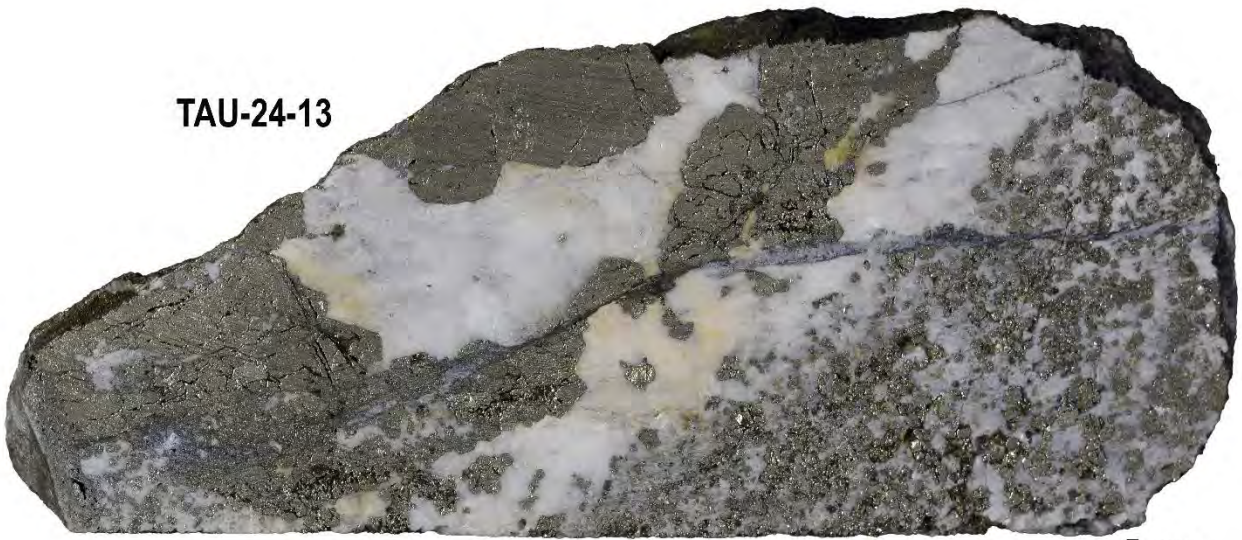
4 cm

TAU-24-12



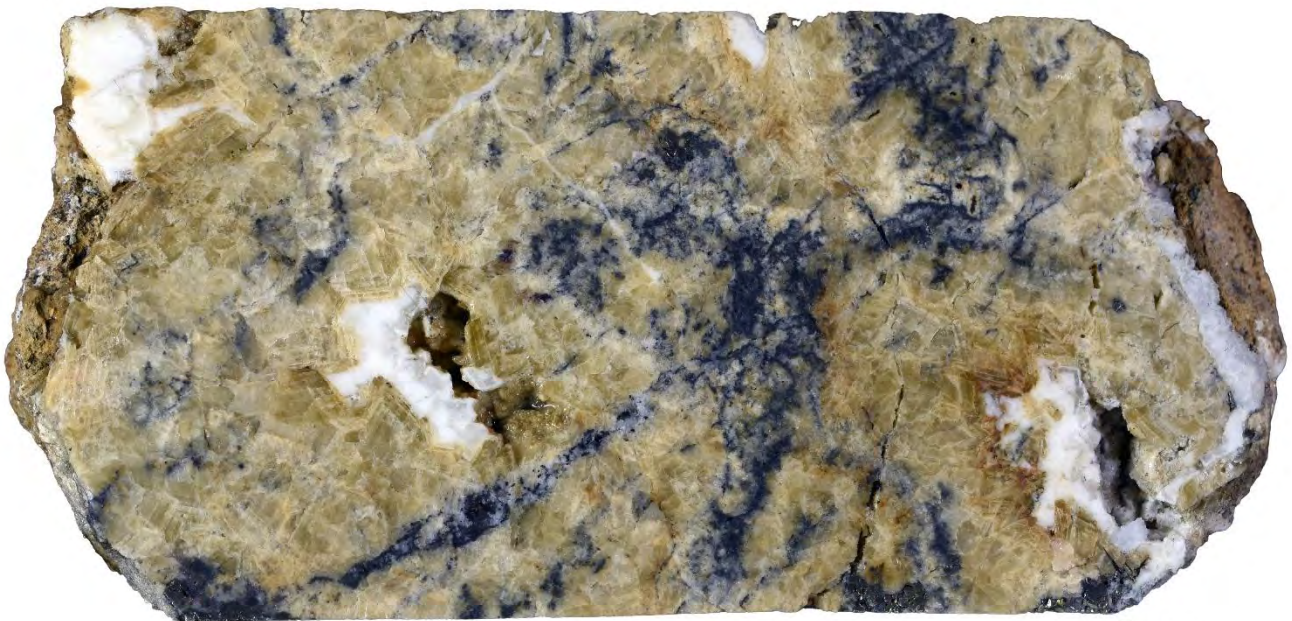
4 cm

TAU-24-13



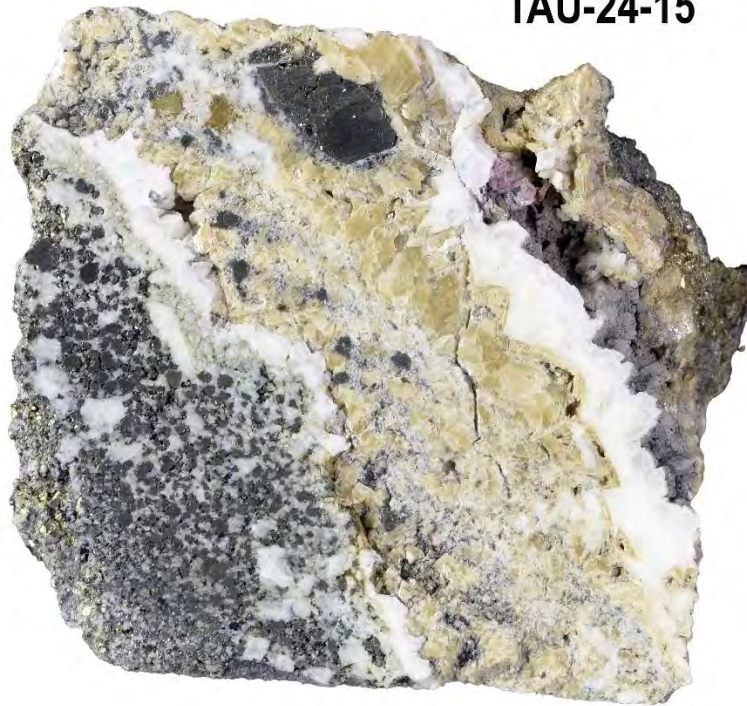
5 cm

TAU-24-14



5 cm

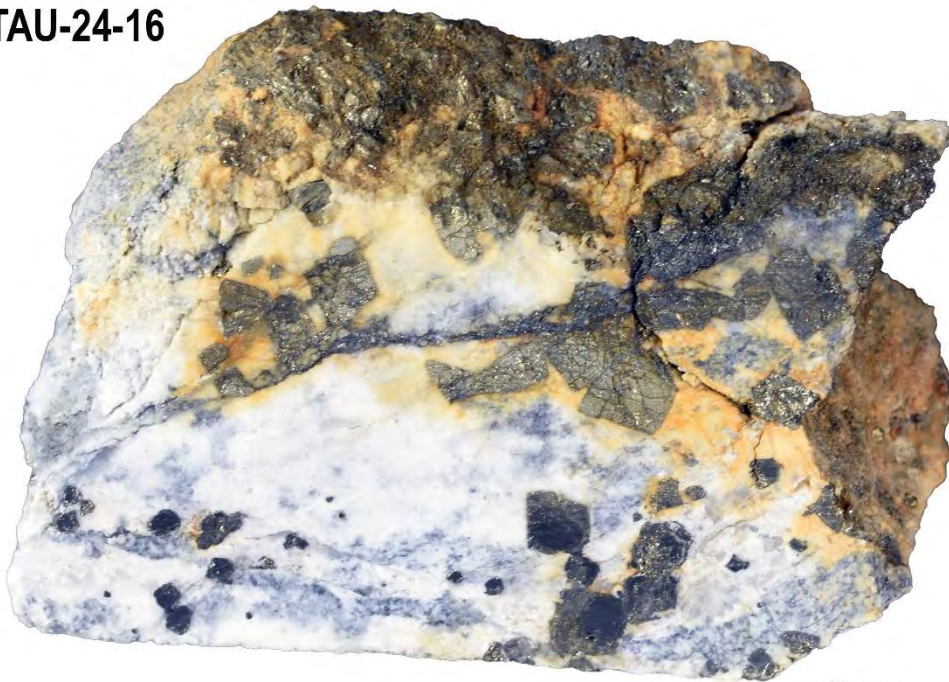
TAU-24-15



3 cm



TAU-24-16



3 cm



TAU-24-17



5 cm



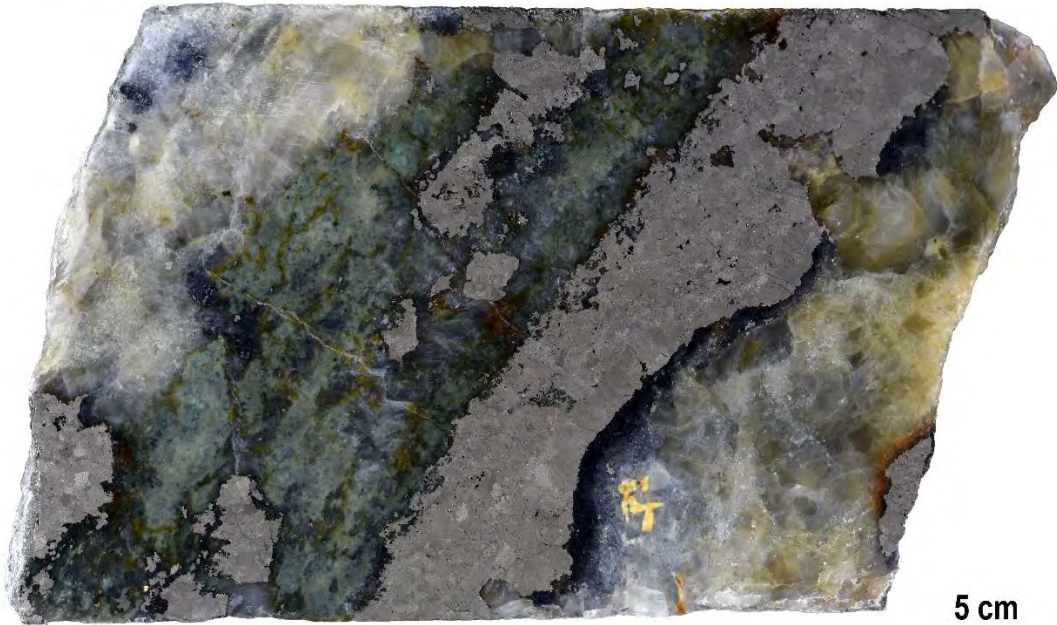
TAU-24-18



5 cm

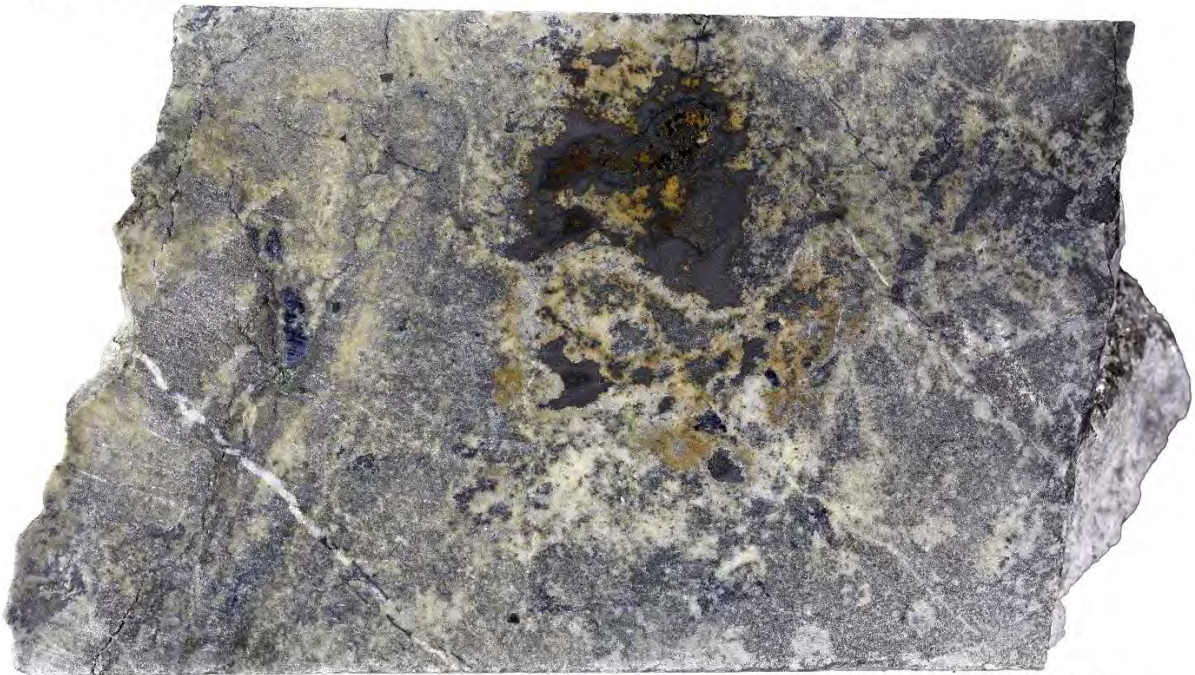


TAU-24-19



5 cm

TAU-24-20



3 cm

TAU-24-21



5 cm



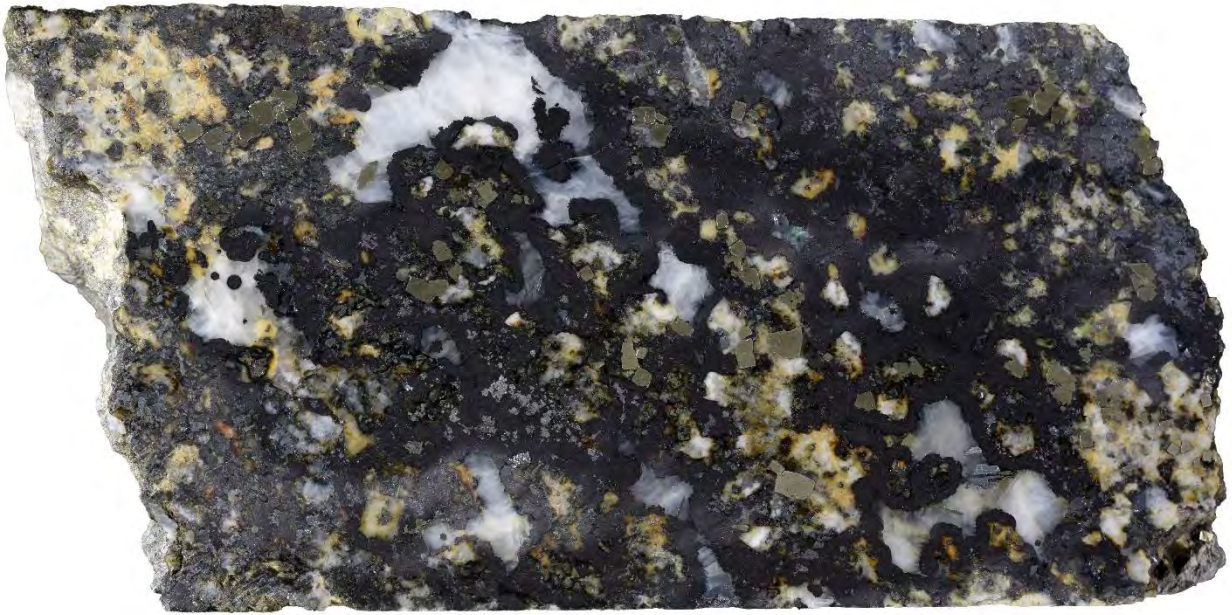
TAU-24-22



4 cm



TAU-24-23

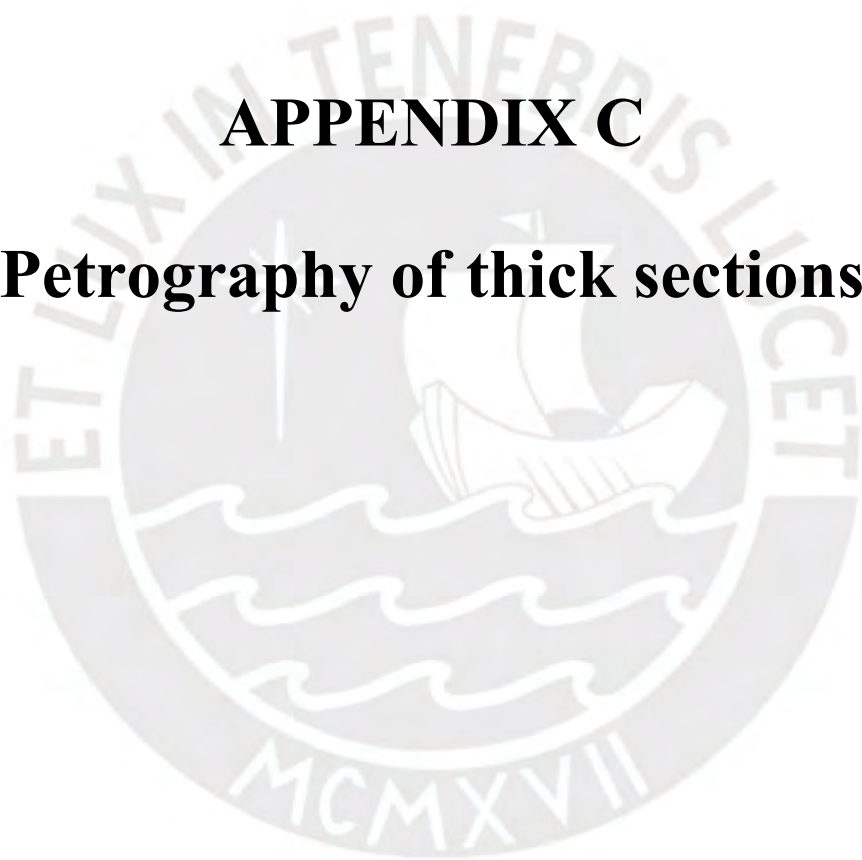


5 cm



MCMXVII

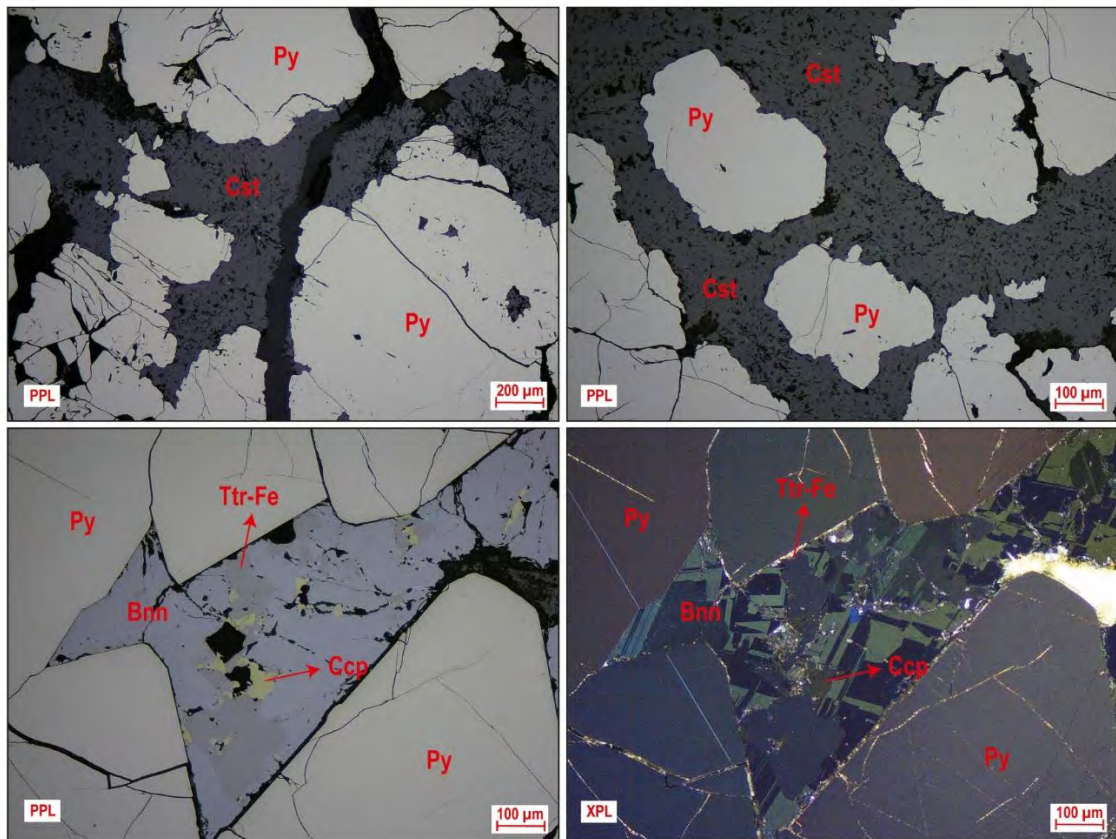
APPENDIX C
Petrography of thick sections



TAU-24-06A

Minerals: Pyrite + Cassiterite + Bournonite + Tetrahedrite-Fe + Chalcopyrite (1)

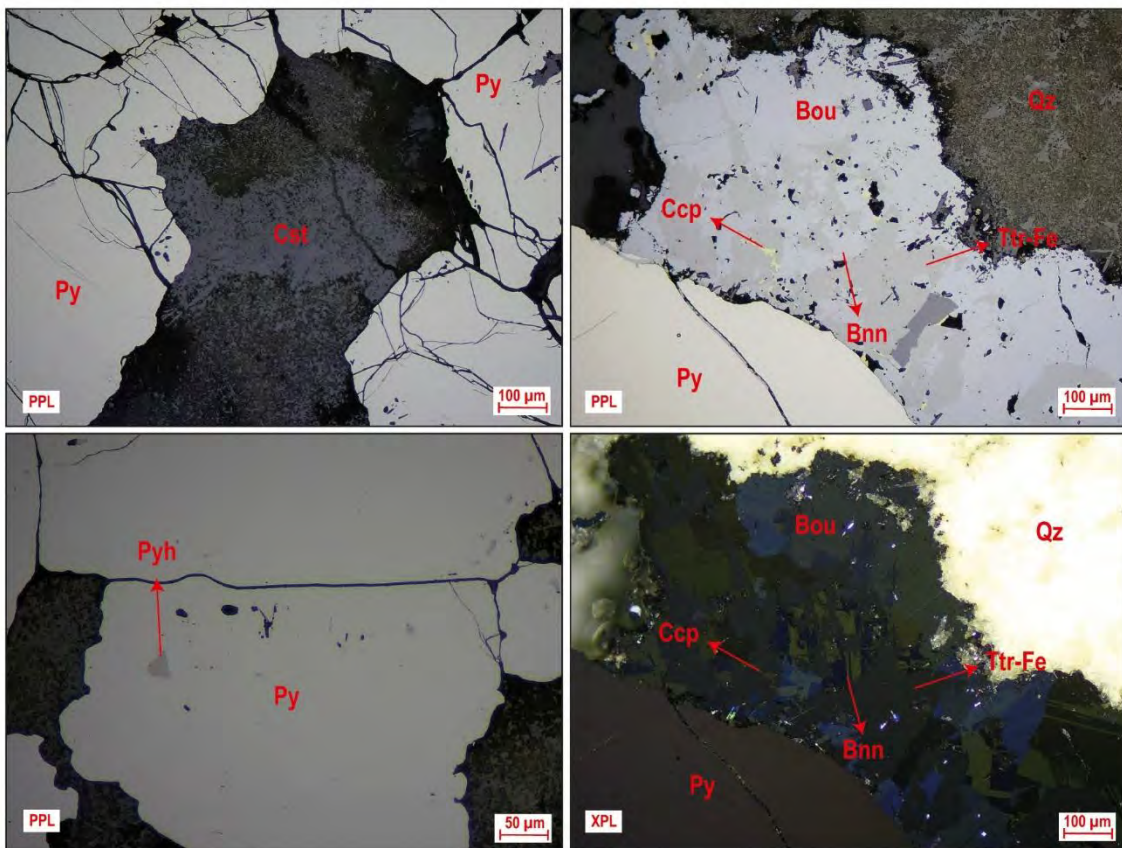
Quartz groundmass with abundant presence of anhedral to subhedral aggregates of pyrite, and to a lesser extent, chalcopyrite (1). Pyrite has replaced cassiterite through edges. Also, anhedral aggregates of bournonite (wheel twin) have filled edges and cavities of pyrite, and have replaced chalcopyrite and tetrahedrite-Fe.



TAU-24-06B

Minerals: Pyrite + Cassiterite + Bourmonite + Boulangerite + Tetrahedrite-Fe \pm Chalcopyrite (1)
 \pm Pyrrhotite.

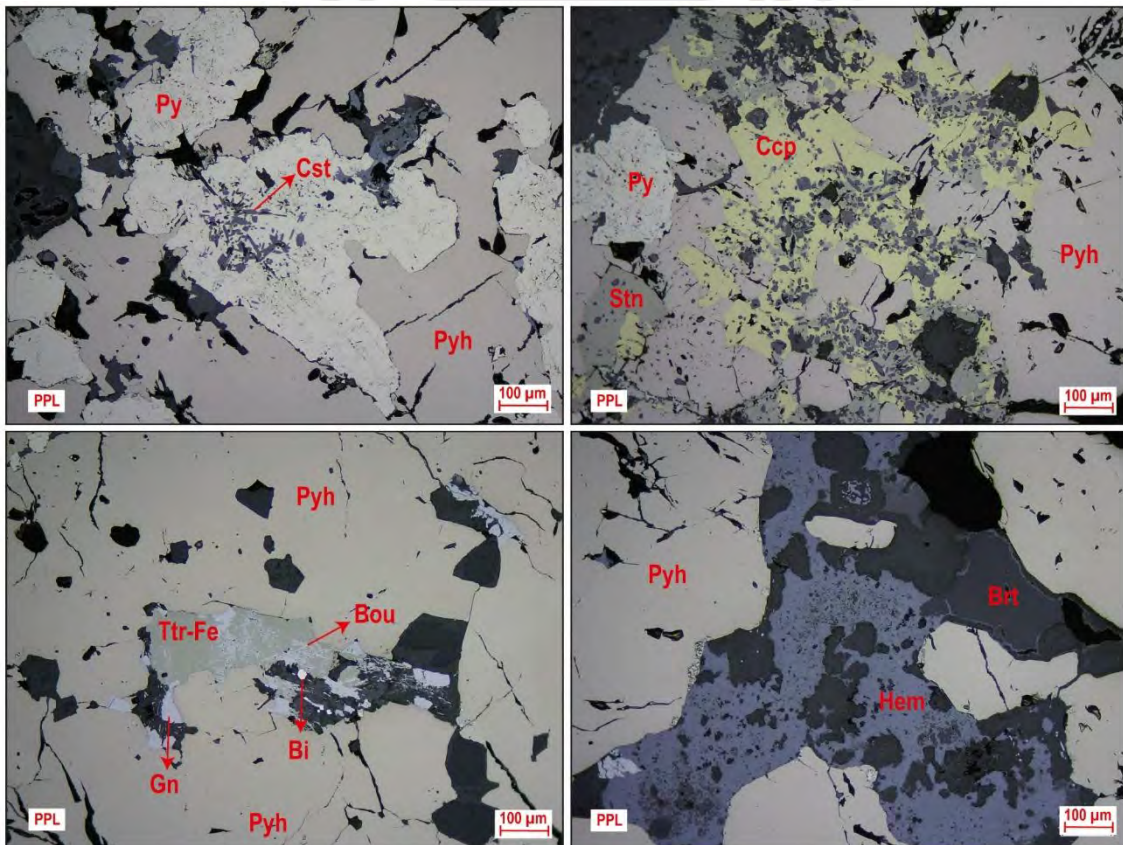
Anhedral to subhedral aggregates of cassiterite are present in a quartz groundmass, whose microfractures, interstices, and rims have been replaced by pyrite. Bourmonite and boulangerite occur as fillers of cavities and open spaces of pyrite, and have replaced chalcopyrite (1) and tetrahedrite-Fe through edges. Occasionally, inclusions of pyrrhotite within pyrite have been observed, with dimensions reaching up to 25 μm .



TAU-24-21A

Minerals: Pyrrhotite + Pyrite + Chalcocopyrite (1) + Stannite + Marcasite + Galena + Tetrahedrite-Fe + Cassiterite + Hematite ± Boulangerite ± Native Bismuth.

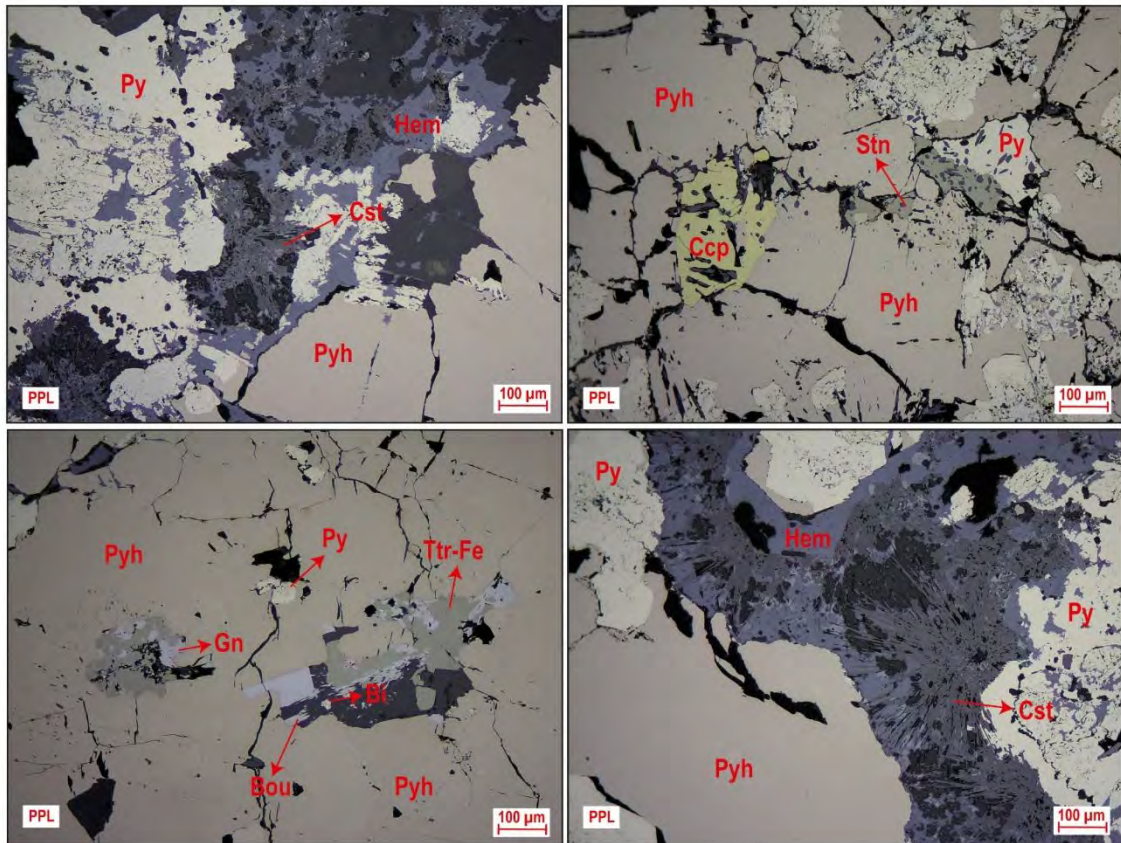
Anhedral to subhedral aggregates of pyrrhotite in barite groundmass, whose microfractures, interstices, and edges have been replaced mainly by pyrite, marcasite, and, to a lesser extent, by chalcocopyrite (1) and stannite. Occasionally, cassiterite grains with sizes up to 100 μm are observed. Small crystals of native bismuth and boulangerite are observed within the galena and Tetrahedrite-Fe intergrowths. In sectors, anhedral aggregates of hematite have overprinted all the previous phases.



TAU-24-21B

Minerals: Pyrite + Pyrrhotite + Cassiterite + Marcasite + Stannite + Chalcopyrite (1) + Galena + Tetrahedrite-Fe ± Boulangerite ± Native Bismute

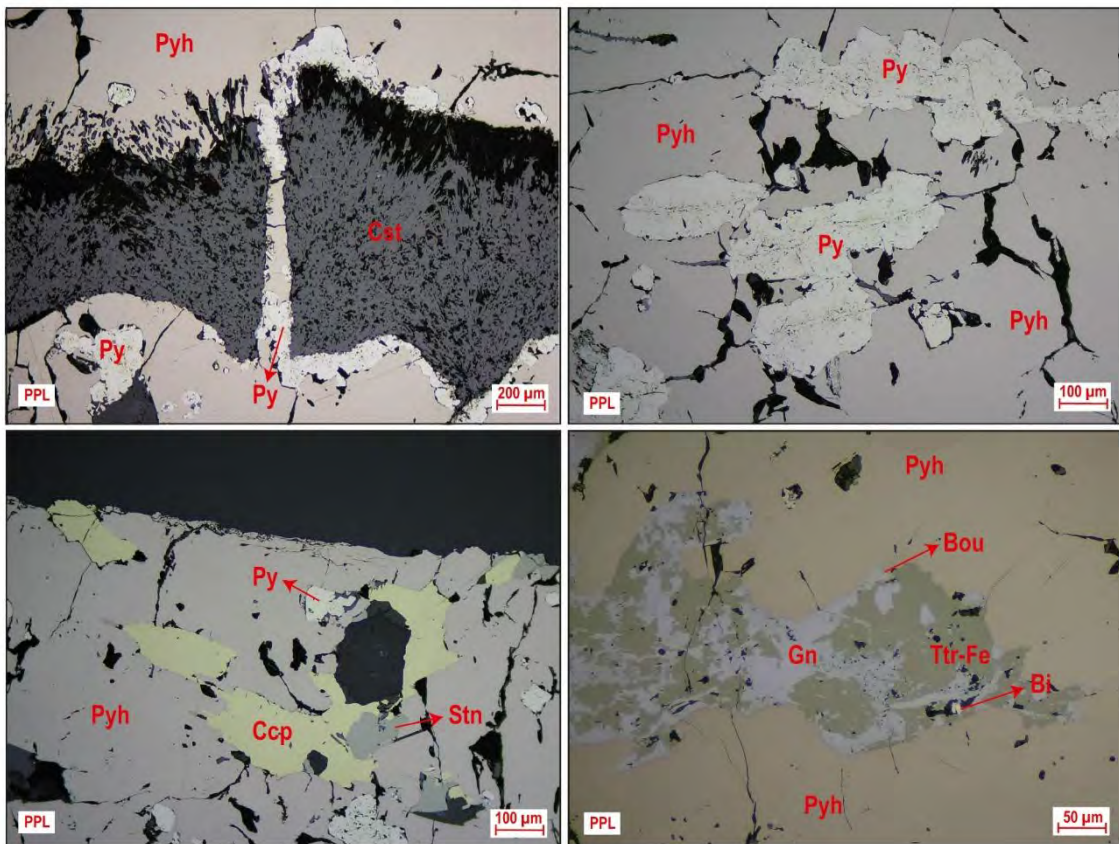
Quartz and barite groundmass with anhedral to subhedral aggregates of pyrrhotite, whose microfractures, interstices and edges have been replaced mainly by pyrite, marcasite and, to a lesser extent, by chalcopyrite (1) and stannite. Also, aggregates of cassiterite “needle tin” are replaced through edges by pyrite, pyrrhotite and stannite. In sectors, Galena with tetrahedrite-Fe are intergrown and with small crystals of boulangerite and native bismuth. Finally, anhedral aggregates of hematite have overprinted all the previous phases.



TAU-24-21C

Minerals: Pyrrhotite + Pyrite + Cassiterite + Chalcopyrite (1) + Tetrahedrite-Fe + Galena + Stannite ± Boulangerite ± Native Bismuth

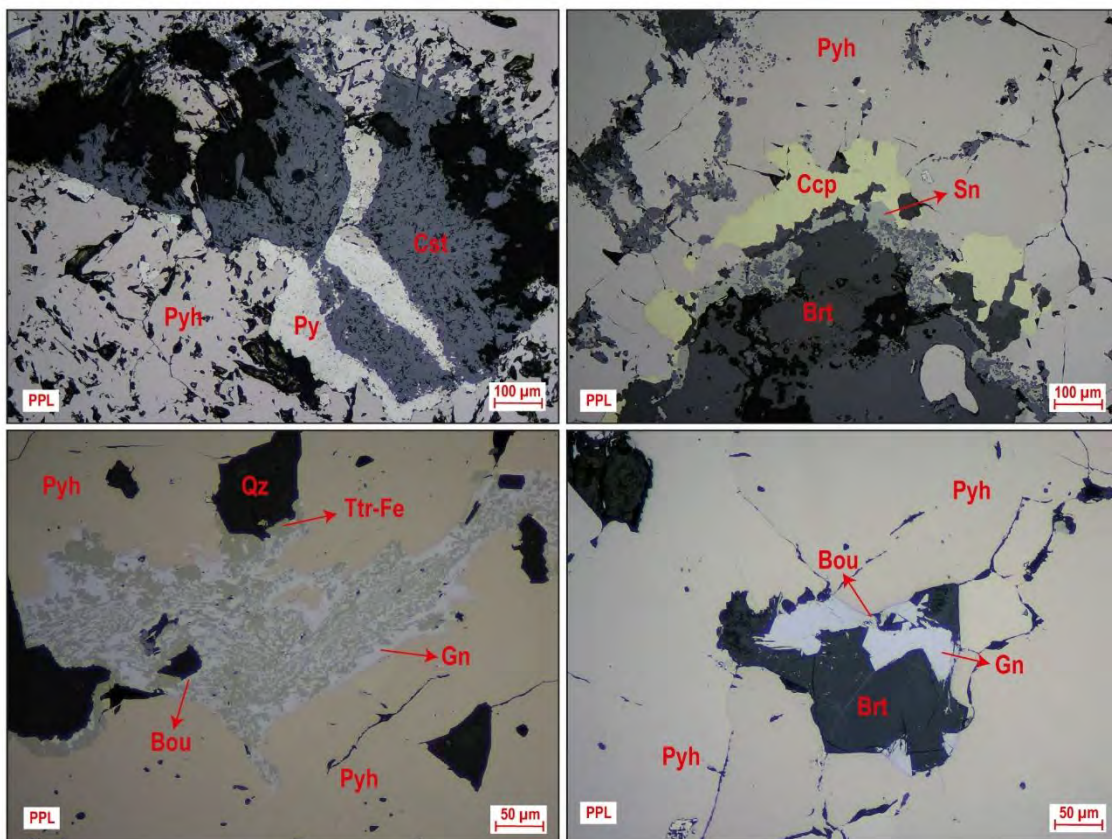
Quartz and barite groundmass with anhedral aggregates of “needle tin” cassiterite that have been replaced through interstices and edges by pyrrhotite, pyrite, and to a lesser extent, chalcopyrite (1) and stannite. Also, there are intergrowths of galena with tetrahedrite-Fe, and small crystals of boulangerite and native bismuth within the galena.



TAU-24-21D

Minerals: Pyrrhotite + Pyrite + Cassiterite + Chalcopyrite (1) + Stannite + Tetrahedrite-Fe + Galena ± Boulangerite ± Hematite

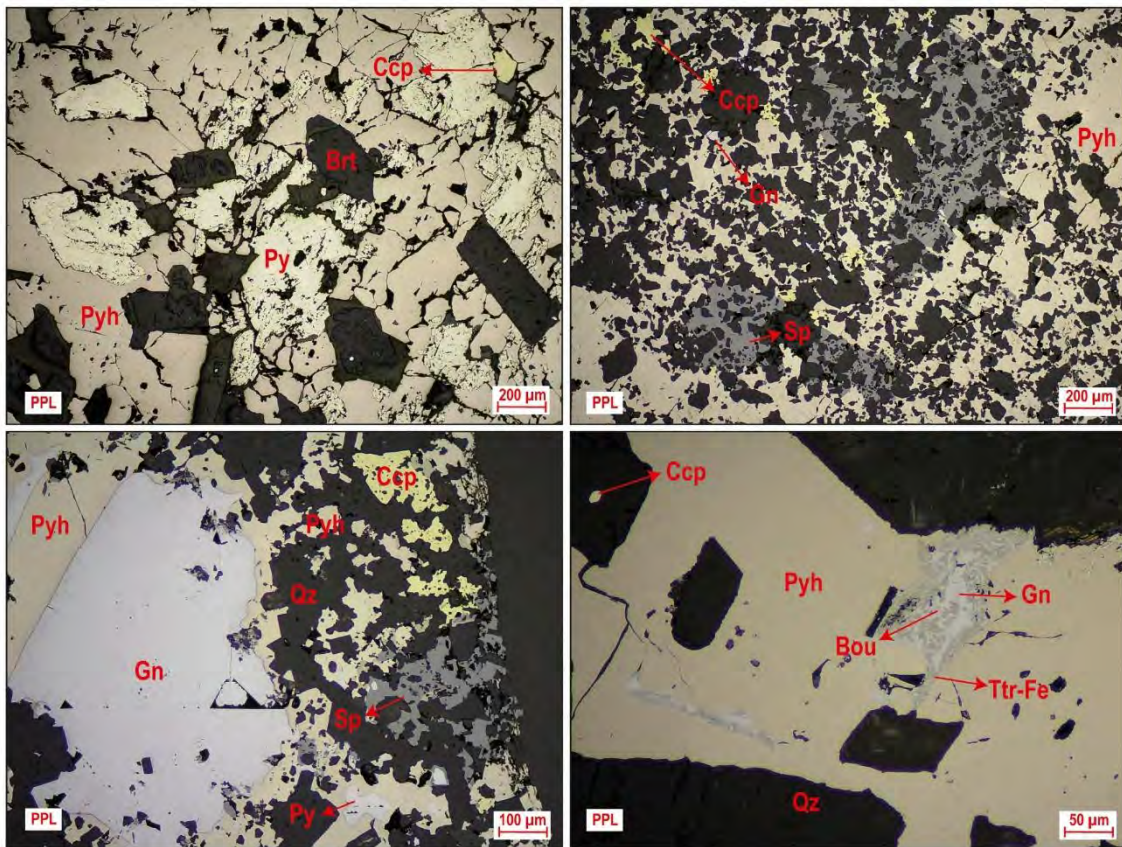
Quartz and barite groundmass with anhedral aggregates of needle tin cassiterite that have been replaced through interstices and edges by pyrrhotite, pyrite and, to a lesser extent, chalcopyrite (1) and stannite. Occasionally, grains of galena and Fe-tetrahedrite are intergrown and inclusions of boulangerite are observed. Galena and hematite are observed replacing cassiterite through edges.



TAU-24-21E

Minerals: Pyrrhotite + Pyrite + Cassiterite + Chalcopyrite (1) + Galena + Sphalerite (2) + Tetrahedrite-Fe ± Boulangerite

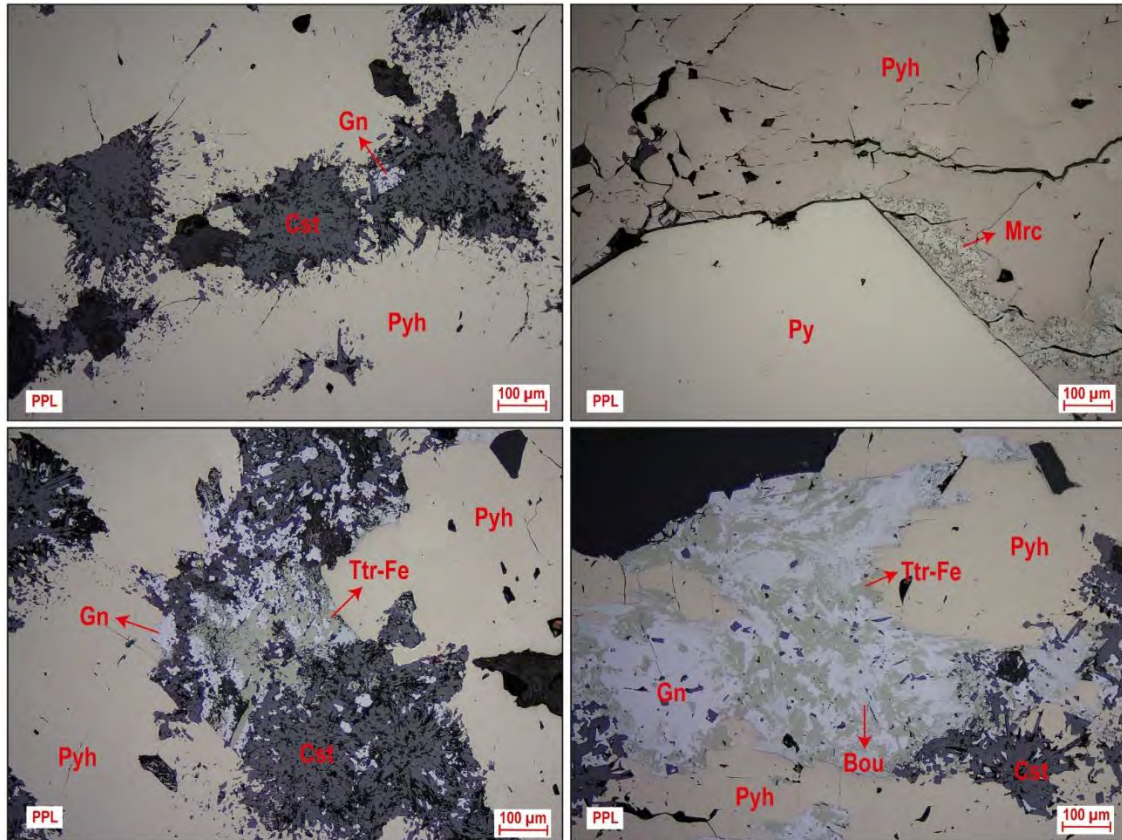
Quartz and barite groundmass with anhedral to subhedral aggregates of pyrrhotite that has been replaced along the edges by pyrite, and to a lesser extent, sphalerite (2) and chalcopyrite (1). Anhedral aggregates of galena have replaced through interstices and open spaces pyrrhotite, and also occur as intergrowths together with Fe-tetrahedrite and boulangerite inclusions.



TAU-24-22A

Minerals: Pyrrhotite + Cassiterite + Pyrite + Marcasite + Tetrahedrite-Fe + Galena + Boulangerite

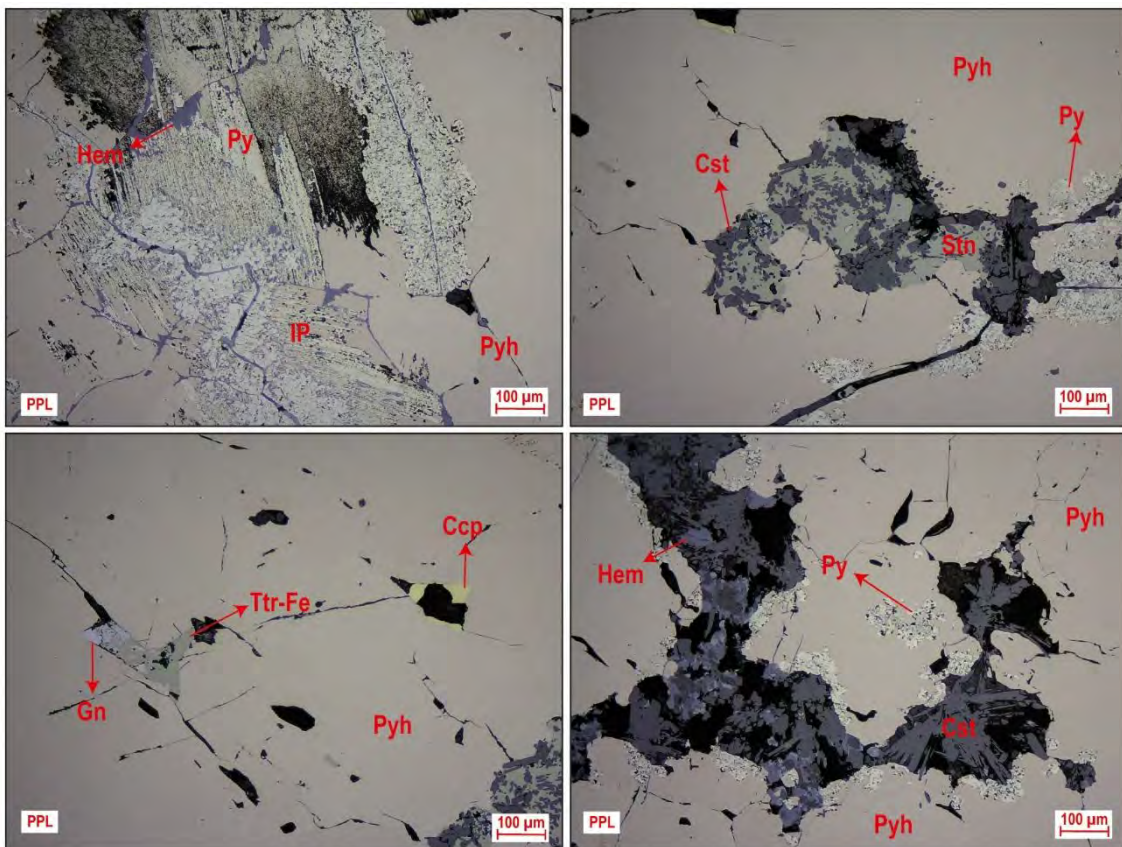
The quartz and barite groundmass contains anhedral aggregates of cassiterite needle tin, which has been replaced through microfractures and interstices by pyrrhotite, pyrite, and marcasite. Pyrite grains contain pyrrhotite inclusions. By sectors, cassiterite has been replaced by intergrowths of tetrahedrite-Fe and galena. Boulangerite inclusions are visible within the galena.



TAU-24-22B

Minerals: Pyrrhotite + Pyrite + IP + Cassiterite + Hematite + Stannite + Tetrahedrite-Fe + Galena + Chalcopyrite (1)

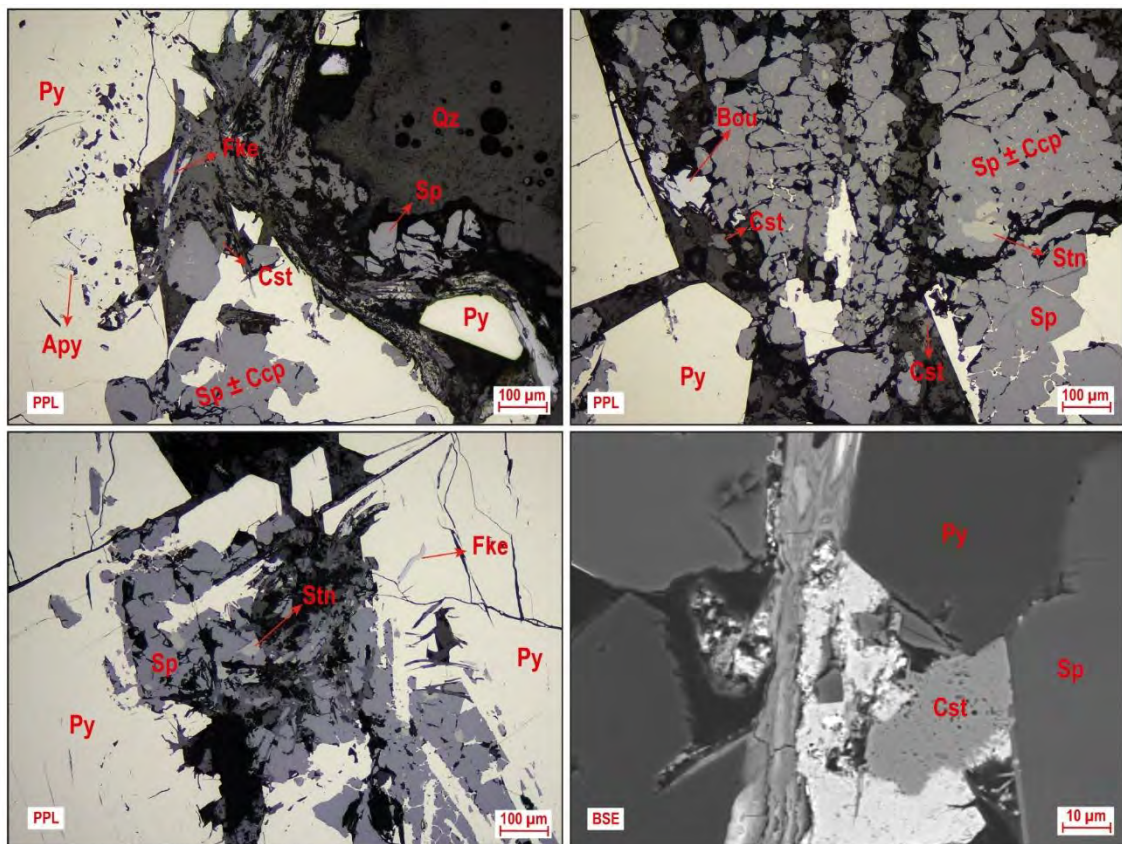
Anhedral to subhedral aggregates of cassiterite in quartz and barite groundmass, whose microfractures, interstices and edges have been replaced mainly by pyrite and intermediate product, and to a lesser extent by chalcopyrite (1) and stannite. Tetrahedrite-Fe and galena appear intergrown as fillers of pyrrhotite interstitials. Finally, anhedral aggregates of hematite have overprinted all the previous phases.



TAU-IF-01-A

Minerals: Pyrite + Sphalerite (1) + Stannite + Arsenopyrite + Franckeite ± Boulangerite ± Chalcopyrite (2) ± Cassiterite

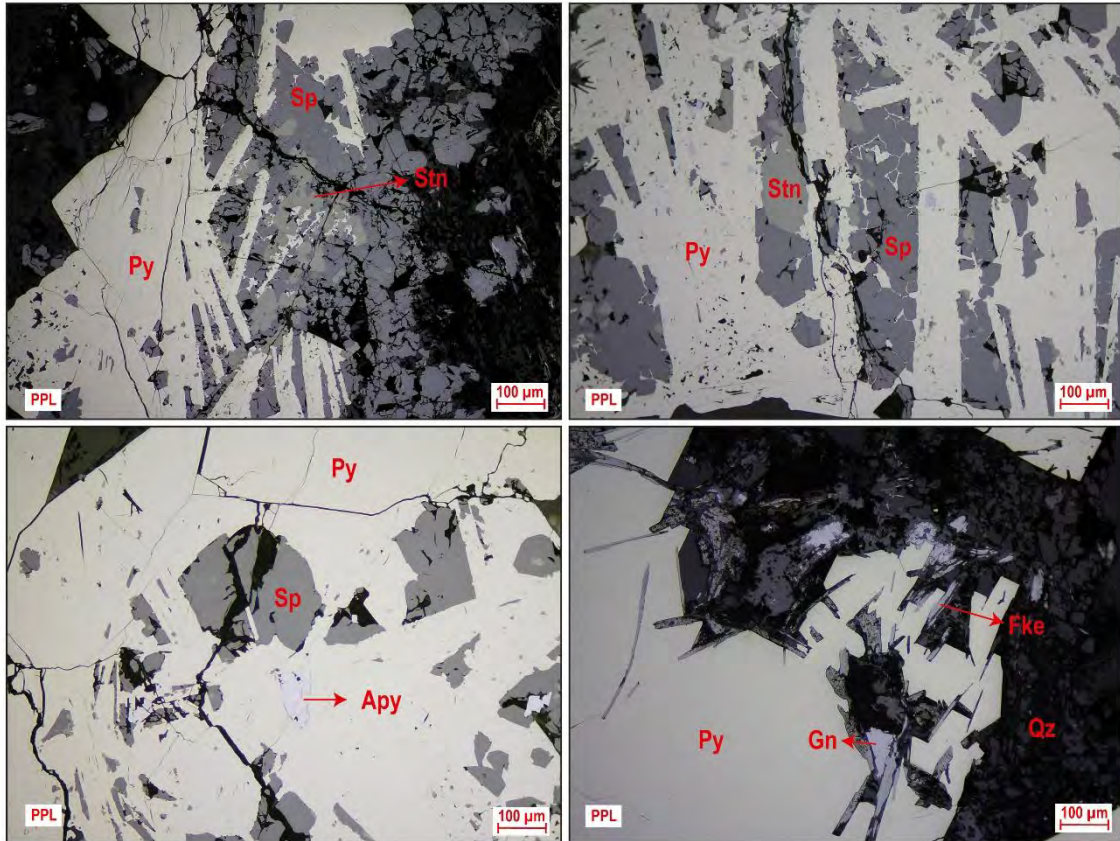
Anhedral to subhedral aggregates of pyrite in quartz groundmass, whose microfractures, interstices and edges have been replaced mainly by sphalerite (1) with disseminations of chalcopyrite (2) and, to a lesser extent, by arsenopyrite. By sectors, the sphalerite is replaced by stannite. Occasionally, grains of boulangerite (up to 100 μm) and cassiterite (up to 20 μm) are observed. Franckeite occurs as a filler of open spaces and pyrite cavities.



TAU-IF-01-B

Minerals: Pyrite + Sphalerite + Stannite + Franckeite + Arsenopyrite + Galena ± Chalcopyrite

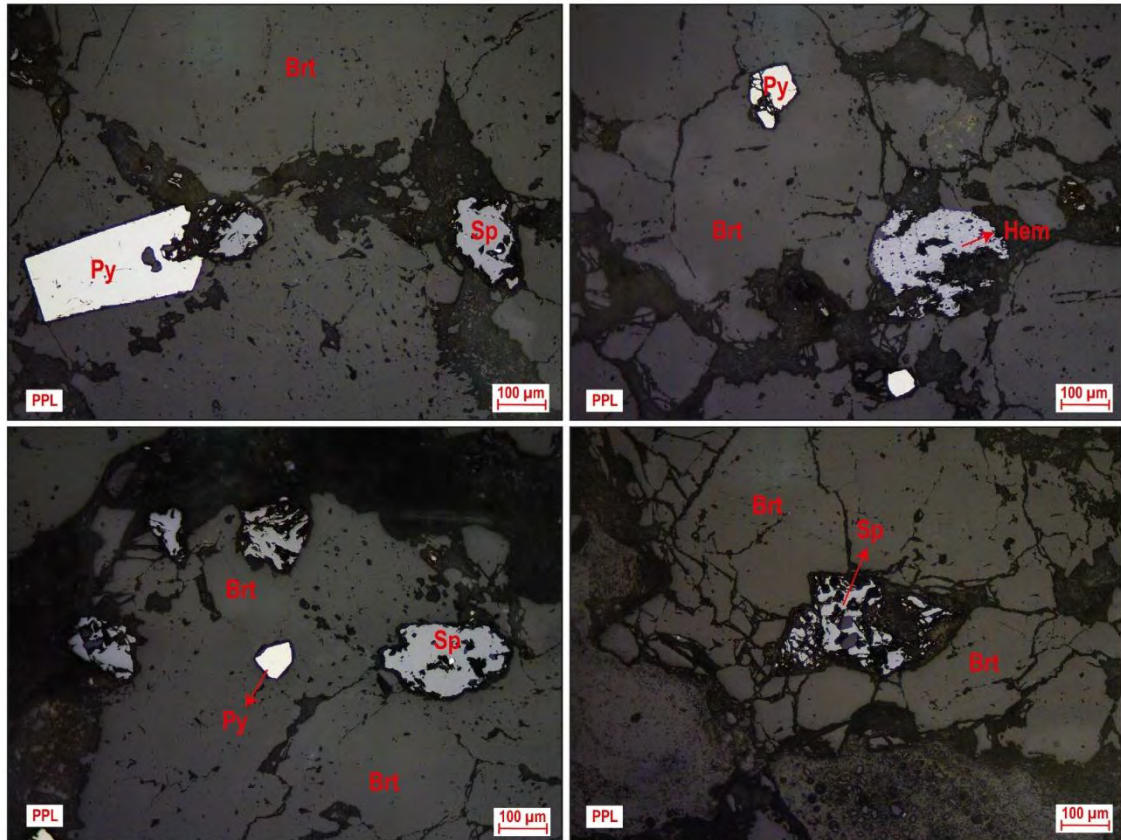
Anhedral to subhedral aggregates of pyrite in quartz groundmass, whose microfractures, interstices and edges have been replaced mainly by sphalerite (1) with disseminations of chalcopyrite (2), stannite and, to a lesser extent, by arsenopyrite. Galena and franckeite appear as fillers of open spaces and pyrite cavities.



TAU-IF-02

Minerals: Pyrite + Sphalerite + Hematite

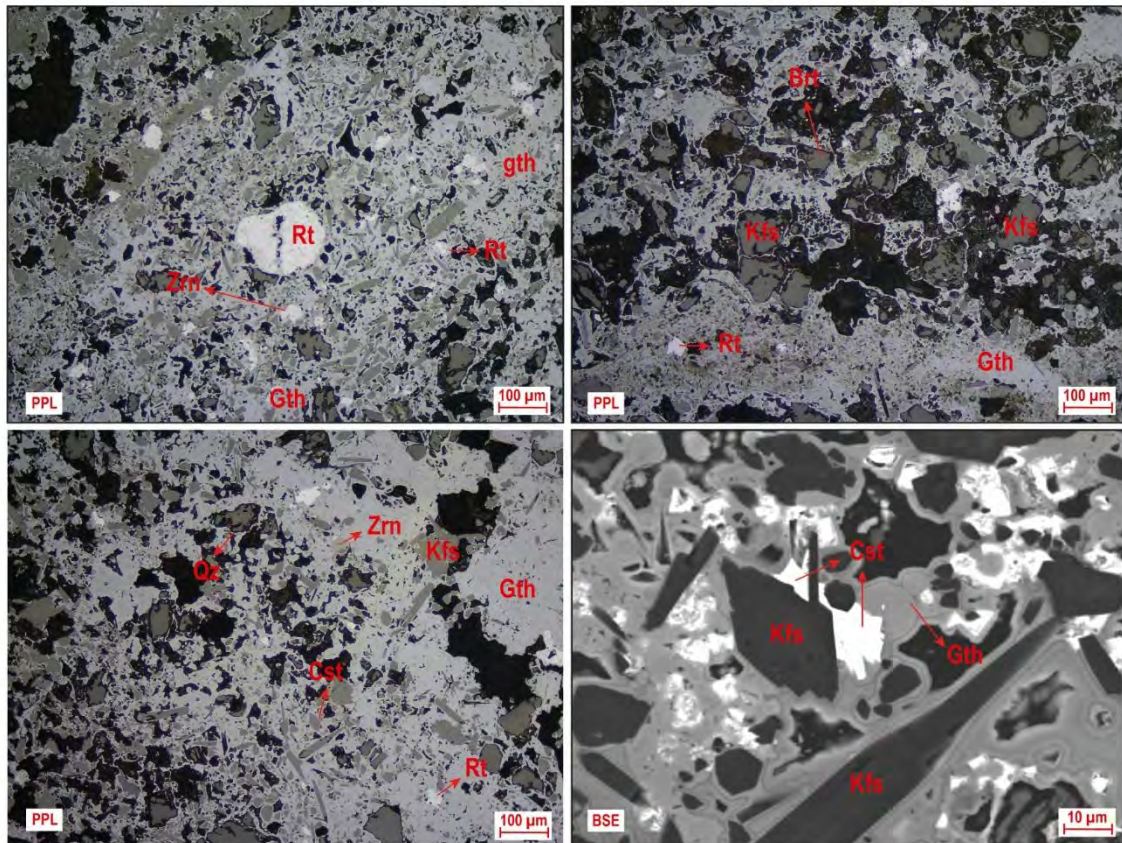
Barite groundmass with anhedral grains of pyrite, sphalerite and hematite.



TAU-IF-03A

Minerals: Hematite + Fe-oxides

Strongly oxidized groundmass with high content of hematite and other Fe oxides. Occasional grains of zircon, rutile and cassiterite.

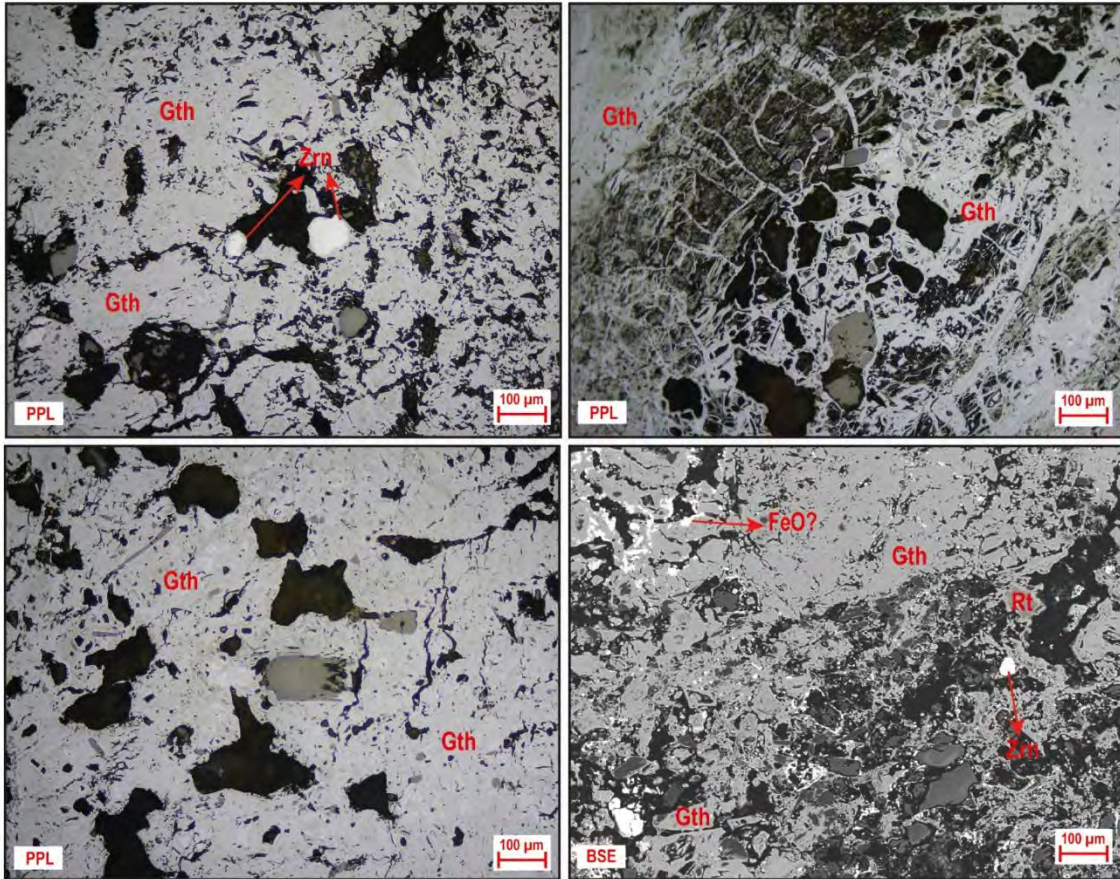


TAU-IF-03B

Minerals: Goethite + Hematite + Fe oxides

Strongly oxidized groundmass with high content of goethite, hematite and other Fe oxides.

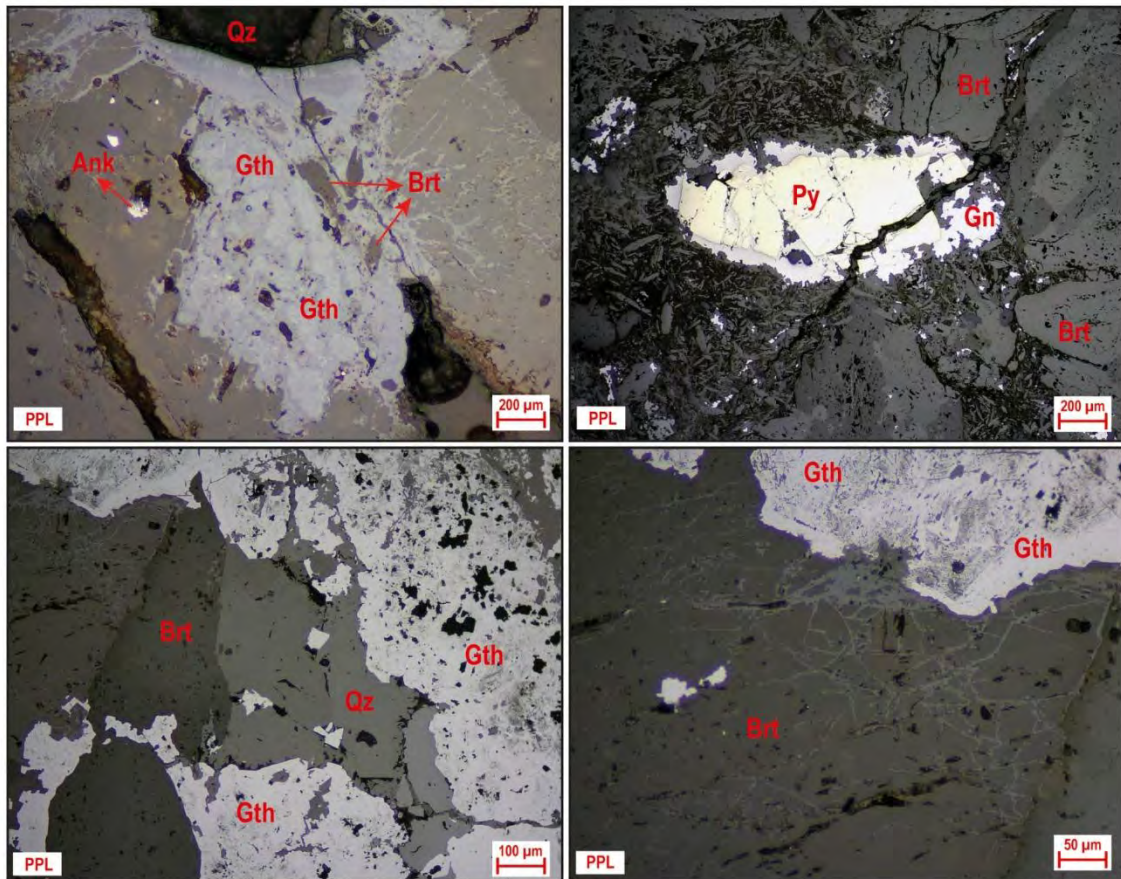
Occasional grains of zircon and rutile along the groundmass.



TAU-IF-05A

Minerals: Goethite + Var. FeO + Galena + Pyrite

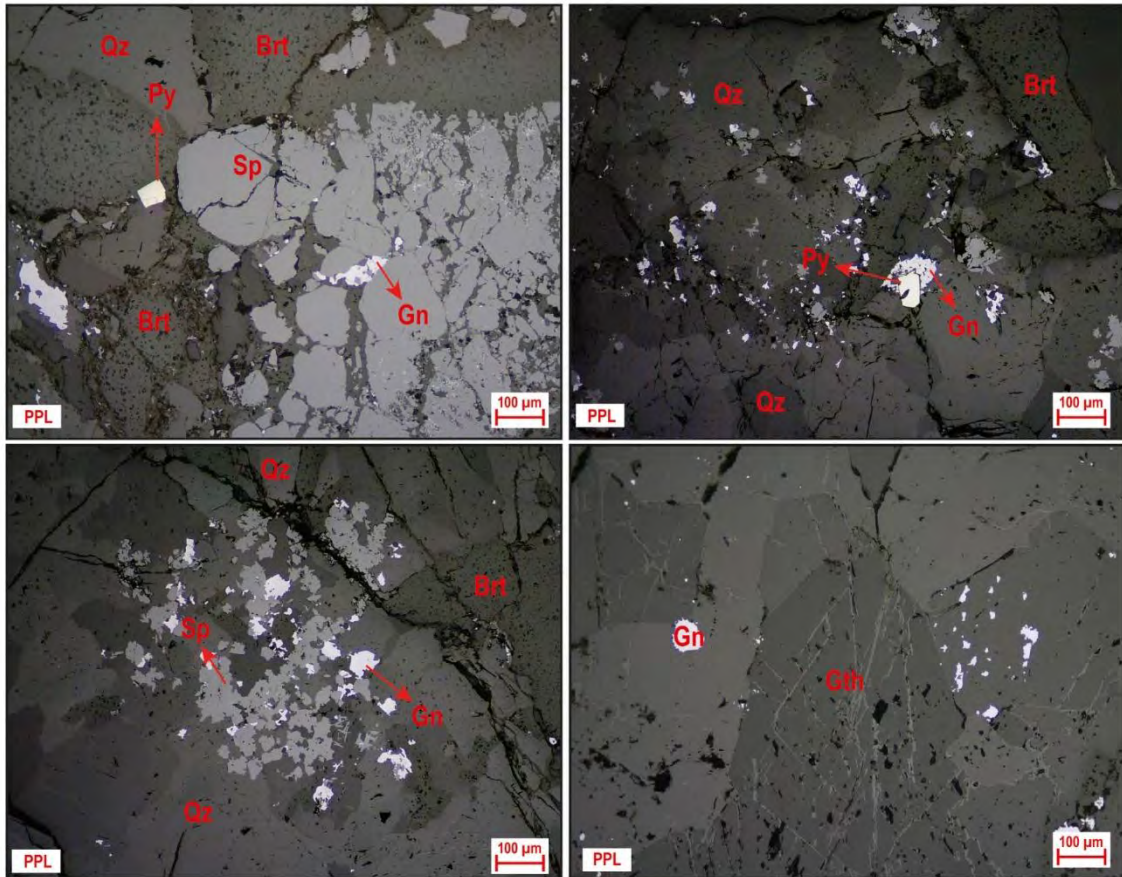
Anhedral aggregates of goethite in a groundmass of quartz and barite. To a lesser extent, pyrite is present with edge replacement by galena.



TAU-IF-05B

Minerals: Sphalerite (2) + Galena + Pyrite

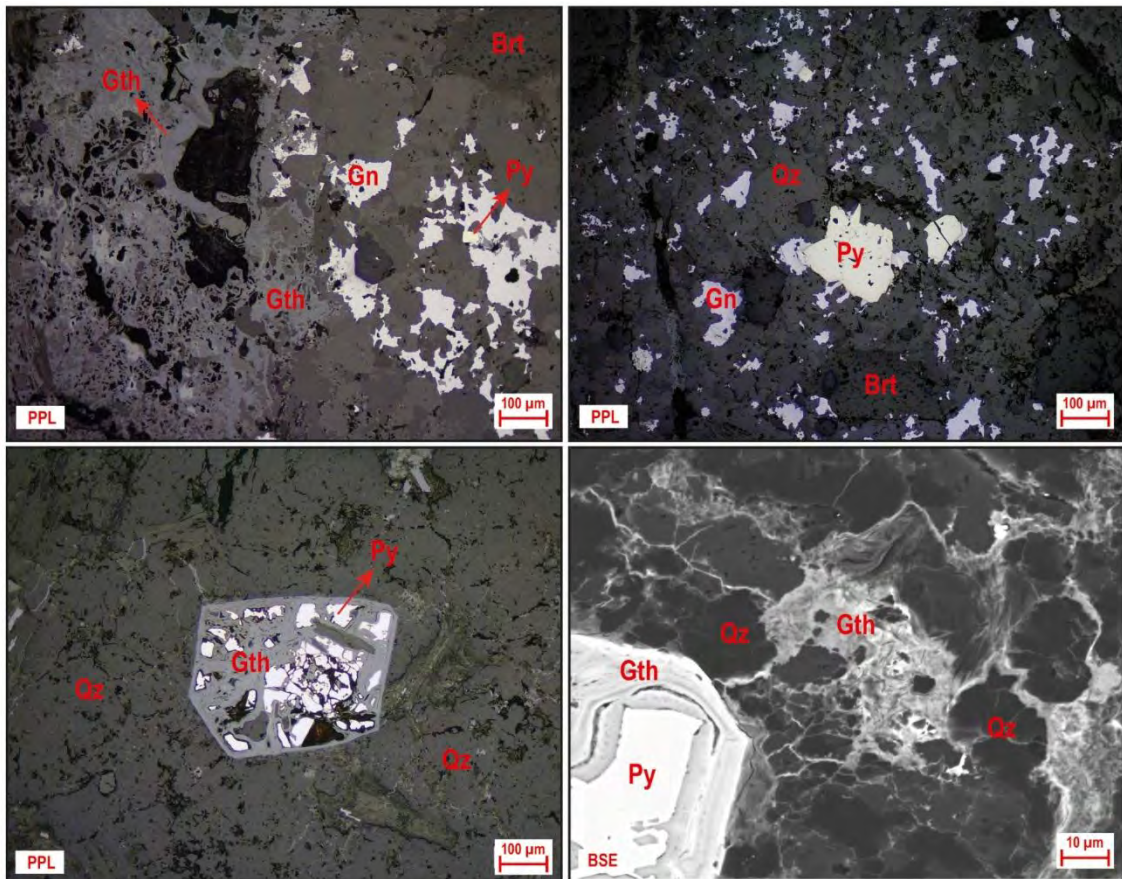
Groundmass of quartz and barite with large presence of anhedral grains of sphalerite (2), and to a lesser extent galena. Occasional pyrite grains up to 40 μm are observed.



TAU-IF-05C

Minerals: Hematite + Galena + Pyrite

Anhydrous aggregates of hematite within a groundmass of quartz and barite that have replaced pyrite through microfractures, interstices and edges. To a lesser extent, galena is observed in contact with pyrite and as irregular masses along the groundmass.

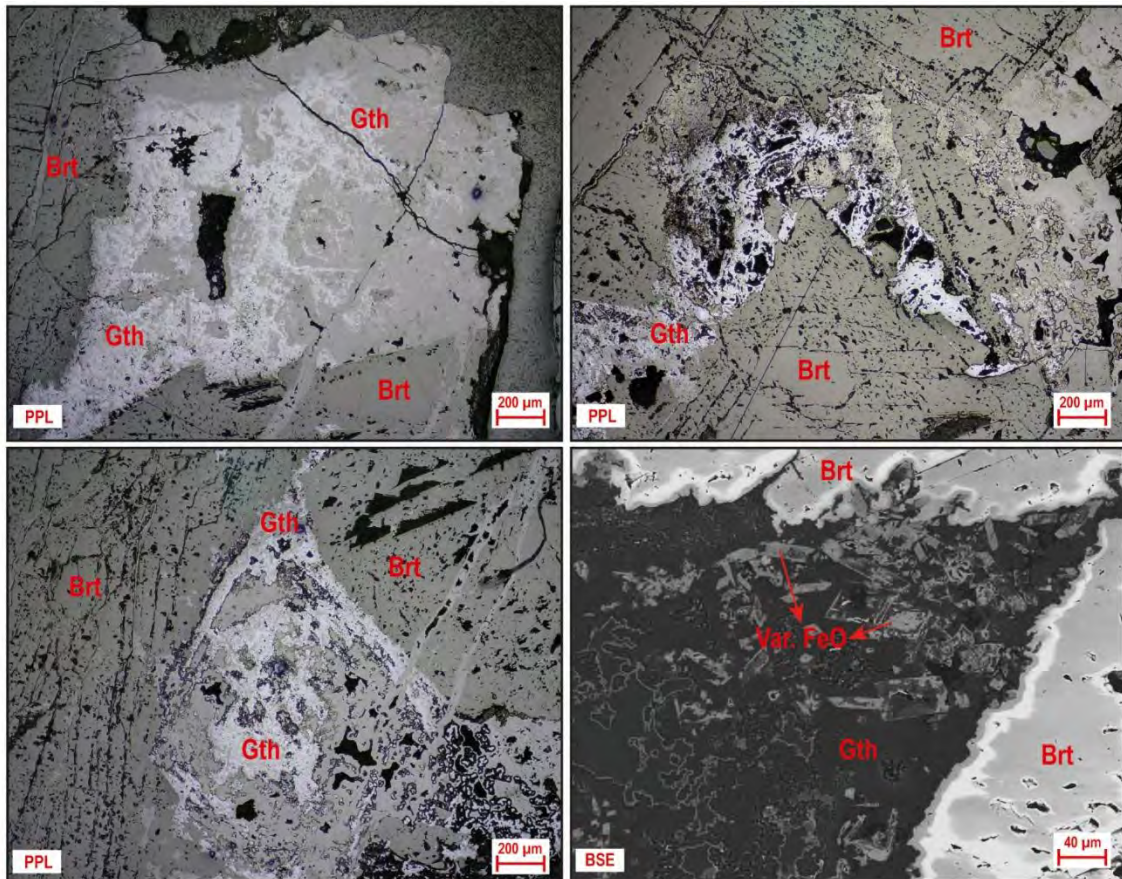


MCMXVIII

TAU-IF-06A

Minerals: Hematite + Var. FeO

Anhydrous Hematite aggregates occurring as irregular and porous masses, which have partially replaced previous unpreserved mineral phases. Also, abundant residual voids and dark spots of probable goethite/limonite are observed. All this within a groundmass of abundant barite.

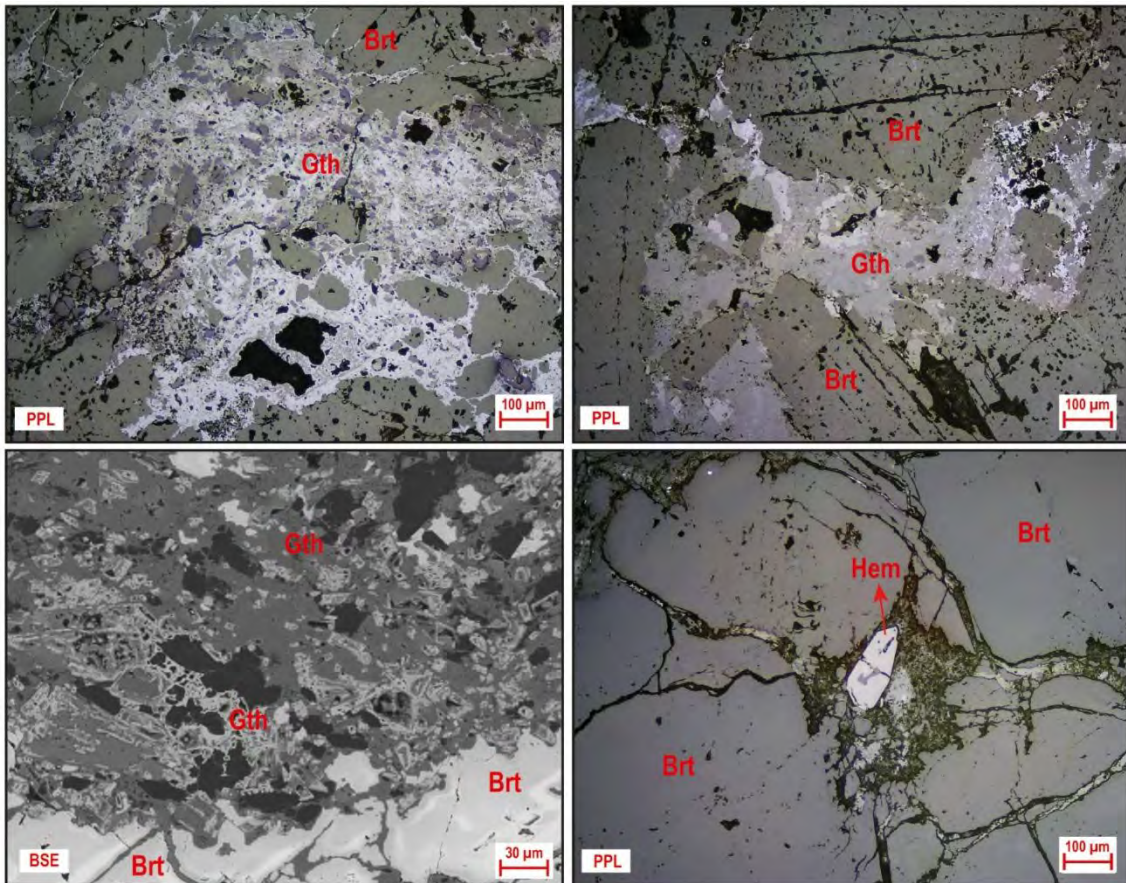


MCMXVIII

TAU-IF-06B

Minerals: Goethite + Var. FeO (As, Sb)

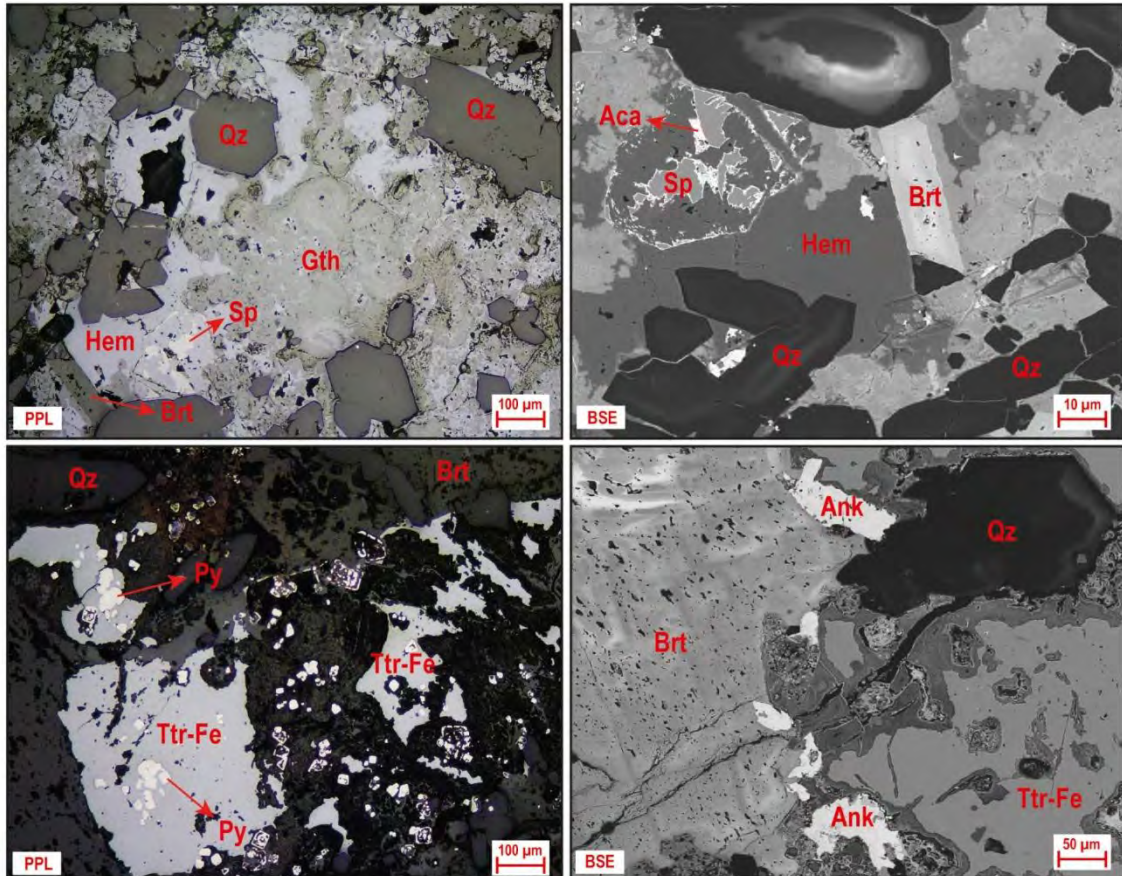
Irregular and porous masses of goethite, along with other Fe oxides, are observed within a groundmass of barite, and to a lesser extent, anhedral aggregates of hematite are observed. These minerals have partially replaced previous unpreserved mineral phases.



TAU-IF-07A

Minerals: Hematite + Tetrahedrite-Fe (Ag) + Pyrite + Sphalerite ± Acanthite

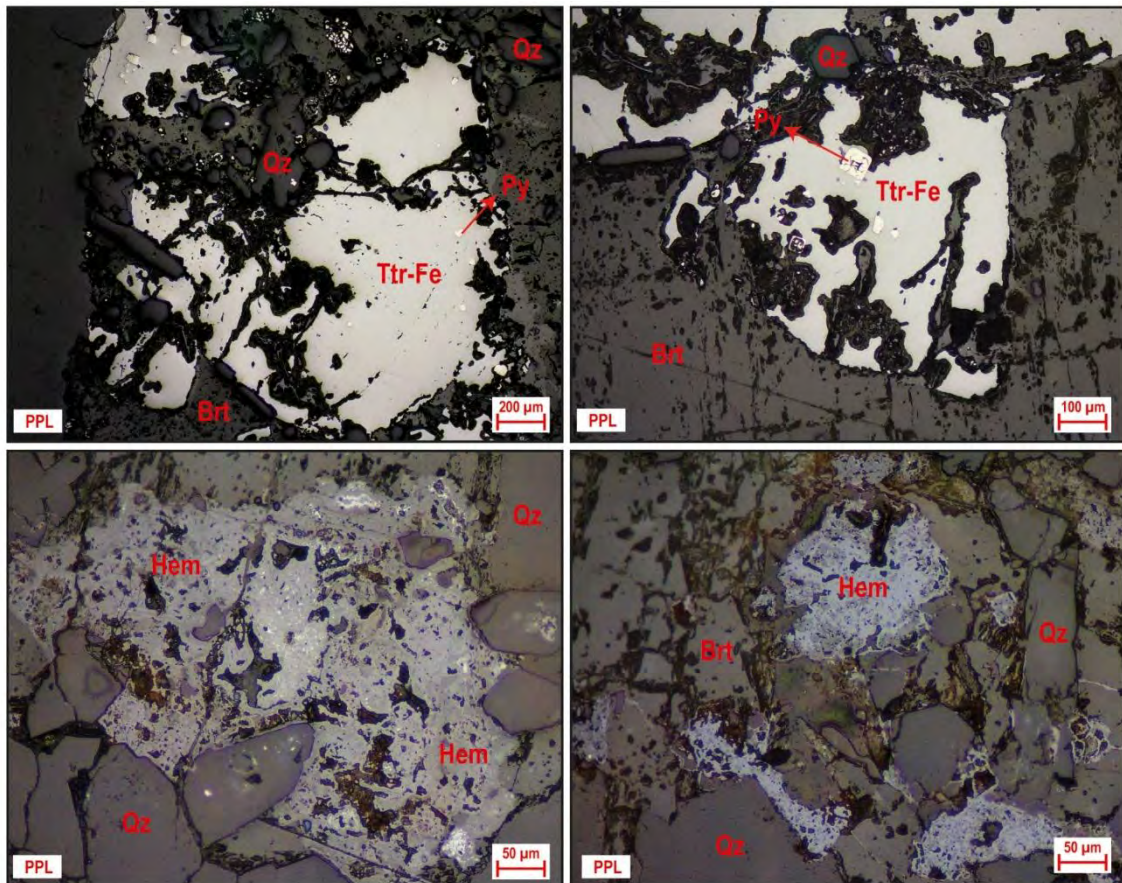
Anhedral aggregates of hematite in a groundmass of barite and quartz that have replaced pre-existing sulfides. Anhedral to subhedral crystals of pyrite are observed that have been replaced by tetrahedrite across their edges. Occasionally, acanthite grains are observed on sphalerite edges with sizes up to 15 μm .



TAU-IF-07B

Minerals: Hematite + tetrahedrite-Fe (Ag) + Pyrite

Anhedral aggregates of hematite on a groundmass of barite and quartz that have replaced pre-existing sulfides. Anhedral to subhedral crystals of tetrahedrite that have replaced pyrite through their edges, interstices and cavities.

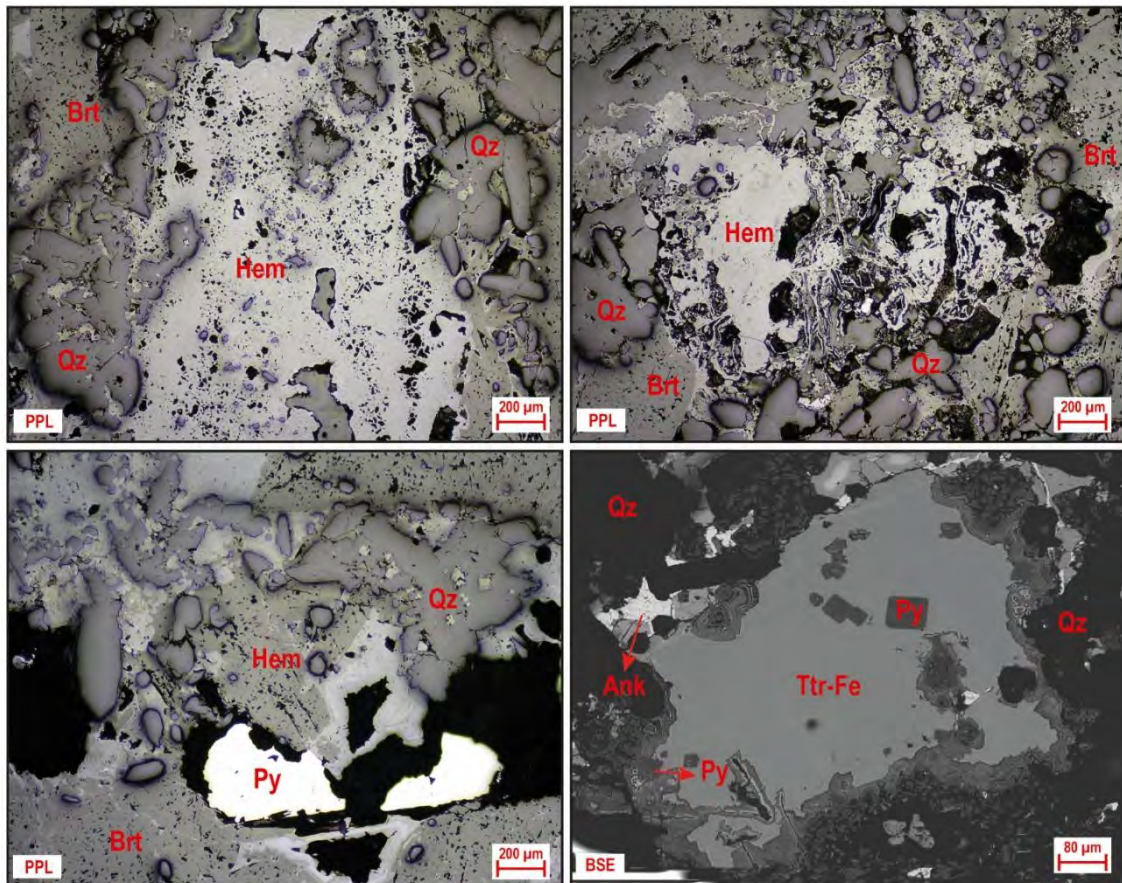


MCMXVIII

TAU-IF-07C

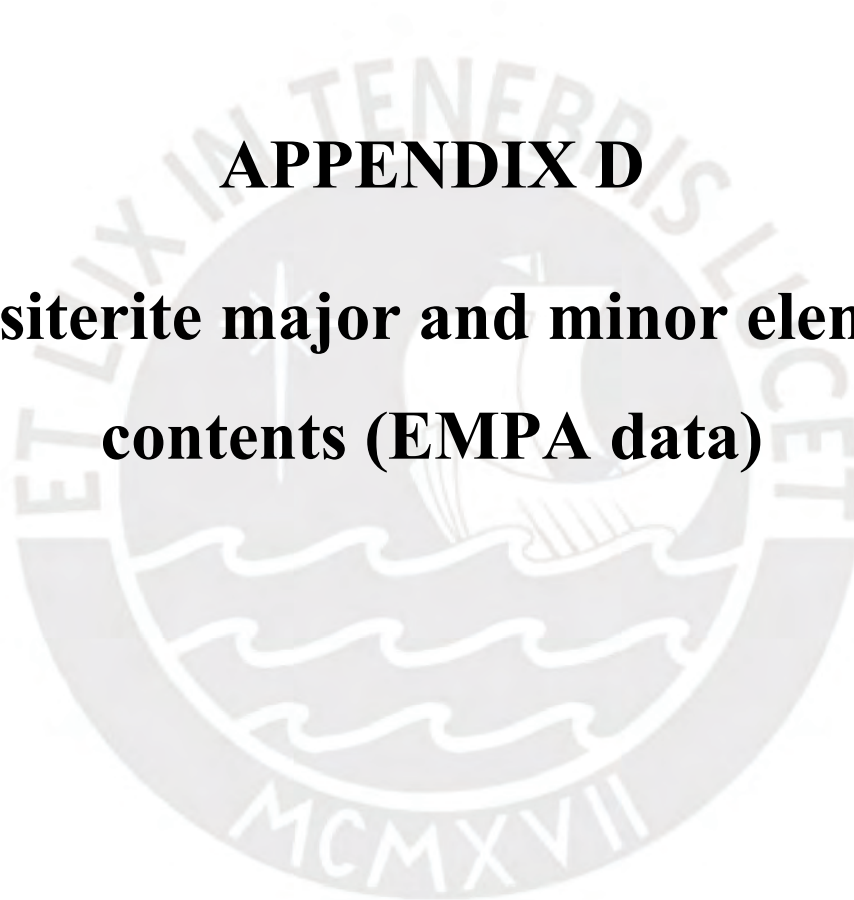
Minerals: Hematite + tetrahedrite-Fe (Ag) + Pyrite

Anhedral aggregates of hematite on a groundmass of barite and quartz that have replaced pre-existing sulfides. Anhedral to subhedral crystals of pyrite are observed that have been replaced by tetrahedrite across their edges.



APPENDIX D

Cassiterite major and minor element contents (EMPA data)



	D.L >	0.2	0.2	0.2	0.1	0.1	0.1	0.15	
Analysis No.	System	SnO ₂	ZrO ₂	Nb ₂ O ₅	FeO	MnO	TiO ₂	Ta ₂ O ₅	Total
Circle b_cst1	Kelly	97.8	b.d.l.	b.d.l.	1.64	b.d.l.	b.d.l.	b.d.l.	99.4
Circle b_cst2	Kelly	98.2	b.d.l.	b.d.l.	1.85	b.d.l.	b.d.l.	b.d.l.	100.0
Circle b_cst3	Kelly	98.0	b.d.l.	b.d.l.	1.81	b.d.l.	b.d.l.	b.d.l.	99.9
Circle b_cst4	Kelly	98.2	b.d.l.	b.d.l.	1.77	b.d.l.	b.d.l.	b.d.l.	100.0
Circle c_cst1	Kelly	98.0	b.d.l.	b.d.l.	1.70	b.d.l.	b.d.l.	b.d.l.	99.7
Circle c_cst2	Kelly	97.4	b.d.l.	b.d.l.	2.17	b.d.l.	b.d.l.	b.d.l.	99.6
Circle c_cst3	Kelly	97.2	b.d.l.	b.d.l.	2.13	b.d.l.	b.d.l.	b.d.l.	99.4
Circle d_cst1	Kelly	99.2	b.d.l.	b.d.l.	1.55	b.d.l.	b.d.l.	b.d.l.	100.8
Circle d_cst2	Kelly	98.3	b.d.l.	b.d.l.	1.33	b.d.l.	b.d.l.	b.d.l.	99.7
Circle d_cst3	Kelly	98.3	b.d.l.	b.d.l.	1.63	b.d.l.	b.d.l.	b.d.l.	100.0
Circle d_cst4	Kelly	98.8	b.d.l.	b.d.l.	1.98	b.d.l.	b.d.l.	b.d.l.	100.7
Circle e_cst1	Kelly	97.8	b.d.l.	b.d.l.	2.35	b.d.l.	b.d.l.	b.d.l.	100.2
Circle e_cst2	Kelly	98.5	b.d.l.	b.d.l.	1.25	b.d.l.	b.d.l.	b.d.l.	99.7
Circle e_cst3	Kelly	98.5	b.d.l.	b.d.l.	1.44	b.d.l.	b.d.l.	b.d.l.	99.9
Circle e_cst4	Kelly	99.6	b.d.l.	b.d.l.	0.87	b.d.l.	b.d.l.	b.d.l.	100.5
Circle a_cst1	Kelly	97.1	b.d.l.	b.d.l.	1.40	b.d.l.	b.d.l.	b.d.l.	98.5
Circle a_cst2	Kelly	97.3	b.d.l.	b.d.l.	0.95	b.d.l.	b.d.l.	b.d.l.	98.3
Circle a_cst3	Kelly	96.6	b.d.l.	b.d.l.	1.65	b.d.l.	b.d.l.	b.d.l.	98.3
Circle a_cst4	Kelly	98.8	b.d.l.	b.d.l.	0.43	b.d.l.	0.11	b.d.l.	99.4
Circle a_cst5	Kelly	96.5	b.d.l.	b.d.l.	1.41	b.d.l.	b.d.l.	b.d.l.	97.9
Circle b_cst1	Kelly	98.7	b.d.l.	b.d.l.	0.12	b.d.l.	b.d.l.	b.d.l.	98.8
Circle b_cst2	Kelly	96.7	b.d.l.	b.d.l.	1.56	b.d.l.	b.d.l.	b.d.l.	98.3
Circle b_cst3	Kelly	96.9	b.d.l.	b.d.l.	1.26	b.d.l.	b.d.l.	b.d.l.	98.1
Circle b_cst4	Kelly	96.9	b.d.l.	b.d.l.	1.82	b.d.l.	b.d.l.	b.d.l.	98.7
Circle c_cst1	Kelly	98.1	b.d.l.	b.d.l.	0.91	b.d.l.	b.d.l.	b.d.l.	99.0
Circle c_cst2	Kelly	96.7	b.d.l.	b.d.l.	1.50	b.d.l.	b.d.l.	b.d.l.	98.2
Circle c_cst3	Kelly	97.7	b.d.l.	b.d.l.	1.69	b.d.l.	b.d.l.	b.d.l.	99.4
Circle c_cst4	Kelly	97.4	b.d.l.	b.d.l.	1.50	b.d.l.	b.d.l.	b.d.l.	98.9
Circle d_cst1	Kelly	97.8	b.d.l.	b.d.l.	1.23	b.d.l.	b.d.l.	b.d.l.	99.0
Circle d_cst2	Kelly	97.4	b.d.l.	b.d.l.	1.74	b.d.l.	b.d.l.	b.d.l.	99.2
Circle e_cst1	Kelly	97.6	b.d.l.	b.d.l.	1.51	b.d.l.	b.d.l.	b.d.l.	99.1
Circle e_cst2	Kelly	96.5	b.d.l.	b.d.l.	1.75	b.d.l.	b.d.l.	b.d.l.	98.2
Circle a_cst1	Kelly	97.6	b.d.l.	b.d.l.	1.00	b.d.l.	b.d.l.	b.d.l.	98.6
Circle a_cst2	Kelly	97.8	b.d.l.	b.d.l.	1.48	b.d.l.	b.d.l.	b.d.l.	99.3
Circle a_cst3	Kelly	98.0	b.d.l.	b.d.l.	1.69	b.d.l.	b.d.l.	b.d.l.	99.7
Circle a_cst4	Kelly	97.3	b.d.l.	b.d.l.	1.67	b.d.l.	b.d.l.	b.d.l.	99.0
Circle a_cst5	Kelly	97.3	b.d.l.	b.d.l.	1.64	b.d.l.	b.d.l.	b.d.l.	99.0
Circle b_cst1	Kelly	97.2	b.d.l.	b.d.l.	1.66	b.d.l.	b.d.l.	b.d.l.	98.8
Circle b_cst2	Kelly	97.4	b.d.l.	b.d.l.	1.57	b.d.l.	b.d.l.	b.d.l.	98.9
Circle b_cst3	Kelly	97.3	b.d.l.	b.d.l.	1.48	b.d.l.	b.d.l.	b.d.l.	98.8
Circle b_cst4	Kelly	97.9	b.d.l.	b.d.l.	1.55	b.d.l.	b.d.l.	b.d.l.	99.4
Circle b_cst5	Kelly	97.7	b.d.l.	b.d.l.	1.61	b.d.l.	b.d.l.	b.d.l.	99.3
Circle c_cst1	Kelly	97.5	b.d.l.	b.d.l.	1.26	b.d.l.	b.d.l.	b.d.l.	98.8
Circle c_cst2	Kelly	97.4	b.d.l.	b.d.l.	1.49	b.d.l.	b.d.l.	b.d.l.	98.9
Circle c_cst3	Kelly	97.4	b.d.l.	b.d.l.	1.31	b.d.l.	b.d.l.	b.d.l.	98.7

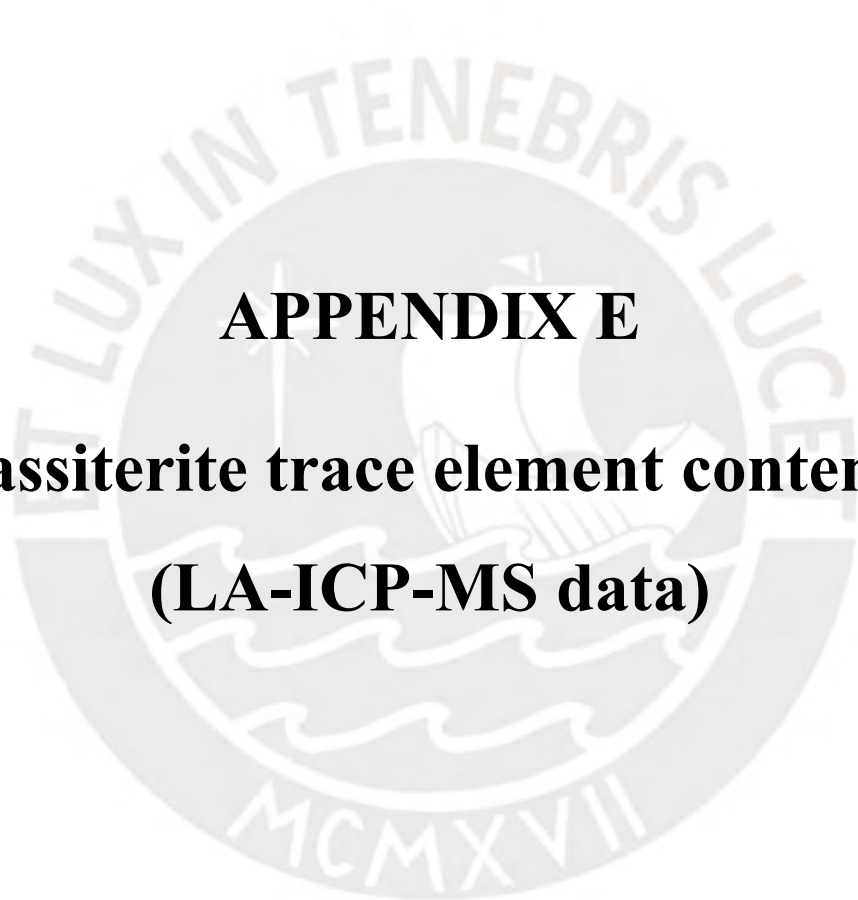
	D.L >	0.2	0.2	0.2	0.1	0.1	0.1	0.15	
Analysis No.	System	SnO ₂	ZrO ₂	Nb ₂ O ₅	FeO	MnO	TiO ₂	Ta ₂ O ₅	Total
Circle c_cst4	Kelly	96.8	b.d.l.	b.d.l.	1.66	b.d.l.	b.d.l.	b.d.l.	98.5
Circle c_cst5	Kelly	97.1	b.d.l.	b.d.l.	1.57	b.d.l.	b.d.l.	b.d.l.	98.7
Circle d_cst1	Kelly	97.1	b.d.l.	b.d.l.	1.42	b.d.l.	b.d.l.	b.d.l.	98.5
Circle d_cst2	Kelly	97.6	b.d.l.	b.d.l.	1.51	b.d.l.	b.d.l.	b.d.l.	99.1
Circle d_cst3	Kelly	99.3	b.d.l.	b.d.l.	0.58	b.d.l.	b.d.l.	b.d.l.	99.9
Circle e_cst1	Kelly	97.9	b.d.l.	b.d.l.	1.49	b.d.l.	b.d.l.	b.d.l.	99.4
Circle e_cst2	Kelly	97.3	b.d.l.	b.d.l.	1.21	b.d.l.	b.d.l.	b.d.l.	98.5
Circle e_cst3	Kelly	98.1	b.d.l.	b.d.l.	1.22	b.d.l.	b.d.l.	b.d.l.	99.3
Circle e_cst4	Kelly	97.7	b.d.l.	b.d.l.	1.58	b.d.l.	b.d.l.	b.d.l.	99.3
Circle e_cst5	Kelly	97.3	b.d.l.	b.d.l.	1.57	b.d.l.	b.d.l.	b.d.l.	98.9
Circle e_cst6	Kelly	97.2	b.d.l.	b.d.l.	1.62	b.d.l.	b.d.l.	b.d.l.	98.9
Circle e_cst7	Kelly	97.8	b.d.l.	b.d.l.	1.25	b.d.l.	b.d.l.	b.d.l.	99.0
Circle f_cst1	Kelly	97.3	b.d.l.	b.d.l.	1.57	b.d.l.	b.d.l.	b.d.l.	98.9
Circle f_cst2	Kelly	97.1	b.d.l.	b.d.l.	1.58	b.d.l.	b.d.l.	b.d.l.	98.7
Circle f_cst3	Kelly	97.6	b.d.l.	b.d.l.	1.58	b.d.l.	b.d.l.	b.d.l.	99.1
Circle f_cst4	Kelly	96.9	b.d.l.	b.d.l.	1.52	b.d.l.	b.d.l.	b.d.l.	98.4
Circle g_cst1	Kelly	97.5	b.d.l.	b.d.l.	1.45	b.d.l.	b.d.l.	b.d.l.	98.9
Circle g_cst2	Kelly	97.3	b.d.l.	b.d.l.	1.51	b.d.l.	b.d.l.	b.d.l.	98.8
Circle g_cst3	Kelly	98.0	b.d.l.	b.d.l.	1.38	b.d.l.	b.d.l.	b.d.l.	99.4
Circle g_cst4	Kelly	97.7	b.d.l.	b.d.l.	1.43	b.d.l.	b.d.l.	b.d.l.	99.1
Circle h_cst1	Kelly	97.2	b.d.l.	b.d.l.	1.56	b.d.l.	b.d.l.	b.d.l.	98.8
Circle h_cst2	Kelly	97.8	b.d.l.	b.d.l.	1.35	b.d.l.	b.d.l.	b.d.l.	99.1
Circle h_cst3	Kelly	97.2	b.d.l.	b.d.l.	1.45	b.d.l.	b.d.l.	b.d.l.	98.7
Circle h_cst4	Kelly	97.7	b.d.l.	b.d.l.	1.50	b.d.l.	b.d.l.	b.d.l.	99.2
Circle i_cst1	Kelly	97.1	b.d.l.	b.d.l.	1.66	b.d.l.	b.d.l.	b.d.l.	98.8
Circle i_cst2	Kelly	97.8	b.d.l.	b.d.l.	1.56	b.d.l.	b.d.l.	b.d.l.	99.4
Circle i_cst3	Kelly	97.5	b.d.l.	b.d.l.	1.38	b.d.l.	b.d.l.	b.d.l.	98.9
Circle i_cst4	Kelly	97.5	b.d.l.	b.d.l.	1.49	b.d.l.	b.d.l.	b.d.l.	99.0
Circle a_cst1	Kelly	98.5	b.d.l.	b.d.l.	0.94	b.d.l.	b.d.l.	b.d.l.	99.4
Circle a_cst2	Kelly	98.3	b.d.l.	b.d.l.	1.24	b.d.l.	b.d.l.	b.d.l.	99.5
Circle a_cst3	Kelly	97.1	b.d.l.	b.d.l.	1.88	b.d.l.	b.d.l.	b.d.l.	99.0
Circle b_cst1	Kelly	96.6	b.d.l.	b.d.l.	2.04	b.d.l.	b.d.l.	b.d.l.	98.6
Circle b_cst2	Kelly	98.3	b.d.l.	b.d.l.	0.78	b.d.l.	b.d.l.	b.d.l.	99.0
Circle b_cst3	Kelly	98.7	b.d.l.	b.d.l.	0.48	b.d.l.	b.d.l.	b.d.l.	99.2
Circle b_cst4	Kelly	98.7	b.d.l.	b.d.l.	0.59	b.d.l.	b.d.l.	b.d.l.	99.3
Circle b_cst5	Kelly	98.0	b.d.l.	b.d.l.	1.33	b.d.l.	b.d.l.	b.d.l.	99.4
Circle c_cst1	Kelly	97.8	b.d.l.	b.d.l.	1.15	b.d.l.	b.d.l.	b.d.l.	99.0
Circle c_cst2	Kelly	98.7	b.d.l.	b.d.l.	0.69	b.d.l.	b.d.l.	b.d.l.	99.4
Circle c_cst3	Kelly	97.2	b.d.l.	b.d.l.	1.78	b.d.l.	b.d.l.	b.d.l.	99.0
Circle d_cst1	Kelly	97.7	b.d.l.	b.d.l.	1.55	b.d.l.	b.d.l.	b.d.l.	99.2
Circle e_cst1	Kelly	98.2	b.d.l.	b.d.l.	0.94	b.d.l.	b.d.l.	b.d.l.	99.1
Circle e_cst2	Kelly	98.3	b.d.l.	b.d.l.	0.44	b.d.l.	b.d.l.	b.d.l.	98.8
Circle e_cst3	Kelly	98.6	b.d.l.	b.d.l.	0.97	b.d.l.	b.d.l.	b.d.l.	99.6
Circle f_cst1	Kelly	97.2	b.d.l.	b.d.l.	2.08	b.d.l.	b.d.l.	b.d.l.	99.2
Circle f_cst2	Kelly	98.2	b.d.l.	b.d.l.	1.41	b.d.l.	b.d.l.	b.d.l.	99.6

	D.L >	0.2	0.2	0.2	0.1	0.1	0.1	0.15	
Analysis No.	System	SnO ₂	ZrO ₂	Nb ₂ O ₅	FeO	MnO	TiO ₂	Ta ₂ O ₅	Total
Circle f_cst3	Kelly	96.9	b.d.l.	b.d.l.	2.19	b.d.l.	b.d.l.	b.d.l.	99.1
Circle a_cst1	Kelly	97.8	b.d.l.	b.d.l.	2.41	b.d.l.	b.d.l.	b.d.l.	100.2
Circle a_cst2	Kelly	98.7	b.d.l.	b.d.l.	1.37	b.d.l.	b.d.l.	b.d.l.	100.1
Circle b_cst1	Kelly	98.2	b.d.l.	b.d.l.	1.71	b.d.l.	b.d.l.	b.d.l.	99.9
Circle b_cst2	Kelly	100.2	b.d.l.	b.d.l.	0.29	b.d.l.	b.d.l.	b.d.l.	100.5
Circle b_cst3	Kelly	98.4	b.d.l.	b.d.l.	1.72	b.d.l.	b.d.l.	b.d.l.	100.2
Circle c_cst1	Kelly	100.6	b.d.l.	b.d.l.	0.14	b.d.l.	b.d.l.	b.d.l.	100.7
Circle a_cst1	Kelly	97.7	b.d.l.	b.d.l.	2.22	b.d.l.	b.d.l.	b.d.l.	99.9
Circle a_cst2	Kelly	99.9	b.d.l.	b.d.l.	0.27	b.d.l.	b.d.l.	b.d.l.	100.2
Circle a_cst3	Kelly	99.8	b.d.l.	b.d.l.	0.46	b.d.l.	b.d.l.	b.d.l.	100.3
Circle b_cst1	Kelly	98.8	b.d.l.	b.d.l.	1.14	b.d.l.	b.d.l.	b.d.l.	99.9
Circle b_cst2	Kelly	98.4	b.d.l.	b.d.l.	1.66	b.d.l.	b.d.l.	b.d.l.	100.1
Circle b_cst3	Kelly	99.1	b.d.l.	b.d.l.	0.65	b.d.l.	b.d.l.	b.d.l.	99.8
Circle b_cst4	Kelly	99.2	b.d.l.	b.d.l.	1.06	b.d.l.	b.d.l.	b.d.l.	100.2
Circle b_cst5	Kelly	100.1	b.d.l.	b.d.l.	b.d.l.	b.d.l.	b.d.l.	b.d.l.	100.1
Circle c_cst1	Kelly	97.0	b.d.l.	b.d.l.	2.16	b.d.l.	b.d.l.	b.d.l.	99.2
Circle c_cst2	Kelly	97.7	b.d.l.	b.d.l.	1.96	b.d.l.	b.d.l.	b.d.l.	99.6
Circle c_cst3	Kelly	98.0	b.d.l.	b.d.l.	1.57	b.d.l.	b.d.l.	b.d.l.	99.6
Circle c_cst4	Kelly	98.5	b.d.l.	b.d.l.	1.69	b.d.l.	b.d.l.	b.d.l.	100.1
Circle c_cst5	Kelly	97.4	b.d.l.	b.d.l.	1.92	b.d.l.	b.d.l.	b.d.l.	99.3
Circle c_cst6	Kelly	97.1	b.d.l.	b.d.l.	2.10	b.d.l.	b.d.l.	b.d.l.	99.2
Circle d_cst1	Kelly	97.4	b.d.l.	b.d.l.	2.24	b.d.l.	b.d.l.	b.d.l.	99.6
Circle d_cst2	Kelly	97.5	b.d.l.	b.d.l.	1.97	b.d.l.	b.d.l.	b.d.l.	99.4
Circle e_cst1	Kelly	98.5	b.d.l.	b.d.l.	1.67	b.d.l.	b.d.l.	b.d.l.	100.2
Circle e_cst2	Kelly	96.6	b.d.l.	b.d.l.	2.19	b.d.l.	b.d.l.	b.d.l.	98.8
Circle e_cst3	Kelly	97.8	b.d.l.	b.d.l.	1.76	b.d.l.	b.d.l.	b.d.l.	99.6
Circle a_cst1	Lorena	98.8	b.d.l.	b.d.l.	0.61	b.d.l.	b.d.l.	b.d.l.	99.4
Circle a_cst2	Lorena	99.4	b.d.l.	b.d.l.	0.55	b.d.l.	0.24	b.d.l.	100.2
Circle b_cst1	Lorena	99.1	b.d.l.	b.d.l.	b.d.l.	b.d.l.	b.d.l.	b.d.l.	99.1
Circle b_cst2	Lorena	97.9	b.d.l.	b.d.l.	1.29	b.d.l.	b.d.l.	b.d.l.	99.2
Circle b_cst3	Lorena	98.1	b.d.l.	b.d.l.	0.32	b.d.l.	0.14	b.d.l.	98.5
Circle b_cst4	Lorena	97.2	b.d.l.	b.d.l.	b.d.l.	b.d.l.	b.d.l.	b.d.l.	97.2
Circle c_cst1	Lorena	99.2	b.d.l.	b.d.l.	0.45	b.d.l.	0.15	b.d.l.	99.8
Circle c_cst2	Lorena	98.9	b.d.l.	b.d.l.	b.d.l.	b.d.l.	b.d.l.	b.d.l.	98.9
Circle c_cst3	Lorena	98.9	b.d.l.	b.d.l.	0.41	b.d.l.	b.d.l.	b.d.l.	99.3
Circle c_cst4	Lorena	98.6	b.d.l.	b.d.l.	0.76	b.d.l.	b.d.l.	b.d.l.	99.4
Circle d_cst1	Lorena	99.8	b.d.l.	b.d.l.	b.d.l.	b.d.l.	b.d.l.	b.d.l.	99.8
Circle d_cst2	Lorena	99.6	b.d.l.	b.d.l.	b.d.l.	b.d.l.	0.12	b.d.l.	99.7
Circle d_cst3	Lorena	99.4	b.d.l.	b.d.l.	b.d.l.	b.d.l.	b.d.l.	b.d.l.	99.4
Circle d_cst4	Lorena	99.6	b.d.l.	b.d.l.	b.d.l.	b.d.l.	0.14	b.d.l.	99.8
Circle d_cst5	Lorena	99.5	b.d.l.	b.d.l.	0.12	b.d.l.	b.d.l.	b.d.l.	99.6
Circle d_cst6	Lorena	100.4	b.d.l.	b.d.l.	b.d.l.	b.d.l.	b.d.l.	b.d.l.	100.4
Circle a_cst1	Lorena	99.0	b.d.l.	b.d.l.	0.52	b.d.l.	b.d.l.	b.d.l.	99.5
Circle a_cst2	Lorena	98.3	b.d.l.	b.d.l.	b.d.l.	b.d.l.	0.41	b.d.l.	98.7
Circle a_cst3	Lorena	98.5	b.d.l.	b.d.l.	0.12	b.d.l.	0.28	b.d.l.	98.9

	D.L >	0.2	0.2	0.2	0.1	0.1	0.1	0.15	
Analysis No.	System	SnO ₂	ZrO ₂	Nb ₂ O ₅	FeO	MnO	TiO ₂	Ta ₂ O ₅	Total
Circle a_cst4	Lorena	98.8	b.d.l.	b.d.l.	b.d.l.	b.d.l.	0.17	b.d.l.	99.0
Circle b_cst1	Lorena	99.2	b.d.l.	b.d.l.	b.d.l.	b.d.l.	b.d.l.	b.d.l.	99.2
Circle b_cst2	Lorena	98.2	b.d.l.	b.d.l.	0.10	b.d.l.	0.20	b.d.l.	98.5
Circle b_cst3	Lorena	98.7	b.d.l.	b.d.l.	0.17	b.d.l.	0.54	b.d.l.	99.4
Circle c_cst1	Lorena	98.7	b.d.l.	b.d.l.	0.15	b.d.l.	b.d.l.	b.d.l.	98.8
Circle c_cst2	Lorena	98.6	b.d.l.	b.d.l.	b.d.l.	b.d.l.	b.d.l.	b.d.l.	98.6
Circle c_cst3	Lorena	97.2	b.d.l.	b.d.l.	0.18	b.d.l.	1.13	b.d.l.	98.5
Circle c_cst4	Lorena	97.7	b.d.l.	b.d.l.	0.21	b.d.l.	0.63	b.d.l.	98.5
Circle c_cst5	Lorena	98.8	b.d.l.	b.d.l.	0.17	b.d.l.	0.32	b.d.l.	99.3
Circle c_cst6	Lorena	98.9	b.d.l.	b.d.l.	0.16	b.d.l.	0.12	b.d.l.	99.2
Circle d_cst1	Lorena	98.6	b.d.l.	b.d.l.	0.16	b.d.l.	0.36	b.d.l.	99.1
Circle d_cst2	Lorena	98.8	b.d.l.	b.d.l.	0.25	b.d.l.	0.11	b.d.l.	99.2
Circle d_cst3	Lorena	99.7	b.d.l.	b.d.l.	0.10	b.d.l.	b.d.l.	b.d.l.	99.8
Circle d_cst4	Lorena	99.7	b.d.l.	b.d.l.	0.18	b.d.l.	b.d.l.	b.d.l.	99.9

b.d.l.—Below detection limit





APPENDIX E

Cassiterite trace element contents
(LA-ICP-MS data)

Trace elements (ppm)	2024-TAU-06-A-circle a-cst1	2024-TAU-06-A-circle a-cst1.1	2024-TAU-06-A-circle a-cst1.2	2024-TAU-06-A-circle a-cst2	2024-TAU-06-A-circle a-cst2.1	2024-TAU-06-A-circle a-cst2.2	2024-TAU-06-A-circle b-cst1	2024-TAU-06-A-circle b-cst2
Sc	18.8	26.2	18.1	19.5	17.5	18.7	2.73	52.8
Ti	897	1074	837	915	884	1068	198	2683
V	244	360	196	305	241	337	69	798
Mn	22.2	23.6	22.7	21.1	21.1	22.3	9.9	59.7
Co	33.3	41.3	26.3	33.0	29.1	35.2	9.18	86.2
Ni	201	248	159	201	177	212	55	528
Cu	9.59	9.18	5.67	4.06	7.34	6.33	1.52	17.2
Zn	12.7	12.8	3.41	3.78	18.5	14.2	3.55	28.9
Ga	47.7	59.1	42.4	51.8	41.8	50.5	12.4	131
Ge	3.65	3.36	3.38	3.09	3.80	2.88	0.96	8.68
As	81.1	113	147	91.4	110	246	44.5	219
Y	3.94	4.61	3.49	3.58	3.20	3.69	1.63	10.12
Zr	14.6	18.2	13.4	14.6	14.4	15.4	3.32	44.7
Nb	7.03	7.46	6.79	7.47	6.88	9.13	2.51	19.24
Cd	0.37	0.40	0.32	0.32	0.26	0.34	0.10	0.96
In	53.6	55.8	50.5	56.8	49.1	51.3	3.80	120
Sb	273	205	291	193	285	193	83.5	634
La	1.61	1.94	1.55	1.68	1.12	1.89	0.82	3.69
Ce	3.75	4.88	3.39	4.19	2.77	4.57	2.28	9.86
Pr	0.52	0.71	0.47	0.59	0.41	0.63	0.33	1.47
Nd	2.39	3.11	2.07	2.70	1.86	2.85	1.48	6.65
Sm	0.80	1.06	0.73	0.89	0.72	0.93	0.46	2.27
Eu	0.58	0.67	0.57	0.61	0.54	0.67	0.37	1.55
Dy	1.05	1.24	0.95	0.98	0.95	1.00	0.42	2.73
Ho	0.18	0.22	0.19	0.18	0.17	0.19	0.08	0.51
Er	0.61	0.71	0.59	0.52	0.55	0.57	0.23	1.56
Tm	0.12	0.12	0.11	0.09	0.10	0.11	0.04	0.29
Yb	1.02	1.05	1.02	0.92	0.93	0.92	0.32	2.57
Lu	0.15	0.16	0.14	0.13	0.14	0.14	0.04	0.37
Hf	0.37	0.40	0.33	0.36	0.34	0.38	0.08	1.15
Ta	0.06	0.05	0.07	0.04	0.05	0.05	0.01	0.13
W	1615	2200	1400	1719	1411	1875	557	4846
Pb	51.9	54.7	55.0	27.2	37.8	31.8	4.06	67.2
Bi	0.65	0.52	0.83	0.18	0.33	0.43	0.12	0.47
Th	2.91	2.35	4.70	2.06	2.03	1.91	0.27	4.00
U	12.6	13.3	12.1	12.5	11.8	12.2	2.94	29.0

Trace elements (ppm)	2024-TAU-06-A-circle b-cst2	2024-TAU-06-A-circle b-cst2.1	2024-TAU-06-A-circle b-cst2.2	2024-TAU-06-A-circle b-cst3	2024-TAU-06-A-circle b-cst4	2024-TAU-06-A-circle c-cst1	2024-TAU-06-A-circle c-cst1.1	2024-TAU-06-A-circle c-cst2
Sc	60.5	68.2	50.3	10.4	1.98	19.0	12.8	1.91
Ti	3128	3300	2309	603	93	923	847	181
V	948	891	610	162	24.0	296	237	54.0
Mn	70.3	72.0	63.1	11.6	2.2	19.3	25.8	4.3
Co	96.4	91.2	71.8	19.4	3.06	22.9	22.2	5.00
Ni	589	553	435	119	18.5	140	135	30.4
Cu	15.1	22.1	13.0	3.42	0.51	7.95	7.61	0.86
Zn	11.7	16.2	22.7	15.3	0.72	7.05	8.25	1.14
Ga	143	145	127	26.3	5.12	42.2	44.0	7.28
Ge	10.7	10.9	7.84	1.81	0.31	3.32	4.20	0.70
As	336	339	211	33	6.95	208	174	17
Y	11.0	11.3	9.55	2.08	0.40	3.15	4.07	0.77
Zr	51.0	50.8	35.4	10.4	1.63	18.2	14.4	3.73
Nb	23.6	29.4	18.9	3.98	0.65	7.67	7.86	1.37
Cd	1.00	0.91	0.66	0.20	0.03	0.22	0.22	0.05
In	128	120	112	29.9	5.90	39.6	37.5	8.01
Sb	751	745	574	120	22.5	254	393	60.8
La	3.93	4.06	3.90	0.87	0.18	1.01	1.16	0.19
Ce	10.1	10.3	9.77	2.22	0.44	2.62	2.90	0.49
Pr	1.45	1.54	1.36	0.31	0.06	0.39	0.42	0.07
Nd	6.64	7.19	6.40	1.43	0.28	1.82	2.00	0.36
Sm	2.37	2.59	2.33	0.50	0.10	0.71	0.84	0.16
Eu	1.57	1.78	1.47	0.33	0.07	0.50	0.60	0.11
Dy	3.11	3.07	2.58	0.56	0.11	0.90	1.17	0.22
Ho	0.56	0.62	0.45	0.11	0.02	0.17	0.22	0.04
Er	1.74	1.80	1.46	0.33	0.06	0.50	0.70	0.13
Tm	0.33	0.35	0.25	0.06	0.01	0.10	0.13	0.02
Yb	2.72	2.88	2.46	0.51	0.10	0.83	1.20	0.23
Lu	0.42	0.43	0.35	0.08	0.01	0.12	0.18	0.03
Hf	1.33	1.23	0.82	0.24	0.04	0.48	0.38	0.10
Ta	0.16	0.19	0.13	0.03	0.01	0.04	0.04	0.01
W	5522	5959	5232	917	170	1655	1690	251
Pb	33.9	64.5	108	7.33	1.56	17.8	45.9	3.82
Bi	0.52	0.52	0.37	0.12	0.04	0.18	0.21	0.07
Th	4.63	6.11	5.89	0.88	0.32	1.57	2.41	0.23
U	32.7	33.2	27.6	6.28	1.21	12	13	2.33

Trace elements (ppm)	2024-TAU-06-A-circle c-cst3	2024-TAU-06-A-circle c-cst3.1	2024-TAU-06-A-circle c-cst4	2024-TAU-06-A-circle d-cst1	2024-TAU-06-A-circle d-cst2	2024-TAU-06-A-circle d-cst3	2024-TAU-06-A-circle d-cst4	2024-TAU-06-A-circle d-cst5
Sc	8.26	12.4	13.5	3.03	1.68	6.81	5.55	11.9
Ti	741	869	735	295	100	475	336	658
V	186	248	216	52.2	23.2	127.1	76.8	162
Mn	19.1	23.9	19.6	6.3	2.6	8.7	9.3	19.3
Co	18.1	21.0	21.8	6.21	2.69	10.8	8.63	16.9
Ni	111	128	133	38.2	16.3	65.9	52.5	102
Cu	4.18	5.57	6.58	1.10	0.78	2.01	2.00	7.52
Zn	8.25	5.40	4.34	1.08	1.62	3.49	2.03	6.51
Ga	33.1	40.9	50.8	7.07	3.43	13.5	14.0	28.3
Ge	2.77	3.70	3.28	0.83	0.40	1.27	1.00	2.23
As	102	114	182	22.6	12.6	25.2	21.9	76.2
Y	2.80	3.76	2.95	1.40	0.58	1.76	1.86	3.84
Zr	11.9	14.3	14.2	4.04	1.74	7.97	5.37	11.2
Nb	6.45	8.11	5.36	2.72	0.87	4.66	3.17	5.76
Cd	0.21	0.23	0.25	0.07	0.03	0.11	0.09	0.18
In	37.8	37.3	67.2	3.35	1.50	7.20	4.64	8.58
Sb	255	336	261	85.7	47.1	120	102	257
La	0.97	1.05	1.06	0.38	0.16	0.52	0.74	1.42
Ce	2.15	2.63	2.44	1.08	0.45	1.51	2.01	3.93
Pr	0.30	0.40	0.35	0.16	0.07	0.22	0.29	0.56
Nd	1.42	1.85	1.63	0.78	0.31	1.02	1.37	2.64
Sm	0.56	0.76	0.69	0.28	0.13	0.36	0.46	0.89
Eu	0.43	0.57	0.49	0.19	0.08	0.25	0.31	0.61
Dy	0.76	1.03	0.86	0.36	0.14	0.44	0.49	1.01
Ho	0.15	0.21	0.16	0.07	0.03	0.08	0.09	0.19
Er	0.52	0.66	0.52	0.21	0.09	0.26	0.26	0.57
Tm	0.09	0.12	0.10	0.04	0.01	0.05	0.04	0.09
Yb	0.87	1.09	0.86	0.31	0.13	0.40	0.36	0.81
Lu	0.13	0.15	0.13	0.04	0.02	0.06	0.05	0.10
Hf	0.31	0.38	0.37	0.12	0.05	0.24	0.16	0.35
Ta	0.03	0.04	0.03	0.02	0.01	0.03	0.02	0.04
W	1185	1535	1393	365	166	580	676	1367
Pb	21.4	12.1	13.0	7.12	2.31	13.1	3.49	10.7
Bi	0.53	0.18	0.16	0.09	0.03	0.14	0.12	0.26
Th	2.24	1.95	2.45	0.21	0.18	0.28	0.29	0.57
U	10.2	12.0	14.13	2.14	1.08	3.64	2.90	6.44

Trace elements (ppm)	2024-TAU-06-A-circle d-cst5.1	2024-TAU-06-A-circle d-cst6	2024-TAU-06-A-circle d-cst6.1	2024-TAU-06-B-circle a-cst1	2024-TAU-06-B-circle a-cst1.1	2024-TAU-06-B-circle a-cst1.2	2024-TAU-06-B-circle a-cst2	2024-TAU-06-B-circle a-cst3
Sc	12.9	3.29	3.71	81.7	47.7	70.8	8.49	7.90
Ti	568	208	183	5891	4559	5632	859	868
V	164	43.7	42.6	1520	1159	1374	180	193
Mn	31.6	5.9	5.1	218	194	160	21.7	21.7
Co	18.4	5.25	4.46	104.2	88.7	89.7	14.5	14.1
Ni	112	32.0	27.4	628	540	544	88.7	86.7
Cu	7.94	1.09	1.97	33.2	34.2	21.0	3.80	3.53
Zn	6.50	1.53	3.17	26.6	28.5	25.7	3.48	13.1
Ga	44.1	8.85	8.57	235	188	157	19.8	16.4
Ge	2.53	0.53	0.49	17.4	16.6	13.8	2.46	2.15
As	69.1	12.5	16.0	716	1392	626	184	176
Y	6.95	1.14	1.02	38.5	34.5	27.1	5.27	3.21
Zr	10.3	3.10	2.91	102	81.1	101	15.4	16.5
Nb	4.85	1.77	1.41	63.2	50.7	52.1	9.71	8.59
Cd	0.21	0.05	0.05	1.07	1.11	0.83	0.14	0.15
In	7.58	5.01	3.93	19.0	16.9	32.4	2.95	3.79
Sb	269	57.5	54.3	1728	2165	1317	269	208
La	3.74	0.60	0.57	19.2	17.6	11.2	1.24	0.83
Ce	10.3	1.64	1.54	52.5	48.5	29.9	3.35	2.25
Pr	1.50	0.24	0.22	7.57	7.06	4.32	0.51	0.34
Nd	6.87	1.06	0.98	34.6	31.8	19.8	2.41	1.65
Sm	2.09	0.31	0.31	11.1	10.3	6.82	0.94	0.65
Eu	1.27	0.22	0.21	7.13	6.24	4.42	0.62	0.41
Dy	1.82	0.29	0.26	10.3	9.00	7.46	1.28	0.83
Ho	0.32	0.05	0.05	1.81	1.61	1.34	0.25	0.16
Er	0.89	0.15	0.14	5.21	4.61	3.92	0.78	0.53
Tm	0.13	0.02	0.02	0.81	0.68	0.65	0.13	0.09
Yb	1.00	0.19	0.16	6.08	5.21	5.26	1.14	0.82
Lu	0.12	0.03	0.02	0.77	0.61	0.69	0.15	0.11
Hf	0.30	0.10	0.10	2.89	2.41	3.08	0.48	0.47
Ta	0.03	0.01	0.01	0.47	0.45	0.48	0.08	0.07
W	1974	404	350	14807	10828	9376	1304	1010
Pb	17.4	3.86	4.40	25.5	25.8	29.0	8.14	13.4
Bi	0.25	0.22	0.03	1.20	2.47	1.13	0.31	0.31
Th	0.70	0.20	0.17	3.91	3.93	3.10	0.58	0.45
U	7.22	1.89	1.70	51.25	45.00	43.18	7.23	6.02

Trace elements (ppm)	2024-TAU-06-B-circle a-cst3.1	2024-TAU-06-B-circle a-cst4	2024-TAU-06-B-circle b-cst1	2024-TAU-06-B-circle b-cst2	2024-TAU-06-B-circle b-cst3	2024-TAU-06-B-circle b-cst3.1	2024-TAU-06-B-circle c-cst1	2024-TAU-06-B-circle c-cst1.1
Sc	10.6	11.9	17.1	11.6	15.6	22.8	35.5	21.6
Ti	1396	905	2167	1134	1414	1740	4737	3103
V	281	236	442	280	359	402	750	566
Mn	26.8	18.1	50.5	31.9	28.4	42.8	66.7	45.3
Co	18.8	15.1	26.9	18.0	19.7	22.3	38.2	41.3
Ni	114	92.3	166	111	119	136	234	253
Cu	4.09	2.45	5.57	6.46	4.75	7.82	13.0	16.0
Zn	5.15	4.00	3.81	4.27	5.92	4.53	7.51	7.25
Ga	23.7	17.5	50.7	38.3	32.4	48.6	49.1	42.7
Ge	3.31	1.91	3.60	2.27	2.87	3.10	6.66	6.10
As	134	91.4	115	158	92.3	252	248	309
Y	6.06	3.30	8.72	5.73	5.51	7.81	14.4	11.1
Zr	26.0	18.8	33.8	16.9	20.3	22.9	54.2	77.1
Nb	14.4	8.44	29.4	13.6	16.2	22.1	64.8	42.0
Cd	0.22	0.19	0.32	0.22	0.20	0.24	0.47	0.39
In	7.97	6.25	4.38	6.24	14.4	8.36	7.89	7.50
Sb	359	193	339	281	283	338	699	623
La	1.28	0.90	4.37	3.35	1.73	3.51	3.39	2.70
Ce	3.54	2.49	12.0	8.86	4.72	9.45	9.42	7.34
Pr	0.53	0.37	1.72	1.27	0.70	1.35	1.40	1.14
Nd	2.67	1.76	7.93	5.70	3.33	6.32	6.87	5.30
Sm	1.05	0.65	2.48	1.72	1.21	2.02	2.74	2.03
Eu	0.73	0.42	1.61	1.03	0.80	1.28	1.75	1.33
Dy	1.54	0.85	2.36	1.53	1.46	2.10	3.67	2.78
Ho	0.30	0.16	0.42	0.28	0.29	0.37	0.70	0.54
Er	0.97	0.50	1.19	0.74	0.83	1.11	2.23	1.74
Tm	0.16	0.08	0.18	0.11	0.14	0.18	0.41	0.31
Yb	1.40	0.74	1.55	0.90	1.19	1.42	3.21	2.48
Lu	0.20	0.10	0.19	0.12	0.16	0.18	0.43	0.34
Hf	0.81	0.55	1.13	0.54	0.68	0.79	1.84	2.39
Ta	0.13	0.08	0.18	0.09	0.11	0.14	0.41	0.26
W	1463	1036	4265	2488	1871	3314	3485	3292
Pb	11.7	4.49	11.5	12.5	14.0	30.9	15.1	14.43
Bi	0.23	0.17	0.15	0.24	0.18	0.46	0.46	0.63
Th	0.70	0.43	1.07	0.88	0.72	1.10	1.59	1.66
U	9.51	6.79	15.9	9.40	11.1	12.4	22.6	22.4

Trace elements (ppm)	2024-TAU-06-B-circle c-cst2	2024-TAU-06-B-circle c-cst2.1	2024-TAU-06-B-circle c-cst3	2024-TAU-06-B-circle c-cst4	2024-TAU-06-B-circle c-cst5	2024-TAU-06-B-circle c-cst6	2024-TAU-06-B-circle d-cst1	2024-TAU-06-B-circle d-cst1.1
Sc	14.9	6.99	75.4	0.35	73.7	45.3	22.8	21.9
Ti	1241	658	3823	24	4504	6334	2415	2888
V	237	138	772	3.6	829	854	573	606
Mn	16.7	22.5	22.9	0.2	39.2	52.0	57.2	54.7
Co	17.4	10.0	31.2	0.22	31.6	43.8	32.0	30.9
Ni	105	60.6	190	1.3	193	267	194	188
Cu	4.18	6.57	9.36	0.11	8.81	10.07	13.65	9.22
Zn	2.77	4.84	2.26	0.07	3.82	8.92	9.75	8.16
Ga	14.6	20.7	17.7	0.14	31.9	28.0	59.3	43.3
Ge	1.92	1.76	2.66	0.04	3.27	6.20	5.78	5.17
As	97.9	76.7	145	2.67	168	251	250	218
Y	3.78	4.17	5.21	0.06	7.76	15.7	11.9	11.0
Zr	27.6	9.68	59.7	0.36	51.2	68.2	31.2	33.4
Nb	14.7	7.98	60.2	0.29	66.0	90.2	28.3	41.6
Cd	0.18	0.10	0.32	0.0021	0.35	0.46	0.34	0.33
In	2.64	1.15	15.2	0.11	12.0	9.97	7.00	9.39
Sb	200	230	276	3.52	405	649	658	532
La	0.91	2.27	1.29	0.016	2.80	3.48	5.17	3.78
Ce	2.53	6.11	3.55	0.045	7.75	9.23	14.10	10.20
Pr	0.38	0.89	0.54	0.007	1.13	1.37	2.05	1.50
Nd	1.74	4.07	2.58	0.033	5.25	6.70	9.57	7.05
Sm	0.69	1.28	0.95	0.013	1.83	2.69	3.11	2.57
Eu	0.43	0.77	0.64	0.008	1.18	1.74	2.00	1.66
Dy	0.91	1.10	1.26	0.016	1.97	3.72	3.24	3.00
Ho	0.18	0.19	0.26	0.003	0.35	0.72	0.58	0.55
Er	0.60	0.55	0.83	0.010	1.10	2.37	1.63	1.67
Tm	0.11	0.08	0.15	0.002	0.17	0.41	0.27	0.29
Yb	0.95	0.62	1.36	0.014	1.40	3.46	2.03	2.23
Lu	0.12	0.07	0.19	0.002	0.18	0.43	0.25	0.29
Hf	0.85	0.31	1.89	0.012	1.68	2.22	0.96	1.05
Ta	0.09	0.05	0.23	0.002	0.29	0.29	0.15	0.22
W	1386	1295	2002	15	3093	2933	3236	3011
Pb	7.33	13.42	51.01	0.49	8.97	18.52	8.87	7.39
Bi	0.18	0.17	0.29	0.008	0.44	0.54	0.45	0.32
Th	0.63	0.43	0.62	0.009	0.91	1.62	2.11	2.07
U	8.27	5.75	14.48	0.11	16.7	25.8	17.9	19.2

Trace elements (ppm)	2024-TAU-06-B-circle d-cst2	2024-TAU-06-B-circle d-cst3	2024-TAU-06-B-circle d-cst4	2024-TAU-21-B-circle b-cst1	2024-TAU-21-B-circle b-cst2	2024-TAU-21-B-circle b-cst2.1	2024-TAU-21-B-circle b-cst2.2	2024-TAU-21-B-circle b-cst3
Sc	39.2	18.9	31.0	3.10	1.07	0.73	0.44	6.52
Ti	4061	2025	3686	227	75	73	33	391
V	1075	524	841	173	47.7	38.6	16.1	251
Mn	119	21.2	52.1	24.1	3.9	7.4	13.9	15.7
Co	51.2	20.9	40.4	14.1	4.07	3.39	4.07	20.0
Ni	314	127	245	86.0	22.8	20.6	8.7	121
Cu	22.9	2.13	23.3	1.79	0.05	0.12	4.79	63.4
Zn	15.6	2.56	8.33	18.4	0.62	2.14	1.59	43.1
Ga	89.4	18.5	38.8	16.2	4.37	3.32	1.25	22.8
Ge	10.65	2.31	5.60	0.23	0.11	0.06	0.05	0.30
As	439	53.0	222	3.06	0.56	0.53	23.4	4.14
Y	20.0	4.02	12.06	0.51	0.35	0.31	0.11	0.75
Zr	49.4	20.1	48.4	13.5	3.54	3.86	1.68	19.7
Nb	58.2	30.3	71.4	2.07	0.61	0.66	0.29	2.95
Cd	0.63	0.24	0.42	0.12	0.04	0.03	0.02	0.30
In	7.43	10.1	11.2	42.4	11.3	8.93	3.26	58.6
Sb	1239	235	660	184	46.2	38.4	17.4	252
La	8.04	1.22	2.84	0.25	0.53	0.46	0.14	0.40
Ce	21.79	3.28	7.65	0.56	1.22	1.05	0.28	0.83
Pr	3.26	0.50	1.16	0.07	0.13	0.11	0.03	0.10
Nd	15.29	2.27	5.50	0.30	0.57	0.49	0.13	0.42
Sm	5.23	0.87	2.27	0.06	0.09	0.08	0.019	0.10
Eu	3.38	0.59	1.48	0.03	0.05	0.04	0.012	0.04
Dy	5.53	1.06	3.07	0.06	0.05	0.05	0.02	0.10
Ho	1.02	0.21	0.57	0.018	0.013	0.011	0.004	0.03
Er	2.96	0.65	1.85	0.073	0.042	0.038	0.013	0.11
Tm	0.49	0.12	0.33	0.015	0.008	0.006	0.003	0.02
Yb	3.62	1.00	2.90	0.28	0.09	0.07	0.03	0.39
Lu	0.43	0.14	0.42	0.08	0.02	0.02	0.01	0.11
Hf	1.75	0.61	1.50	0.40	0.10	0.11	0.05	0.55
Ta	0.33	0.09	0.25	0.066	0.017	0.02	0.009	0.082
W	5807	1835	2902	184	66.1	58.8	20.0	249
Pb	29.7	3.79	25.3	14.1	1.70	2.47	131	19.8
Bi	0.75	0.09	0.47	0.13	0.01	0.00	1.70	0.21
Th	3.75	0.76	2.11	1.50	0.30	0.26	0.16	2.22
U	32.3	12.7	24.8	3.32	0.87	0.71	0.27	4.55

Trace elements (ppm)	2024-TAU-21-B-circle b-cst3.1	2024-TAU-21-B-circle b-cst4	2024-TAU-21-B-circle c-cst1	2024-TAU-21-B-circle c-cst2	2024-TAU-21-B-circle d-cst1	2024-TAU-21-B-circle d-cst2	2024-TAU-21-B-circle d-cst3	2024-TAU-21-B-circle d-cst4
Sc	4.94	0.37	0.91	0.64	0.64	1.02	0.89	0.23
Ti	265	33	62	50	45	55	47	13
V	143	24.9	27.1	37.6	43.8	47.7	40.1	9.5
Mn	18.3	3.8	3.0	4.0	2.6	2.9	2.9	3.7
Co	11.2	2.77	2.16	3.45	3.78	3.93	3.28	0.85
Ni	67.8	14.1	13.2	21.0	22.8	23.9	19.8	5.2
Cu	0.93	0.02	0.03	0.03	0.05	0.05	0.04	0.01
Zn	10.8	0.26	0.16	0.19	0.31	0.20	0.17	0.05
Ga	12.5	2.57	2.21	3.81	4.47	4.85	4.05	0.98
Ge	0.08	0.08	0.05	0.11	0.08	0.09	0.08	0.04
As	3.11	0.35	0.47	0.63	0.76	0.63	0.46	0.08
Y	0.48	0.31	0.34	0.35	0.18	0.22	0.32	0.52
Zr	12.7	1.79	2.71	3.05	2.92	3.20	2.39	0.74
Nb	2.43	0.22	0.53	0.45	0.48	0.56	0.43	0.10
Cd	0.13	0.02	0.02	0.03	0.04	0.03	0.03	0.01
In	31.5	6.84	5.37	9.97	11.9	12.6	10.4	2.52
Sb	137	29.8	24.0	43.8	49.8	51.7	43.4	10.0
La	0.23	0.46	0.49	0.59	0.11	0.36	0.59	0.78
Ce	0.50	1.16	1.12	1.39	0.27	0.74	1.36	1.98
Pr	0.06	0.13	0.12	0.15	0.03	0.09	0.15	0.23
Nd	0.247	0.552	0.540	0.63	0.14	0.36	0.64	1.03
Sm	0.05	0.09	0.09	0.10	0.03	0.05	0.09	0.17
Eu	0.03	0.05	0.05	0.05	0.01	0.02	0.05	0.08
Dy	0.06	0.05	0.06	0.05	0.02	0.03	0.04	0.07
Ho	0.02	0.01	0.01	0.01	0.01	0.01	0.01	0.02
Er	0.08	0.03	0.04	0.04	0.02	0.03	0.04	0.05
Tm	0.02	0.01	0.01	0.01	0.01	0.01	0.01	0.01
Yb	0.25	0.05	0.06	0.07	0.08	0.08	0.08	0.04
Lu	0.07	0.01	0.02	0.02	0.02	0.03	0.02	0.01
Hf	0.36	0.05	0.08	0.09	0.08	0.09	0.07	0.02
Ta	0.07	0.01	0.02	0.01	0.01	0.01	0.01	0.003
W	155	48	113	120	49	103	102	92.5
Pb	16.2	2.6	0.39	1.98	0.12	0.16	0.15	0.03
Bi	0.13	0.00	0.00	0.00	0.00	0.00	0.00	0.00
Th	1.76	0.09	0.33	0.25	0.35	0.39	0.35	0.03
U	2.65	0.49	0.46	0.74	0.90	0.96	0.79	0.17

Trace element (ppm)	2024-TAU-21-B-circle e-cst1	2024-TAU-21-B-circle e-cst1.1	2024-TAU-21-B-circle e-cst1.2	2024-TAU-21-B-circle e-cst2	2024-TAU-21-B-circle e-cst2.1	2024-TAU-21-B-circle e-cst3	2024-TAU-21-B-circle e-cst4	2024-TAU-21-B-circle e-cst4.1
Sc	1.03	1.18	1.68	0.45	0.96	2.98	1.51	0.85
Ti	142	156	236	46.7	72.4	150	123	60.4
V	60.5	35.0	70.3	43.6	65.9	92.9	102	70.3
Mn	5.9	12.3	25.0	11.2	14.1	20.9	12.7	7.4
Co	4.72	3.65	4.95	4.29	5.57	6.43	8.51	6.25
Ni	26.7	15.2	28.9	24.9	33.9	38.6	51.1	36.9
Cu	0.09	0.26	0.11	3014	1.19	0.64	9.81	3223
Zn	0.41	0.46	1.29	66.7	2.33	5.56	9.23	66.5
Ga	5.22	2.38	5.57	4.59	6.56	7.70	10.0	7.68
Ge	0.16	0.08	0.10	0.18	0.10	0.09	0.11	0.20
As	0.93	32.8	1.40	0.61	0.93	1.72	1.42	0.81
Y	0.60	0.71	0.92	0.15	0.26	0.41	0.36	0.18
Zr	4.33	3.41	4.57	2.80	4.44	6.17	6.61	3.63
Nb	0.90	0.72	1.07	0.42	0.81	1.18	1.16	0.48
Cd	0.04	0.03	0.06	0.85	0.07	0.08	0.11	0.75
In	12.9	5.74	13.6	13.7	17.4	18.3	26.5	20.8
Sb	55.4	29.3	58.1	68.5	77.1	75.4	119	111
La	0.67	0.73	0.75	0.08	0.13	0.21	0.19	0.09
Ce	1.62	1.86	1.55	0.18	0.29	0.46	0.41	0.18
Pr	0.17	0.21	0.19	0.02	0.03	0.06	0.05	0.02
Nd	0.71	0.84	0.71	0.09	0.15	0.24	0.22	0.09
Sm	0.12	0.14	0.12	0.02	0.02	0.04	0.03	0.02
Eu	0.06	0.07	0.06	0.01	0.01	0.02	0.02	0.01
Dy	0.11	0.13	0.16	0.02	0.03	0.06	0.05	0.02
Ho	0.03	0.03	0.04	0.005	0.01	0.02	0.01	0.01
Er	0.10	0.11	0.17	0.02	0.04	0.06	0.06	0.03
Tm	0.02	0.02	0.02	0.004	0.01	0.01	0.01	0.01
Yb	0.16	0.13	0.22	0.07	0.11	0.16	0.18	0.12
Lu	0.04	0.02	0.05	0.02	0.03	0.04	0.05	0.03
Hf	0.14	0.10	0.14	0.08	0.12	0.18	0.19	0.10
Ta	0.02	0.02	0.03	0.01	0.02	0.03	0.03	0.01
W	88.6	68.2	93.9	34.2	72.6	96.0	109	67.0
Pb	4.88	12.66	19.72	4.65	3.18	9.20	3.10	3.85
Bi	0.00	0.08	0.00	0.32	0.01	0.02	0.05	0.33
Th	0.68	0.56	0.89	0.13	0.54	1.06	0.80	0.38
U	1.11	0.58	1.21	0.88	1.33	1.51	2.03	1.44

Trace element (ppm)	2024-TAU-21-C-circle a-cst1	2024-TAU-21-C-circle a-cst3	2024-TAU-21-C-circle a-cst4	2024-TAU-21-C-circle a-cst5	2024-TAU-21-C-circle b-cst2	2024-TAU-21-C-circle b-cst3	2024-TAU-21-C-circle b-cst3.1	2024-TAU-21-C-circle c-cst1
Sc	3.30	0.42	0.08	0.20	1.14	0.22	0.55	0.38
Ti	241	46.9	10.2	27.1	153	43.6	85.1	28.3
V	146	28.8	6.0	13.8	68.2	21.7	47.9	15.8
Mn	7.8	4.5	6.6	4.1	5.3	1.2	5.8	15.8
Co	11.7	3.42	0.56	1.30	8.56	3.61	4.35	1.62
Ni	72.6	16.0	3.2	7.9	34.8	13.7	26.0	9.7
Cu	1.64	0.06	0.01	0.04	0.25	0.98	0.62	0.09
Zn	16.5	0.40	0.20	0.32	1.50	1.14	2.33	0.28
Ga	10.7	2.40	0.44	1.11	3.51	1.64	3.65	1.56
Ge	0.13	0.07	0.02	0.05	0.09	0.05	0.09	0.06
As	2.22	10.7	0.13	0.32	15.9	10.35	1.60	0.50
Y	0.39	0.22	0.05	0.22	0.14	0.05	0.11	0.23
Zr	12.7	2.22	0.48	1.21	8.23	2.28	4.58	2.02
Nb	2.44	0.39	0.08	0.12	1.69	0.45	0.83	0.18
Cd	0.13	0.02	0.01	0.01	0.06	0.02	0.04	0.02
In	28.9	5.84	1.05	2.24	9.18	4.25	9.21	3.92
Sb	129	30.4	5.3	10.9	46.2	21.3	43.8	17.9
La	0.31	0.19	0.05	0.16	0.09	0.04	0.13	0.30
Ce	0.62	0.43	0.14	0.40	0.19	0.08	0.28	0.67
Pr	0.07	0.05	0.02	0.05	0.03	0.01	0.03	0.07
Nd	0.30	0.22	0.08	0.22	0.10	0.04	0.13	0.29
Sm	0.05	0.04	0.02	0.05	0.02	0.01	0.02	0.05
Eu	0.03	0.04	0.01	0.04	0.02	0.01	0.02	0.05
Dy	0.05	0.03	0.01	0.03	0.02	0.005	0.01	0.03
Ho	0.01	0.01	0.002	0.01	0.00	0.001	0.003	0.01
Er	0.05	0.02	0.01	0.02	0.02	0.01	0.01	0.03
Tm	0.01	0.00	0.001	0.003	0.005	0.002	0.003	0.004
Yb	0.18	0.06	0.01	0.03	0.07	0.02	0.05	0.05
Lu	0.05	0.01	0.00	0.01	0.02	0.01	0.02	0.01
Hf	0.36	0.06	0.01	0.03	0.27	0.07	0.15	0.07
Ta	0.05	0.01	0.001	0.002	0.04	0.01	0.02	0.01
W	129	57.4	9.7	33.6	54.2	21.3	53.1	13.7
Pb	5.84	1.91	0.10	0.38	23.1	13.2	66.1	0.12
Bi	0.07	0.10	0.005	0.002	0.48	0.20	0.22	0.001
Th	0.58	0.11	0.01	0.01	0.29	0.05	0.10	0.04
U	2.26	0.46	0.08	0.17	0.80	0.33	0.70	0.30

Trace element (ppm)	2024-TAU-21-C-circle c-cst2	2024-TAU-21-C-circle d-cst1	2024-TAU-21-C-circle d-cst2	2024-TAU-21-D-circle a-cst1	2024-TAU-21-D-circle a-cst2	2024-TAU-21-D-circle a-cst3	2024-TAU-21-D-circle a-cst4	2024-TAU-21-D-circle a-cst5
Sc	0.70	0.29	0.20	0.17	0.53	0.13	1.87	2.54
Ti	50.4	30.2	27.3	20.3	69.8	21.0	220	190
V	27.0	19.1	17.6	12.7	38.6	9.8	144	103
Mn	26.9	0.84	1.04	0.70	2.07	0.51	9.52	6.92
Co	2.74	1.65	2.21	1.98	4.35	2.08	13.9	9.22
Ni	16.6	9.9	9.5	7.1	22.9	6.2	82.0	54.2
Cu	2.92	0.01	0.10	0.01	0.04	0.02	0.22	0.12
Zn	0.86	0.15	0.18	0.16	0.25	0.25	2.55	1.49
Ga	2.78	1.63	1.45	1.07	3.43	0.68	13.21	8.94
Ge	0.09	0.06	0.06	0.04	0.08	0.05	0.24	0.14
As	0.57	0.50	17.9	1.18	2.63	1.36	1.46	1.15
Y	0.39	0.17	0.18	0.02	0.08	0.02	0.26	0.18
Zr	3.14	1.34	1.17	0.93	3.00	0.94	10.25	7.92
Nb	0.15	0.27	0.22	0.15	0.67	0.12	2.12	1.53
Cd	0.03	0.02	0.02	0.01	0.03	0.01	0.13	0.09
In	6.48	4.30	3.78	2.67	8.84	1.80	33.7	23.2
Sb	30.9	23.2	23.7	12.7	42.2	9.9	153	102
La	0.60	0.15	0.13	0.01	0.05	0.02	0.18	0.11
Ce	1.11	0.38	0.33	0.03	0.11	0.03	0.36	0.23
Pr	0.12	0.05	0.04	0.00	0.01	0.004	0.04	0.03
Nd	0.49	0.21	0.19	0.01	0.04	0.02	0.18	0.11
Sm	0.08	0.05	0.05	0.002	0.01	0.003	0.04	0.03
Eu	0.14	0.05	0.05	0.002	0.01	0.002	0.03	0.02
Dy	0.06	0.03	0.03	0.003	0.01	0.003	0.04	0.02
Ho	0.01	0.01	0.01	0.001	0.00	0.001	0.01	0.01
Er	0.05	0.02	0.02	0.003	0.01	0.002	0.04	0.03
Tm	0.01	0.004	0.004	0.001	0.004	0.001	0.01	0.01
Yb	0.08	0.04	0.04	0.01	0.06	0.01	0.19	0.13
Lu	0.02	0.01	0.01	0.004	0.02	0.003	0.06	0.04
Hf	0.10	0.04	0.04	0.03	0.10	0.03	0.35	0.27
Ta	0.01	0.01	0.00	0.003	0.01	0.002	0.04	0.04
W	15.4	30.4	27.5	9.05	45.9	5.74	124	89.6
Pb	0.25	0.71	10.30	0.58	0.98	4.64	2.69	8.61
Bi	0.002	0.000	0.07	0.004	0.01	0.003	0.01	0.002
Th	0.04	0.04	0.04	0.03	0.19	0.02	0.47	0.43
U	0.47	0.31	0.28	0.20	0.71	0.13	2.52	1.76

Trace element (ppm)	2024-TAU-21-D-circle a-cst5.1	2024-TAU-21-D-circle b-cst1	2024-TAU-21-D-circle b-cst1.1	2024-TAU-21-D-circle b-cst1.2	2024-TAU-21-D-circle b-cst2	2024-TAU-21-D-circle b-cst2.1	2024-TAU-21-D-circle b-cst2.2	2024-TAU-21-D-circle b-cst3
Sc	2.16	3.36	2.95	3.24	3.58	5.02	3.02	1.87
Ti	236	238	211	235	251	318	219	141
V	129	201	215	206	178	193	175	157
Mn	9.00	11.8	13.5	10.7	9.55	9.32	9.49	12.4
Co	12.1	14.3	16.1	14.2	12.1	13.3	12.1	12.5
Ni	69.5	85.6	97.7	84.9	73.7	80.0	72.5	74.9
Cu	0.36	0.26	0.26	0.31	0.33	0.36	0.42	0.63
Zn	5.73	3.39	4.71	4.43	2.80	2.58	2.15	9.85
Ga	10.4	18.2	19.1	19.7	15.7	17.9	16.8	14.6
Ge	0.19	0.28	0.21	0.25	0.23	0.18	0.21	0.16
As	1.41	2.75	2.73	2.47	1.95	2.12	2.28	3.03
Y	0.25	0.39	0.43	0.37	0.32	0.35	0.32	0.37
Zr	9.99	7.90	8.47	6.55	7.52	8.61	6.44	6.26
Nb	1.89	2.32	2.50	1.79	1.95	1.99	1.75	2.02
Cd	0.13	0.15	0.18	0.15	0.12	0.14	0.11	0.15
In	27.1	35.5	40.0	38.2	31.0	36.4	33.1	30.5
Sb	121	172	191	181	140	168	150	160
La	0.16	0.24	0.28	0.20	0.19	0.18	0.20	0.20
Ce	0.34	0.48	0.58	0.40	0.41	0.38	0.42	0.41
Pr	0.04	0.06	0.07	0.05	0.05	0.05	0.05	0.05
Nd	0.18	0.23	0.29	0.21	0.20	0.19	0.21	0.21
Sm	0.04	0.05	0.05	0.05	0.04	0.04	0.05	0.04
Eu	0.02	0.04	0.04	0.03	0.03	0.03	0.03	0.03
Dy	0.03	0.06	0.05	0.05	0.04	0.04	0.04	0.05
Ho	0.01	0.02	0.01	0.01	0.01	0.01	0.01	0.01
Er	0.03	0.07	0.07	0.06	0.05	0.06	0.05	0.06
Tm	0.01	0.02	0.02	0.02	0.02	0.02	0.02	0.02
Yb	0.17	0.29	0.30	0.31	0.26	0.28	0.25	0.25
Lu	0.05	0.09	0.10	0.09	0.08	0.08	0.08	0.08
Hf	0.34	0.22	0.23	0.18	0.22	0.25	0.20	0.17
Ta	0.04	0.03	0.03	0.02	0.03	0.04	0.02	0.02
W	106	194	193	191	147	174	150	177
Pb	6.46	4.15	5.17	4.77	4.77	3.90	3.00	7.47
Bi	0.008	0.006	0.005	0.011	0.006	0.005	0.004	0.04
Th	0.48	1.69	1.39	1.56	1.23	1.59	1.18	1.39
U	2.11	3.13	3.43	3.21	2.62	3.04	2.72	2.73

Trace element (ppm)	2024-TAU-21-D-circle b-cst3.1	2024-TAU-21-D-circle b-cst3.2	2024-TAU-21-D-circle b-cst4	2024-TAU-21-D-circle b-cst4.1	2024-TAU-21-D-circle b-cst5	2024-TAU-21-D-circle c-cst1	2024-TAU-21-D-circle c-cst1.1	2024-TAU-21-D-circle c-cst1.2
Sc	1.61	2.93	3.07	1.63	1.11	1.52	1.81	2.14
Ti	122	203	245	138	94.2	108	127	152
V	163	175	164	156	114	127	172	177
Mn	10.5	10.7	12.2	10.5	7.3	8.7	10.1	11.1
Co	13.1	12.0	12.9	12.1	10.4	10.3	12.8	13.1
Ni	78.0	72.4	76.9	72.4	54.3	58.2	77.8	80.0
Cu	0.21	0.34	1.69	0.83	1.14	0.14	0.21	0.26
Zn	5.20	5.20	4.46	4.36	2.47	1.13	2.25	3.02
Ga	15.4	16.1	15.7	15.0	11.2	12.0	16.5	17.2
Ge	0.28	0.26	0.14	0.19	0.22	0.20	0.23	0.23
As	1.82	2.28	4.01	2.52	19.92	2.99	1.78	2.47
Y	0.30	0.35	0.47	0.31	0.23	0.25	0.31	0.34
Zr	5.40	6.62	8.12	5.65	3.98	3.91	4.27	4.66
Nb	1.56	1.76	2.54	1.72	1.28	1.48	1.23	1.75
Cd	0.14	0.12	0.14	0.12	0.10	0.12	0.16	0.15
In	32.4	31.9	31.7	31.1	23.1	24.8	34.1	35.7
Sb	158	155	185	150	119	124	167	177
La	0.19	0.20	0.20	0.21	0.13	0.15	0.19	0.20
Ce	0.42	0.42	0.40	0.42	0.27	0.31	0.41	0.40
Pr	0.05	0.05	0.05	0.05	0.03	0.04	0.05	0.05
Nd	0.21	0.23	0.20	0.21	0.15	0.15	0.21	0.20
Sm	0.05	0.05	0.05	0.04	0.04	0.04	0.04	0.05
Eu	0.03	0.03	0.04	0.03	0.02	0.02	0.03	0.03
Dy	0.05	0.05	0.06	0.03	0.03	0.03	0.04	0.05
Ho	0.01	0.01	0.02	0.01	0.01	0.01	0.01	0.01
Er	0.05	0.06	0.08	0.05	0.04	0.04	0.05	0.06
Tm	0.01	0.02	0.02	0.01	0.01	0.01	0.01	0.02
Yb	0.22	0.27	0.33	0.24	0.18	0.19	0.26	0.29
Lu	0.07	0.09	0.10	0.07	0.05	0.06	0.07	0.09
Hf	0.16	0.20	0.25	0.19	0.11	0.09	0.11	0.12
Ta	0.01	0.03	0.05	0.02	0.01	0.01	0.01	0.01
W	133	170	262	143	117	122	131	188
Pb	6.13	6.00	27.34	179.16	16.73	10.77	3.98	4.39
Bi	0.00	0.01	0.08	0.54	0.12	0.01	0.00	0.01
Th	0.68	1.49	3.01	0.90	0.75	0.79	0.65	1.36
U	2.75	2.89	3.31	2.71	2.04	2.19	2.90	3.14

Trace element (ppm)	2024-TAU-21-D-circle c-cst2	2024-TAU-21-D-circle c-cst2.1	2024-TAU-21-D-circle c-cst3	2024-TAU-21-D-circle c-cst3.1	2024-TAU-21-D-circle c-cst4	2024-TAU-21-D-circle c-cst4.1	2024-TAU-21-D-circle c-cst4.2	2024-TAU-21-D-circle c-cst5
Sc	1.88	2.00	2.17	1.80	0.16	0.10	0.10	0.15
Ti	132	144	155	127	12.4	8.66	10.0	12.3
V	186	194	177	167	16.6	8.7	8.2	14.4
Mn	11.8	11.4	12.8	10.3	42.7	106	56.8	57.9
Co	14.8	14.9	13.6	12.8	1.55	0.91	0.94	1.45
Ni	88.8	89.8	81.4	77.7	9.21	5.42	5.65	8.29
Cu	0.34	0.23	0.28	0.19	0.02	b.d.l.	0.00	0.02
Zn	2.67	2.66	2.91	2.30	0.35	0.09	0.07	0.23
Ga	18.5	19.4	16.1	16.4	1.83	0.90	0.83	1.42
Ge	0.24	0.24	0.20	0.24	0.06	0.04	0.03	0.03
As	2.25	2.19	3.01	2.68	0.17	0.07	0.07	0.26
Y	0.33	0.31	0.38	0.30	0.14	0.15	0.14	0.13
Zr	4.81	4.71	5.55	4.38	0.40	0.28	0.30	0.44
Nb	1.42	1.60	2.08	1.52	0.07	0.04	0.04	0.13
Cd	0.19	0.19	0.14	0.15	0.02	0.01	0.01	0.02
In	37.4	39.8	34.4	33.6	3.48	1.73	1.56	2.82
Sb	186	199	172	168	17.2	8.5	7.7	13.7
La	0.21	0.20	0.24	0.19	0.31	0.64	0.42	0.39
Ce	0.45	0.39	0.49	0.39	0.74	1.29	0.94	0.87
Pr	0.06	0.05	0.06	0.05	0.08	0.13	0.10	0.09
Nd	0.23	0.21	0.25	0.20	0.32	0.52	0.38	0.37
Sm	0.05	0.04	0.05	0.05	0.05	0.07	0.05	0.05
Eu	0.03	0.03	0.03	0.03	0.04	0.04	0.04	0.04
Dy	0.05	0.05	0.06	0.04	0.02	0.02	0.02	0.02
Ho	0.012	0.011	0.012	0.011	0.005	0.005	0.004	0.004
Er	0.06	0.05	0.06	0.04	0.014	0.014	0.012	0.014
Tm	0.018	0.016	0.018	0.015	0.0024	0.0018	0.0018	0.0022
Yb	0.27	0.28	0.28	0.24	0.03	0.02	0.02	0.03
Lu	0.09	0.09	0.09	0.08	0.008	0.004	0.004	0.007
Hf	0.11	0.12	0.13	0.10	0.008	0.005	0.006	0.010
Ta	0.01	0.01	0.01	0.01	0.00	0.0003	0.0003	0.0008
W	160	177	170	150	19.0	11.2	13.2	16.7
Pb	4.32	4.02	4.11	3.00	1.30	0.52	0.70	1.25
Bi	0.010	0.007	0.008	0.006	0.0011	0.0007	0.0009	0.0012
Th	0.78	0.92	1.16	0.84	0.05	0.02	0.02	0.06
U	3.29	3.40	3.09	2.95	0.30	0.14	0.13	0.23

Trace element (ppm)	2024-TAU-21-D-circle c-cst5.1	2024-TAU-21-D-circle d-cst1	2024-TAU-21-D-circle d-cst1.1	2024-TAU-21-D-circle d-cst1.2	2024-TAU-21-D-circle d-cst2	2024-TAU-21-D-circle d-cst3	2024-TAU-21-D-circle d-cst3.1	2024-TAU-21-D-circle e-cst1.1
Sc	0.08	0.35	1.34	0.35	2.41	0.44	1.88	3.43
Ti	6.97	29.5	111	30.3	172	32.9	115	244
V	8.0	34.9	130	36.3	165	31.5	54.3	167
Mn	35.7	2.71	9.50	4.11	9.91	3.55	4.2	9.2
Co	0.83	4.39	10.5	3.99	12.3	2.37	3.57	13.0
Ni	4.83	21.5	61.5	20.8	72.1	13.9	21.2	77.4
Cu	0.01	15220	1.14	9187	0.36	0.07	0.17	0.69
Zn	0.24	275	5.65	164	4.50	1.49	2.71	10.43
Ga	0.82	3.48	11.23	3.76	14.12	2.68	4.43	13.9
Ge	0.03	0.44	0.17	0.32	0.13	0.04	0.04	0.14
As	0.11	0.50	1.40	0.60	2.10	0.40	0.96	2.92
Y	0.11	0.06	0.25	0.09	0.31	0.07	0.12	0.35
Zr	0.21	0.86	3.40	0.92	4.76	0.95	2.33	9.62
Nb	0.04	0.23	1.40	0.29	1.71	0.37	0.75	2.38
Cd	0.01	3.19	0.15	2.09	0.14	0.03	0.04	0.19
In	1.54	13.23	22.85	12.11	28.56	5.42	7.92	33.4
Sb	7.5	102	115	84.6	145	27.0	42.4	153
La	0.25	0.03	0.12	0.04	0.13	0.03	0.05	0.22
Ce	0.61	0.06	0.27	0.08	0.29	0.07	0.10	0.44
Pr	0.06	0.01	0.03	0.01	0.04	0.01	0.01	0.05
Nd	0.27	0.03	0.14	0.04	0.15	0.04	0.05	0.22
Sm	0.04	0.009	0.03	0.012	0.03	0.01	0.01	0.05
Eu	0.032	0.006	0.02	0.009	0.03	0.01	0.01	0.03
Dy	0.018	0.007	0.03	0.010	0.04	0.01	0.02	0.04
Ho	0.004	0.002	0.01	0.003	0.01	0.002	0.004	0.013
Er	0.011	0.01	0.04	0.01	0.05	0.01	0.02	0.06
Tm	0.002	0.002	0.01	0.003	0.02	0.002	0.01	0.02
Yb	0.017	0.04	0.15	0.05	0.23	0.05	0.09	0.24
Lu	0.004	0.01	0.05	0.02	0.07	0.01	0.03	0.07
Hf	0.005	0.02	0.06	0.02	0.11	0.02	0.07	0.28
Ta	0.0003	0.001	0.011	0.002	0.02	0.004	0.02	0.03
W	11.2	30.1	100	33.9	159	28.3	61.4	156
Pb	2.43	11.38	1.38	7.84	1.70	0.76	0.86	7.61
Bi	0.0032	1.04	0.004	0.60	0.01	0.001	0.01	0.03
Th	0.02	0.11	0.47	0.15	1.17	0.18	0.79	1.04
U	0.12	0.53	1.86	0.67	2.54	0.48	0.79	2.77

Trace element (ppm)	2024-TAU-21-D-circle e-cst2	2024-TAU-21-D-circle e-cst2.1	2024-TAU-21-D-circle e-cst3	2024-TAU-21-D-circle e-cst4	2024-TAU-21-D-circle e-cst4.1	2024-TAU-21-D-circle e-cst4.2	2024-TAU-21-D-circle e-cst5	2024-TAU-21-D-circle e-cst6
Sc	1.60	3.26	1.91	2.36	3.98	4.91	1.82	2.30
Ti	144	229	155	198	271	313	157	181
V	149	158	161	184	197	187	154	143
Mn	8.7	9.0	8.7	11.1	10.5	11.2	8.1	7.7
Co	12.3	12.4	12.8	15.2	15.1	14.7	12.7	11.1
Ni	73.0	75.1	77.0	90.5	90.8	88.9	76.1	67.8
Cu	0.48	0.50	0.45	0.41	0.44	7.90	0.81	0.32
Zn	6.35	6.75	4.60	3.22	4.94	2.56	4.39	1.46
Ga	14.2	13.5	16.2	17.8	17.8	16.7	13.9	12.6
Ge	0.21	0.17	0.21	0.27	0.29	0.23	0.22	0.21
As	2.69	2.60	2.66	2.32	2.60	2.59	3.25	3.00
Y	0.32	0.33	0.32	0.39	0.39	0.42	0.26	0.30
Zr	6.08	9.11	6.13	7.88	9.48	10.95	6.94	7.06
Nb	1.65	2.34	1.46	2.13	2.31	2.98	1.58	1.91
Cd	0.17	0.16	0.17	0.18	0.20	0.17	0.16	0.13
In	31.9	32.6	34.3	40.8	41.9	42.3	31.6	29.0
Sb	152	149	164	186	190	191	148	136
La	0.17	0.20	0.17	0.23	0.25	0.25	0.14	0.17
Ce	0.33	0.40	0.35	0.47	0.50	0.52	0.28	0.35
Pr	0.04	0.05	0.04	0.06	0.06	0.06	0.03	0.04
Nd	0.18	0.19	0.18	0.23	0.27	0.25	0.13	0.16
Sm	0.03	0.04	0.03	0.05	0.06	0.05	0.03	0.04
Eu	0.03	0.02	0.02	0.03	0.03	0.03	0.02	0.02
Dy	0.04	0.04	0.03	0.05	0.06	0.04	0.03	0.04
Ho	0.01	0.01	0.01	0.01	0.01	0.01	0.01	0.01
Er	0.05	0.05	0.05	0.05	0.06	0.07	0.03	0.05
Tm	0.01	0.01	0.01	0.02	0.02	0.02	0.01	0.01
Yb	0.25	0.25	0.25	0.29	0.30	0.29	0.19	0.22
Lu	0.07	0.07	0.08	0.08	0.09	0.08	0.06	0.06
Hf	0.16	0.25	0.17	0.23	0.27	0.30	0.18	0.19
Ta	0.01	0.03	0.02	0.02	0.03	0.04	0.02	0.02
W	156	156	172	174	164	177	135	137
Pb	4.79	4.49	3.81	1.83	2.11	1.87	4.97	1.10
Bi	0.02	0.02	0.02	0.01	0.02	0.01	0.04	0.01
Th	1.14	1.08	1.06	0.96	1.02	1.25	0.66	0.88
U	2.67	2.72	2.87	3.28	3.30	3.38	2.52	2.37

Trace element (ppm)	2024-TAU-21-D-circle e-cst7	2024-TAU-21-D-circle f-cst1	2024-TAU-21-D-circle f-cst1.1	2024-TAU-21-D-circle f-cst1.2	2024-TAU-21-D-circle f-cst1.3	2024-TAU-21-D-circle f-cst1.4	2024-TAU-21-D-circle f-cst2	2024-TAU-21-D-circle f-cst2.1
Sc	1.98	2.81	3.50	4.45	3.77	3.05	3.91	3.32
Ti	146	166	197	234	209	178	226	196
V	101	176	182	195	197	193	202	205
Mn	5.6	12.5	11.6	12.0	12.2	11.2	12.0	12.6
Co	7.87	12.8	12.4	12.9	13.0	13.1	13.1	13.5
Ni	46.5	77.9	75.3	77.3	78.8	79.0	78.8	81.9
Cu	0.33	0.20	0.24	0.19	0.21	0.16	0.24	0.31
Zn	1.44	1.70	1.91	2.01	2.38	2.24	4.90	6.91
Ga	7.86	16.22	17.0	18.3	18.9	19.0	19.4	20.1
Ge	0.12	0.18	0.21	0.24	0.22	0.22	0.25	0.24
As	2.98	3.32	2.77	2.66	2.66	2.51	2.52	2.47
Y	0.20	0.49	0.45	0.49	0.51	0.44	0.54	0.52
Zr	5.66	3.83	3.94	4.46	4.02	3.40	3.79	3.28
Nb	1.42	1.47	1.46	1.38	1.40	1.14	1.36	1.17
Cd	0.09	0.15	0.17	0.15	0.16	0.16	0.16	0.16
In	18.9	34.4	33.3	34.5	37.4	38.3	36.8	38.4
Sb	85.3	163	160	167	180	186	176	184
La	0.13	0.25	0.22	0.23	0.24	0.20	0.24	0.23
Ce	0.25	0.54	0.47	0.51	0.55	0.46	0.54	0.53
Pr	0.03	0.07	0.06	0.06	0.07	0.06	0.07	0.07
Nd	0.13	0.28	0.26	0.26	0.28	0.25	0.29	0.29
Sm	0.03	0.07	0.06	0.06	0.06	0.06	0.07	0.06
Eu	0.02	0.03	0.03	0.03	0.04	0.03	0.04	0.03
Dy	0.03	0.08	0.05	0.06	0.06	0.06	0.07	0.07
Ho	0.01	0.02	0.01	0.02	0.02	0.02	0.02	0.02
Er	0.04	0.08	0.06	0.08	0.08	0.06	0.08	0.09
Tm	0.01	0.02	0.02	0.02	0.02	0.02	0.02	0.02
Yb	0.13	0.29	0.29	0.30	0.33	0.31	0.34	0.34
Lu	0.04	0.09	0.09	0.09	0.10	0.09	0.10	0.10
Hf	0.15	0.08	0.09	0.11	0.10	0.07	0.09	0.07
Ta	0.02	0.02	0.02	0.03	0.03	0.02	0.02	0.02
W	81.5	161	169	184	192	187	204	195
Pb	1.73	0.91	0.73	0.84	1.19	1.41	1.42	1.61
Bi	0.009	0.007	0.005	0.005	0.005	0.006	0.005	0.005
Th	0.52	1.10	1.34	1.54	1.70	1.35	1.81	1.53
U	1.54	2.92	2.86	2.99	3.37	3.32	3.29	3.36

Trace element (ppm)	2024-TAU-21-D-circle f-cst2.2	2024-TAU-21-D-circle f-cst2.3	2024-TAU-21-D-circle f-cst2.4	2024-TAU-21-D-circle f-cst2.5	2024-TAU-21-D-circle f-cst3	2024-TAU-21-D-circle f-cst3.1	2024-TAU-21-D-circle f-cst3.2	2024-TAU-21-D-circle f-cst3.3
Sc	3.16	3.31	3.33	5.05	3.51	3.39	2.04	2.02
Ti	198	206	202	283	204	203	133	136
V	199	196	202	208	209	204	182	189
Mn	14.5	13.6	13.0	14.3	12.2	13.2	11.0	13.4
Co	13.7	13.2	13.3	13.3	13.9	13.8	13.3	14.1
Ni	83.7	80.6	81.2	81.1	84.0	83.5	81.0	85.4
Cu	0.23	0.24	0.18	0.19	0.19	0.23	0.12	0.25
Zn	8.14	7.25	5.44	3.41	3.06	3.63	2.40	3.18
Ga	19.4	19.0	19.7	20.2	20.1	19.2	18.1	18.5
Ge	0.28	0.24	0.24	0.22	0.24	0.22	0.31	0.21
As	3.17	3.00	2.42	2.79	2.17	2.70	1.89	2.17
Y	0.58	0.56	0.54	0.58	0.51	0.56	0.43	0.52
Zr	3.65	3.80	3.46	4.34	3.68	3.92	2.90	3.24
Nb	1.57	1.64	1.24	1.44	1.11	1.45	1.04	1.40
Cd	0.17	0.17	0.18	0.17	0.14	0.17	0.18	0.17
In	38.6	36.4	37.5	36.6	38.8	36.8	37.1	39.0
Sb	191	184	180	181	182	181	179	185
La	0.26	0.25	0.25	0.248	0.237	0.254	0.201	0.276
Ce	0.57	0.55	0.56	0.552	0.528	0.574	0.467	0.592
Pr	0.07	0.07	0.07	0.070	0.063	0.070	0.057	0.078
Nd	0.32	0.30	0.32	0.275	0.297	0.305	0.239	0.329
Sm	0.06	0.06	0.07	0.052	0.061	0.065	0.055	0.065
Eu	0.04	0.04	0.03	0.036	0.033	0.039	0.031	0.037
Dy	0.07	0.07	0.07	0.078	0.068	0.073	0.052	0.069
Ho	0.02	0.02	0.02	0.019	0.018	0.019	0.014	0.017
Er	0.09	0.09	0.09	0.087	0.082	0.085	0.062	0.073
Tm	0.02	0.02	0.02	0.024	0.019	0.022	0.016	0.019
Yb	0.37	0.36	0.34	0.373	0.307	0.324	0.269	0.292
Lu	0.11	0.10	0.10	0.104	0.092	0.098	0.082	0.090
Hf	0.08	0.09	0.07	0.096	0.091	0.085	0.055	0.065
Ta	0.02	0.02	0.02	0.034	0.021	0.019	0.011	0.010
W	234	226	201	233	186	201	141	149
Pb	1.44	2.43	2.15	2.02	3.53	4.44	3.17	4.64
Bi	0.004	0.006	0.006	0.005	0.003	0.005	0.003	0.005
Th	2.29	2.21	1.65	2.38	1.32	1.77	0.74	0.86
U	3.54	3.37	3.30	3.39	3.29	3.25	3.11	3.23

Trace element (ppm)	2024-TAU-21-D-circle f-cst4	2024-TAU-21-D-circle f-cst4.1	2024-TAU-21-D-circle f-cst4.2	2024-TAU-21-D-circle g-cst1	2024-TAU-21-D-circle g-cst1.1	2024-TAU-21-D-circle g-cst1.2	2024-TAU-21-D-circle g-cst1.3	2024-TAU-21-D-circle g-cst2.1
Sc	1.68	1.64	2.98	1.02	0.52	0.82	1.80	1.06
Ti	124	124	187	72	37	55	116	78
V	190	190	199	132	64.9	93	192	102
Mn	12.7	9.9	13.2	7.1	5.9	13.3	12.6	7.2
Co	14.7	14.6	13.9	9.85	5.15	6.98	13.4	7.29
Ni	88.5	89.6	84.5	59.8	30.9	42.4	82.8	43.7
Cu	0.17	0.17	0.17	165	0.18	0.17	0.45	810
Zn	2.13	2.14	2.13	10.8	2.46	2.16	5.16	60.9
Ga	19.6	19.9	19.9	13.4	6.50	9.11	19.1	9.66
Ge	0.25	0.29	0.23	0.19	0.10	0.11	0.27	0.13
As	2.28	2.35	2.77	1.35	0.71	1.04	2.07	1.78
Y	0.46	0.36	0.48	0.19	0.13	0.22	0.33	0.21
Zr	2.79	2.76	3.33	1.86	1.06	1.54	2.98	1.62
Nb	1.08	1.15	1.30	0.58	0.35	0.62	1.09	0.72
Cd	0.19	0.19	0.16	0.17	0.07	0.08	0.17	0.87
In	40.6	41.4	39.0	25.5	12.5	17.3	37.4	21.5
Sb	204	202	191	126	60.7	87.4	189	95.8
La	0.21	0.17	0.20	0.13	0.09	0.17	0.21	0.14
Ce	0.45	0.37	0.44	0.26	0.18	0.35	0.46	0.28
Pr	0.06	0.05	0.06	0.03	0.02	0.04	0.05	0.03
Nd	0.23	0.18	0.23	0.12	0.09	0.16	0.22	0.13
Sm	0.05	0.04	0.06	0.03	0.02	0.04	0.04	0.02
Eu	0.03	0.03	0.04	0.02	0.012	0.03	0.03	0.02
Dy	0.05	0.04	0.06	0.03	0.02	0.03	0.04	0.03
Ho	0.014	0.013	0.02	0.007	0.004	0.006	0.011	0.007
Er	0.06	0.05	0.07	0.028	0.018	0.03	0.06	0.04
Tm	0.02	0.02	0.02	0.009	0.005	0.008	0.02	0.009
Yb	0.29	0.29	0.33	0.17	0.09	0.14	0.30	0.16
Lu	0.09	0.09	0.10	0.05	0.03	0.04	0.09	0.05
Hf	0.06	0.06	0.07	0.04	0.02	0.03	0.07	0.03
Ta	0.007	0.010	0.016	0.002	0.001	0.003	0.007	0.005
W	187	177	223	112	55.9	88.8	187	105
Pb	3.21	2.78	2.77	4.32	2.64	2.23	3.61	7.36
Bi	0.006	0.011	0.008	0.008	0.004	0.004	0.012	0.18
Th	1.10	0.96	1.80	0.43	0.21	0.46	0.95	0.75
U	3.45	3.44	3.38	2.20	1.08	1.52	3.38	1.66

Trace element (ppm)	2024-TAU-21-D-circle g-cst3	2024-TAU-21-D-circle g-cst3.1	2024-TAU-21-D-circle g-cst3.2	2024-TAU-21-D-circle g-cst3.3	2024-TAU-21-D-circle g-cst3.4	2024-TAU-21-D-circle g-cst3.5	2024-TAU-21-D-circle g-cst4	2024-TAU-21-D-circle g-cst4.1
Sc	1.35	1.85	1.49	2.13	2.67	3.01	2.69	2.19
Ti	90	120	96	141	171	193	175	150
V	115	153	103	180	209	240	238	227
Mn	12.4	14.3	13.5	13.3	16.1	16.2	14.8	12.3
Co	8.04	10.9	7.49	12.60	14.6	16.7	17.1	16.5
Ni	48.5	66.5	45.3	77.1	89.3	102	106	100
Cu	0.15	0.26	0.23	0.38	0.84	0.85	0.58	0.89
Zn	2.39	3.48	2.43	5.10	7.76	6.18	5.44	12.02
Ga	10.12	13.51	8.53	15.4	17.5	21.0	21.7	21.5
Ge	0.11	0.16	0.10	0.23	0.20	0.26	0.35	0.33
As	1.19	1.95	2.01	2.00	2.55	3.11	3.27	2.81
Y	0.23	0.31	0.28	0.32	0.39	0.45	0.45	0.38
Zr	2.18	3.10	2.55	3.63	4.46	4.86	4.58	3.80
Nb	0.97	1.45	1.24	1.66	2.09	2.11	2.02	1.66
Cd	0.09	0.14	0.09	0.16	0.16	0.20	0.20	0.21
In	20.9	28.3	17.6	32.1	36.6	43.4	44.0	44.0
Sb	99.4	139	93.6	154	178	215	221	217
La	0.18	0.25	0.18	0.25	0.33	0.35	0.30	0.25
Ce	0.38	0.50	0.37	0.51	0.69	0.72	0.63	0.54
Pr	0.04	0.06	0.04	0.06	0.08	0.09	0.07	0.07
Nd	0.17	0.23	0.16	0.23	0.31	0.32	0.28	0.24
Sm	0.04	0.04	0.03	0.05	0.06	0.06	0.06	0.04
Eu	0.02	0.03	0.02	0.03	0.04	0.04	0.04	0.03
Dy	0.02	0.03	0.03	0.04	0.05	0.06	0.05	0.05
Ho	0.008	0.010	0.008	0.009	0.011	0.02	0.02	0.012
Er	0.03	0.05	0.04	0.05	0.07	0.07	0.07	0.05
Tm	0.011	0.014	0.01	0.01	0.02	0.02	0.02	0.02
Yb	0.15	0.23	0.18	0.24	0.30	0.35	0.31	0.30
Lu	0.05	0.07	0.05	0.08	0.08	0.10	0.11	0.10
Hf	0.04	0.05	0.05	0.06	0.08	0.09	0.08	0.07
Ta	0.004	0.008	0.008	0.009	0.010	0.014	0.013	0.009
W	98.7	142	126	151	181	215	235	208
Pb	1.94	2.28	1.60	2.57	4.16	4.33	6.04	5.65
Bi	0.004	0.005	0.004	0.009	0.02	0.02	0.03	0.03
Th	0.60	0.94	1.15	0.88	1.09	1.33	1.41	1.09
U	1.75	2.45	1.68	2.71	3.12	3.69	3.87	3.71

Trace element (ppm)	2024-TAU-21-D-circle g-cst4.2	2024-TAU-21-D-circle g-cst4.3	2024-TAU-21-D-circle g-cst4.4	2024-TAU-21-D-circle g-cst4.5	2024-TAU-21-D-circle h-cst1	2024-TAU-21-D-circle h-cst1.1	2024-TAU-21-D-circle h-cst1.2	2024-TAU-21-D-circle h-cst2
Sc	2.43	2.61	2.42	2.44	3.61	4.29	3.85	0.74
Ti	165	170	163	163	248	283	236	57
V	234	225	222	216	158	186	195	88.6
Mn	11.1	11.0	13.4	15.0	10.6	11.1	12.3	6.8
Co	16.6	16.1	16.5	15.5	9.80	11.5	13.0	6.72
Ni	101	97.7	101	94.6	60.1	70.0	79.1	40.9
Cu	0.79	0.98	0.53	0.51	0.15	0.22	0.18	0.09
Zn	9.51	10.93	6.76	7.15	0.92	1.99	1.30	0.43
Ga	21.1	19.8	20.0	19.9	14.4	17.7	18.5	9.0
Ge	0.33	0.30	0.26	0.26	0.17	0.21	0.20	0.13
As	2.53	2.91	3.35	2.98	1.99	2.45	3.30	3.10
Y	0.35	0.34	0.43	0.41	0.38	0.41	0.51	0.22
Zr	4.12	4.29	4.71	4.06	3.30	3.44	3.69	1.55
Nb	1.81	1.91	2.35	1.85	1.27	1.33	1.62	0.64
Cd	0.22	0.17	0.20	0.18	0.11	0.13	0.14	0.06
In	43.8	41.2	42.2	41.0	26.8	32.3	34.5	18.6
Sb	209	203	212	206	125	155	182	92
La	0.25	0.25	0.30	0.28	0.17	0.17	0.21	0.11
Ce	0.54	0.52	0.64	0.59	0.36	0.38	0.46	0.24
Pr	0.06	0.06	0.07	0.07	0.05	0.05	0.06	0.03
Nd	0.25	0.25	0.28	0.28	0.19	0.19	0.22	0.11
Sm	0.04	0.05	0.05	0.05	0.05	0.05	0.05	0.03
Eu	0.03	0.03	0.04	0.03	0.02	0.03	0.03	0.02
Dy	0.05	0.04	0.05	0.05	0.05	0.05	0.07	0.03
Ho	0.01	0.01	0.01	0.01	0.01	0.01	0.02	0.01
Er	0.06	0.06	0.07	0.07	0.06	0.07	0.08	0.03
Tm	0.02	0.02	0.02	0.02	0.02	0.02	0.02	0.010
Yb	0.30	0.30	0.34	0.32	0.24	0.31	0.35	0.15
Lu	0.10	0.09	0.10	0.10	0.07	0.09	0.10	0.04
Hf	0.08	0.08	0.08	0.08	0.07	0.07	0.07	0.03
Ta	0.01	0.01	0.01	0.01	0.02	0.02	0.02	0.003
W	186	197	233	213	151	202	251	85.0
Pb	5.41	5.45	3.89	2.98	1.42	1.14	1.04	0.26
Bi	0.018	0.027	0.017	0.014	0.004	0.008	0.007	0.002
Th	0.94	1.19	1.45	1.40	1.62	2.14	2.71	0.46
U	3.61	3.43	3.70	3.51	2.24	2.79	3.18	1.64

Trace element (ppm)	2024-TAU-21-D-circle h-cst2.1	2024-TAU-21-D-circle h-cst2.2	2024-TAU-21-D-circle h-cst2.3	2024-TAU-21-D-circle h-cst2.4	2024-TAU-21-D-circle h-cst3	2024-TAU-21-D-circle h-cst3.1	2024-TAU-21-D-circle h-cst3.2	2024-TAU-21-D-circle h-cst3.3
Sc	0.98	1.75	1.64	2.23	2.51	2.08	3.20	3.73
Ti	76	123	114	142	153	130	205	247
V	122	170	149	165	139	122	170	186
Mn	10.0	10.1	10.0	9.9	9.6	9.2	11.4	10.0
Co	9.67	12.1	10.2	11.0	9.24	7.95	11.42	11.87
Ni	59.3	74.0	62.5	68.1	56.7	48.0	69.0	72.8
Cu	0.14	0.17	0.14	0.11	0.13	0.11	0.23	0.11
Zn	0.74	1.23	0.95	0.94	0.77	0.58	1.04	1.13
Ga	12.8	16.3	14.5	15.4	13.1	11.3	16.1	18.7
Ge	0.15	0.24	0.19	0.21	0.21	0.16	0.12	0.20
As	2.88	2.09	2.10	1.83	1.90	1.46	2.58	2.33
Y	0.33	0.39	0.34	0.37	0.36	0.30	0.45	0.37
Zr	2.11	2.67	2.15	2.61	2.68	2.14	3.33	3.30
Nb	0.90	1.13	1.01	1.10	1.19	0.90	1.46	1.04
Cd	0.11	0.15	0.12	0.13	0.09	0.09	0.14	0.13
In	26.1	34.0	29.7	31.3	25.4	21.4	30.8	33.8
Sb	132	166	147	151	125	101	156	168
La	0.16	0.19	0.17	0.19	0.17	0.14	0.19	0.14
Ce	0.35	0.41	0.36	0.39	0.37	0.32	0.41	0.29
Pr	0.04	0.05	0.04	0.05	0.04	0.04	0.05	0.04
Nd	0.17	0.21	0.18	0.19	0.18	0.16	0.21	0.14
Sm	0.04	0.05	0.04	0.04	0.04	0.04	0.04	0.03
Eu	0.02	0.02	0.02	0.02	0.03	0.02	0.03	0.03
Dy	0.04	0.05	0.05	0.05	0.05	0.04	0.05	0.05
Ho	0.01	0.01	0.01	0.01	0.01	0.01	0.02	0.01
Er	0.05	0.06	0.05	0.06	0.06	0.05	0.07	0.06
Tm	0.01	0.02	0.01	0.02	0.01	0.01	0.02	0.02
Yb	0.22	0.27	0.23	0.25	0.23	0.19	0.29	0.28
Lu	0.07	0.08	0.07	0.07	0.07	0.05	0.08	0.09
Hf	0.03	0.05	0.04	0.06	0.06	0.04	0.07	0.07
Ta	0.003	0.01	0.01	0.01	0.01	0.01	0.02	0.03
W	136	145	138	144	154	113	208	210
Pb	0.47	0.53	0.45	0.48	0.53	0.38	0.78	0.85
Bi	0.002	0.005	0.003	0.003	0.005	0.003	0.006	0.003
Th	0.77	0.86	0.92	1.05	1.39	1.00	2.12	1.95
U	2.36	2.89	2.49	2.61	2.24	1.82	2.79	2.94

Trace element (ppm)	2024-TAU-21-D-circle h-cst4	2024-TAU-21-D-circle h-cst4.1	2024-TAU-21-D-circle h-cst4.2	2024-TAU-21-D-circle h-cst4.3	2024-TAU-21-D-circle h-cst4.4	2024-TAU-21-D-circle i-cst1	2024-TAU-21-D-circle i-cst2	2024-TAU-21-D-circle i-cst2.1
Sc	2.51	1.98	1.79	2.40	2.01	1.24	2.02	4.96
Ti	172	137	120	162	136	88	144	290
V	149	154	147	186	137	106	166	201
Mn	9.5	12.4	12.2	11.8	11.3	29.8	13.6	13.1
Co	9.59	10.9	10.6	13.4	9.75	8.33	11.9	13.7
Ni	58.2	66.7	64.0	82.4	59.0	43.4	72.4	84.2
Cu	0.11	0.16	0.15	0.20	0.14	130	0.62	0.39
Zn	0.81	0.98	0.97	0.94	0.84	15.4	1.62	2.19
Ga	14.7	14.6	14.3	18.4	12.9	8.90	16.7	19.6
Ge	0.21	0.15	0.20	0.16	0.17	0.15	0.21	0.27
As	1.69	1.82	1.81	2.21	1.87	13.5	2.30	3.39
Y	0.30	0.37	0.35	0.43	0.34	0.27	0.54	0.65
Zr	2.27	2.69	2.41	3.34	2.71	0.93	1.25	2.77
Nb	0.89	1.23	1.05	1.46	1.19	0.53	0.76	1.31
Cd	0.12	0.11	0.13	0.18	0.11	0.19	0.13	0.16
In	27.9	29.2	28.7	37.4	26.0	19.7	36.8	43.7
Sb	123	138	143	182	126	89.5	164	198
La	0.14	0.19	0.16	0.20	0.16	0.16	0.24	0.27
Ce	0.31	0.40	0.35	0.44	0.32	0.37	0.56	0.61
Pr	0.04	0.05	0.04	0.05	0.04	0.04	0.07	0.08
Nd	0.15	0.19	0.18	0.22	0.19	0.21	0.30	0.32
Sm	0.03	0.05	0.04	0.05	0.04	0.04	0.05	0.06
Eu	0.02	0.02	0.02	0.03	0.02	0.02	0.03	0.04
Dy	0.03	0.05	0.04	0.05	0.04	0.04	0.07	0.08
Ho	0.01	0.01	0.01	0.02	0.01	0.01	0.02	0.02
Er	0.04	0.06	0.05	0.07	0.05	0.04	0.08	0.09
Tm	0.01	0.02	0.01	0.02	0.02	0.01	0.02	0.03
Yb	0.22	0.22	0.23	0.30	0.23	0.15	0.31	0.38
Lu	0.06	0.07	0.07	0.09	0.06	0.04	0.09	0.11
Hf	0.05	0.05	0.05	0.06	0.06	0.01	0.02	0.07
Ta	0.01	0.01	0.01	0.01	0.01	0.004	0.005	0.02
W	122	142	141	185	141	94.3	154	208
Pb	1.07	1.38	1.19	1.10	2.24	4.85	1.04	1.45
Bi	0.003	0.003	0.003	0.004	0.004	0.209	0.005	0.011
Th	0.92	1.05	1.04	1.34	1.15	0.64	1.13	2.42
U	2.20	2.43	2.39	3.11	2.21	1.50	2.78	3.44

Trace element (ppm)	2024-TAU-21-D-circle i-cst2.2	2024-TAU-21-D-circle i-cst3	2024-TAU-21-D-circle i-cst3.1	2024-TAU-21-D-circle i-cst3.2	2024-TAU-21-D-circle i-cst4	2024-TAU-22-A-circle a-cst1	2024-TAU-22-A-circle a-cst2	2024-TAU-22-A-circle a-cst3
Sc	2.76	2.92	2.79	2.27	1.09	2.60	2.58	1.83
Ti	203	199	197	161	72	115	151	139
V	209	186	185	182	59.1	97.1	113.3	88.3
Mn	14.5	16.4	12.1	12.6	3.9	7.8	10.5	12.9
Co	15.2	12.7	12.3	12.4	5.95	9.32	11.9	10.4
Ni	92.3	77.9	75.8	75.3	24.1	57.5	72.7	64.0
Cu	0.33	0.34	0.33	0.49	0.17	0.17	0.25	0.14
Zn	1.59	2.10	3.44	5.69	1.67	0.84	0.85	0.69
Ga	23.4	19.0	19.0	18.9	5.95	7.34	8.87	7.27
Ge	0.30	0.22	0.23	0.20	0.11	0.14	0.20	0.20
As	2.83	3.41	2.64	2.52	43.00	9.00	10.51	9.16
Y	0.59	0.61	0.59	0.55	0.17	0.33	0.39	0.34
Zr	1.63	1.94	1.60	1.20	0.66	5.76	6.86	6.27
Nb	0.87	1.05	0.90	0.70	0.27	0.90	1.08	1.01
Cd	0.16	0.13	0.13	0.12	0.04	0.09	0.16	0.11
In	48.1	40.4	39.9	40.4	12.1	27.1	35.3	29.7
Sb	225	188	183	180	60.8	101	153	111
La	0.24	0.29	0.27	0.26	0.09	0.21	0.28	0.25
Ce	0.54	0.62	0.59	0.58	0.19	0.45	0.56	0.53
Pr	0.07	0.08	0.07	0.07	0.02	0.05	0.07	0.06
Nd	0.29	0.33	0.30	0.30	0.09	0.19	0.25	0.26
Sm	0.06	0.08	0.06	0.07	0.02	0.03	0.06	0.05
Eu	0.04	0.04	0.04	0.03	0.01	0.03	0.04	0.06
Dy	0.08	0.08	0.08	0.08	0.02	0.05	0.06	0.06
Ho	0.02	0.02	0.02	0.02	0.01	0.01	0.01	0.01
Er	0.09	0.09	0.09	0.08	0.03	0.06	0.07	0.06
Tm	0.03	0.02	0.02	0.02	0.01	0.01	0.01	0.01
Yb	0.39	0.39	0.36	0.31	0.11	0.18	0.22	0.17
Lu	0.11	0.11	0.11	0.09	0.03	0.05	0.05	0.04
Hf	0.03	0.04	0.03	0.02	0.01	0.14	0.17	0.15
Ta	0.01	0.01	0.01	0.01	0.01	0.01	0.02	0.02
W	236	209	186	158	58.5	182	205	175
Pb	0.99	1.08	1.10	1.42	8.68	27.6	7662	75.5
Bi	0.008	0.020	0.014	0.016	0.425	0.031	67.6	0.021
Th	1.80	1.84	1.70	1.14	0.53	2.07	2.22	1.24
U	3.80	3.41	3.28	3.14	0.95	3.47	4.43	3.56

Trace element (ppm)	2024-TAU-22-A-circle a-cst3.1	2024-TAU-22-A-circle b-cst1	2024-TAU-22-A-circle b-cst1.1	2024-TAU-22-A-circle b-cst1.2	2024-TAU-22-A-circle b-cst2	2024-TAU-22-A-circle b-cst2.1	2024-TAU-22-A-circle b-cst2.2	2024-TAU-22-A-circle b-cst3
Sc	3.66	5.15	6.96	7.48	1.41	2.29	2.94	2.07
Ti	229	348	457	451	121	137	160	112
V	171	224	273	278	68.6	84.9	96.2	65.6
Mn	16.7	33.8	36.4	57.5	9.3	10.4	12.1	11.4
Co	18.3	24.9	28.3	27.8	8.47	8.95	9.97	6.83
Ni	112	151	172	172	51.9	54.9	61.3	42.8
Cu	0.40	1.40	0.61	1.52	566	0.44	0.36	0.28
Zn	1.42	15.05	5.84	9.26	39.3	2.58	2.95	1.40
Ga	13.0	15.6	16.0	16.7	4.91	6.11	6.26	3.98
Ge	0.27	0.64	0.65	0.76	0.30	0.39	0.54	0.22
As	10.5	9.16	8.61	6.74	6.26	3.17	11.47	6.03
Y	0.64	1.04	1.29	1.55	0.34	0.68	0.80	0.45
Zr	11.3	13.9	18.4	19.2	4.24	5.71	7.04	5.05
Nb	1.79	2.05	2.94	3.30	0.62	0.98	1.25	0.91
Cd	0.19	0.33	0.34	0.45	0.66	0.13	0.13	0.09
In	51.8	70.7	71.8	70.8	38.6	27.0	28.2	17.2
Sb	199	301	404	231	383	97.5	100	62.9
La	0.48	0.86	1.06	1.36	0.28	0.47	0.55	0.34
Ce	0.98	1.77	2.05	2.67	0.57	1.01	1.22	0.72
Pr	0.12	0.21	0.25	0.31	0.07	0.13	0.15	0.09
Nd	0.41	0.78	0.92	1.18	0.24	0.47	0.57	0.32
Sm	0.08	0.17	0.18	0.25	0.06	0.11	0.12	0.07
Eu	0.07	0.25	0.27	0.36	0.10	0.19	0.23	0.11
Dy	0.09	0.21	0.22	0.26	0.07	0.13	0.16	0.09
Ho	0.02	0.04	0.05	0.06	0.01	0.03	0.03	0.02
Er	0.11	0.17	0.20	0.23	0.05	0.10	0.11	0.07
Tm	0.03	0.03	0.04	0.05	0.01	0.02	0.02	0.01
Yb	0.31	0.34	0.45	0.53	0.10	0.18	0.22	0.15
Lu	0.08	0.08	0.10	0.12	0.02	0.04	0.05	0.03
Hf	0.30	0.33	0.42	0.46	0.10	0.14	0.17	0.11
Ta	0.03	0.03	0.04	0.04	0.01	0.02	0.01	0.01
W	304	544	714	894	172	359	441	261
Pb	42.7	3234	2136	872	25299	967	1137	552
Bi	0.042	4.04	1.88	0.13	135	0.13	0.10	0.06
Th	2.81	2.18	4.14	4.52	0.37	1.65	1.95	1.93
U	6.52	7.45	8.06	7.66	2.42	2.90	2.96	2.01

Trace element (ppm)	2024-TAU-22-A-circle b-cst4	2024-TAU-22-A-circle b-cst4.1	2024-TAU-22-A-circle b-cst5	2024-TAU-22-A-circle b-cst5.1	2024-TAU-22-A-circle b-cst5.2	2024-TAU-22-A-circle b-cst5.3	2024-TAU-22-A-circle b-cst5.4	2024-TAU-22-A-circle c-cst1
Sc	2.61	1.88	1.55	3.24	1.27	3.56	3.22	1.74
Ti	143	112	135	234	87	226	212	176
V	86.6	70.8	71.4	114.0	44.3	140.6	136.4	80.7
Mn	9.9	10.4	7.9	22.9	8.3	15.8	14.2	62.3
Co	8.87	7.52	8.92	12.83	5.25	15.96	15.36	8.92
Ni	54.4	46.0	54.6	78.3	32.3	97.8	94.3	54.9
Cu	0.19	0.18	2.42	2.82	0.89	3.80	0.90	1.10
Zn	1.17	1.15	1.20	24.08	7.24	4.68	2.79	2.74
Ga	5.47	5.02	4.71	7.29	3.12	10.28	10.15	5.25
Ge	0.21	0.22	0.46	0.84	0.47	1.09	0.77	0.84
As	14.38	2.45	70.3	36.1	26.6	28.9	44.1	78.0
Y	0.45	0.31	0.42	1.25	0.54	1.35	1.10	1.26
Zr	5.94	4.45	4.57	9.33	3.31	9.44	8.98	5.55
Nb	1.02	0.70	0.63	1.64	0.51	1.44	1.36	0.68
Cd	0.13	0.11	0.70	0.22	0.09	0.51	0.28	0.47
In	23.7	21.9	27.2	36.1	16.1	53.5	49.7	34.8
Sb	108	77.7	962	261	178	868	310	306
La	0.34	0.27	0.34	0.86	0.37	0.88	0.74	0.71
Ce	0.71	0.54	0.71	1.88	0.81	1.92	1.57	1.66
Pr	0.08	0.06	0.09	0.23	0.10	0.23	0.19	0.20
Nd	0.33	0.24	0.33	0.91	0.40	0.93	0.74	0.80
Sm	0.07	0.05	0.09	0.22	0.11	0.23	0.18	0.23
Eu	0.09	0.07	0.15	0.40	0.20	0.43	0.33	0.42
Dy	0.07	0.06	0.09	0.25	0.12	0.27	0.22	0.29
Ho	0.02	0.01	0.02	0.06	0.03	0.06	0.05	0.06
Er	0.07	0.05	0.07	0.18	0.09	0.21	0.16	0.20
Tm	0.01	0.01	0.01	0.03	0.01	0.03	0.03	0.03
Yb	0.16	0.12	0.10	0.28	0.12	0.33	0.30	0.22
Lu	0.04	0.03	0.02	0.05	0.02	0.07	0.06	0.04
Hf	0.14	0.11	0.12	0.24	0.08	0.23	0.23	0.13
Ta	0.01	0.01	0.01	0.03	0.01	0.02	0.02	0.02
W	242	177	217	808	323	666	510	326
Pb	459	283	102449	3458	2186	43547	15485	43553
Bi	5.20	0.029	656	0.42	3.96	483	207	278
Th	1.57	0.78	0.36	1.64	0.36	2.51	1.67	0.21
U	2.72	2.38	2.36	3.67	1.47	5.10	4.93	2.63

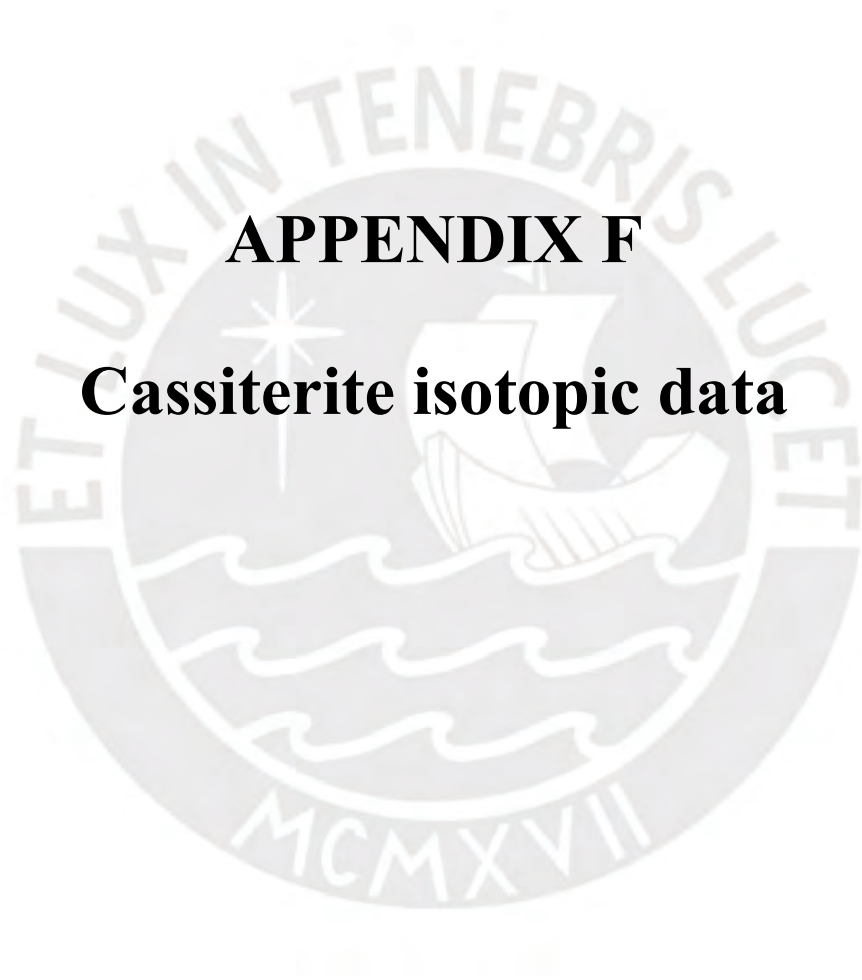
Trace element (ppm)	2024-TAU-22-A-circle c-cst2	2024-TAU-22-A-circle c-cst2.1	2024-TAU-22-A-circle c-cst3	2024-TAU-22-A-circle c-cst3.1	2024-TAU-22-A-circle c-cst3.2	2024-TAU-22-A-circle c-cst3.3	2024-TAU-22-A-circle c-cst3.4	2024-TAU-22-A-circle c-cst3.5
Sc	1.37	1.92	4.32	4.16	2.32	4.00	3.91	3.68
Ti	124	179	360	404	235	359	356	383
V	57.0	83.2	175	204	112	191	180	182
Mn	34.5	7.7	21.1	15.6	15.4	18.4	22.0	15.3
Co	5.86	8.77	19.2	21.2	12.0	19.9	18.8	19.9
Ni	36.4	53.3	117	130	72.6	122	114	121
Cu	0.75	0.38	9.56	2.48	2.80	1.86	2.32	1.54
Zn	1.62	3.70	3.10	9.87	11.1	17.7	25.1	6.67
Ga	2.70	4.95	8.10	12.2	6.52	11.8	10.6	12.1
Ge	0.50	0.51	1.44	1.08	0.74	1.53	1.28	1.08
As	77.8	3.61	252	104	68.3	25.5	5.34	19.6
Y	0.62	0.63	1.67	1.28	0.82	1.72	1.69	1.08
Zr	4.33	6.35	12.7	13.6	7.52	12.7	13.1	12.4
Nb	0.60	0.89	1.35	1.54	0.88	1.57	1.81	1.46
Cd	0.35	0.11	1.51	0.66	0.53	0.39	0.39	0.47
In	16.7	26.5	56.9	64.6	35.6	60.8	54.6	62.4
Sb	966	115	2172	1444	1795	292	202	593
La	0.47	0.46	1.20	0.86	0.62	1.15	1.17	0.81
Ce	0.98	0.98	2.57	1.89	1.31	2.50	2.63	1.73
Pr	0.12	0.12	0.31	0.22	0.15	0.32	0.31	0.22
Nd	0.48	0.46	1.16	0.88	0.60	1.20	1.24	0.81
Sm	0.12	0.11	0.37	0.23	0.16	0.30	0.34	0.19
Eu	0.22	0.21	0.59	0.40	0.28	0.58	0.58	0.37
Dy	0.13	0.14	0.39	0.27	0.18	0.36	0.38	0.23
Ho	0.03	0.03	0.08	0.05	0.04	0.08	0.08	0.05
Er	0.10	0.10	0.27	0.19	0.12	0.24	0.26	0.16
Tm	0.01	0.02	0.04	0.03	0.02	0.04	0.04	0.03
Yb	0.11	0.15	0.32	0.30	0.18	0.36	0.37	0.29
Lu	0.02	0.03	0.05	0.06	0.04	0.08	0.07	0.06
Hf	0.11	0.17	0.32	0.34	0.19	0.30	0.31	0.32
Ta	0.01	0.02	0.03	0.04	0.02	0.04	0.04	0.04
W	233	256	594	440	288	667	705	444
Pb	35937	2316	188398	43062	46240	16692	5727	18055
Bi	311	1.16	1766	476	309	58.6	3.00	126
Th	0.24	0.47	0.31	0.77	0.34	0.73	1.02	0.53
U	1.46	2.77	3.90	6.48	3.38	6.07	5.42	6.52

Trace element (ppm)	2024-TAU-22-A-circle c-cst3.6	2024-TAU-22-A-circle d-cst1	2024-TAU-22-A-circle d-cst1.1	2024-TAU-22-A-circle d-cst1.2	2024-TAU-22-A-circle d-cst1.3	2024-TAU-22-A-circle d-cst1.4	2024-TAU-22-A-circle f-cst1	2024-TAU-22-A-circle f-cst2
Sc	0.72	3.68	2.24	0.62	0.79	1.71	0.58	0.34
Ti	59	330	216	63	73	170	85	65
V	27.9	163	104	24.7	31.5	73.7	31.9	19.8
Mn	264	21.4	54.9	151	121	109	5.2	3.4
Co	3.36	17.5	11.8	3.02	3.79	8.12	3.26	2.07
Ni	20.7	107	73.7	18.7	23.7	50.0	19.8	12.7
Cu	0.21	2.03	4.05	0.86	0.60	7.32	0.01	0.01
Zn	0.99	5.27	4.08	0.93	0.80	3.90	0.16	0.16
Ga	1.48	11.02	8.35	1.31	1.78	3.69	1.89	1.17
Ge	0.26	0.63	0.42	0.13	0.16	0.33	0.12	0.05
As	14.9	3.85	5.96	5.80	2.95	2.83	1.20	0.58
Y	0.56	0.74	0.53	0.27	0.27	0.44	0.25	0.20
Zr	2.13	13.20	7.84	2.11	2.55	5.99	4.37	2.81
Nb	0.25	1.83	1.06	0.29	0.31	0.84	0.61	0.40
Cd	0.15	0.53	0.35	0.24	0.44	0.25	0.03	0.02
In	9.89	51.7	36.4	8.16	9.95	20.2	8.92	5.06
Sb	190	407	761	342	808	821	55.6	29.3
La	0.75	0.65	0.45	0.36	0.36	0.51	0.63	0.37
Ce	1.76	1.30	0.92	0.75	0.78	1.03	1.26	0.74
Pr	0.18	0.16	0.11	0.08	0.09	0.12	0.12	0.07
Nd	0.71	0.56	0.41	0.33	0.33	0.46	0.47	0.30
Sm	0.14	0.13	0.09	0.07	0.07	0.10	0.06	0.04
Eu	0.21	0.21	0.14	0.11	0.10	0.15	0.08	0.06
Dy	0.11	0.15	0.10	0.06	0.05	0.09	0.03	0.03
Ho	0.02	0.03	0.02	0.01	0.01	0.02	0.01	0.01
Er	0.07	0.12	0.08	0.03	0.03	0.06	0.02	0.02
Tm	0.01	0.02	0.01	0.01	0.01	0.01	0.004	0.002
Yb	0.08	0.25	0.17	0.04	0.05	0.11	0.04	0.02
Lu	0.01	0.06	0.04	0.01	0.01	0.02	0.01	0.01
Hf	0.05	0.35	0.19	0.06	0.07	0.16	0.11	0.08
Ta	0.00	0.05	0.03	0.01	0.01	0.02	0.02	0.01
W	112	457	320	84.8	88.9	204	51.6	34.3
Pb	14378	2732	5322	24425	66145	9515	0.64	0.37
Bi	150	5.07	21.9	225	594	105	0.002	0.001
Th	0.08	1.06	0.71	0.06	0.12	0.31	0.05	0.02
U	0.70	5.89	4.11	0.59	0.82	2.07	1.16	0.67

Trace element (ppm)	2024-TAU-22-A-circle f-cst3	2024-TAU-22-A-circle f-cst3.1	2024-TAU-22-B-circle a-cst1	2024-TAU-22-B-circle a-cst1.1	2024-TAU-22-B-circle b-cst1	2024-TAU-22-B-circle b-cst2	2024-TAU-22-B-circle b-cst3	2024-TAU-22-B-circle c-cst1
Sc	0.71	0.34	5.98	4.20	2.29	0.18	1.88	0.11
Ti	100	57	552	462	264	29.3	185	14.7
V	38.6	18.1	247.0	184.6	133	9.9	114	5.0
Mn	6.0	5.2	25.1	26.8	9.5	0.7	7.9	2.5
Co	3.98	1.90	28.37	20.98	15.0	1.13	12.8	0.55
Ni	24.3	11.6	175.7	128.5	90.6	6.8	79.7	3.4
Cu	0.01	0.01	0.26	0.72	0.18	0.04	0.15	6.62
Zn	0.15	0.12	1.91	2.09	3.00	0.72	1.02	0.29
Ga	2.30	0.96	14.79	10.03	8.35	0.63	7.63	0.30
Ge	0.09	0.08	0.32	0.26	0.20	0.02	0.15	0.01
As	1.34	1.11	5.63	9.20	2.49	0.24	2.34	0.25
Y	0.24	0.32	0.54	0.40	0.26	0.09	0.22	0.02
Zr	5.64	2.93	39.31	28.22	21.5	8.75	18.2	0.94
Nb	0.68	0.27	3.81	2.60	1.92	0.19	1.47	0.08
Cd	0.05	0.02	0.34	0.30	0.17	0.01	0.12	0.02
In	10.56	4.15	81.74	55.10	43.2	2.94	39.2	1.54
Sb	80.1	34.9	309.1	209.8	168	12.5	160	6.5
La	1.10	0.72	0.43	0.35	0.35	0.05	0.43	0.04
Ce	1.99	1.47	0.77	0.63	0.56	0.08	0.64	0.07
Pr	0.19	0.14	0.09	0.07	0.06	0.007	0.06	0.01
Nd	0.68	0.56	0.31	0.29	0.22	0.03	0.22	0.02
Sm	0.08	0.09	0.07	0.06	0.03	0.004	0.03	0.004
Eu	0.11	0.12	0.06	0.06	0.03	0.006	0.03	0.006
Dy	0.03	0.05	0.07	0.06	0.04	0.011	0.03	0.003
Ho	0.01	0.01	0.02	0.01	0.01	0.003	0.008	0.001
Er	0.02	0.03	0.08	0.06	0.04	0.010	0.03	0.002
Tm	0.004	0.004	0.021	0.014	0.009	0.002	0.007	0.0005
Yb	0.05	0.03	0.29	0.18	0.15	0.02	0.12	0.005
Lu	0.01	0.01	0.08	0.05	0.04	0.004	0.04	0.001
Hf	0.15	0.08	1.11	0.83	0.56	0.24	0.49	0.03
Ta	0.02	0.01	0.20	0.14	0.08	0.01	0.06	0.003
W	61.1	34.6	238	135	142	22.0	136	8.70
Pb	0.60	2.46	8.91	24.8	0.88	0.18	3.14	0.31
Bi	0.002	0.001	0.029	0.036	0.016	0.007	0.015	0.003
Th	0.06	0.02	0.81	0.39	0.38	0.03	0.37	0.01
U	1.33	0.54	10.21	6.94	5.41	0.40	4.92	0.19

Trace element (ppm)	2024-TAU-22-B-circle c-cst1.1	2024-TAU-22-C-circle a-cst1	2024-TAU-22-C-circle a-cst2	2024-TAU-22-C-circle b-cst1	2024-TAU-22-C-circle b-cst2	2024-TAU-22-C-circle b-cst3	2024-TAU-22-C-circle b-cst4	2024-TAU-22-C-circle c-cst1
Sc	0.11	20.15	1.16	0.72	1.29	5.96	4.33	3.06
Ti	10.4	468	38.4	34.8	56.1	154	150	91
V	4.4	235	23.5	17.0	33.7	70.8	99.5	56.9
Mn	3.0	30.6	10.8	191	274	10.4	22.6	37.5
Co	0.46	27.4	2.92	2.15	4.01	8.71	11.6	7.02
Ni	2.8	169	17.8	13.1	24.4	52.9	70.8	42.9
Cu	64.5	0.39	0.03	0.02	0.02	0.12	0.19	0.11
Zn	0.96	18.0	1.77	0.56	0.98	4.65	8.15	1.14
Ga	0.24	15.3	1.43	0.99	2.04	4.33	6.75	3.71
Ge	0.02	0.40	0.04	0.05	0.07	0.07	0.27	0.13
As	0.23	4.85	0.45	0.25	0.52	1.61	1.87	1.00
Y	0.01	0.51	0.06	0.15	0.24	0.17	0.18	0.13
Zr	0.84	26.4	2.82	1.88	3.22	8.54	9.07	7.71
Nb	0.09	4.52	0.37	0.22	0.40	1.44	1.27	0.88
Cd	0.03	0.35	0.03	0.03	0.05	0.11	0.13	0.08
In	1.21	88.0	8.85	5.55	12	26	39	22.7
Sb	6.1	372	35.7	20.2	45.3	106.1	154	93.8
La	0.05	0.36	0.06	0.15	0.28	0.12	0.15	0.11
Ce	0.08	0.71	0.12	0.37	0.60	0.23	0.26	0.22
Pr	0.01	0.08	0.01	0.04	0.07	0.03	0.03	0.02
Nd	0.03	0.32	0.05	0.16	0.28	0.10	0.11	0.09
Sm	0.003	0.05	0.01	0.03	0.05	0.02	0.02	0.02
Eu	0.004	0.05	0.01	0.04	0.06	0.02	0.02	0.02
Dy	0.002	0.07	0.01	0.02	0.04	0.02	0.03	0.02
Ho	0.0004	0.02	0.002	0.01	0.01	0.01	0.01	0.004
Er	0.002	0.09	0.01	0.02	0.03	0.03	0.03	0.02
Tm	0.0003	0.02	0.002	0.003	0.005	0.01	0.01	0.005
Yb	0.004	0.30	0.03	0.03	0.05	0.09	0.13	0.07
Lu	0.001	0.09	0.01	0.01	0.01	0.02	0.04	0.02
Hf	0.03	0.64	0.07	0.04	0.07	0.19	0.23	0.19
Ta	0.004	0.06	0.006	0.003	0.01	0.02	0.02	0.02
W	11.5	246	18.2	13.0	21.1	77.8	78.4	39.1
Pb	0.29	7.61	0.16	0.14	0.21	0.81	0.96	16.3
Bi	0.007	0.115	0.002	0.001	0.002	0.012	0.013	0.003
Th	0.01	0.86	0.05	0.02	0.06	0.28	0.24	0.12
U	0.15	10.95	1.03	0.62	1.35	3.09	4.85	2.70

Trace element (ppm)	2024-TAU-22-C-circle c-cst2	2024-TAU-22-C-circle c-cst3	2024-TAU-22-C-circle c-cst4	2024-TAU-22-C-circle c-cst5	2024-TAU-22-C-circle c-cst6	2024-TAU-22-C-circle d-cst1	2024-TAU-22-C-circle d-cst2	2024-TAU-22-C-circle e-cst3
Sc	4.95	1.09	3.25	2.03	9.37	10.7	21.7	0.81
Ti	144	61.3	98.1	81.6	280	350	448	48.7
V	95.9	30.5	81.8	60.7	135	200	233	22.1
Mn	23.1	177	15.4	207	77.9	69.5	21.1	230
Co	12.0	3.82	9.73	7.38	17.6	24.0	25.0	2.53
Ni	74.0	23.2	59.7	45.5	110	147	153	15.4
Cu	0.06	201	0.15	0.03	0.20	0.62	0.26	0.01
Zn	0.75	9.46	1.91	0.97	7.56	22.7	6.68	0.23
Ga	6.98	1.94	6.36	4.31	9.08	12.0	14.2	1.23
Ge	0.19	0.08	0.11	0.13	0.26	0.37	0.36	0.05
As	2.04	0.63	1.77	1.24	4.26	3.38	3.91	0.27
Y	0.25	0.19	0.37	0.26	0.36	0.46	0.43	0.18
Zr	11.5	3.54	7.70	6.13	20.8	22.7	23.5	2.74
Nb	1.55	0.47	1.11	0.66	3.11	2.78	3.87	0.36
Cd	0.15	0.18	0.11	0.09	0.21	0.29	0.29	0.03
In	43.0	11.8	36.8	25.7	55.5	72.7	82.2	6.70
Sb	173	41.8	154	99.0	232	298	325	23.9
La	0.23	0.19	0.81	0.16	0.29	0.42	0.29	0.11
Ce	0.41	0.46	1.57	0.36	0.54	0.76	0.56	0.28
Pr	0.04	0.05	0.17	0.04	0.06	0.09	0.07	0.03
Nd	0.18	0.20	0.68	0.15	0.23	0.34	0.25	0.12
Sm	0.03	0.04	0.13	0.03	0.04	0.07	0.05	0.02
Eu	0.03	0.05	0.16	0.04	0.04	0.07	0.05	0.03
Dy	0.03	0.03	0.08	0.03	0.05	0.07	0.07	0.03
Ho	0.01	0.01	0.02	0.01	0.01	0.02	0.02	0.01
Er	0.04	0.02	0.06	0.04	0.04	0.07	0.06	0.02
Tm	0.01	0.005	0.01	0.01	0.01	0.02	0.02	0.004
Yb	0.14	0.05	0.15	0.10	0.18	0.21	0.26	0.04
Lu	0.04	0.01	0.04	0.03	0.05	0.06	0.07	0.01
Hf	0.28	0.09	0.18	0.15	0.48	0.52	0.56	0.06
Ta	0.03	0.01	0.02	0.01	0.05	0.05	0.05	0.01
W	85.8	38.5	95.9	52.9	134	162	188	18.0
Pb	0.59	0.67	0.83	0.35	1.48	1.54	1.42	0.26
Bi	0.009	0.006	0.012	0.007	0.017	0.017	0.026	0.001
Th	0.32	0.06	0.29	0.17	0.58	0.39	0.78	0.03
U	5.13	1.30	4.35	2.89	6.62	8.71	10.2	0.75



APPENDIX F

Cassiterite isotopic data

Spot	Duration (s)							Final Data (Corrected)				
		²⁰⁶ Pb (cps)	2σ (abs)	²⁰⁷ Pb (cps)	2σ (abs)	²³⁸ U (cps)	2σ (abs)	Yankee-corrected ²³⁸ U/ ²⁰⁶ Pb	1σ (abs)	ROM ² -corrected ²⁰⁷ Pb/ ²⁰⁶ Pb	1σ (abs)	Error correlation
TAU-06-A-circle a-cst1	18.05	269203	15655	224287	12476	587310	7710	1.252	0.033	0.835	0.005	0.220
TAU-06-A-circle a-cst1.1	26.00	233959	19751	194724	17150	522463	15234	1.296	0.044	0.834	0.005	-0.353
TAU-06-A-circle a-cst1.2	26.99	464390	84870	385077	70738	749294	13756	0.936	0.087	0.831	0.004	-0.037
TAU-06-A-circle a-cst2	31.79	187613	38815	157347	32439	630008	9237	1.964	0.198	0.840	0.005	-0.017
TAU-06-A-circle a-cst2.1	32.07	311032	20870	257973	19034	670859	13091	1.248	0.037	0.831	0.003	-0.184
TAU-06-A-circle a-cst2.2	22.27	160981	20324	133391	16958	552702	10151	1.996	0.120	0.830	0.005	0.068
TAU-06-A-circle b-cst1	22.93	76981	5029	65756	4674	537528	4335	4.029	0.140	0.856	0.011	0.128
TAU-06-A-circle b-cst2	38.00	184641	67685	153514	58117	569777	8574	1.769	0.338	0.833	0.008	-0.074
TAU-06-A-circle b-cst2	38.00	80384	18816	62440	13068	474174	9547	3.231	0.399	0.778	0.006	0.035
TAU-06-A-circle b-cst2.1	17.34	63056	7453	52437	6373	579049	8819	5.251	0.323	0.833	0.011	-0.194
TAU-06-A-circle b-cst2.2	14.53	105890	5761	89840	5384	693233	12197	3.848	0.083	0.850	0.005	0.018
TAU-06-A-circle b-cst3	14.55	75425	2328	62913	2154	533168	9666	4.079	0.076	0.835	0.009	-0.024
TAU-06-A-circle b-cst4	26.89	94600	12277	77223	10079	646784	10784	3.931	0.264	0.818	0.006	-0.245
TAU-06-A-circle c-cst1	23.05	164311	16708	135985	13752	865283	12239	3.041	0.158	0.829	0.005	0.209
TAU-06-A-circle c-cst1.1	38.01	546000	154685	454511	131175	979327	18767	0.914	0.156	0.834	0.003	-0.328
TAU-06-A-circle c-cst2	24.58	146604	29795	120318	24448	754991	11797	2.983	0.311	0.822	0.005	-0.457
TAU-06-A-circle c-cst3	17.86	191451	31583	158786	26051	914754	10298	2.770	0.233	0.831	0.006	0.210
TAU-06-A-circle c-cst3.1	23.32	88117	6274	72416	5469	909753	11016	5.980	0.202	0.823	0.006	-0.150
TAU-06-A-circle c-cst4	38.00	160883	15732	132850	13206	1078328	11391	3.867	0.193	0.827	0.003	-0.132
TAU-06-A-circle d-cst1	38.01	343402	49490	283885	41097	635039	18077	1.066	0.081	0.828	0.006	-0.294
TAU-06-A-circle d-cst2	38.01	249079	22369	205544	18871	724699	19648	1.683	0.067	0.827	0.004	-0.266
TAU-06-A-circle d-cst3	33.52	320438	23898	264453	20443	591576	18882	1.066	0.034	0.827	0.005	-0.015

Spot	Duration (s)							Final Data (Corrected)				
		²⁰⁶ Pb (cps)	2σ (abs)	²⁰⁷ Pb (cps)	2σ (abs)	²³⁸ U (cps)	2σ (abs)	Yankee-corrected ²³⁸ U/ ²⁰⁶ Pb	1σ (abs)	ROM ² -corrected ²⁰⁷ Pb/ ²⁰⁶ Pb	1σ (abs)	Error correlation
TAU-06-A-circle d-cst4	38.00	116752	11597	96976	9754	596192	13800	2.974	0.132	0.832	0.006	-0.051
TAU-06-A-circle d-cst5	33.73	183955	32133	151081	26264	680591	17581	2.177	0.178	0.823	0.007	0.094
TAU-06-A-circle d-cst5.1	28.71	199360	28225	158765	20485	660489	17115	1.896	0.144	0.798	0.006	-0.320
TAU-06-A-circle d-cst6	18.80	85100	23350	69451	19134	597614	7851	4.080	0.564	0.817	0.008	-0.262
TAU-06-A-circle d-cst6.1	38.00	266832	54872	218821	45799	651056	14121	1.383	0.154	0.821	0.005	0.009
TAU-06-B-circle a-cst1	26.53	64558	4723	52763	4115	868990	19296	7.755	0.275	0.819	0.006	-0.363
TAU-06-B-circle a-cst1.1	30.54	74241	6264	60593	5654	878174	20835	6.836	0.266	0.817	0.006	-0.304
TAU-06-B-circle a-cst1.2	32.25	76796	8233	63455	6988	766917	15218	5.779	0.293	0.828	0.006	-0.064
TAU-06-B-circle a-cst2	38.01	144748	27231	118687	22302	805293	15883	3.181	0.312	0.821	0.009	0.016
TAU-06-B-circle a-cst3	38.00	247688	24666	202145	19630	669571	20839	1.565	0.070	0.817	0.010	0.142
TAU-06-B-circle a-cst3.1	35.25	162850	21622	135159	17985	822827	21677	2.869	0.210	0.831	0.004	0.017
TAU-06-B-circle a-cst4	18.87	35521	3367	28175	2584	686822	6586	11.135	0.563	0.794	0.013	0.273
TAU-06-B-circle b-cst1	38.01	109280	12839	94238	14265	959238	30863	5.002	0.331	0.864	0.006	-0.044
TAU-06-B-circle b-cst2	34.20	180529	19516	150097	16345	854209	9066	2.710	0.158	0.833	0.004	-0.126
TAU-06-B-circle b-cst3	38.01	189130	21407	156167	18156	933511	18961	2.906	0.160	0.827	0.004	-0.147
TAU-06-B-circle b-cst3.1	38.01	359777	49171	298833	41414	924893	27156	1.470	0.105	0.832	0.004	-0.273
TAU-06-B-circle c-cst1	28.39	81639	13652	66411	11362	979413	36438	7.030	0.547	0.815	0.006	-0.137
TAU-06-B-circle c-cst1.1	36.69	93106	20491	77024	17227	896635	18053	5.548	0.610	0.829	0.007	-0.063
TAU-06-B-circle c-cst2	21.81	59335	15091	48029	12441	817907	8280	7.918	1.034	0.811	0.009	0.002
TAU-06-B-circle c-cst2.1	27.45	294151	51003	246467	43659	920109	20564	1.779	0.158	0.839	0.005	-0.269
TAU-06-B-circle c-cst3	23.78	413431	21365	344767	17852	838056	28522	1.160	0.029	0.835	0.004	0.040
TAU-06-B-circle c-cst4	38.02	558258	111465	465065	94042	815846	34029	0.893	0.082	0.834	0.003	-0.065

Spot	Duration (s)							Final Data (Corrected)				
		²⁰⁶ Pb (cps)	2σ (abs)	²⁰⁷ Pb (cps)	2σ (abs)	²³⁸ U (cps)	2σ (abs)	Yankee-corrected ²³⁸ U/ ²⁰⁶ Pb	1σ (abs)	ROM ²⁻ corrected ²⁰⁷ Pb/ ²⁰⁶ Pb	1σ (abs)	Error correlation
TAU-06-B-circle c-cst5	17.63	31657	2502	24959	1707	905130	12787	15.781	0.859	0.790	0.009	0.477
TAU-06-B-circle c-cst6	18.61	97696	31786	80021	26644	1019355	15115	6.000	1.014	0.820	0.011	-0.220
TAU-06-B-circle d-cst1	38.00	79135	7167	64486	5721	959995	17762	6.965	0.287	0.816	0.004	0.048
TAU-06-B-circle d-cst1.1	26.82	56355	1641	46341	1342	987186	18984	10.125	0.165	0.824	0.007	0.223
TAU-06-B-circle d-cst2	31.55	115281	23800	94586	18524	955369	8243	5.145	0.384	0.822	0.006	0.255
TAU-06-B-circle d-cst3	18.46	24831	1052	19091	923	994407	31603	22.905	0.417	0.770	0.010	-0.186
TAU-06-B-circle d-cst4	19.09	76176	7452	61675	6719	991017	13323	7.465	0.422	0.811	0.007	-0.470
TAU-21-B-circle b-cst1	38.00	239026	11409	202537	10331	356267	9741	0.857	0.016	0.849	0.003	-0.142
TAU-21-B-circle b-cst2	24.15	87157	1995	73126	1930	351605	4351	2.303	0.038	0.840	0.005	-0.072
TAU-21-B-circle b-cst2.1	38.00	169676	8247	142517	7247	305380	10817	1.030	0.021	0.841	0.004	-0.042
TAU-21-B-circle b-cst2.2	22.94	7762038	1647872	6516603	1380275	214116	14262	0.017	0.001	0.841	0.002	0.238
TAU-21-B-circle b-cst3	37.10	1332300	569215	1116361	478478	373376	9295	0.154	0.034	0.839	0.011	0.069
TAU-21-B-circle b-cst3.1	38.02	353949	16762	305408	18937	366407	13875	0.581	0.016	0.864	0.006	0.011
TAU-21-B-circle b-cst4	38.00	252107	28027	211781	23556	316701	8644	0.697	0.040	0.841	0.005	0.134
TAU-21-B-circle c-cst1	38.01	40402	3076	33612	2427	312533	9141	4.331	0.172	0.833	0.008	0.366
TAU-21-B-circle c-cst2	38.00	141701	15165	119939	13846	324348	5691	1.322	0.067	0.848	0.004	-0.250
TAU-21-B-circle d-cst1	18.56	13471	1309	10103	1103	408557	3525	17.208	0.881	0.751	0.028	-0.246
TAU-21-B-circle d-cst2	18.53	7888	746	6203	520	363434	5280	26.533	1.214	0.788	0.032	0.727
TAU-21-B-circle d-cst3	38.02	11272	741	8854	702	371426	8371	18.911	0.532	0.787	0.020	0.314
TAU-21-B-circle d-cst4	14.79	4928	636	3778	478	203542	13271	23.627	1.452	0.768	0.046	0.642
TAU-21-B-circle e-cst1	38.00	251885	15828	209985	12674	362141	8946	0.826	0.021	0.835	0.004	0.303
TAU-21-B-circle e-cst1.1	38.02	1163234	78915	932184	44274	332441	12457	0.162	0.006	0.803	0.003	0.193

Spot	Duration (s)							Final Data (Corrected)				
		²⁰⁶ Pb (cps)	2σ (abs)	²⁰⁷ Pb (cps)	2σ (abs)	²³⁸ U (cps)	2σ (abs)	Yankee-corrected ²³⁸ U/ ²⁰⁶ Pb	1σ (abs)	ROM ² -corrected ²⁰⁷ Pb/ ²⁰⁶ Pb	1σ (abs)	Error correlation
TAU-21-B-circle e-cst1.2	38.02	979435	19742	824092	17497	380945	7808	0.222	0.003	0.843	0.003	0.043
TAU-21-B-circle e-cst2	38.01	274699	7075	229356	6041	323646	10993	0.657	0.019	0.836	0.005	0.088
TAU-21-B-circle e-cst2.1	38.00	142572	8008	118900	7087	371916	11186	1.499	0.027	0.835	0.005	-0.148
TAU-21-B-circle e-cst3	23.12	273028	11551	230063	9885	360642	6193	0.751	0.015	0.844	0.004	0.018
TAU-21-B-circle e-cst4	30.91	94598	4526	78260	3801	376082	9259	2.280	0.043	0.829	0.006	0.149
TAU-21-B-circle e-cst4.1	28.28	165353	10016	139461	8455	360131	9372	1.249	0.033	0.845	0.005	0.130
TAU-21-C-circle a-cst1	38.00	131553	17030	111768	14928	313484	8003	1.350	0.092	0.851	0.005	-0.018
TAU-21-C-circle a-cst1.1	15.02	4170415	1271626	3528839	1082026	276095	6678	0.038	0.006	0.848	0.005	-0.327
TAU-21-C-circle a-cst2	17.67	25735461	4058094	21628834	3333174	172618	5732	0.004	0.000	0.842	0.009	0.042
TAU-21-C-circle a-cst3	38.01	206566	33369	175300	29063	255138	5378	0.718	0.057	0.850	0.006	-0.197
TAU-21-C-circle a-cst4	35.14	45169	8350	37801	6835	236322	8263	2.874	0.300	0.838	0.020	0.158
TAU-21-C-circle a-cst5	16.41	43988	3626	36442	3046	171575	2088	2.226	0.091	0.830	0.009	0.072
TAU-21-C-circle b-cst1	34.20	89500341	29126476	74343411	2479140 3	186789	8410	0.001	0.000	0.832	0.018	0.052
TAU-21-C-circle b-cst2	38.00	1262391	374713	1048970	310702	215155	3057	0.098	0.015	0.832	0.004	0.035
TAU-21-C-circle b-cst3	38.01	1362766	124760	1145113	105708	210632	11368	0.087	0.004	0.842	0.002	-0.095
TAU-21-C-circle b-cst3.1	38.00	2969614	1296437	2841589	1226967	245893	8609	0.047	0.011	0.958	0.012	-0.071
TAU-21-C-circle c-cst1	31.80	14976	1022	12192	1030	247012	3260	9.458	0.365	0.815	0.012	0.000
TAU-21-C-circle c-cst2	27.19	18234	1289	14981	1024	219412	3342	6.862	0.218	0.823	0.010	0.288
TAU-21-C-circle d-cst1	38.01	103805	3917	86911	3707	287603	8900	1.577	0.024	0.839	0.008	0.028
TAU-21-C-circle d-cst2	38.00	1596638	322166	1349309	272732	263458	13206	0.082	0.011	0.846	0.003	-0.085
TAU-21-D-circle a-cst1	25.94	121483	6553	99873	3387	244451	11167	1.094	0.062	0.823	0.005	0.403
TAU-21-D-circle a-cst2	27.67	65058	7070	54258	6357	306013	4676	2.681	0.131	0.835	0.008	-0.336

Spot	Duration (s)							Final Data (Corrected)				
		²⁰⁶ Pb (cps)	2σ (abs)	²⁰⁷ Pb (cps)	2σ (abs)	²³⁸ U (cps)	2σ (abs)	Yankee-corrected ²³⁸ U/ ²⁰⁶ Pb	1σ (abs)	ROM ² -corrected ²⁰⁷ Pb/ ²⁰⁶ Pb	1σ (abs)	Error correlation
TAU-21-D-circle a-cst3	38.02	1208851	142349	1015063	120208	192047	2206	0.090	0.006	0.841	0.002	-0.170
TAU-21-D-circle a-cst4	38.01	52639	1587	43872	1489	311428	10611	3.329	0.084	0.835	0.005	0.066
TAU-21-D-circle a-cst5	38.00	249866	10517	209129	8985	323486	4302	0.738	0.016	0.838	0.003	-0.038
TAU-21-D-circle a-cst5.1	31.25	143150	7370	119647	6167	291515	9514	1.138	0.047	0.837	0.005	0.146
TAU-21-D-circle b-cst1	35.03	74356	2076	62127	1546	352209	10159	2.712	0.046	0.837	0.005	0.427
TAU-21-D-circle b-cst1.1	34.48	82375	4145	68313	3351	347797	8839	2.407	0.046	0.831	0.005	0.218
TAU-21-D-circle b-cst1.2	38.01	86980	5284	71974	4556	364490	6071	2.397	0.065	0.829	0.004	-0.135
TAU-21-D-circle b-cst2	34.88	98552	1820	82344	1436	341371	11601	1.956	0.036	0.837	0.004	0.413
TAU-21-D-circle b-cst2.1	34.94	73655	2898	61610	2251	366385	8955	2.836	0.046	0.838	0.006	0.242
TAU-21-D-circle b-cst2.2	34.95	61956	1766	51713	1420	363125	9510	3.352	0.047	0.836	0.006	0.564
TAU-21-D-circle b-cst3	38.00	152873	6741	127554	5701	355331	7553	1.323	0.028	0.836	0.004	0.242
TAU-21-D-circle b-cst3.1	38.02	119038	4294	100388	3542	341580	6480	1.633	0.028	0.845	0.005	0.207
TAU-21-D-circle b-cst3.2	38.00	111891	3622	93475	3096	348398	7899	1.768	0.029	0.837	0.004	0.174
TAU-21-D-circle b-cst4	20.74	260343	5924	217918	4998	360961	12141	0.785	0.020	0.838	0.003	-0.152
TAU-21-D-circle b-cst4.1	38.02	2048470	652395	1787261	538202	344921	11196	0.082	0.016	0.874	0.023	0.051
TAU-21-D-circle b-cst5	14.81	200781	12530	169030	11143	324951	10952	0.924	0.025	0.843	0.008	-0.158
TAU-21-D-circle c-cst1	38.01	262568	12869	220253	10594	353600	10366	0.753	0.027	0.840	0.004	0.102
TAU-21-D-circle c-cst1.1	38.00	75940	3055	62679	2751	351747	8242	2.634	0.048	0.827	0.006	0.164
TAU-21-D-circle c-cst1.2	38.02	80451	2772	66960	2440	372971	8458	2.630	0.049	0.834	0.005	0.048
TAU-21-D-circle c-cst2	38.00	71078	1941	59944	1815	349725	7179	2.767	0.044	0.845	0.006	0.290
TAU-21-D-circle c-cst2.1	38.00	66572	2614	54952	2350	356987	9509	3.052	0.044	0.827	0.005	0.072
TAU-21-D-circle c-cst3	38.00	75149	3376	62462	2657	361383	9236	2.764	0.042	0.833	0.006	0.456

Spot	Duration (s)							Final Data (Corrected)				
		²⁰⁶ Pb (cps)	2σ (abs)	²⁰⁷ Pb (cps)	2σ (abs)	²³⁸ U (cps)	2σ (abs)	Yankee-corrected ²³⁸ U/ ²⁰⁶ Pb	1σ (abs)	ROM ²⁻ corrected ²⁰⁷ Pb/ ²⁰⁶ Pb	1σ (abs)	Error correlation
TAU-21-D-circle c-cst3.1	38.01	57200	1552	47603	1444	361703	10742	3.565	0.073	0.834	0.006	-0.142
TAU-21-D-circle c-cst4	38.00	172629	2223	144794	2360	255243	7583	0.829	0.016	0.840	0.003	0.198
TAU-21-D-circle c-cst4.1	38.00	104506	2643	87476	2375	181151	6626	0.972	0.024	0.838	0.004	0.005
TAU-21-D-circle c-cst4.2	38.00	141736	4338	117423	2772	166011	4606	0.664	0.013	0.830	0.004	0.260
TAU-21-D-circle c-cst5	38.00	192360	7158	161584	6444	230874	5880	0.681	0.013	0.841	0.003	-0.052
TAU-21-D-circle c-cst5.1	38.01	571069	27730	485861	26840	184529	3002	0.185	0.005	0.852	0.005	-0.011
TAU-21-D-circle d-cst1	34.23	790834	66978	666642	56761	230227	3845	0.166	0.006	0.844	0.004	-0.036
TAU-21-D-circle d-cst1.1	35.19	33947	2241	28219	1893	307087	6497	5.008	0.177	0.833	0.007	0.115
TAU-21-D-circle d-cst1.2	38.00	471585	10019	397414	8058	263451	10170	0.314	0.005	0.844	0.004	0.020
TAU-21-D-circle d-cst2	38.01	34786	1699	28724	1479	326434	16679	5.274	0.134	0.827	0.005	0.090
TAU-21-D-circle d-cst3	24.83	70936	1917	59553	1798	299916	9450	2.402	0.035	0.841	0.006	0.217
TAU-21-D-circle d-cst3.1	38.00	60617	5767	50209	4733	343460	11459	3.275	0.122	0.830	0.006	0.007
TAU-21-D-circle e-cst1.1	32.36	141486	4973	118774	4143	340011	10432	1.365	0.020	0.841	0.004	0.131
TAU-21-D-circle e-cst2	30.54	92535	3277	77314	2915	340013	14900	2.045	0.073	0.837	0.006	-0.027
TAU-21-D-circle e-cst2.1	38.01	91390	3554	76749	3077	350676	7616	2.184	0.034	0.841	0.004	0.098
TAU-21-D-circle e-cst3	38.00	76920	6424	63537	5272	360987	8214	2.682	0.106	0.827	0.005	-0.074
TAU-21-D-circle e-cst4	38.01	30461	1162	24780	928	350163	11262	6.361	0.122	0.815	0.005	0.300
TAU-21-D-circle e-cst4.1	38.01	36474	2216	29517	1818	358346	8845	5.615	0.139	0.811	0.007	-0.051
TAU-21-D-circle e-cst4.2	32.63	31669	959	26367	740	360455	8375	6.478	0.077	0.834	0.005	0.459
TAU-21-D-circle e-cst5	29.01	100250	3128	83057	2647	309157	9183	1.742	0.044	0.830	0.005	-0.005
TAU-21-D-circle e-cst6	38.01	26128	1476	21271	1166	342339	8251	7.560	0.151	0.815	0.008	0.191
TAU-21-D-circle e-cst7	29.21	63209	4756	52034	3906	327620	9103	2.956	0.096	0.825	0.005	0.101

Spot	Duration (s)							Final Data (Corrected)				
		²⁰⁶ Pb (cps)	2σ (abs)	²⁰⁷ Pb (cps)	2σ (abs)	²³⁸ U (cps)	2σ (abs)	Yankee-corrected ²³⁸ U/ ²⁰⁶ Pb	1σ (abs)	ROM ² -corrected ²⁰⁷ Pb/ ²⁰⁶ Pb	1σ (abs)	Error correlation
TAU-21-D-circle f-cst1	38.02	18390	885	15088	826	366846	9042	11.377	0.203	0.822	0.010	-0.054
TAU-21-D-circle f-cst1.1	38.00	15564	532	12303	468	371175	6726	13.497	0.195	0.792	0.009	0.462
TAU-21-D-circle f-cst1.2	38.00	17213	703	13511	359	373398	9354	12.344	0.205	0.786	0.009	0.812
TAU-21-D-circle f-cst1.3	38.00	21083	713	16867	667	375114	9362	10.124	0.139	0.801	0.008	0.270
TAU-21-D-circle f-cst1.4	38.01	25321	733	20584	560	373005	8091	8.388	0.096	0.814	0.008	0.398
TAU-21-D-circle f-cst2	38.02	26631	1301	21648	1103	379219	7902	8.131	0.156	0.814	0.008	0.249
TAU-21-D-circle f-cst2.1	22.81	31847	2399	26503	1855	388981	8197	6.969	0.232	0.834	0.010	0.380
TAU-21-D-circle f-cst2.2	38.00	26038	1202	20810	1051	394844	9538	8.652	0.158	0.801	0.009	0.155
TAU-21-D-circle f-cst2.3	33.01	43297	1733	35879	1384	385933	7063	5.089	0.083	0.830	0.007	0.399
TAU-21-D-circle f-cst2.4	27.44	35751	1083	29835	898	375525	5273	5.980	0.092	0.836	0.008	0.493
TAU-21-D-circle f-cst2.5	31.01	35399	1095	28979	953	387771	9180	6.237	0.095	0.820	0.008	0.356
TAU-21-D-circle f-cst3	38.00	61337	2841	51063	2366	372207	8914	3.469	0.058	0.834	0.004	0.075
TAU-21-D-circle f-cst3.1	33.65	78593	4688	65525	4050	369181	6925	2.674	0.063	0.835	0.005	-0.042
TAU-21-D-circle f-cst3.2	38.00	60282	4343	50046	3491	367465	8766	3.499	0.102	0.832	0.005	0.288
TAU-21-D-circle f-cst3.3	33.99	79892	4172	66234	3452	358320	7220	2.563	0.056	0.830	0.005	0.195
TAU-21-D-circle f-cst4	38.00	55318	2475	46155	3058	379795	13516	3.905	0.066	0.836	0.006	-0.214
TAU-21-D-circle f-cst4.1	38.01	48112	2615	39711	2135	380168	6688	4.483	0.118	0.827	0.005	0.034
TAU-21-D-circle f-cst4.2	26.96	49939	1346	41730	1314	379310	9807	4.322	0.073	0.837	0.007	-0.139
TAU-21-D-circle g-cst1	38.01	109850	3578	91886	3043	360635	9796	1.846	0.053	0.838	0.004	-0.004
TAU-21-D-circle g-cst1.1	38.01	127547	3698	106487	3050	335773	10570	1.480	0.038	0.836	0.005	0.196
TAU-21-D-circle g-cst1.2	38.01	80740	1806	67187	1416	357474	6594	2.532	0.028	0.833	0.005	0.466
TAU-21-D-circle g-cst1.3	27.23	56854	1602	46589	1132	352528	7855	3.538	0.061	0.821	0.006	0.473

Spot	Duration (s)							Final Data (Corrected)				
		²⁰⁶ Pb (cps)	2σ (abs)	²⁰⁷ Pb (cps)	2σ (abs)	²³⁸ U (cps)	2σ (abs)	Yankee-corrected ²³⁸ U/ ²⁰⁶ Pb	1σ (abs)	ROM ² -corrected ²⁰⁷ Pb/ ²⁰⁶ Pb	1σ (abs)	Error correlation
TAU-21-D-circle g-cst2	38.01	3131871	700505	2599924	589228	233694	27265	0.030	0.004	0.832	0.005	0.062
TAU-21-D-circle g-cst2.1	37.61	278854	50382	227987	35068	356948	15279	0.720	0.062	0.819	0.021	0.530
TAU-21-D-circle g-cst3	38.00	61181	3679	51046	3154	352032	5940	3.287	0.082	0.836	0.004	-0.030
TAU-21-D-circle g-cst3.1	38.02	52796	2776	43740	2387	360856	8414	3.924	0.076	0.830	0.005	0.066
TAU-21-D-circle g-cst3.2	38.01	54306	2775	45144	2268	365752	9099	3.861	0.074	0.833	0.005	0.233
TAU-21-D-circle g-cst3.3	38.01	52325	2125	43296	1844	353476	9212	3.864	0.060	0.829	0.006	0.225
TAU-21-D-circle g-cst3.4	38.00	73047	5787	60545	4906	351833	9244	2.782	0.084	0.830	0.005	0.005
TAU-21-D-circle g-cst3.5	38.00	67441	2474	55136	2125	369653	8834	3.129	0.054	0.819	0.004	0.075
TAU-21-D-circle g-cst4	38.02	88537	3772	74116	3221	370214	9667	2.390	0.042	0.838	0.005	0.016
TAU-21-D-circle g-cst4.1	33.62	85847	7091	71200	5826	366191	8297	2.460	0.087	0.831	0.006	0.190
TAU-21-D-circle g-cst4.2	38.00	83250	5991	69338	4927	361515	8514	2.497	0.077	0.834	0.005	0.097
TAU-21-D-circle g-cst4.3	34.39	85699	3777	71373	3111	354378	8239	2.370	0.043	0.834	0.005	0.242
TAU-21-D-circle g-cst4.4	38.00	61117	2179	50662	1974	371515	11015	3.474	0.045	0.830	0.005	-0.072
TAU-21-D-circle g-cst4.5	32.45	48726	1692	39911	1463	371244	7158	4.364	0.067	0.820	0.006	0.172
TAU-21-D-circle h-cst1	26.09	35326	1024	29018	731	354687	6846	5.751	0.083	0.823	0.008	0.622
TAU-21-D-circle h-cst1.1	33.07	24228	1173	19951	1012	396009	7325	9.334	0.169	0.825	0.008	0.118
TAU-21-D-circle h-cst1.2	38.00	20968	1075	16812	712	411380	11120	11.268	0.203	0.803	0.011	0.558
TAU-21-D-circle h-cst2	34.20	9067	425	7118	362	356742	9527	22.631	0.376	0.786	0.014	0.456
TAU-21-D-circle h-cst2.1	35.37	11707	623	9226	611	367558	10010	18.080	0.339	0.789	0.013	-0.124
TAU-21-D-circle h-cst2.2	27.91	10191	292	8105	368	369968	6737	20.572	0.392	0.797	0.019	0.650
TAU-21-D-circle h-cst2.3	36.55	10965	386	8727	357	383859	6939	19.977	0.314	0.797	0.012	0.266
TAU-21-D-circle h-cst2.4	38.01	11015	425	8825	435	375268	10328	19.537	0.294	0.803	0.012	0.347

Spot	Duration (s)							Final Data (Corrected)				
		²⁰⁶ Pb (cps)	2σ (abs)	²⁰⁷ Pb (cps)	2σ (abs)	²³⁸ U (cps)	2σ (abs)	Yankee-corrected ²³⁸ U/ ²⁰⁶ Pb	1σ (abs)	ROM ² -corrected ²⁰⁷ Pb/ ²⁰⁶ Pb	1σ (abs)	Error correlation
TAU-21-D-circle h-cst3	38.01	14593	810	11611	671	381197	9312	15.194	0.281	0.797	0.010	0.191
TAU-21-D-circle h-cst3.1	19.16	11838	389	9150	286	358720	4859	17.438	0.279	0.774	0.015	0.623
TAU-21-D-circle h-cst3.2	38.01	17975	1015	14557	921	403073	10225	12.940	0.262	0.811	0.011	0.076
TAU-21-D-circle h-cst3.3	38.00	19043	512	15334	547	407543	10363	12.320	0.171	0.807	0.010	0.245
TAU-21-D-circle h-cst4	38.01	29373	1482	24142	1147	381333	8067	7.474	0.161	0.823	0.007	0.356
TAU-21-D-circle h-cst4.1	38.02	33137	1079	27200	898	373220	7919	6.467	0.093	0.822	0.007	0.194
TAU-21-D-circle h-cst4.2	38.02	29718	942	24207	780	385460	8147	7.448	0.102	0.816	0.007	0.532
TAU-21-D-circle h-cst4.3	38.01	21919	656	17674	632	395419	10662	10.333	0.154	0.808	0.009	0.023
TAU-21-D-circle h-cst4.4	38.00	59593	2427	49477	2155	383206	9555	3.722	0.050	0.832	0.005	-0.196
TAU-21-D-circle i-cst1	38.00	189053	22767	155451	18637	354529	10220	1.048	0.075	0.824	0.011	0.203
TAU-21-D-circle i-cst2	38.00	24649	1187	20056	930	409022	10243	9.545	0.165	0.815	0.009	0.583
TAU-21-D-circle i-cst2.1	38.02	29108	1644	23829	1208	434224	13952	8.622	0.148	0.820	0.008	0.531
TAU-21-D-circle i-cst2.2	27.51	17558	1131	14227	1001	436102	11028	14.351	0.341	0.812	0.011	0.111
TAU-21-D-circle i-cst3	26.15	18118	825	14135	604	391947	8756	12.509	0.221	0.781	0.009	0.132
TAU-21-D-circle i-cst3.1	38.01	22267	1779	18440	1573	412812	11268	10.752	0.338	0.829	0.009	0.279
TAU-21-D-circle i-cst3.2	38.00	30726	3025	25078	2598	403449	9336	7.666	0.323	0.818	0.008	-0.149
TAU-21-D-circle i-cst4	38.41	713333	116285	592248	103266	387935	6045	0.318	0.025	0.832	0.008	-0.091
TAU-22-A-circle a-cst1	38.00	789582	79583	662544	67514	632907	17147	0.457	0.025	0.840	0.003	-0.116
TAU-22-A-circle a-cst2	38.00	16692562 ₈	26959600	140552690	2310588 ₈	629882	11459	0.002	0.000	0.843	0.011	-0.255
TAU-22-A-circle a-cst3	38.00	2160516	386583	1823271	326031	561416	13838	0.155	0.013	0.845	0.002	0.011
TAU-22-A-circle a-cst3.1	38.01	616834	12060	517821	9342	598848	11980	0.554	0.008	0.841	0.002	0.191
TAU-22-A-circle b-cst1	38.00	33529401	1932046	28096270	1571218	500542	14876	0.009	0.000	0.839	0.004	0.318

Spot	Duration (s)							Final Data (Corrected)				
		²⁰⁶ Pb (cps)	2σ (abs)	²⁰⁷ Pb (cps)	2σ (abs)	²³⁸ U (cps)	2σ (abs)	Yankee-corrected ²³⁸ U/ ²⁰⁶ Pb	1σ (abs)	ROM ²⁻ corrected ²⁰⁷ Pb/ ²⁰⁶ Pb	1σ (abs)	Error correlation
TAU-22-A-circle b-cst1.1	38.01	20087308	1139105	16906135	958073	480870	12896	0.014	0.000	0.843	0.002	0.041
TAU-22-A-circle b-cst1.2	38.00	8212736	282166	6866434	230746	464538	12222	0.033	0.001	0.837	0.002	0.398
TAU-22-A-circle b-cst2	29.35	64646555 0	36194889	548813515	2940339 9	450301	12796	0.000	0.000	0.850	0.009	0.334
TAU-22-A-circle b-cst2.1	38.02	29019493	1899612	24173387	1520433	539284	13517	0.011	0.000	0.834	0.002	0.289
TAU-22-A-circle b-cst2.2	38.01	30051853	1386595	25586218	1376847	495383	17882	0.009	0.000	0.853	0.010	0.124
TAU-22-A-circle b-cst3	38.01	20909616	935687	17614094	794960	484115	13154	0.013	0.000	0.844	0.002	0.055
TAU-22-A-circle b-cst4	33.00	12082635	365357	10234169	320111	530080	7677	0.025	0.001	0.848	0.003	0.125
TAU-22-A-circle b-cst4.1	38.00	9987557	440492	8370886	368199	536027	15358	0.031	0.001	0.840	0.002	0.042
TAU-22-A-circle b-cst5	19.64	16445472 44	12640809 9	137918110 4	1060711 39	384064	4730	0.000	0.000	0.840	0.006	0.049
TAU-22-A-circle b-cst5.1	33.81	64231716	4589535	54548084	4009224	418009	6343	0.004	0.000	0.851	0.003	0.404
TAU-22-A-circle b-cst5.2	38.00	94584920	4361293	79150790	3593088	379913	20535	0.002	0.000	0.838	0.002	-0.074
TAU-22-A-circle b-cst5.3	17.60	12876073 6	11651822	108282033	9450924	535960	7599	0.002	0.000	0.842	0.004	0.220
TAU-22-A-circle b-cst5.4	24.28	92834192	16087662	77446838	1318538 8	534835	6426	0.003	0.000	0.836	0.004	0.448
TAU-22-A-circle c-cst1	38.00	11377487 57	10551265 0	956758069	8714621 5	440144	11561	0.000	0.000	0.842	0.006	0.165
TAU-22-A-circle c-cst2	38.00	14410726 34	98733022	123299910 4	8360215 1	365362	12686	0.000	0.000	0.857	0.011	0.297
TAU-22-A-circle c-cst2.1	38.01	64802063	7091754	54906122	5958210	495779	19478	0.004	0.000	0.849	0.003	-0.031
TAU-22-A-circle c-cst3	38.03	22945903 72	92433590	194795025 3	7694919 5	293398	9549	0.000	0.000	0.850	0.008	0.304
TAU-22-A-circle c-cst3.1	38.01	47899046 8	66212858	388111639	4563404 4	477134	7278	0.001	0.000	0.812	0.012	0.433
TAU-22-A-circle c-cst3.2	38.01	91864862 5	77656042	772703789	6347066 8	423928	13355	0.000	0.000	0.843	0.004	0.185

Spot	Duration (s)							Final Data (Corrected)				
		²⁰⁶ Pb (cps)	2σ (abs)	²⁰⁷ Pb (cps)	2σ (abs)	²³⁸ U (cps)	2σ (abs)	Yankee-corrected ²³⁸ U/ ²⁰⁶ Pb	1σ (abs)	ROM ²⁻ -corrected ²⁰⁷ Pb/ ²⁰⁶ Pb	1σ (abs)	Error correlation
TAU-22-A-circle c-cst3.3	38.00	21454204 6	23153372	181584103	1985774 2	475323	9795	0.001	0.000	0.848	0.006	-0.047
TAU-22-A-circle c-cst3.4	38.00	76883855	5968535	64674775	4967866	451617	11827	0.003	0.000	0.843	0.002	0.034
TAU-22-A-circle c-cst3.5	38.00	24327128 8	27911658	196944045	1933944 4	517464	14830	0.001	0.000	0.811	0.008	0.217
TAU-22-A-circle d-cst1	38.00	40410493	4093489	33933887	3380683	536635	16649	0.008	0.000	0.841	0.003	0.088
TAU-22-A-circle d-cst1.1	38.01	11249781 9	19550506	94342803	1637004 7	549369	11784	0.003	0.000	0.840	0.008	0.189
TAU-22-A-circle d-cst1.2	38.00	17025591 87	10740875 4	143085531 5	8501984 9	242819	4026	0.000	0.000	0.842	0.010	0.352
TAU-22-A-circle d-cst1.3	38.00	33123982 80	19500936 3	279018245 2	1596648 28	262640	6274	0.000	0.000	0.844	0.007	0.271
TAU-22-A-circle d-cst1.4	38.00	23431992 5	66418898	199290939	5666486 6	359048	15329	0.001	0.000	0.852	0.004	-0.069
TAU-22-A-circle f-cst1	38.01	42665	1590	35439	1175	523689	12988	7.113	0.177	0.832	0.011	0.337
TAU-22-A-circle f-cst2	17.44	36442	2902	29677	2116	457471	12082	7.349	0.249	0.816	0.013	0.546
TAU-22-A-circle f-cst3	29.10	35434	1601	28624	1273	474262	17702	7.743	0.175	0.809	0.010	0.316
TAU-22-A-circle f-cst3.1	38.02	239865	9373	201733	7638	413201	7676	0.999	0.018	0.842	0.005	0.096
TAU-22-B-circle a-cst1	18.34	76476	6318	61678	5281	575760	9080	4.380	0.170	0.808	0.006	-0.367
TAU-22-B-circle a-cst1.1	29.72	168936	17477	140023	14274	488694	11778	1.697	0.077	0.830	0.006	-0.022
TAU-22-B-circle b-cst1	18.47	16628	2038	13234	1914	562495	12076	20.048	1.116	0.797	0.017	-0.190
TAU-22-B-circle b-cst2	38.00	29317	2573	23626	1879	532123	16675	10.584	0.362	0.807	0.016	0.562
TAU-22-B-circle b-cst3	13.34	61271	5494	51517	5110	588797	10037	5.600	0.224	0.842	0.007	-0.158
TAU-22-B-circle c-cst1	36.32	138115	11530	112661	9101	516870	6721	2.173	0.101	0.817	0.004	0.251
TAU-22-B-circle c-cst1.1	28.70	138563	3528	112637	2712	481862	21218	1.994	0.058	0.814	0.006	0.240
TAU-22-C-circle a-cst1	28.40	59850	8074	48768	6624	621225	11745	5.939	0.463	0.816	0.008	0.077

Spot	Duration (s)							Final Data (Corrected)				
		²⁰⁶ Pb (cps)	2σ (abs)	²⁰⁷ Pb (cps)	2σ (abs)	²³⁸ U (cps)	2σ (abs)	Yankee-corrected ²³⁸ U/ ²⁰⁶ Pb	1σ (abs)	ROM ²⁻ -corrected ²⁰⁷ Pb/ ²⁰⁶ Pb	1σ (abs)	Error correlation
TAU-22-C-circle a-cst2	19.79	11792	764	8955	833	546718	7693	26.992	0.793	0.761	0.026	0.227
TAU-22-C-circle b-cst1	23.57	13077	778	10494	548	448149	7951	19.884	0.677	0.804	0.023	0.382
TAU-22-C-circle b-cst2	15.25	14029	1067	10768	769	534802	18873	22.255	0.752	0.769	0.020	0.501
TAU-22-C-circle b-cst3	38.01	23992	2762	20099	2879	592510	19152	14.518	0.692	0.839	0.009	0.225
TAU-22-C-circle b-cst4	35.52	16856	723	13503	648	582739	9283	20.036	0.380	0.802	0.015	0.742
TAU-22-C-circle b-cst5	28.53	22318	1005	17557	849	559844	11579	14.646	0.307	0.788	0.012	0.255
TAU-22-C-circle c-cst1	38.00	550431	33270	464230	28345	580624	10038	0.615	0.016	0.845	0.003	-0.031
TAU-22-C-circle c-cst2	29.96	13507	1133	10461	935	684870	12723	29.735	1.115	0.776	0.016	0.189
TAU-22-C-circle c-cst3	38.01	42062	1940	34421	1598	506249	10092	7.025	0.157	0.820	0.006	0.202
TAU-22-C-circle c-cst4	38.01	23094	1519	18709	1257	721236	12027	18.161	0.554	0.811	0.010	0.054
TAU-22-C-circle c-cst5	32.73	12354	719	9539	560	617451	22714	29.532	0.621	0.773	0.016	0.430
TAU-22-C-circle c-cst6	38.00	23280	2184	17785	1666	612811	12581	15.443	0.645	0.765	0.009	0.187
TAU-22-C-circle d-cst1	22.37	12579	1185	9607	987	562786	18965	26.352	1.042	0.765	0.013	0.299
TAU-22-C-circle d-cst2	31.84	14275	1639	10621	1319	667397	9756	27.338	1.472	0.745	0.014	0.213
TAU-22-C-circle e-cst3	21.92	24983	3494	20738	3219	399973	24518	8.939	0.881	0.831	0.014	-0.122

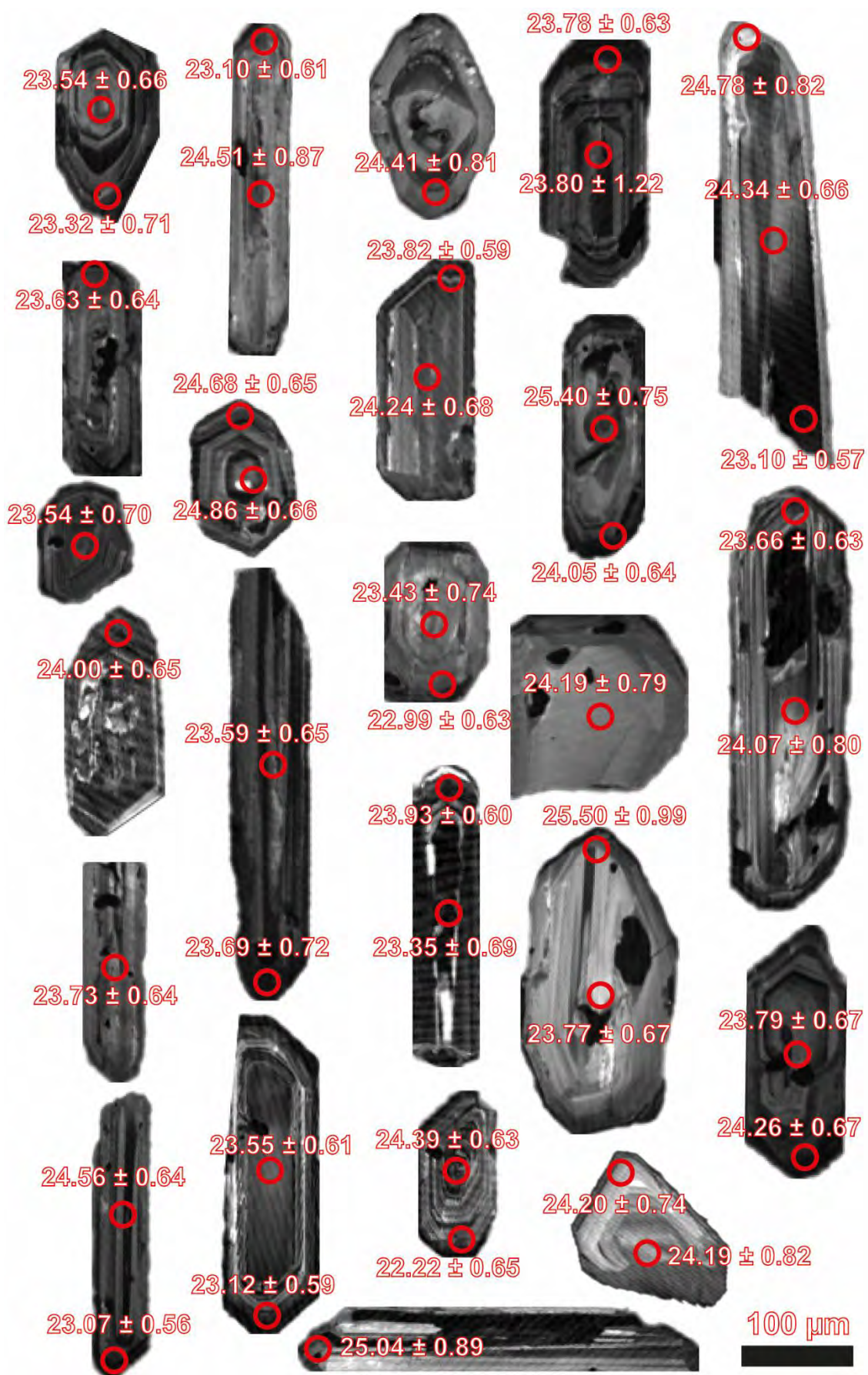
APPENDIX G
Zircon CL-SEM images





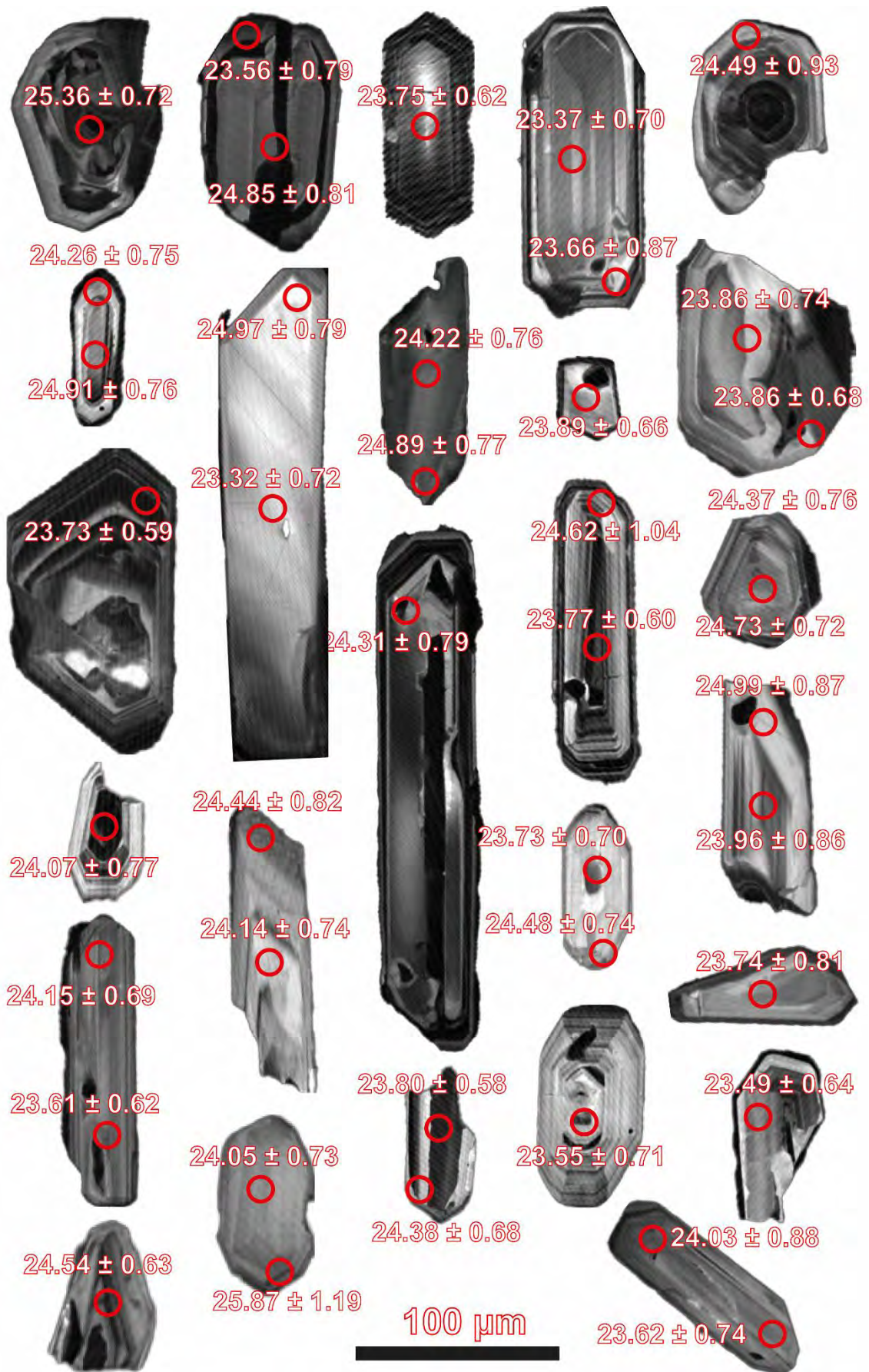


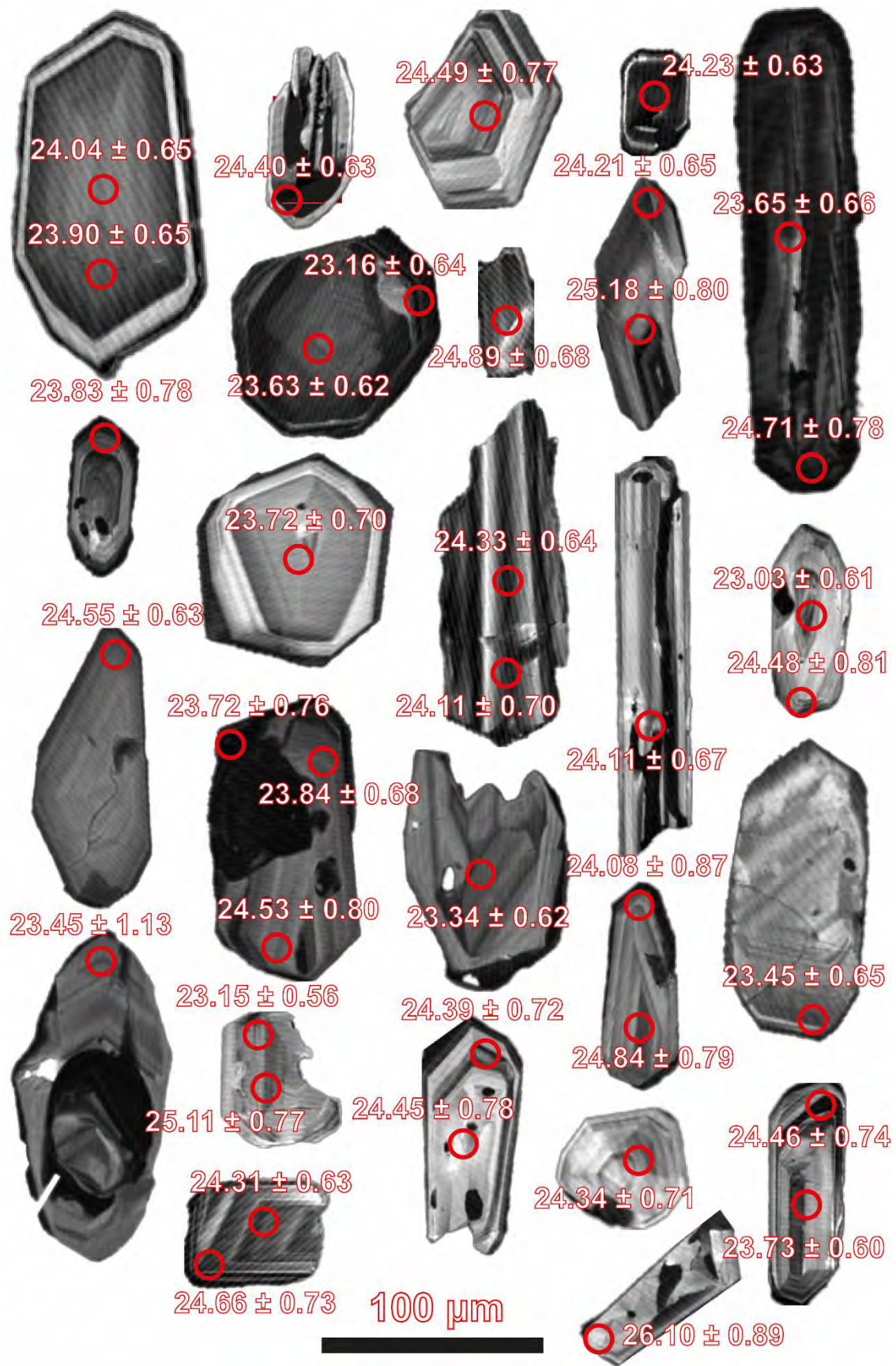






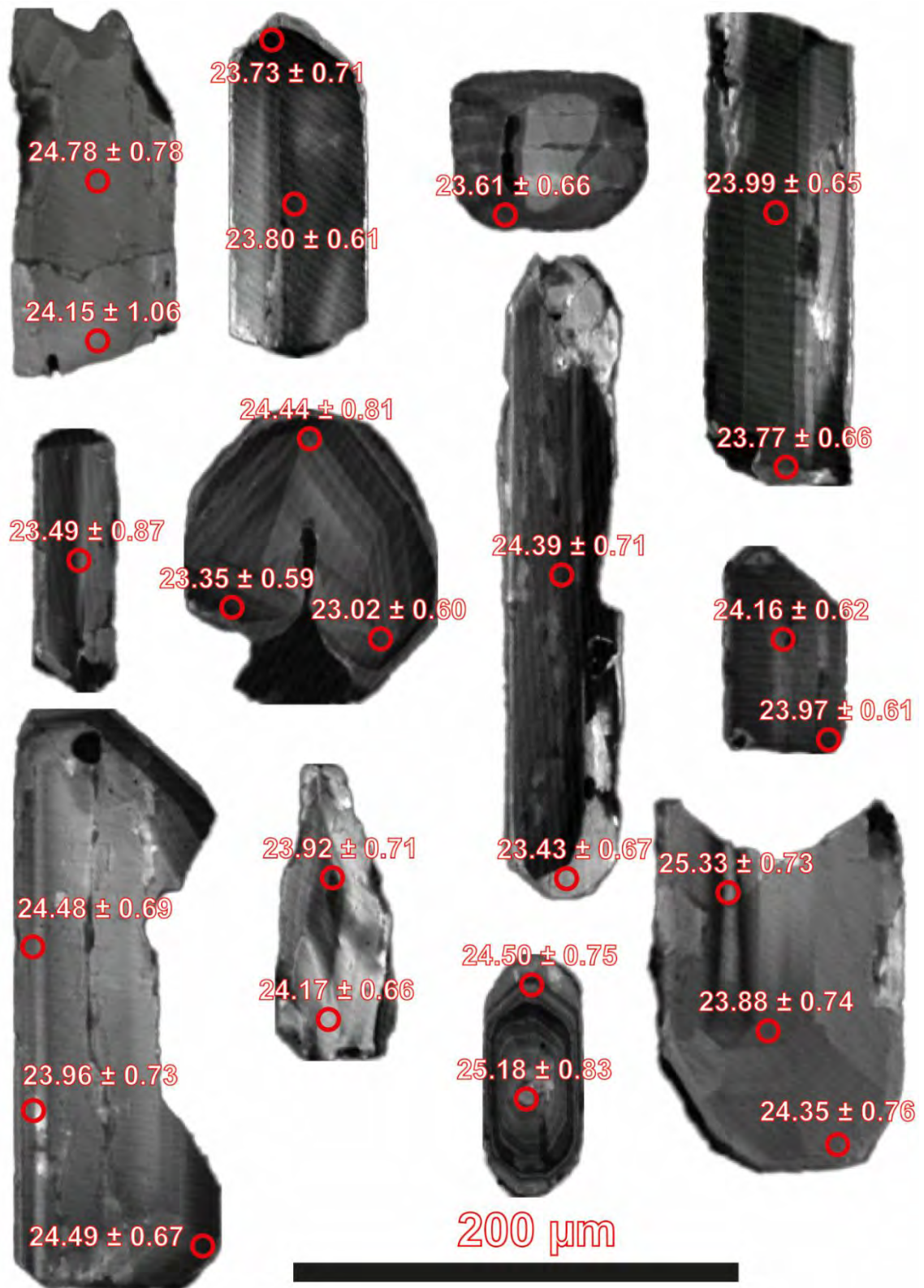
TC-23-02







TC-23-03



APPENDIX H

Zircon isotopic data



Spot	Rating	Isotopic ratios						Dates (Ma)			
	(0=worst, 3=best)	²⁰⁷ Pb/ ²³⁵ U	±2σ (abs.)	²⁰⁶ Pb/ ²³⁸ U	±2σ (abs.)	²⁰⁷ Pb/ ²⁰⁶ Pb	±2σ (abs.)	²⁰⁷ Pb/ ²³⁵ U	±2σ (abs.)	²⁰⁶ Pb/ ²³⁸ U	±2σ (abs.)
TAU-23-1_002	3	0.0251	0.0019	0.0037	0.00012	0.0498	0.0038	25.17	1.86	23.72	0.75
TAU-23-1_003	3	0.0257	0.0022	0.0037	0.00012	0.0508	0.0044	25.74	2.16	23.71	0.80
TAU-23-1_009	3	0.0246	0.0011	0.0036	0.00009	0.0493	0.0021	24.68	1.07	23.39	0.60
TAU-23-1_011	3	0.0255	0.0018	0.0038	0.00013	0.0493	0.0039	25.57	1.80	24.41	0.81
TAU-23-1_012	3	0.0252	0.0014	0.0037	0.00010	0.0502	0.0030	25.22	1.41	23.54	0.66
TAU-23-1_016	3	0.0245	0.0028	0.0038	0.00014	0.0467	0.0051	24.52	2.74	24.51	0.87
TAU-23-1_017	3	0.0234	0.0015	0.0036	0.00009	0.0475	0.0032	23.46	1.51	23.10	0.61
TAU-23-1_018	3	0.0235	0.0012	0.0037	0.00011	0.0457	0.0024	23.61	1.21	24.11	0.68
TAU-23-1_023	3	0.0240	0.0013	0.0036	0.00010	0.0490	0.0026	24.11	1.31	22.92	0.61
TAU-23-1_024	3	0.0249	0.0016	0.0037	0.00010	0.0491	0.0033	25.43	1.86	24.05	0.66
TAU-23-1_025	3	0.0262	0.0020	0.0038	0.00011	0.0496	0.0036	26.21	1.97	24.63	0.70
TAU-23-1_026	3	0.0249	0.0015	0.0037	0.00010	0.0485	0.0027	24.92	1.48	23.92	0.63
TAU-23-1_027	3	0.0230	0.0020	0.0037	0.00011	0.0447	0.0039	23.07	1.97	23.97	0.68
TAU-23-1_028	3	0.0231	0.0016	0.0036	0.00010	0.0463	0.0033	23.20	1.58	23.40	0.64
TAU-23-1_029	3	0.0229	0.0018	0.0036	0.00011	0.0461	0.0037	22.99	1.83	23.17	0.71
TAU-23-1_030	3	0.0254	0.0011	0.0039	0.00010	0.0474	0.0022	25.42	1.09	25.05	0.67
TAU-23-1_031	3	0.0248	0.0011	0.0038	0.00011	0.0478	0.0021	24.88	1.11	24.24	0.68
TAU-23-1_032	3	0.0239	0.0010	0.0037	0.00009	0.0467	0.0017	23.95	0.95	23.82	0.59
TAU-23-1_035	3	0.0251	0.0019	0.0037	0.00010	0.0492	0.0035	25.16	1.88	23.63	0.64
TAU-23-1_038	3	0.0255	0.0012	0.0039	0.00010	0.0479	0.0021	25.60	1.14	24.86	0.66
TAU-23-1_039	3	0.0252	0.0014	0.0038	0.00010	0.0476	0.0026	25.21	1.35	24.68	0.65
TAU-23-1_040	3	0.0239	0.0017	0.0038	0.00010	0.0461	0.0035	23.95	1.69	24.39	0.67
TAU-23-1_041	3	0.0239	0.0018	0.0037	0.00011	0.0463	0.0034	23.97	1.81	24.08	0.68
TAU-23-1_043	3	0.0239	0.0010	0.0037	0.00010	0.0469	0.0018	23.98	0.95	23.78	0.62

Spot	Rating	Isotopic ratios						Dates (Ma)			
	(0=worst, 3=best)	²⁰⁷ Pb/ ²³⁵ U	±2σ (abs.)	²⁰⁶ Pb/ ²³⁸ U	±2σ (abs.)	²⁰⁷ Pb/ ²⁰⁶ Pb	±2σ (abs.)	²⁰⁷ Pb/ ²³⁵ U	±2σ (abs.)	²⁰⁶ Pb/ ²³⁸ U	±2σ (abs.)
TAU-23-1_044	3	0.0242	0.0015	0.0036	0.00010	0.0482	0.0032	24.22	1.50	23.42	0.64
TAU-23-1_045	3	0.0232	0.0012	0.0035	0.00010	0.0475	0.0026	23.30	1.22	22.84	0.63
TAU-23-1_048	3	0.0235	0.0025	0.0036	0.00011	0.0470	0.0052	23.57	2.51	23.43	0.74
TAU-23-1_049	3	0.0238	0.0013	0.0036	0.00010	0.0483	0.0026	23.87	1.29	22.99	0.63
TAU-23-1_050	3	0.0240	0.0020	0.0037	0.00011	0.0477	0.0039	24.10	1.97	23.54	0.70
TAU-23-1_051	3	0.0237	0.0019	0.0037	0.00012	0.0468	0.0038	23.76	1.85	23.73	0.77
TAU-23-1_053	3	0.0236	0.0013	0.0037	0.00010	0.0457	0.0024	23.73	1.32	24.04	0.62
TAU-23-1_057	3	0.0247	0.0018	0.0037	0.00011	0.0490	0.0036	24.76	1.75	23.55	0.70
TAU-23-1_058	3	0.0251	0.0014	0.0037	0.00010	0.0490	0.0029	25.17	1.39	23.96	0.66
TAU-23-1_060	3	0.0230	0.0011	0.0035	0.00009	0.0473	0.0022	23.07	1.12	22.60	0.58
TAU-23-1_061	3	0.0234	0.0013	0.0036	0.00011	0.0466	0.0021	23.50	1.28	23.35	0.69
TAU-23-1_062	3	0.0255	0.0009	0.0037	0.00009	0.0497	0.0015	25.53	0.87	23.93	0.60
TAU-23-1_064	3	0.0249	0.0010	0.0037	0.00010	0.0482	0.0017	24.95	1.00	24.00	0.65
TAU-23-1_065	3	0.0251	0.0010	0.0037	0.00009	0.0488	0.0018	25.16	0.99	23.94	0.59
TAU-23-1_066	3	0.0236	0.0014	0.0037	0.00010	0.0467	0.0027	23.63	1.38	23.54	0.63
TAU-23-1_067	3	0.0234	0.0008	0.0036	0.00009	0.0467	0.0014	23.49	0.83	23.36	0.60
TAU-23-1_069	3	0.0231	0.0019	0.0037	0.00011	0.0459	0.0041	23.14	1.84	24.06	0.71
TAU-23-1_070	3	0.0256	0.0030	0.0038	0.00013	0.0493	0.0061	25.62	2.95	24.27	0.82
TAU-23-1_071	3	0.0244	0.0016	0.0037	0.00010	0.0484	0.0033	24.49	1.56	23.59	0.65
TAU-23-1_072	3	0.0243	0.0025	0.0037	0.00011	0.0480	0.0046	24.40	2.45	23.69	0.72
TAU-23-1_075	3	0.0238	0.0025	0.0036	0.00014	0.0483	0.0050	23.84	2.50	23.03	0.87
TAU-23-1_076	3	0.0245	0.0025	0.0037	0.00012	0.0487	0.0052	24.59	2.49	23.66	0.78
TAU-23-1_080	3	0.0262	0.0015	0.0039	0.00014	0.0489	0.0028	26.24	1.48	25.04	0.89
TAU-23-1_081	3	0.0250	0.0014	0.0038	0.00010	0.0477	0.0023	25.03	1.35	24.39	0.63

Spot	Rating	Isotopic ratios						Dates (Ma)			
	(0=worst, 3=best)	²⁰⁷ Pb/ ²³⁵ U	±2σ (abs.)	²⁰⁶ Pb/ ²³⁸ U	±2σ (abs.)	²⁰⁷ Pb/ ²⁰⁶ Pb	±2σ (abs.)	²⁰⁷ Pb/ ²³⁵ U	±2σ (abs.)	²⁰⁶ Pb/ ²³⁸ U	±2σ (abs.)
TAU-23-1_083	3	0.0257	0.0019	0.0037	0.00010	0.0503	0.0035	25.74	1.88	23.73	0.64
TAU-23-1_085	3	0.0246	0.0011	0.0038	0.00010	0.0467	0.0020	24.70	1.11	24.56	0.64
TAU-23-1_086	3	0.0227	0.0008	0.0036	0.00009	0.0459	0.0015	22.81	0.81	23.07	0.56
TAU-23-1_087	3	0.0250	0.0026	0.0038	0.00013	0.0477	0.0050	25.07	2.55	24.59	0.83
TAU-23-1_088	3	0.0236	0.0007	0.0037	0.00009	0.0469	0.0013	23.64	0.70	23.56	0.58
TAU-23-1_089	3	0.0251	0.0014	0.0037	0.00010	0.0494	0.0029	25.14	1.37	23.79	0.67
TAU-23-1_090	3	0.0239	0.0013	0.0038	0.00010	0.0460	0.0025	24.00	1.31	24.26	0.67
TAU-23-1_093	3	0.0248	0.0029	0.0038	0.00012	0.0482	0.0058	24.81	2.87	24.14	0.79
TAU-23-1_094	3	0.0267	0.0024	0.0038	0.00011	0.0510	0.0045	26.76	2.41	24.43	0.73
TAU-23-1_095	3	0.0238	0.0012	0.0037	0.00009	0.0472	0.0023	23.90	1.19	23.55	0.61
TAU-23-1_096	3	0.0239	0.0009	0.0036	0.00009	0.0483	0.0016	24.00	0.86	23.12	0.59
TAU-23-1_097	3	0.0237	0.0015	0.0036	0.00010	0.0478	0.0030	23.73	1.50	23.11	0.65
TAU-23-1_098	3	0.0254	0.0019	0.0037	0.00011	0.0509	0.0039	25.50	1.86	23.81	0.70
TAU-23-1_100	3	0.0249	0.0016	0.0038	0.00010	0.0474	0.0030	25.00	1.58	24.60	0.66
TAU-23-1_101	3	0.0242	0.0025	0.0038	0.00011	0.0457	0.0044	24.26	2.47	24.16	0.74
TAU-23-1_103	3	0.0233	0.0016	0.0037	0.00010	0.0465	0.0033	23.41	1.60	23.51	0.63
TAU-23-1_104	3	0.0230	0.0018	0.0036	0.00010	0.0462	0.0035	23.11	1.75	23.30	0.65
TAU-23-1_105	3	0.0239	0.0011	0.0036	0.00011	0.0477	0.0021	23.99	1.13	23.43	0.71
TAU-23-1_108	3	0.0248	0.0013	0.0038	0.00010	0.0480	0.0024	24.83	1.25	24.13	0.64
TAU-23-1_110	3	0.0232	0.0009	0.0037	0.00010	0.0456	0.0017	23.27	0.88	23.78	0.63
TAU-23-1_111	3	0.0234	0.0010	0.0036	0.00009	0.0472	0.0018	23.49	0.96	23.15	0.58
TAU-23-1_112	3	0.0243	0.0013	0.0037	0.00010	0.0479	0.0023	24.40	1.26	23.72	0.63
TAU-23-1_113	3	0.0235	0.0009	0.0036	0.00009	0.0475	0.0018	23.59	0.93	23.10	0.57
TAU-23-1_114	3	0.0246	0.0015	0.0038	0.00010	0.0473	0.0028	24.68	1.46	24.34	0.66

Spot	Rating	Isotopic ratios						Dates (Ma)			
	(0=worst, 3=best)	²⁰⁷ Pb/ ²³⁵ U	±2σ (abs.)	²⁰⁶ Pb/ ²³⁸ U	±2σ (abs.)	²⁰⁷ Pb/ ²⁰⁶ Pb	±2σ (abs.)	²⁰⁷ Pb/ ²³⁵ U	±2σ (abs.)	²⁰⁶ Pb/ ²³⁸ U	±2σ (abs.)
TAU-23-1_116	3	0.0232	0.0019	0.0037	0.00011	0.0460	0.0038	23.29	1.89	23.58	0.74
TAU-23-1_117	3	0.0247	0.0013	0.0038	0.00010	0.0476	0.0024	24.77	1.27	24.27	0.62
TAU-23-1_121	3	0.0223	0.0012	0.0035	0.00009	0.0470	0.0024	22.40	1.17	22.56	0.60
TAU-23-1_125	3	0.0235	0.0010	0.0037	0.00009	0.0464	0.0017	23.61	0.99	23.80	0.60
TAU-23-1_126	3	0.0236	0.0014	0.0038	0.00011	0.0456	0.0024	23.67	1.36	24.17	0.68
TAU-23-1_127	3	0.0253	0.0011	0.0038	0.00010	0.0487	0.0020	25.36	1.07	24.26	0.67
TAU-23-1_128	3	0.0269	0.0025	0.0038	0.00018	0.0520	0.0044	26.92	2.49	24.16	1.13
TAU-23-1_129	3	0.0245	0.0011	0.0037	0.00009	0.0478	0.0020	24.57	1.09	23.96	0.58
TAU-23-1_131	3	0.0240	0.0013	0.0037	0.00010	0.0467	0.0023	24.10	1.25	24.05	0.64
TAU-23-1_132	3	0.0256	0.0020	0.0038	0.00012	0.0494	0.0035	25.67	1.96	24.19	0.79
TAU-23-1_135	3	0.0241	0.0009	0.0037	0.00009	0.0472	0.0016	24.14	0.90	23.79	0.60
TAU-23-1_137	3	0.0238	0.0010	0.0037	0.00010	0.0471	0.0021	23.88	1.02	23.63	0.62
TAU-23-1_138	3	0.0246	0.0017	0.0036	0.00011	0.0497	0.0033	24.68	1.65	23.16	0.69
TAU-23-1_139	3	0.0242	0.0010	0.0036	0.00009	0.0481	0.0017	24.23	1.00	23.39	0.60
TAU-23-1_142	3	0.0238	0.0017	0.0037	0.00011	0.0467	0.0034	23.90	1.67	23.89	0.70
TAU-23-1_146	3	0.0246	0.0016	0.0037	0.00010	0.0484	0.0034	24.62	1.60	23.77	0.67
TAU-23-1_149	3	0.0260	0.0020	0.0037	0.00010	0.0512	0.0037	26.04	1.94	23.66	0.63
TAU-23-1_150	3	0.0251	0.0011	0.0038	0.00010	0.0484	0.0021	25.12	1.12	24.15	0.61
TAU-23-1_151	3	0.0257	0.0014	0.0038	0.00010	0.0488	0.0026	25.71	1.38	24.47	0.66
TAU-23-1_153	3	0.0231	0.0018	0.0037	0.00012	0.0451	0.0034	23.13	1.77	23.92	0.78
TAU-23-1_154	3	0.0248	0.0023	0.0036	0.00012	0.0496	0.0046	24.88	2.24	23.48	0.78
TAU-23-1_165	3	0.0249	0.0019	0.0038	0.00011	0.0481	0.0037	25.00	1.92	24.20	0.74
TAU-23-1_166	3	0.0266	0.0017	0.0038	0.00013	0.0515	0.0035	26.63	1.68	24.19	0.82
TAU-23-1_168	3	0.0238	0.0023	0.0036	0.00012	0.0476	0.0040	23.87	2.23	23.21	0.74

Spot	Rating	Isotopic ratios						Dates (Ma)			
	(0=worst, 3=best)	²⁰⁷ Pb/ ²³⁵ U	±2σ (abs.)	²⁰⁶ Pb/ ²³⁸ U	±2σ (abs.)	²⁰⁷ Pb/ ²⁰⁶ Pb	±2σ (abs.)	²⁰⁷ Pb/ ²³⁵ U	±2σ (abs.)	²⁰⁶ Pb/ ²³⁸ U	±2σ (abs.)
TAU-23-1_001	2	0.0252	0.0033	0.0037	0.00013	0.0500	0.0061	25.26	3.30	23.64	0.86
TAU-23-1_004	2	0.0236	0.0011	0.0035	0.00010	0.0490	0.0020	23.72	1.08	22.56	0.62
TAU-23-1_006	2	0.0232	0.0015	0.0035	0.00010	0.0486	0.0028	23.23	1.45	22.25	0.62
TAU-23-1_008	2	0.0253	0.0012	0.0038	0.00016	0.0486	0.0020	25.33	1.17	24.40	1.01
TAU-23-1_013	2	0.0249	0.0020	0.0036	0.00011	0.0500	0.0042	24.95	2.01	23.32	0.71
TAU-23-1_019	2	0.0226	0.0008	0.0035	0.00009	0.0463	0.0017	22.70	0.79	22.77	0.55
TAU-23-1_047	2	0.0251	0.0021	0.0036	0.00009	0.0504	0.0041	25.14	2.05	23.21	0.59
TAU-23-1_054	2	0.0266	0.0016	0.0039	0.00014	0.0496	0.0025	26.63	1.57	24.93	0.92
TAU-23-1_056	2	0.0266	0.0023	0.0038	0.00013	0.0512	0.0035	26.68	2.30	24.75	0.85
TAU-23-1_068	2	0.0239	0.0018	0.0035	0.00010	0.0492	0.0033	23.98	1.75	22.62	0.62
TAU-23-1_073	2	0.0250	0.0024	0.0036	0.00013	0.0505	0.0046	25.06	2.35	23.07	0.80
TAU-23-1_074	2	0.0271	0.0023	0.0038	0.00013	0.0518	0.0042	27.14	2.23	24.39	0.84
TAU-23-1_077	2	0.0230	0.0013	0.0035	0.00010	0.0471	0.0023	23.13	1.27	22.78	0.66
TAU-23-1_078	2	0.0259	0.0017	0.0038	0.00012	0.0500	0.0032	25.97	1.67	24.23	0.79
TAU-23-1_082	2	0.0227	0.0013	0.0035	0.00010	0.0478	0.0027	22.82	1.29	22.22	0.65
TAU-23-1_099	2	0.0224	0.0017	0.0036	0.00012	0.0453	0.0035	22.49	1.68	23.11	0.74
TAU-23-1_106	2	0.0233	0.0013	0.0038	0.00010	0.0446	0.0023	23.36	1.27	24.36	0.66
TAU-23-1_107	2	0.0252	0.0026	0.0038	0.00014	0.0480	0.0051	25.27	2.62	24.60	0.89
TAU-23-1_109	2	0.0260	0.0024	0.0037	0.00019	0.0510	0.0034	26.07	2.33	23.80	1.22
TAU-23-1_115	2	0.0266	0.0032	0.0039	0.00013	0.0499	0.0055	26.61	3.12	24.78	0.82
TAU-23-1_118	2	0.0247	0.0010	0.0038	0.00010	0.0473	0.0016	24.82	1.03	24.40	0.63
TAU-23-1_120	2	0.0268	0.0031	0.0040	0.00014	0.0490	0.0056	26.88	3.09	25.55	0.90
TAU-23-1_123	2	0.0264	0.0013	0.0037	0.00012	0.0519	0.0025	26.44	1.32	23.73	0.78
TAU-23-1_130	2	0.0265	0.0020	0.0039	0.00012	0.0488	0.0037	26.58	1.96	25.40	0.75

Spot	Rating	Isotopic ratios						Dates (Ma)			
	(0=worst, 3=best)	²⁰⁷ Pb/ ²³⁵ U	±2σ (abs.)	²⁰⁶ Pb/ ²³⁸ U	±2σ (abs.)	²⁰⁷ Pb/ ²⁰⁶ Pb	±2σ (abs.)	²⁰⁷ Pb/ ²³⁵ U	±2σ (abs.)	²⁰⁶ Pb/ ²³⁸ U	±2σ (abs.)
TAU-23-1_134	2	0.0237	0.0016	0.0035	0.00011	0.0489	0.0032	23.76	1.62	22.62	0.71
TAU-23-1_136	2	0.0244	0.0029	0.0038	0.00015	0.0471	0.0064	24.48	2.90	24.72	0.98
TAU-23-1_141	2	0.0240	0.0010	0.0036	0.00009	0.0486	0.0018	24.12	0.98	23.08	0.59
TAU-23-1_143	2	0.0256	0.0029	0.0036	0.00013	0.0526	0.0058	25.70	2.82	22.86	0.81
TAU-23-1_145	2	0.0256	0.0009	0.0039	0.00010	0.0478	0.0015	25.64	0.91	24.96	0.63
TAU-23-1_147	2	0.0249	0.0032	0.0040	0.00015	0.0456	0.0057	24.99	3.13	25.50	0.99
TAU-23-1_148	2	0.0267	0.0025	0.0037	0.00012	0.0518	0.0051	26.70	2.49	24.07	0.80
TAU-23-1_152	2	0.0254	0.0014	0.0037	0.00010	0.0495	0.0026	25.47	1.40	23.96	0.66
TAU-23-1_158	2	0.0264	0.0012	0.0040	0.00011	0.0474	0.0017	26.50	1.17	25.96	0.71
TAU-23-1_160	2	0.0262	0.0015	0.0039	0.00013	0.0491	0.0027	26.27	1.50	24.86	0.85
TAU-23-1_164	2	0.0252	0.0011	0.0037	0.00011	0.0493	0.0021	25.26	1.04	23.80	0.68
TAU-23-1_167	2	0.0269	0.0010	0.0038	0.00011	0.0511	0.0013	26.91	0.96	24.49	0.69
TAU-23-1_005	1	0.6276	0.0226	0.0763	0.00211	0.0598	0.0017	494.37	14.07	473.83	12.64
TAU-23-1_079	1	0.0355	0.0051	0.0044	0.00020	0.0575	0.0077	35.32	4.96	28.59	1.28
TAU-23-1_092	1	0.0356	0.0022	0.0038	0.00010	0.0682	0.0037	35.49	2.15	24.28	0.66
TAU-23-1_102	1	0.0299	0.0026	0.0036	0.00012	0.0606	0.0047	29.87	2.51	22.96	0.80
TAU-23-1_133	1	0.0291	0.0032	0.0037	0.00014	0.0571	0.0060	29.05	3.14	23.83	0.93
TAU-23-1_155	1	0.0290	0.0033	0.0037	0.00012	0.0559	0.0055	28.98	3.24	24.02	0.75
TAU-23-1_156	1	0.0256	0.0010	0.0036	0.00010	0.0514	0.0021	25.64	0.97	23.21	0.63
TAU-23-1_159	1	0.0286	0.0029	0.0037	0.00014	0.0554	0.0051	28.60	2.91	24.09	0.93
TAU-23-1_007	0	0.8977	0.1060	0.0112	0.00090	0.5595	0.0335	632.48	61.49	71.71	5.76
TAU-23-1_010	0	0.3618	0.0217	0.0305	0.00099	0.0861	0.0047	313.20	16.26	193.94	6.22
TAU-23-1_015	0	0.0482	0.0043	0.0039	0.00020	0.0890	0.0061	47.76	4.16	25.39	1.29
TAU-23-1_022	0	3.8169	0.2065	0.0365	0.00288	0.7678	0.0662	1594.49	43.61	230.96	17.92

Spot	Rating	Isotopic ratios						Dates (Ma)			
	(0=worst, 3=best)	²⁰⁷ Pb/ ²³⁵ U	±2σ (abs.)	²⁰⁶ Pb/ ²³⁸ U	±2σ (abs.)	²⁰⁷ Pb/ ²⁰⁶ Pb	±2σ (abs.)	²⁰⁷ Pb/ ²³⁵ U	±2σ (abs.)	²⁰⁶ Pb/ ²³⁸ U	±2σ (abs.)
TAU-23-1_033	0	0.1634	0.0196	0.0050	0.00033	0.2352	0.0258	153.37	17.13	32.43	2.10
TAU-23-1_034	0	0.0526	0.0073	0.0039	0.00015	0.0982	0.0139	51.90	7.08	24.99	0.98
TAU-23-1_036	0	0.6413	0.0371	0.0589	0.00371	0.0818	0.0054	505.87	25.01	368.41	22.56
TAU-23-1_042	0	0.3280	0.0317	0.0066	0.00042	0.3595	0.0240	287.02	24.39	42.35	2.70
TAU-23-1_046	0	0.1538	0.0140	0.0053	0.00027	0.2085	0.0158	144.54	12.47	34.10	1.76
TAU-23-1_052	0	0.0841	0.0060	0.0043	0.00012	0.1421	0.0083	81.81	5.59	27.38	0.79
TAU-23-1_055	0	1.5515	0.1055	0.1249	0.00455	0.0889	0.0039	941.96	44.86	758.13	26.18
TAU-23-1_059	0	0.0591	0.0068	0.0038	0.00012	0.1121	0.0109	58.09	6.48	24.16	0.80
TAU-23-1_063	0	0.0871	0.0070	0.0043	0.00013	0.1453	0.0094	84.57	6.60	27.60	0.82
TAU-23-1_084	0	0.0289	0.0014	0.0034	0.00011	0.0611	0.0027	28.91	1.43	21.83	0.70
TAU-23-1_091	0	0.0957	0.0186	0.0051	0.00032	0.1360	0.0242	91.27	16.94	32.76	2.04
TAU-23-1_119	0	0.0504	0.0039	0.0038	0.00013	0.0962	0.0068	49.84	3.73	24.47	0.85
TAU-23-1_122	0	0.0705	0.0129	0.0041	0.00018	0.1187	0.0166	68.45	11.90	26.65	1.14
TAU-23-1_124	0	0.0762	0.0072	0.0043	0.00013	0.1268	0.0109	74.38	6.84	27.88	0.86
TAU-23-1_140	0	0.0494	0.0059	0.0039	0.00011	0.0912	0.0093	48.79	5.67	24.87	0.72
TAU-23-1_014	0	1.7687	0.0491	0.1724	0.00489	0.0745	0.0016	1033.65	17.99	1025.42	26.89
TAU-23-1_020	0	0.9135	0.0403	0.1073	0.00279	0.0619	0.0025	657.04	21.44	656.78	16.25
TAU-23-1_021	0	0.9045	0.0373	0.1045	0.00363	0.0628	0.0020	653.44	20.05	640.47	21.19
TAU-23-1_037	0	1.1614	0.0365	0.1276	0.00334	0.0659	0.0017	781.66	17.11	774.16	19.07
TAU-23-1_144	0	4.7014	0.1736	0.3143	0.01016	0.1083	0.0029	1766.16	30.54	1761.29	49.47
TAU-23-1_157	0	3.2792	0.1256	0.2532	0.00899	0.0938	0.0027	1474.77	29.81	1454.55	46.19
TAU-23-1_161	0	0.4825	0.0224	0.0628	0.00262	0.0557	0.0014	399.32	15.25	392.63	15.84
TAU-23-1_162	0	0.2641	0.0084	0.0371	0.00094	0.0515	0.0013	237.85	6.77	235.02	5.83
TAU-23-1_163	0	0.2547	0.0070	0.0358	0.00095	0.0515	0.0011	230.30	5.64	226.82	5.94

Spot	Rating	Isotopic ratios						Dates (Ma)			
	(0=worst, 3=best)	²⁰⁷ Pb/ ²³⁵ U	±2σ (abs.)	²⁰⁶ Pb/ ²³⁸ U	±2σ (abs.)	²⁰⁷ Pb/ ²⁰⁶ Pb	±2σ (abs.)	²⁰⁷ Pb/ ²³⁵ U	±2σ (abs.)	²⁰⁶ Pb/ ²³⁸ U	±2σ (abs.)
TAU-23-2_010	3	0.0240	0.0011	0.0037	0.00012	0.0481	0.0022	24.08	1.12	23.56	0.79
TAU-23-2_011	3	0.0244	0.0010	0.0037	0.00010	0.0479	0.0020	24.50	0.99	23.75	0.62
TAU-23-2_024	3	0.0239	0.0007	0.0037	0.00009	0.0467	0.0011	23.99	0.68	23.73	0.59
TAU-23-2_027	3	0.0246	0.0022	0.0037	0.00011	0.0473	0.0039	24.66	2.17	23.86	0.74
TAU-23-2_028	3	0.0247	0.0018	0.0037	0.00011	0.0481	0.0035	24.73	1.77	23.86	0.68
TAU-23-2_031	3	0.0234	0.0018	0.0036	0.00011	0.0469	0.0036	23.44	1.74	23.32	0.72
TAU-23-2_032	3	0.0251	0.0018	0.0039	0.00012	0.0471	0.0033	25.19	1.77	24.97	0.79
TAU-23-2_033	3	0.0262	0.0025	0.0038	0.00012	0.0504	0.0047	26.25	2.51	24.22	0.76
TAU-23-2_034	3	0.0271	0.0028	0.0039	0.00012	0.0510	0.0054	27.14	2.80	24.89	0.77
TAU-23-2_037	3	0.0234	0.0015	0.0037	0.00011	0.0461	0.0030	23.48	1.47	23.72	0.70
TAU-23-2_039	3	0.0237	0.0017	0.0038	0.00011	0.0447	0.0032	23.72	1.73	24.73	0.72
TAU-23-2_040	3	0.0241	0.0017	0.0038	0.00012	0.0465	0.0031	24.15	1.69	24.37	0.76
TAU-23-2_045	3	0.0241	0.0025	0.0037	0.00013	0.0491	0.0059	24.14	2.42	23.96	0.86
TAU-23-2_046	3	0.0251	0.0028	0.0039	0.00014	0.0468	0.0051	25.16	2.73	24.99	0.87
TAU-23-2_048	3	0.0270	0.0032	0.0038	0.00016	0.0514	0.0058	27.03	3.18	24.62	1.04
TAU-23-2_049	3	0.0229	0.0013	0.0037	0.00011	0.0455	0.0025	23.00	1.25	23.55	0.71
TAU-23-2_051	3	0.0248	0.0013	0.0039	0.00011	0.0465	0.0024	24.83	1.25	24.89	0.68
TAU-23-2_054	3	0.0241	0.0016	0.0037	0.00010	0.0477	0.0032	24.17	1.61	23.61	0.62
TAU-23-2_055	3	0.0241	0.0018	0.0038	0.00011	0.0468	0.0036	24.15	1.75	24.15	0.69
TAU-23-2_056	3	0.0253	0.0026	0.0038	0.00012	0.0487	0.0047	25.32	2.57	24.14	0.74
TAU-23-2_059	3	0.0236	0.0015	0.0037	0.00011	0.0472	0.0031	23.64	1.48	23.73	0.70
TAU-23-2_060	3	0.0259	0.0017	0.0038	0.00011	0.0494	0.0032	25.94	1.65	24.48	0.74
TAU-23-2_065	3	0.0250	0.0018	0.0037	0.00010	0.0498	0.0037	25.55	1.95	23.89	0.66
TAU-23-2_068	3	0.0235	0.0021	0.0037	0.00013	0.0464	0.0043	23.62	2.13	23.74	0.81

Spot	Rating	Isotopic ratios						Dates (Ma)			
	(0=worst, 3=best)	²⁰⁷ Pb/ ²³⁵ U	±2σ (abs.)	²⁰⁶ Pb/ ²³⁸ U	±2σ (abs.)	²⁰⁷ Pb/ ²⁰⁶ Pb	±2σ (abs.)	²⁰⁷ Pb/ ²³⁵ U	±2σ (abs.)	²⁰⁶ Pb/ ²³⁸ U	±2σ (abs.)
TAU-23-2_071	3	0.0236	0.0016	0.0038	0.00010	0.0449	0.0029	23.69	1.58	24.55	0.63
TAU-23-2_080	3	0.0249	0.0010	0.0038	0.00012	0.0471	0.0021	24.94	1.00	24.71	0.78
TAU-23-2_081	3	0.0256	0.0022	0.0037	0.00011	0.0492	0.0038	25.65	2.16	24.05	0.73
TAU-23-2_083	3	0.0243	0.0014	0.0038	0.00010	0.0462	0.0023	24.42	1.35	24.54	0.63
TAU-23-2_086	3	0.0236	0.0015	0.0037	0.00010	0.0459	0.0030	23.67	1.49	24.04	0.65
TAU-23-2_087	3	0.0244	0.0010	0.0037	0.00010	0.0476	0.0018	24.50	0.98	23.90	0.65
TAU-23-2_088	3	0.0236	0.0012	0.0038	0.00011	0.0453	0.0022	23.72	1.17	24.34	0.71
TAU-23-2_093	3	0.0249	0.0016	0.0038	0.00010	0.0481	0.0032	24.98	1.61	24.17	0.65
TAU-23-2_094	3	0.0246	0.0019	0.0038	0.00012	0.0470	0.0035	24.64	1.90	24.34	0.74
TAU-23-2_095	3	0.0252	0.0011	0.0038	0.00013	0.0479	0.0019	25.24	1.09	24.51	0.87
TAU-23-2_096	3	0.0241	0.0010	0.0037	0.00009	0.0470	0.0018	24.15	1.03	23.80	0.58
TAU-23-2_097	3	0.0252	0.0013	0.0038	0.00011	0.0483	0.0025	25.30	1.32	24.38	0.68
TAU-23-2_100	3	0.0238	0.0009	0.0037	0.00011	0.0461	0.0013	23.87	0.90	23.84	0.68
TAU-23-2_101	3	0.0261	0.0021	0.0038	0.00012	0.0495	0.0036	26.15	2.03	24.53	0.80
TAU-23-2_102	3	0.0238	0.0015	0.0036	0.00010	0.0466	0.0023	23.91	1.45	23.34	0.62
TAU-23-2_105	3	0.0261	0.0015	0.0038	0.00010	0.0498	0.0029	26.14	1.49	24.40	0.63
TAU-23-2_109	3	0.0245	0.0013	0.0038	0.00010	0.0471	0.0024	24.54	1.26	24.21	0.65
TAU-23-2_110	3	0.0254	0.0015	0.0038	0.00012	0.0482	0.0026	25.45	1.46	24.49	0.77
TAU-23-2_111	3	0.0245	0.0012	0.0038	0.00010	0.0471	0.0020	24.62	1.16	24.23	0.63
TAU-23-2_112	3	0.0234	0.0012	0.0037	0.00010	0.0461	0.0023	23.48	1.23	23.63	0.62
TAU-23-2_113	3	0.0229	0.0013	0.0036	0.00010	0.0460	0.0026	22.95	1.26	23.16	0.64
TAU-23-2_116	3	0.0241	0.0011	0.0036	0.00009	0.0482	0.0021	24.13	1.07	23.20	0.60
TAU-23-2_119	3	0.0249	0.0014	0.0038	0.00011	0.0473	0.0024	24.93	1.39	24.39	0.72
TAU-23-2_122	3	0.0243	0.0016	0.0037	0.00009	0.0474	0.0031	24.39	1.61	23.73	0.60

Spot	Rating	Isotopic ratios						Dates (Ma)			
	(0=worst, 3=best)	²⁰⁷ Pb/ ²³⁵ U	±2σ (abs.)	²⁰⁶ Pb/ ²³⁸ U	±2σ (abs.)	²⁰⁷ Pb/ ²⁰⁶ Pb	±2σ (abs.)	²⁰⁷ Pb/ ²³⁵ U	±2σ (abs.)	²⁰⁶ Pb/ ²³⁸ U	±2σ (abs.)
TAU-23-2_123	3	0.0259	0.0012	0.0038	0.00011	0.0492	0.0024	25.92	1.19	24.46	0.74
TAU-23-2_124	3	0.0242	0.0014	0.0037	0.00010	0.0467	0.0028	24.24	1.43	24.11	0.67
TAU-23-2_126	3	0.0254	0.0022	0.0039	0.00012	0.0466	0.0036	25.49	2.16	24.84	0.79
TAU-23-2_127	3	0.0245	0.0027	0.0037	0.00013	0.0476	0.0056	24.54	2.67	24.08	0.87
TAU-23-2_129	3	0.0248	0.0012	0.0037	0.00012	0.0481	0.0026	24.82	1.18	23.83	0.78
TAU-23-2_130	3	0.0257	0.0020	0.0039	0.00012	0.0477	0.0038	25.74	1.96	25.11	0.77
TAU-23-2_131	3	0.0240	0.0013	0.0036	0.00009	0.0482	0.0024	24.08	1.29	23.15	0.56
TAU-23-2_132	3	0.0250	0.0010	0.0038	0.00010	0.0478	0.0018	25.08	1.04	24.31	0.63
TAU-23-2_133	3	0.0257	0.0012	0.0038	0.00011	0.0483	0.0018	25.73	1.15	24.66	0.73
TAU-23-2_134	3	0.0228	0.0016	0.0036	0.00010	0.0461	0.0031	22.92	1.57	23.03	0.61
TAU-23-2_136	3	0.0244	0.0027	0.0037	0.00014	0.0475	0.0052	24.45	2.65	24.03	0.88
TAU-23-2_137	3	0.0235	0.0023	0.0037	0.00012	0.0464	0.0049	23.58	2.24	23.62	0.74
TAU-23-2_138	3	0.0250	0.0010	0.0038	0.00010	0.0478	0.0016	25.11	1.03	24.33	0.64
TAU-23-2_139	3	0.0258	0.0017	0.0037	0.00011	0.0497	0.0033	25.81	1.64	24.11	0.70
TAU-23-2_003	2	0.0259	0.0019	0.0039	0.00011	0.0478	0.0038	25.95	1.92	25.36	0.72
TAU-23-2_009	2	0.0273	0.0034	0.0039	0.00013	0.0511	0.0063	27.32	3.38	24.85	0.81
TAU-23-2_013	2	0.0245	0.0018	0.0036	0.00011	0.0488	0.0036	25.18	2.12	23.37	0.70
TAU-23-2_014	2	0.0263	0.0025	0.0037	0.00014	0.0517	0.0044	26.37	2.44	23.66	0.87
TAU-23-2_019	2	0.0265	0.0028	0.0038	0.00014	0.0503	0.0049	26.54	2.73	24.49	0.93
TAU-23-2_023	2	0.0265	0.0038	0.0036	0.00018	0.0528	0.0077	26.47	3.72	23.45	1.13
TAU-23-2_036	2	0.0264	0.0033	0.0041	0.00014	0.0474	0.0057	26.40	3.22	26.10	0.89
TAU-23-2_047	2	0.0242	0.0010	0.0037	0.00009	0.0476	0.0021	24.28	1.04	23.77	0.60
TAU-23-2_057	2	0.0272	0.0023	0.0038	0.00013	0.0514	0.0044	27.24	2.23	24.44	0.82
TAU-23-2_058	2	0.0264	0.0013	0.0040	0.00012	0.0475	0.0024	26.43	1.33	25.97	0.77

Spot	Rating	Isotopic ratios						Dates (Ma)			
	(0=worst, 3=best)	²⁰⁷ Pb/ ²³⁵ U	±2σ (abs.)	²⁰⁶ Pb/ ²³⁸ U	±2σ (abs.)	²⁰⁷ Pb/ ²⁰⁶ Pb	±2σ (abs.)	²⁰⁷ Pb/ ²³⁵ U	±2σ (abs.)	²⁰⁶ Pb/ ²³⁸ U	±2σ (abs.)
TAU-23-2_067	2	0.0290	0.0052	0.0038	0.00012	0.0558	0.0104	28.94	5.15	24.31	0.79
TAU-23-2_069	2	0.0268	0.0016	0.0039	0.00011	0.0505	0.0036	26.85	1.58	24.89	0.73
TAU-23-2_075	2	0.0250	0.0013	0.0037	0.00010	0.0490	0.0027	25.05	1.31	23.49	0.64
TAU-23-2_077	2	0.0254	0.0014	0.0039	0.00012	0.0477	0.0025	25.46	1.42	24.91	0.76
TAU-23-2_078	2	0.0262	0.0017	0.0038	0.00012	0.0504	0.0035	26.21	1.72	24.26	0.75
TAU-23-2_079	2	0.0249	0.0012	0.0037	0.00010	0.0489	0.0021	24.95	1.22	23.65	0.66
TAU-23-2_082	2	0.0267	0.0017	0.0040	0.00019	0.0482	0.0022	26.79	1.69	25.87	1.19
TAU-23-2_092	2	0.0262	0.0037	0.0037	0.00012	0.0507	0.0071	26.28	3.63	24.07	0.77
TAU-23-2_099	2	0.0257	0.0024	0.0037	0.00012	0.0508	0.0051	25.79	2.40	23.72	0.76
TAU-23-2_106	2	0.0252	0.0020	0.0036	0.00010	0.0493	0.0034	25.25	1.98	23.24	0.64
TAU-23-2_108	2	0.0256	0.0017	0.0039	0.00012	0.0475	0.0033	25.71	1.70	25.18	0.80
TAU-23-2_115	2	0.0240	0.0008	0.0036	0.00010	0.0473	0.0012	24.11	0.80	23.45	0.65
TAU-23-2_118	2	0.0297	0.0037	0.0038	0.00012	0.0565	0.0071	29.71	3.66	24.45	0.78
TAU-23-2_135	2	0.0259	0.0019	0.0038	0.00013	0.0492	0.0033	26.00	1.89	24.48	0.81
TAU-23-2_001	1	0.0285	0.0013	0.0038	0.00010	0.0548	0.0028	28.48	1.28	24.48	0.62
TAU-23-2_012	1	0.0262	0.0008	0.0037	0.00009	0.0507	0.0013	26.29	0.79	24.06	0.59
TAU-23-2_018	1	0.0263	0.0011	0.0037	0.00011	0.0514	0.0019	26.40	1.13	23.89	0.71
TAU-23-2_038	1	0.0288	0.0021	0.0039	0.00018	0.0530	0.0032	28.80	2.11	25.14	1.18
TAU-23-2_050	1	0.0325	0.0022	0.0035	0.00009	0.0664	0.0043	32.48	2.12	22.73	0.60
TAU-23-2_061	1	0.0286	0.0019	0.0040	0.00014	0.0515	0.0030	28.64	1.88	25.93	0.88
TAU-23-2_098	1	0.0333	0.0023	0.0037	0.00011	0.0645	0.0043	33.28	2.30	24.03	0.68
TAU-23-2_103	1	0.0271	0.0009	0.0036	0.00009	0.0544	0.0017	27.20	0.88	23.17	0.56
TAU-23-2_117	1	0.0256	0.0013	0.0036	0.00011	0.0514	0.0026	25.68	1.32	23.20	0.73
TAU-23-2_002	0	0.0656	0.0065	0.0041	0.00013	0.1163	0.0114	64.37	6.23	26.26	0.86

Spot	Rating	Isotopic ratios						Dates (Ma)			
	(0=worst, 3=best)	²⁰⁷ Pb/ ²³⁵ U	±2σ (abs.)	²⁰⁶ Pb/ ²³⁸ U	±2σ (abs.)	²⁰⁷ Pb/ ²⁰⁶ Pb	±2σ (abs.)	²⁰⁷ Pb/ ²³⁵ U	±2σ (abs.)	²⁰⁶ Pb/ ²³⁸ U	±2σ (abs.)
TAU-23-2_004	0	0.0422	0.0016	0.0038	0.00009	0.0805	0.0029	41.94	1.58	24.40	0.61
TAU-23-2_005	0	0.0517	0.0037	0.0040	0.00015	0.0954	0.0083	52.33	4.32	25.95	0.95
TAU-23-2_006	0	0.0315	0.0012	0.0042	0.00011	0.0538	0.0017	31.52	1.15	27.30	0.73
TAU-23-2_007	0	0.0850	0.0102	0.0050	0.00016	0.1228	0.0133	82.54	9.48	32.08	1.02
TAU-23-2_008	0	0.0342	0.0017	0.0043	0.00016	0.0578	0.0030	34.09	1.66	27.65	1.05
TAU-23-2_017	0	0.0541	0.0071	0.0073	0.00076	0.0532	0.0026	53.39	6.89	46.83	4.88
TAU-23-2_020	0	0.0879	0.0084	0.0045	0.00014	0.1411	0.0118	85.46	7.77	28.93	0.91
TAU-23-2_021	0	0.0421	0.0018	0.0042	0.00011	0.0727	0.0028	41.91	1.72	27.00	0.71
TAU-23-2_022	0	1.7323	0.0993	0.1161	0.00602	0.1079	0.0034	1018.60	36.19	707.90	34.73
TAU-23-2_025	0	54.2849	1.7840	0.4672	0.01704	0.8443	0.0209	4070.74	32.73	2468.48	74.61
TAU-23-2_026	0	22.1069	1.5650	0.1924	0.01400	0.8344	0.0208	3165.51	69.70	1130.24	75.38
TAU-23-2_029	0	0.0375	0.0021	0.0037	0.00012	0.0731	0.0031	37.40	2.03	24.04	0.76
TAU-23-2_030	0	0.0514	0.0043	0.0043	0.00015	0.0878	0.0073	51.87	4.58	27.76	0.95
TAU-23-2_035	0	0.0861	0.0038	0.0042	0.00011	0.1471	0.0058	83.84	3.53	27.29	0.71
TAU-23-2_052	0	0.9530	0.0423	0.0952	0.00407	0.0725	0.0013	677.64	22.65	585.99	24.09
TAU-23-2_053	0	0.4131	0.0182	0.0419	0.00176	0.0712	0.0019	350.42	13.02	264.48	10.89
TAU-23-2_062	0	0.0298	0.0019	0.0041	0.00015	0.0531	0.0025	29.82	1.83	26.15	0.94
TAU-23-2_063	0	0.0303	0.0019	0.0035	0.00012	0.0634	0.0033	30.26	1.92	22.23	0.76
TAU-23-2_064	0	0.0509	0.0060	0.0040	0.00020	0.0904	0.0100	50.21	5.73	25.73	1.25
TAU-23-2_066	0	6.1361	0.4055	0.0561	0.00337	0.7944	0.0272	1989.14	57.02	351.47	20.54
TAU-23-2_070	0	0.0546	0.0046	0.0041	0.00014	0.0955	0.0073	53.85	4.38	26.57	0.92
TAU-23-2_074	0	0.6760	0.0204	0.0707	0.00232	0.0692	0.0012	524.05	12.32	440.48	13.96
TAU-23-2_076	0	0.0310	0.0014	0.0039	0.00015	0.0575	0.0022	31.03	1.41	25.27	0.98
TAU-23-2_085	0	0.2091	0.0276	0.0056	0.00026	0.2670	0.0305	191.64	23.44	36.11	1.68

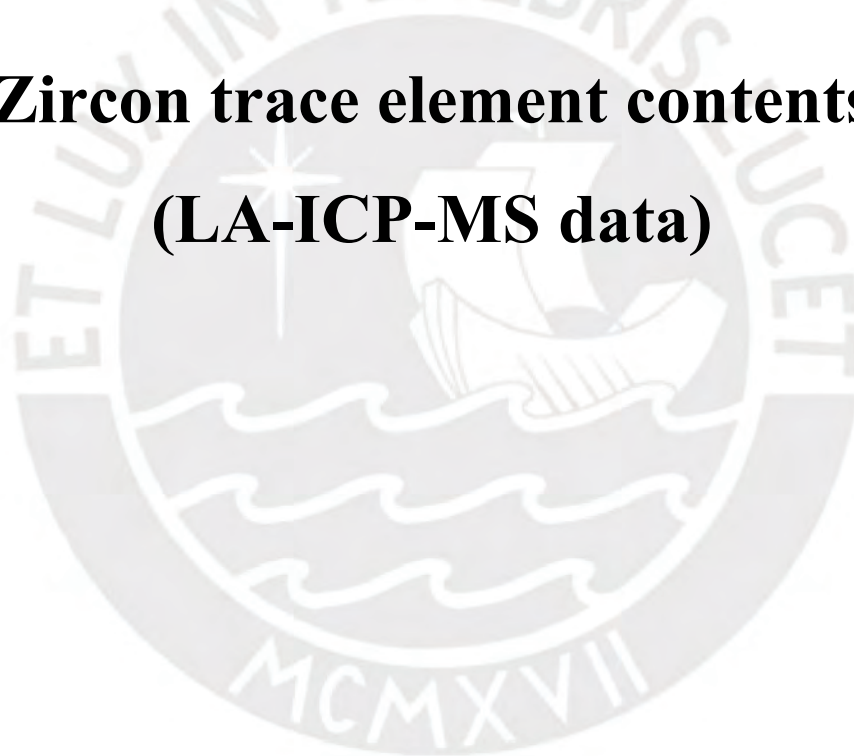
Spot	Rating	Isotopic ratios						Dates (Ma)			
	(0=worst, 3=best)	²⁰⁷ Pb/ ²³⁵ U	±2σ (abs.)	²⁰⁶ Pb/ ²³⁸ U	±2σ (abs.)	²⁰⁷ Pb/ ²⁰⁶ Pb	±2σ (abs.)	²⁰⁷ Pb/ ²³⁵ U	±2σ (abs.)	²⁰⁶ Pb/ ²³⁸ U	±2σ (abs.)
TAU-23-2_104	0	59.7604	5.4478	0.5196	0.05017	0.8345	0.0180	4156.91	94.03	2686.43	213.82
TAU-23-2_107	0	0.0544	0.0038	0.0047	0.00015	0.0833	0.0054	53.77	3.69	30.38	0.99
TAU-23-2_125	0	0.1776	0.0069	0.0053	0.00015	0.2429	0.0078	165.89	5.95	33.96	0.98
TAU-23-2_128	0	0.0276	0.0015	0.0034	0.00013	0.0586	0.0022	27.63	1.44	21.83	0.82
TAU-23-2_140	0	0.4641	0.0268	0.0082	0.00031	0.4082	0.0122	385.44	19.11	52.73	2.01
TAU-23-2_141	0	0.0270	0.0008	0.0039	0.00011	0.0510	0.0010	27.08	0.77	24.78	0.71
TAU-23-2_015	0	0.4021	0.0203	0.0525	0.00206	0.0555	0.0018	342.95	14.67	329.73	12.61
TAU-23-2_016	0	2.2466	0.0579	0.1992	0.00682	0.0825	0.0019	1202.21	27.20	1170.64	36.51
TAU-23-2_041	0	0.9312	0.0370	0.1079	0.00296	0.0625	0.0017	667.69	19.30	660.29	17.22
TAU-23-2_042	0	0.2259	0.0076	0.0321	0.00104	0.0510	0.0012	206.72	6.28	203.46	6.50
TAU-23-2_043	0	0.2830	0.0135	0.0392	0.00106	0.0523	0.0023	252.81	10.65	247.77	6.56
TAU-23-2_044	0	0.2343	0.0243	0.0330	0.00293	0.0514	0.0024	213.16	20.03	209.26	18.30
TAU-23-2_072	0	0.2290	0.0103	0.0330	0.00098	0.0501	0.0017	209.08	8.44	209.57	6.14
TAU-23-2_073	0	0.2180	0.0069	0.0312	0.00081	0.0507	0.0013	200.11	5.80	197.86	5.05
TAU-23-2_084	0	0.8912	0.0324	0.1031	0.00253	0.0621	0.0022	646.55	17.17	632.54	14.79
TAU-23-2_089	0	0.2521	0.0083	0.0360	0.00088	0.0507	0.0016	228.16	6.75	228.09	5.46
TAU-23-2_090	0	0.2717	0.0108	0.0375	0.00110	0.0525	0.0016	243.91	8.65	237.04	6.87
TAU-23-2_091	0	0.6596	0.0470	0.0836	0.00409	0.0571	0.0034	513.33	28.91	517.35	24.35
TAU-23-2_114	0	0.6944	0.0275	0.0845	0.00217	0.0594	0.0021	534.92	16.33	522.65	12.90
TAU-23-2_120	0	0.5731	0.0216	0.0728	0.00190	0.0568	0.0019	459.42	13.85	453.26	11.39
TAU-23-2_121	0	0.5794	0.0230	0.0749	0.00235	0.0558	0.0016	463.22	14.84	465.54	14.09
TAU-23-3_012	3	0.0243	0.0013	0.0037	0.00010	0.0475	0.0026	24.38	1.30	23.80	0.61
TAU-23-3_013	3	0.0250	0.0013	0.0037	0.00011	0.0496	0.0026	25.04	1.24	23.73	0.71
TAU-23-3_015	3	0.0239	0.0013	0.0037	0.00010	0.0471	0.0025	24.01	1.33	23.61	0.66

Spot	Rating	Isotopic ratios						Dates (Ma)			
	(0=worst, 3=best)	²⁰⁷ Pb/ ²³⁵ U	±2σ (abs.)	²⁰⁶ Pb/ ²³⁸ U	±2σ (abs.)	²⁰⁷ Pb/ ²⁰⁶ Pb	±2σ (abs.)	²⁰⁷ Pb/ ²³⁵ U	±2σ (abs.)	²⁰⁶ Pb/ ²³⁸ U	±2σ (abs.)
TAU-23-3_030	3	0.0253	0.0012	0.0037	0.00010	0.0490	0.0022	25.32	1.19	23.99	0.65
TAU-23-3_031	3	0.0241	0.0011	0.0037	0.00010	0.0471	0.0021	24.15	1.10	23.77	0.66
TAU-23-3_034	3	0.0258	0.0021	0.0039	0.00013	0.0477	0.0038	25.83	2.10	25.18	0.83
TAU-23-3_035	3	0.0247	0.0015	0.0038	0.00012	0.0470	0.0026	24.80	1.47	24.50	0.75
TAU-23-3_047	3	0.0247	0.0009	0.0038	0.00010	0.0476	0.0018	24.74	0.91	24.16	0.62
TAU-23-3_048	3	0.0251	0.0012	0.0037	0.00009	0.0487	0.0023	25.19	1.24	23.97	0.61
TAU-23-3_052	3	0.0237	0.0015	0.0036	0.00009	0.0480	0.0028	23.79	1.51	23.02	0.60
TAU-23-3_053	3	0.0263	0.0017	0.0038	0.00013	0.0505	0.0034	26.34	1.65	24.44	0.81
TAU-23-3_059	3	0.0243	0.0024	0.0038	0.00011	0.0465	0.0042	24.39	2.33	24.39	0.71
TAU-23-3_060	3	0.0237	0.0017	0.0036	0.00010	0.0474	0.0036	23.74	1.72	23.43	0.67
TAU-23-3_061	3	0.0240	0.0025	0.0038	0.00011	0.0455	0.0048	24.07	2.49	24.48	0.69
TAU-23-3_062	3	0.0255	0.0025	0.0037	0.00011	0.0497	0.0049	25.49	2.52	23.96	0.73
TAU-23-3_064	3	0.0251	0.0023	0.0038	0.00010	0.0479	0.0044	25.12	2.30	24.49	0.67
TAU-23-3_065	3	0.0243	0.0017	0.0037	0.00011	0.0477	0.0035	24.36	1.65	23.92	0.71
TAU-23-3_066	3	0.0236	0.0016	0.0038	0.00010	0.0461	0.0033	23.68	1.59	24.17	0.66
TAU-23-3_067	3	0.0251	0.0024	0.0039	0.00011	0.0461	0.0042	25.18	2.39	25.33	0.73
TAU-23-3_068	3	0.0253	0.0022	0.0037	0.00012	0.0497	0.0042	25.38	2.13	23.88	0.74
TAU-23-3_069	3	0.0247	0.0016	0.0038	0.00012	0.0477	0.0034	24.78	1.62	24.35	0.76
TAU-23-3_001	2	0.0278	0.0028	0.0038	0.00012	0.0526	0.0057	27.78	2.79	24.78	0.78
TAU-23-3_002	2	0.0274	0.0029	0.0038	0.00016	0.0531	0.0056	27.47	2.85	24.15	1.06
TAU-23-3_050	2	0.0261	0.0022	0.0037	0.00014	0.0517	0.0044	26.12	2.21	23.49	0.87
TAU-23-3_051	2	0.0225	0.0013	0.0036	0.00009	0.0448	0.0026	22.59	1.32	23.35	0.59
TAU-23-3_017	0	3.3972	0.1014	0.2404	0.00633	0.1020	0.0022	1502.21	23.11	1388.54	32.86
TAU-23-3_018	0	14.6538	0.6601	0.1337	0.00654	0.7955	0.0250	2785.31	42.97	808.16	37.18

Spot	Rating	Isotopic ratios						Dates (Ma)			
	(0=worst, 3=best)	²⁰⁷ Pb/ ²³⁵ U	±2σ (abs.)	²⁰⁶ Pb/ ²³⁸ U	±2σ (abs.)	²⁰⁷ Pb/ ²⁰⁶ Pb	±2σ (abs.)	²⁰⁷ Pb/ ²³⁵ U	±2σ (abs.)	²⁰⁶ Pb/ ²³⁸ U	±2σ (abs.)
TAU-23-3_021	0	0.2908	0.0248	0.0339	0.00262	0.0618	0.0023	258.38	19.39	214.74	16.31
TAU-23-3_024	0	5.8864	0.1440	0.2971	0.00782	0.1431	0.0024	1958.39	21.27	1676.73	38.80
TAU-23-3_025	0	0.4484	0.0201	0.0552	0.00220	0.0589	0.0019	375.98	14.10	346.11	13.44
TAU-23-3_039	0	0.7908	0.0473	0.0691	0.00290	0.0825	0.0026	589.89	26.70	430.41	17.47
TAU-23-3_040	0	0.0514	0.0038	0.0071	0.00040	0.0522	0.0030	50.89	3.62	45.71	2.57
TAU-23-3_041	0	23.8695	1.2654	0.2073	0.00933	0.8326	0.0304	3250.97	53.32	1212.74	49.73
TAU-23-3_044	0	5.8230	0.1453	0.3452	0.00909	0.1221	0.0022	1949.40	21.68	1911.46	43.62
TAU-23-3_063	0	0.0532	0.0064	0.0039	0.00012	0.0972	0.0106	52.47	6.15	25.38	0.77
TAU-23-3_033	0	2.8550	0.1136	0.2323	0.00904	0.0888	0.0024	1368.96	29.91	1346.12	47.27
TAU-23-3_003	0	2.2896	0.0660	0.2073	0.00550	0.0793	0.0016	1208.15	20.04	1214.30	29.36
TAU-23-3_004	0	2.2940	0.0536	0.2046	0.00500	0.0810	0.0015	1210.03	16.52	1199.61	26.76
TAU-23-3_005	0	0.6589	0.0199	0.0813	0.00217	0.0584	0.0015	513.66	12.26	504.02	12.92
TAU-23-3_006	0	0.7075	0.0297	0.0866	0.00243	0.0589	0.0022	542.74	17.61	535.39	14.40
TAU-23-3_007	0	0.7266	0.0204	0.0890	0.00224	0.0589	0.0013	554.21	12.06	549.54	13.23
TAU-23-3_008	0	0.4413	0.0261	0.0567	0.00338	0.0562	0.0023	370.89	18.47	355.33	20.60
TAU-23-3_009	0	0.2793	0.0146	0.0380	0.00103	0.0530	0.0026	249.66	11.50	240.52	6.39
TAU-23-3_010	0	0.2608	0.0096	0.0376	0.00095	0.0501	0.0016	235.09	7.73	237.85	5.92
TAU-23-3_011	0	0.2496	0.0076	0.0360	0.00088	0.0501	0.0014	226.13	6.24	228.05	5.48
TAU-23-3_014	0	1.8152	0.0780	0.1740	0.00481	0.0754	0.0030	1047.77	28.23	1033.87	26.43
TAU-23-3_016	0	4.0072	0.1342	0.2812	0.00771	0.1031	0.0036	1634.89	26.97	1597.08	38.83
TAU-23-3_019	0	0.5462	0.0144	0.0709	0.00177	0.0556	0.0012	442.28	9.48	441.68	10.68
TAU-23-3_020	0	0.2459	0.0094	0.0349	0.00096	0.0509	0.0019	223.12	7.64	221.08	6.00
TAU-23-3_022	0	0.8399	0.0332	0.0986	0.00266	0.0615	0.0022	617.79	18.36	606.26	15.60
TAU-23-3_023	0	0.8499	0.0383	0.1001	0.00254	0.0614	0.0025	622.73	20.90	614.81	14.90

Spot	Rating	Isotopic ratios						Dates (Ma)			
	(0=worst, 3=best)	²⁰⁷ Pb/ ²³⁵ U	±2σ (abs.)	²⁰⁶ Pb/ ²³⁸ U	±2σ (abs.)	²⁰⁷ Pb/ ²⁰⁶ Pb	±2σ (abs.)	²⁰⁷ Pb/ ²³⁵ U	±2σ (abs.)	²⁰⁶ Pb/ ²³⁸ U	±2σ (abs.)
TAU-23-3_026	0	0.7470	0.0236	0.0907	0.00231	0.0591	0.0015	565.89	13.78	559.79	13.64
TAU-23-3_027	0	0.7417	0.0216	0.0918	0.00237	0.0584	0.0016	562.93	12.58	566.01	13.97
TAU-23-3_028	0	0.5899	0.0248	0.0739	0.00200	0.0576	0.0021	470.51	15.93	459.63	12.02
TAU-23-3_029	0	0.7024	0.0255	0.0849	0.00274	0.0597	0.0018	540.03	15.33	525.37	16.28
TAU-23-3_032	0	5.0123	0.1596	0.3287	0.00859	0.1101	0.0030	1819.90	26.98	1831.72	41.62
TAU-23-3_036	0	1.5447	0.0796	0.1525	0.00468	0.0732	0.0036	946.24	31.72	914.92	26.15
TAU-23-3_037	0	1.7227	0.0495	0.1710	0.00420	0.0731	0.0018	1016.08	18.38	1017.41	23.11
TAU-23-3_038	0	1.5305	0.0980	0.1545	0.00574	0.0715	0.0035	941.32	39.44	926.14	32.08
TAU-23-3_042	0	2.4001	0.0656	0.2105	0.00509	0.0824	0.0017	1241.67	19.68	1231.20	27.08
TAU-23-3_043	0	2.6439	0.0864	0.2236	0.00684	0.0855	0.0022	1311.93	24.17	1300.73	36.02
TAU-23-3_045	0	1.8575	0.0733	0.1763	0.00525	0.0761	0.0023	1065.42	26.14	1046.37	28.72
TAU-23-3_046	0	1.9624	0.0927	0.1818	0.00504	0.0783	0.0031	1101.88	31.92	1076.68	27.54
TAU-23-3_049	0	0.6602	0.0216	0.0811	0.00199	0.0592	0.0021	514.64	13.17	502.53	11.88
TAU-23-3_054	0	1.6910	0.0710	0.1642	0.00467	0.0747	0.0030	1003.67	26.87	979.71	25.86
TAU-23-3_055	0	1.4322	0.0663	0.1474	0.00529	0.0703	0.0025	901.16	27.76	886.33	29.69
TAU-23-3_056	0	1.8223	0.0604	0.1723	0.00508	0.0766	0.0018	1052.83	21.62	1024.37	27.94
TAU-23-3_057	0	1.5024	0.0439	0.1524	0.00463	0.0714	0.0017	930.92	17.57	914.44	25.84
TAU-23-3_058	0	1.6064	0.0421	0.1593	0.00459	0.0731	0.0016	972.40	16.43	952.50	25.52

APPENDIX I
Zircon trace element contents
(LA-ICP-MS data)



Spot (ppm)	TAU-23-1_001	TAU-23-1_002	TAU-23-1_003	TAU-23-1_004	TAU-23-1_005	TAU-23-1_006	TAU-23-1_007	TAU-23-1_008	TAU-23-1_009	TAU-23-1_010
Al	16.9	9.48	b.d.l.	b.d.l.	64.9	11.2	18016	5.47	b.d.l.	1280
P	154	317	180	217	340	196	289	799	105	1578
Ti	7.29	10.5	4.59	1.85	11.4	2.77	25.17	5.59	4.50	14.5
Y	792	1043	1230	1081	1117	839	1045	2606	3013	2953
Nb	1.05	2.71	1.43	5.38	6.15	4.35	3.73	16.97	8.15	12.67
La	0.08	b.d.l.	0.04	b.d.l.	0.27	0.07	11.66	0.07	0.05	1.31
Ce	12.89	34.32	5.23	10.58	18.06	7.39	24.60	24.51	61.12	19.19
Pr	0.35	0.25	0.46	0.13	0.15	0.14	2.62	0.24	0.67	1.82
Nd	6.51	3.95	7.60	2.30	1.79	1.82	20.0	4.17	10.1	15.7
Sm	12.1	7.38	13.3	5.94	3.00	4.73	22.3	11.4	16.0	23.8
Eu	2.91	3.07	2.86	0.74	0.52	0.57	5.57	2.72	5.82	7.02
Gd	41.3	31.2	49.8	31.4	17.3	23.2	61.7	59.0	68.4	86.0
Tb	9.48	8.85	13.33	9.77	6.53	7.12	13.7	19.1	22.1	25.8
Dy	96.2	99.3	136	108	88.0	83.7	122	235	263	279
Ho	27.8	35.1	43.4	36.9	37.0	28.4	36.2	85.9	94.7	94.2
Er	115	161	185	164	192	132	157	421	451	445
Tm	23.0	33.0	35.9	33.6	44.6	27.5	32.7	98.1	97.9	94.9
Yb	196	294	307	285	432	242	303	953	863	832
Lu	35.1	58.0	56.9	54.1	90.0	45.8	58.6	176	162	162
Hf	10896	8703	8760	10937	10956	12386	8851	12138	8147	10552
Ta	0.52	1.10	0.69	2.87	3.43	3.04	2.82	12.65	2.63	3.57
Pb	1.05	0.88	0.93	2.52	12.8	2.25	39.9	3.65	2.11	24.2
Th	483	375	370	1138	250	1108	1053	1684	889	1815
U	460	355	541	1717	496	1758	1365	6079	1225	1159

Spot (ppm)	TAU-23-1 011	TAU-23-1 012	TAU-23-1 013	TAU-23-1 014	TAU-23-1 015	TAU-23-1 016	TAU-23-1 017	TAU-23-1 018	TAU-23-1 019	TAU-23-1 020
Al	2.46	b.d.l.	43.6	38.9	810	b.d.l.	b.d.l.	9.33	b.d.l.	40.52
P	143	211	4516	452	413	193	244	275	386	315
Ti	4.75	2.71	8.83	5.76	30.9	5.55	6.94	4.31	1.91	17.6
Y	558	1167	1084	2215	799	1985	1675	5112	1558	528
Nb	1.95	4.60	3.43	4.06	5.09	2.48	5.40	11.19	15.36	2.23
La	b.d.l.	b.d.l.	45.03	b.d.l.	3.09	0.06	b.d.l.	0.12	0.07	0.03
Ce	4.13	5.93	130.99	17.70	13.52	9.78	21.94	101.87	10.89	21.40
Pr	0.07	0.08	17.75	0.17	1.49	0.62	0.24	1.69	0.11	0.31
Nd	1.30	1.42	80.6	2.49	6.97	10.6	4.39	26.7	1.69	5.32
Sm	3.22	3.45	25.2	6.77	4.48	19.7	10.7	45.2	5.10	8.85
Eu	0.70	0.63	2.11	0.90	1.17	3.91	3.41	12.8	0.51	3.56
Gd	15.9	22.0	45.1	47.5	14.2	79.9	54.3	182	31.4	34.9
Tb	5.00	7.85	11.2	16.1	4.93	21.2	16.1	51.0	11.3	8.61
Dy	54.3	101	116	203	65.3	220	175	534	142	70.9
Ho	19.0	40.5	38.0	77.6	25.2	68.8	57.7	174	51.2	18.1
Er	84.4	198	167	347	127	284	245	732	244	60.6
Tm	17.5	43.2	33.7	67.2	28.2	55.1	47.9	142	52.8	9.78
Yb	160	396	301	551	270	455	401	1150	475	73.2
Lu	30.9	77.2	56.9	104	55.4	83.6	75.7	204	90.0	12.3
Hf	9711	9542	9544	7456	11033	8836	8571	9264	12667	9256
Ta	1.26	2.50	1.80	1.02	5.54	1.00	1.79	3.06	8.91	0.77
Pb	0.56	0.90	1.33	17.6	2.40	1.09	2.29	4.53	2.87	3.26
Th	237	383	646	153	486	470	1052	2051	1264	51.4
U	623	1057	1053	385	1976	650	982	1901	4501	50.9

Spot (ppm)	TAU-23-1 021	TAU-23-1 022	TAU-23-1 023	TAU-23-1 024	TAU-23-1 025	TAU-23-1 026	TAU-23-1 027	TAU-23-1 028	TAU-23-1 029	TAU-23-1 030
Al	26.37	44860	b.d.l.	3.28	3.19	2.25	9.52	4.87	b.d.l.	1.78
P	361	80	162	144	297	385	93	195	223	175
Ti	12.5	23.7	1.11	3.54	7.01	5.36	8.98	6.20	5.93	4.02
Y	488	32	677	1061	2269	1405	467	491	1882	802
Nb	1.90	0.08	3.41	1.50	3.07	4.35	0.54	1.36	2.34	2.55
La	0.06	1.72	b.d.l.	b.d.l.	0.10	0.13	b.d.l.	b.d.l.	0.08	b.d.l.
Ce	13.56	2.34	3.16	4.48	6.96	6.18	2.23	2.92	6.49	6.62
Pr	0.14	0.22	0.02	0.35	0.98	0.20	0.17	0.09	0.54	0.14
Nd	2.31	0.65	0.51	6.08	17.1	2.95	2.84	1.32	9.72	2.25
Sm	6.22	0.20	1.94	11.1	32.1	6.01	5.82	3.43	18.1	4.85
Eu	1.03	0.14	0.18	1.86	5.08	1.14	1.19	0.55	3.25	0.92
Gd	27.5	0.59	11.7	42.7	112	31.6	21.9	14.2	72.0	24.6
Tb	6.91	0.24	4.39	11.2	27.0	10.3	5.23	4.20	19.3	7.30
Dy	64.4	2.88	57.9	113	261	128	50.8	47.8	195	81.4
Ho	16.6	1.09	23.1	36.6	77.2	47.1	15.9	16.6	63.1	27.8
Er	59.2	5.56	114	154	303	221	65.8	76.7	265	123
Tm	10.2	1.28	26.4	30.5	58.9	45.0	13.1	16.1	52.3	24.8
Yb	79.2	10.3	253	262	479	399	113	146	438	211
Lu	13.6	2.12	49.6	47.5	86.1	77.8	20.6	28.5	83.7	40.6
Hf	11498	1331	13636	9371	8658	8728	9479	10456	8780	10003
Ta	0.80	0.24	3.25	0.65	0.83	1.45	0.35	0.97	0.94	1.29
Pb	5.91	6.47	0.45	0.92	2.68	1.32	0.53	0.71	1.60	1.70
Th	92.7	11.6	196	400	1043	584	227	324	718	693
U	131	46.5	1209	647	934	894	366	643	823	916

Spot (ppm)	TAU-23-1 031	TAU-23-1 032	TAU-23-1 033	TAU-23-1 034	TAU-23-1 035	TAU-23-1 036	TAU-23-1 037	TAU-23-1 038	TAU-23-1 039	TAU-23-1 040
Al	b.d.l.	b.d.l.	6753	326	3.45	362	b.d.l.	2.29	b.d.l.	2.09
P	248	259	100	110	136	282	135	233	200	180
Ti	9.17	17.5	33.2	5.50	6.46	27.5	7.02	4.60	6.76	4.51
Y	5145	4237	386	1272	1120	1180	553	2016	895	1303
Nb	9.53	26.97	1.28	2.22	4.46	1.60	6.36	4.51	4.69	1.41
La	0.21	0.07	1.32	0.20	b.d.l.	0.19	b.d.l.	0.07	1.37	b.d.l.
Ce	165.26	256.91	4.54	46.41	58.15	3.78	4.21	9.22	11.80	3.75
Pr	2.67	1.55	0.42	0.61	0.22	0.46	0.01	0.47	0.69	0.33
Nd	42.0	27.5	2.88	9.04	3.63	6.16	0.42	8.66	5.69	5.66
Sm	62.9	48.4	2.69	13.4	7.49	9.13	1.20	17.7	9.43	11.3
Eu	26.8	19.9	0.57	5.83	3.58	1.34	0.11	3.13	1.83	2.19
Gd	224	180	13.4	49.2	36.3	40.9	8.04	71.3	36.8	48.4
Tb	58.8	46.8	3.57	13.3	10.6	11.7	3.08	19.4	9.80	13.2
Dy	575	465	38.3	136	114	128	43.1	204	95.6	137
Ho	175	142	13.2	44.6	38.9	42.7	18.0	66.8	31.3	44.5
Er	707	586	57.5	190	171	181	94.3	288	132	194
Tm	134	111	11.9	36.3	35.3	34.5	21.4	56.0	26.2	38.6
Yb	1080	890	107	307	305	291	198	478	220	333
Lu	190	157	20.5	59.0	58.0	55.6	38.7	87.5	40.3	62.5
Hf	7605	7783	9235	9226	9883	9069	14582	9053	10076	9385
Ta	2.03	5.51	0.48	0.91	1.90	0.64	3.83	1.48	1.74	0.76
Pb	5.80	11.2	0.80	1.34	2.45	1.89	3.23	2.86	3.02	0.88
Th	2520	4972	78.2	417	1117	28.9	40.7	1208	1233	348
U	1360	2556	178	328	822	51.4	180	1546	1536	542

Spot (ppm)	TAU-23-1 041	TAU-23-1 042	TAU-23-1 043	TAU-23-1 044	TAU-23-1 045	TAU-23-1 046	TAU-23-1 047	TAU-23-1 048	TAU-23-1 049	TAU-23-1 050
Al	b.d.l.	25523	8.88	3.25	25.20	5703	b.d.l.	5.45	4.54	5.34
P	237	120	228	209	248	269	200	281	169	175
Ti	3.78	149	1.41	3.94	2.66	44.0	3.48	8.75	4.41	4.17
Y	937	396	730	1715	1909	1984	1449	667	971	956
Nb	2.48	2.44	4.00	1.46	4.07	6.26	6.27	2.15	4.41	3.10
La	b.d.l.	7.03	b.d.l.	0.08	0.04	1.94	b.d.l.	b.d.l.	b.d.l.	b.d.l.
Ce	4.16	18.06	3.58	5.96	9.81	15.55	12.19	3.33	8.12	7.50
Pr	0.12	2.05	0.02	0.75	0.40	1.09	0.17	0.10	0.13	0.14
Nd	2.15	9.43	0.36	11.3	6.69	11.6	3.66	1.69	2.94	2.28
Sm	4.30	4.03	1.63	17.8	13.3	18.5	8.01	3.38	7.41	5.12
Eu	0.80	0.86	0.14	3.34	1.84	2.21	1.23	0.71	1.19	0.87
Gd	20.9	12.5	10.6	69.7	60.7	73.5	41.7	18.1	34.7	28.1
Tb	6.65	3.62	4.34	18.5	17.8	20.1	12.9	5.38	9.34	8.33
Dy	82.1	37.1	60.9	185	189	207	145	62.3	104	93.7
Ho	31.2	13.2	24.2	58.9	63.9	67.3	48.9	22.1	34.2	32.3
Er	152	62.5	126	249	277	293	224	105	150	147
Tm	32.6	14.0	29.5	48.0	55.1	57.2	45.3	22.2	30.3	31.0
Yb	290	128	289	407	472	484	402	201	263	268
Lu	59.1	25.3	57.3	75.9	85.9	89.2	74.0	39.6	49.6	51.2
Hf	8695	7765	13325	9168	10223	7486	11359	9439	9638	10608
Ta	1.04	1.61	4.45	0.71	1.61	1.93	2.53	0.97	1.82	1.60
Pb	0.51	4.47	0.47	0.93	1.58	8.58	1.82	0.29	1.70	1.28
Th	224	137	206	421	680	1480	899	126	699	583
U	530	415	1679	605	1035	1411	1324	326	1069	919

Spot (ppm)	TAU-23-1 051	TAU-23-1 052	TAU-23-1 053	TAU-23-1 054	TAU-23-1 055	TAU-23-1 056	TAU-23-1 057	TAU-23-1 058	TAU-23-1 059	TAU-23-1 060
Al	b.d.l.	2093	17.33	33.84	6123	b.d.l.	16.06	2.46	452	2.31
P	183	223	270	306	7974	179	260	234	1306	271
Ti	4.03	20.24	5.66	4.81	81.7	4.45	10.93	3.43	8.08	4.39
Y	1322	1149	5506	2310	1311	565	1243	816	2994	1102
Nb	1.26	6.24	16.46	13.91	1.64	1.54	1.51	2.50	5.52	5.63
La	b.d.l.	1.50	0.14	0.19	30.68	b.d.l.	b.d.l.	b.d.l.	6.65	0.06
Ce	3.82	11.69	261.57	21.96	88.31	25.37	3.31	6.54	49.13	10.71
Pr	0.36	0.43	1.70	0.44	11.57	0.09	0.47	0.13	3.90	0.19
Nd	6.27	3.69	28.4	6.76	62.8	1.70	8.17	2.70	38.1	3.25
Sm	11.7	7.22	54.9	15.2	27.3	3.89	16.2	6.41	44.2	7.80
Eu	2.10	1.30	20.3	1.99	5.21	1.22	2.95	0.93	5.88	1.12
Gd	48.4	37.3	231	69.6	66.8	16.4	55.8	29.0	145	36.6
Tb	13.1	10.8	64.1	19.7	15.5	4.80	13.8	7.91	36.3	10.8
Dy	139	120	601	219	149	53.6	133.2	85.4	345	115
Ho	46.3	40.4	176	74.1	45.4	18.5	41.8	28.0	104	38.2
Er	201	177	677	336	187	88.0	179	124	412	167
Tm	39.7	36.2	119	69.5	35.7	17.9	34.4	24.5	76.9	34.0
Yb	343	306	910	606	295	161	298	211	619	289
Lu	64.2	58.4	148	111	56.3	31.1	55.9	40.0	109	53.9
Hf	9112	9432	8583	9357	6879	10464	8367	10682	9065	10450
Ta	0.68	2.38	3.91	5.27	0.50	1.01	0.63	1.35	1.30	2.29
Pb	0.81	4.65	4.71	5.77	23.8	0.52	1.34	2.09	3.75	3.52
Th	340	910	2286	2381	245	227	560	898	1209	1607
U	570	1193	1869	3074	309	410	716	1215	1087	1595

Spot (ppm)	TAU-23-1 061	TAU-23-1 062	TAU-23-1 063	TAU-23-1 064	TAU-23-1 065	TAU-23-1 066	TAU-23-1 067	TAU-23-1 068	TAU-23-1 069	TAU-23-1 070
Al	28.7	3.43	2621	30.9	11.9	3.24	b.d.l.	9.91	2.96	3.90
P	681	315	397	784	335	186	324	466	140	177
Ti	5.02	1.74	16.99	1.89	3.96	2.34	5.40	3.10	5.25	4.91
Y	5436	1115	10094	1582	4516	832	2880	1449	1140	910
Nb	18.02	7.63	22.24	8.09	7.84	3.33	9.85	8.34	0.79	2.97
La	0.19	b.d.l.	2.46	0.08	0.12	b.d.l.	0.07	4.55	b.d.l.	b.d.l.
Ce	32.62	11.39	199.03	4.31	20.96	7.18	19.03	25.15	3.55	8.71
Pr	1.57	0.11	2.21	0.09	1.32	0.12	0.63	1.68	0.39	0.15
Nd	26.9	1.70	22.9	1.09	23.7	1.59	12.3	10.4	6.29	2.80
Sm	46.4	4.46	48.5	2.86	44.8	4.38	25.2	9.82	11.8	7.24
Eu	4.29	0.35	14.5	0.30	7.43	0.70	4.22	1.19	2.27	1.26
Gd	194	23.3	251	19.7	177	24.2	105	44.3	45.0	33.0
Tb	55.0	8.14	81.5	8.93	48.6	7.32	29.1	13.1	12.3	9.37
Dy	571	100	940	128	495	82.2	300	147	125	97.5
Ho	183	37.7	327	51.8	156	29.0	96.7	49.0	40.1	31.1
Er	765	179	1416	277	641	129	416	217	171	139
Tm	147	40.0	277	67.0	124	26.4	81.1	45.1	33.5	27.6
Yb	1204	373	2231	669	1001	234	682	392	280	235
Lu	218	71.8	383	133	178	44.2	124	72.7	53.3	44.4
Hf	8104	13555	7780	14003	9049	10906	9110	12410	9024	9474
Ta	6.23	8.00	5.98	9.38	1.97	1.93	3.40	3.93	0.45	1.17
Pb	5.11	2.06	11.9	1.14	5.52	1.49	4.90	3.51	0.55	1.48
Th	2232	763	3047	498	2471	652	2309	1756	234	607
U	3872	3147	2235	5639	1990	1064	2230	2348	365	746

Spot (ppm)	TAU-23-1 071	TAU-23-1 072	TAU-23-1 073	TAU-23-1 074	TAU-23-1 075	TAU-23-1 076	TAU-23-1 077	TAU-23-1 078	TAU-23-1 079	TAU-23-1 080
Al	6.13	b.d.l.	b.d.l.	14.2	1.47	10.5	4.03	b.d.l.	86.7	b.d.l.
P	176	153	242	197	174	230	229	168	153	134
Ti	5.60	0.82	10.9	4.17	9.93	7.09	3.22	4.38	4.04	2.62
Y	1009	765	3525	718	941	470	2566	846	736	1331
Nb	2.10	2.96	5.44	3.66	0.61	0.93	5.73	3.37	1.88	2.04
La	b.d.l.	b.d.l.	0.27	0.08	0.06	b.d.l.	0.09	b.d.l.	0.17	0.04
Ce	3.20	3.18	106.57	6.83	2.12	1.36	15.45	7.85	4.88	6.69
Pr	0.29	b.d.l.	2.47	0.11	0.37	0.07	0.53	0.11	0.27	0.44
Nd	5.19	0.49	33.5	1.80	5.77	1.34	9.24	2.42	3.73	7.33
Sm	11.1	1.76	45.2	4.57	9.94	2.68	17.3	5.16	6.00	14.0
Eu	3.00	0.17	22.8	0.61	1.98	0.59	2.38	1.02	1.13	2.16
Gd	45.2	12.4	159	19.2	38.7	11.8	78.8	25.6	23.9	52.3
Tb	11.7	4.83	41.3	6.27	10.5	3.65	23.5	7.75	7.21	14.2
Dy	113	65.0	397	71.6	107	41.8	260	86.3	76.9	147
Ho	34.7	26.1	121	25.2	33.7	15.8	86.3	29.0	26.5	47.7
Er	147	134	486	113	143	75.9	378	131	115	202
Tm	29.5	31.7	90.4	23.4	28.2	16.9	77.9	27.0	24.6	40.1
Yb	264	308	730	206	243	157	671	236	218	340
Lu	48.4	60.7	129	38.5	46.4	32.7	121	42.8	41.5	61.6
Hf	10158	16043	7903	10791	9069	9805	11205	10752	10522	9232
Ta	0.97	3.49	1.04	1.72	0.36	0.52	3.15	1.72	1.45	0.92
Pb	1.46	0.48	2.31	2.14	0.48	0.23	2.04	1.90	1.18	1.16
Th	642	218	1013	789	210	101	959	893	278	471
U	891	1632	485	1180	295	284	2257	1087	669	697

Spot (ppm)	TAU-23-1 081	TAU-23-1 082	TAU-23-1 083	TAU-23-1 084	TAU-23-1 085	TAU-23-1 086	TAU-23-1 087	TAU-23-1 088	TAU-23-1 089	TAU-23-1 090
Al	b.d.l.	40.7	b.d.l.	95.2	b.d.l.	b.d.l.	b.d.l.	b.d.l.	b.d.l.	b.d.l.
P	222	543	247	277	269	242	127	165	138	178
Ti	6.18	2.83	5.20	9.43	4.23	1.99	3.90	2.68	4.94	2.57
Y	1798	2357	1787	1251	3254	1821	1052	1631	894	1099
Nb	12.11	13.50	2.35	4.27	6.43	15.51	1.33	13.57	2.77	6.65
La	b.d.l.	0.09	0.05	0.88	0.12	b.d.l.	b.d.l.	b.d.l.	b.d.l.	b.d.l.
Ce	135.05	7.72	4.14	14.98	23.71	17.55	9.88	38.23	7.78	24.72
Pr	0.42	0.16	0.36	0.85	1.72	0.14	0.23	0.13	0.18	0.11
Nd	7.96	1.70	6.73	5.50	31.2	2.68	3.73	2.60	3.12	1.90
Sm	18.6	4.07	13.4	6.65	51.3	7.76	7.99	7.52	6.25	4.79
Eu	6.75	0.58	2.46	2.29	11.2	0.76	2.94	1.72	1.16	1.36
Gd	82.0	31.7	56.8	27.7	162	46.5	33.2	42.4	30.6	27.4
Tb	21.2	13.2	16.3	9.40	39.6	14.8	9.74	13.7	8.73	9.14
Dy	203	186	179	112	371	172	108	155	94.7	107
Ho	60.2	73.9	60.7	42.6	109.4	59.0	36.5	53.7	31.5	37.1
Er	238	383	273	201	444	272	162	248	138	170
Tm	44.3	89.4	54.8	42.4	84.5	55.5	33.1	51.8	27.5	36.1
Yb	359	834	477	378	687	484	288	460	237	311
Lu	63.4	166	93.3	75.9	123	90.7	55.8	84.9	45.0	58.4
Hf	9694	14147	8234	10049	8228	12203	8574	12020	9377	11355
Ta	3.93	8.97	0.88	2.45	1.43	7.26	0.76	6.51	1.22	3.24
Pb	4.36	1.51	1.20	1.26	4.97	3.53	0.57	3.89	0.94	1.81
Th	1939	773	488	610	2279	1759	232	1614	381	735
U	1429	4803	698	1200	1633	3191	366	2573	616	1248

Spot (ppm)	TAU-23-1_091	TAU-23-1_092	TAU-23-1_093	TAU-23-1_094	TAU-23-1_095	TAU-23-1_096	TAU-23-1_097	TAU-23-1_098	TAU-23-1_099	TAU-23-1_100
Al	52.4	25.3	12.7	8.63	b.d.l.	2.48	1.54	7.40	18.8	b.d.l.
P	1796	268	246	260	260	398	144	127	383	143
Ti	2.03	6.60	11.38	7.99	6.41	1.40	9.25	7.02	9.72	6.53
Y	204	1401	604	530	3948	1512	1621	789	3450	1234
Nb	0.40	9.06	1.38	1.60	5.54	10.83	1.92	0.91	15.07	6.56
La	14.61	0.04	b.d.l.	0.04	0.20	b.d.l.	0.10	b.d.l.	0.34	b.d.l.
Ce	37.52	17.64	2.34	2.62	125.39	12.76	10.69	3.44	272.00	73.13
Pr	5.05	0.34	0.15	0.09	2.27	0.04	0.80	0.29	1.86	0.18
Nd	23.6	7.13	2.40	1.59	37.6	0.99	13.5	4.72	32.5	3.61
Sm	6.55	17.8	4.32	3.37	59.6	3.75	23.9	9.54	52.8	7.99
Eu	0.79	2.65	0.90	0.62	21.6	0.60	7.81	2.62	19.9	3.97
Gd	9.35	65.0	17.7	15.8	201	25.3	75.1	35.1	188	41.7
Tb	2.17	16.0	5.18	4.62	47.7	9.61	18.7	9.09	43.2	12.0
Dy	21.7	157	56.8	50.2	443	130	181	87.5	395	131
Ho	7.17	48.7	20.4	17.9	132	49.0	56.3	27.7	115	43.2
Er	31.5	205	97.5	85.3	521	246	233	118	449	187
Tm	6.33	40.4	20.3	17.8	97.4	57.2	45.4	23.4	80.7	37.3
Yb	55.2	342	189	166	784	543	390	198	638	320
Lu	11.4	64.1	37.6	34.0	140	105	72.1	37.3	115	58.9
Hf	3670	9146	8749	9265	8697	13503	8595	9399	7578	9122
Ta	0.36	3.13	0.60	0.79	1.77	8.08	0.74	0.44	4.55	2.52
Pb	0.63	6.92	0.32	0.25	3.67	1.80	1.75	0.84	6.84	2.36
Th	67	2668	121	110	1635	754	786	366	3007	1043
U	144	2457	305	292	1144	3875	839	493	1680	835

Spot (ppm)	TAU-23-1_101	TAU-23-1_102	TAU-23-1_103	TAU-23-1_104	TAU-23-1_105	TAU-23-1_106	TAU-23-1_107	TAU-23-1_108	TAU-23-1_109	TAU-23-1_110
Al	b.d.l.	12.3	3.75	3.22	2.83	4.01	6.65	b.d.l.	b.d.l.	b.d.l.
P	104	161	200	173	227	180	102	185	161	222
Ti	3.63	1.91	5.61	4.13	2.10	1.25	1.89	3.07	2.58	2.90
Y	918	1040	1922	1069	3271	827	534	1153	2533	1452
Nb	1.06	5.16	1.60	2.84	5.70	4.83	1.63	8.00	3.41	8.27
La	b.d.l.	0.45	0.04	b.d.l.	0.11	b.d.l.	b.d.l.	b.d.l.	b.d.l.	b.d.l.
Ce	4.04	11.26	4.79	5.84	18.54	3.90	3.28	30.08	13.05	20.22
Pr	0.25	0.20	0.64	0.11	1.05	0.05	0.04	0.09	0.57	0.20
Nd	4.36	2.54	10.1	2.30	16.4	0.66	0.79	1.68	9.49	3.23
Sm	8.16	5.48	19.6	5.40	28.7	1.62	1.93	4.52	20.5	8.97
Eu	1.50	0.60	4.04	1.18	3.16	0.21	0.38	1.51	2.64	1.07
Gd	34.3	26.6	78.6	27.7	117	12.4	13.0	27.6	87.2	47.0
Tb	9.60	8.81	20.9	8.83	33.0	5.01	4.22	9.24	24.8	14.1
Dy	98.7	100	206	103	341	70.1	49.9	110	258	149
Ho	32.2	35.8	64.5	37.2	109	27.5	18.1	38.9	86.7	50.2
Er	140	166	274	170	463	146	84.8	183	364	216
Tm	27.9	34.7	53.2	35.2	88.7	35.2	17.8	38.9	72.0	43.3
Yb	238	315	446	311	755	327	166	348	596	365
Lu	44.3	60.3	82.6	59.5	138	65.6	32.5	64.9	108	68.0
Hf	9532	11768	9159	9736	9552	13899	11150	11738	12483	11430
Ta	0.64	3.53	0.75	1.12	2.39	5.26	1.49	4.70	2.37	4.00
Pb	0.52	2.37	1.24	0.87	2.21	0.55	0.23	1.65	1.67	2.55
Th	230	796	539	353	1026	233	116	743	817	1167
U	377	1864	697	647	1500	1878	446	1915	1434	1854

Spot (ppm)	TAU-23-1_111	TAU-23-1_112	TAU-23-1_113	TAU-23-1_114	TAU-23-1_115	TAU-23-1_116	TAU-23-1_117	TAU-23-1_118	TAU-23-1_119	TAU-23-1_120
Al	b.d.l.	6.86	8.66	b.d.l.	10.7	2.06	b.d.l.	6.28	2082	23.7
P	333	140	938	397	278	201	210	452	208	239
Ti	2.19	3.32	3.87	2.91	7.94	6.05	8.60	4.84	14.7	2.98
Y	4149	1069	6363	2345	651	2086	1895	11418	1436	1418
Nb	9.59	6.64	20.52	5.75	1.45	4.68	10.56	34.59	16.93	1.40
La	0.09	0.05	0.45	0.09	b.d.l.	0.05	b.d.l.	0.73	1.86	0.06
Ce	32.0	24.8	67.6	18.2	2.70	34.5	72.9	220	42.2	4.74
Pr	1.27	0.12	4.39	1.24	0.07	0.60	0.33	8.77	0.92	0.36
Nd	21.1	2.05	61.4	18.8	1.30	9.75	6.07	128	9.53	5.63
Sm	39.7	4.92	86.0	25.1	3.23	17.4	16.1	186	14.4	11.4
Eu	4.10	1.46	13.5	4.30	0.55	7.10	6.46	23.5	2.40	1.74
Gd	161	28.5	288	91.4	16.4	69.4	71.0	589	55.4	51.3
Tb	44.0	9.02	72.5	24.2	5.25	20.3	20.0	151	14.7	14.4
Dy	445	105	704	242	61.1	214	201	1391	150	152
Ho	142	36.7	216	78.3	22.0	71.4	63.9	414	49.0	50.1
Er	580	166	866	339	103	310	264	1591	209	218
Tm	110	34.6	165	66.7	21.5	61.5	51.8	291	41.2	42.6
Yb	904	305	1313	565	193	526	437	2259	347	352
Lu	162	57.7	229	104	37.6	97.8	80.6	373	61.7	66.1
Hf	10561	10804	9998	9347	9663	8139	8640	8599	9374	9373
Ta	3.36	3.54	4.23	1.94	0.74	1.55	3.42	5.01	4.57	0.82
Pb	4.50	1.25	5.97	1.26	0.48	2.17	6.05	17.6	11.6	1.18
Th	2085	580	2818	552	195	874	2690	8252	4950	422
U	2673	1188	2762	870	405	807	1590	5180	2820	616

Spot (ppm)	TAU-23-1 121	TAU-23-1 122	TAU-23-1 123	TAU-23-1 124	TAU-23-1 125	TAU-23-1 126	TAU-23-1 127	TAU-23-1 128	TAU-23-1 129	TAU-23-1 130
Al	7.52	3790	15.7	7.26	10.1	1.67	2.38	88.6	b.d.l.	177
P	236	262	333	265	325	234	177	220	318	99
Ti	4.95	16.5	5.18	15.1	3.07	2.09	4.12	6.98	2.78	2.99
Y	1047	2463	1408	3425	5764	1061	2577	1294	972	785
Nb	4.53	7.89	8.99	30.90	16.80	4.24	26.86	5.78	4.56	5.78
La	0.06	2.76	b.d.l.	0.24	0.11	b.d.l.	0.18	0.36	0.34	b.d.l.
Ce	8.66	121.47	21.50	184.28	48.25	9.22	95.20	17.10	9.84	20.19
Pr	0.16	1.90	0.26	0.97	1.75	0.14	0.22	0.49	0.23	0.05
Nd	2.77	21.11	4.12	18.4	30.0	2.63	4.18	7.59	2.80	1.11
Sm	7.23	30.9	11.6	41.2	53.7	5.68	12.0	13.0	5.30	2.86
Eu	1.06	11.7	1.81	13.7	5.57	0.87	4.40	2.67	0.64	0.90
Gd	33.2	108	49.7	158	213	30.9	65.7	49.6	27.1	15.5
Tb	10.1	28.3	13.9	39.9	60.1	9.38	21.3	13.3	8.62	5.89
Dy	110	276	148	376	622	105	241	136	95.0	73.0
Ho	36.6	85.7	48.2	114	195	36.3	84.4	43.9	33.6	27.4
Er	160	347	213	457	807	159	373	192	152	128
Tm	32.8	67.5	42.3	88.3	157	33.4	77.0	39.1	31.8	28.5
Yb	286	559	370	705	1257	291	667	333	282	254
Lu	52.9	99.0	68.2	124	217	54.2	118	60.0	54.0	48.8
Hf	10935	9976	10634	9193	9617	10793	12981	9390	11298	12418
Ta	2.32	1.85	3.39	6.52	4.23	2.33	8.34	1.81	2.66	3.08
Pb	2.52	6.94	4.75	16.1	6.94	1.88	5.61	5.24	2.11	0.79
Th	1277	2413	2021	5404	3217	864	2526	2479	977	322
U	1622	1043	2080	3442	3347	1346	2762	1286	1581	793

Spot (ppm)	TAU-23-1_131	TAU-23-1_132	TAU-23-1_133	TAU-23-1_134	TAU-23-1_135	TAU-23-1_136	TAU-23-1_137	TAU-23-1_138	TAU-23-1_139	TAU-23-1_140
Al	1.47	4.51	56.7	11.6	10.9	9.72	b.d.l.	b.d.l.	6.89	1396
P	235	180	114	299	585	152	159	232	397	238
Ti	3.22	7.65	5.19	6.10	4.58	6.64	3.52	11.3	1.83	28.0
Y	1155	1231	246	4247	3025	468	1084	1725	1339	5696
Nb	4.86	0.66	0.52	9.04	43.35	0.97	4.57	3.47	8.14	15.56
La	b.d.l.	0.06	0.05	0.29	1.91	b.d.l.	b.d.l.	0.04	b.d.l.	0.69
Ce	13.46	2.88	1.75	282.99	61.43	1.99	11.50	51.45	6.35	157.03
Pr	0.19	0.41	0.04	2.91	1.08	0.07	0.18	0.52	0.08	2.97
Nd	3.13	6.12	0.64	46.2	9.80	1.43	2.72	7.45	0.99	42.9
Sm	8.22	9.92	1.33	70.1	18.5	3.02	6.94	13.6	2.92	69.0
Eu	1.37	1.98	0.33	24.56	1.98	0.71	1.25	6.90	0.35	26.2
Gd	38.7	44.8	6.50	237	84.9	12.9	34.9	64.0	19.9	241
Tb	11.4	12.6	1.98	57.0	26.6	3.75	10.6	17.5	8.28	63.9
Dy	121	135	22.4	494	288	43.36	112	177	108	628
Ho	41.4	44.1	7.81	143	98.8	15.5	37.9	57.7	43.6	193
Er	178	188	37.6	534	428	74.7	163	237	225	797
Tm	35.8	37.2	8.31	97.7	88.5	15.6	32.8	47.1	53.1	156
Yb	311	319	78.7	763	764	143	287	397	505	1280
Lu	58.7	59.9	15.7	133	135	29.2	53.4	72.3	102	225
Hf	10389	8922	10961	8515	10603	9048	10838	8220	14197	7556
Ta	2.42	0.48	0.36	2.05	9.59	0.54	2.10	1.17	8.38	4.26
Pb	2.86	0.61	0.30	3.76	7.75	0.27	2.27	1.82	1.09	9.23
Th	1238	273	118	1707	3686	107	1072	824	511	3216
U	1446	408	294	1010	4643	260	1347	545	3980	2402

Spot (ppm)	TAU-23-1 141	TAU-23-1 142	TAU-23-1 143	TAU-23-1 144	TAU-23-1 145	TAU-23-1 146	TAU-23-1 147	TAU-23-1 148	TAU-23-1 149	TAU-23-1 150
Al	3.02	b.d.l.	b.d.l.	15.8	2.13	2.59	6.26	b.d.l.	7.18	3.22
P	349	162	376	227	469	177	105	159	226	369
Ti	1.38	4.16	2.23	11.1	1.60	8.26	6.31	5.55	4.96	5.22
Y	1284	1770	1299	1747	1308	1440	864	2078	1974	6049
Nb	8.73	2.08	7.77	2.47	8.52	2.08	1.18	2.56	6.60	14.48
La	b.d.l.	0.06	0.65	b.d.l.	0.07	0.07	0.05	0.10	0.07	0.20
Ce	5.57	8.90	10.33	12.93	4.24	5.27	4.99	8.94	18.37	121.68
Pr	0.03	0.61	0.43	0.48	0.05	0.40	0.33	0.91	0.44	2.65
Nd	0.80	9.76	4.02	6.90	0.60	6.44	5.39	14.5	7.41	41.0
Sm	2.87	16.4	5.20	11.7	2.28	12.2	9.57	24.4	16.0	66.9
Eu	0.29	3.02	0.88	0.41	0.24	3.20	2.52	5.34	2.85	21.64
Gd	20.0	64.4	30.8	55.1	17.2	50.0	35.6	87.3	70.7	244
Tb	8.03	17.8	11.1	16.0	7.50	14.32	9.40	23.2	19.7	65.8
Dy	109	185	135	180	104	147	96.1	225	204	658
Ho	42.7	60.7	50.4	61.4	42.9	49.3	31.6	70.4	67.5	208
Er	213	257	257	255	228	214	138	291	282	847
Tm	51.1	50.9	64.5	48.2	53.8	43.7	27.3	55.1	55.0	162
Yb	497	438	593	391	541	380	233	457	459	1325
Lu	95.4	80.0	111	68.2	106	72.5	44.8	85.2	86.7	231
Hf	12947	8286	17773	9060	14008	9094	10546	8055	9193	8722
Ta	8.33	1.22	7.79	1.08	8.36	0.84	0.49	0.95	2.47	3.55
Pb	1.06	0.78	2.05	42.0	0.75	1.37	0.92	1.63	2.48	8.43
Th	481	336	872	228	325	609	357	679	1069	3673
U	3543	616	4187	274	3723	721	411	766	1337	2334

Spot (ppm)	TAU-23-1 151	TAU-23-1 152	TAU-23-1 153	TAU-23-1 154	TAU-23-1 155	TAU-23-1 156	TAU-23-1 157	TAU-23-1 158	TAU-23-1 159	TAU-23-1 160
Al	14.6	6.30	5.36	7.20	2586	154	b.d.l.	b.d.l.	93.9	b.d.l.
P	218	237	276	206	382	455	250	416	439	281
Ti	2.67	2.09	8.53	7.56	23.4	1.90	10.3	1.08	8.84	2.46
Y	1064	1580	837	597	3482	1431	918	1014	2770	1267
Nb	6.13	10.83	2.71	1.94	21.86	9.78	1.72	5.45	12.19	9.61
La	0.28	0.23	b.d.l.	b.d.l.	3.83	0.07	b.d.l.	b.d.l.	0.20	b.d.l.
Ce	11.36	14.21	3.76	2.89	231.96	5.70	26.23	5.77	34.26	16.65
Pr	0.17	0.44	0.12	0.09	2.18	0.10	0.06	b.d.l.	1.08	0.09
Nd	2.11	5.43	2.30	1.68	21.3	1.05	1.31	0.50	17.3	1.84
Sm	4.68	9.36	4.89	3.72	28.1	3.53	3.20	2.02	35.2	4.99
Eu	0.66	1.84	0.84	0.72	11.4	0.33	1.08	0.30	3.46	0.92
Gd	23.3	41.7	22.1	16.7	109	21.3	17.6	13.5	158	28.1
Tb	8.26	13.3	6.56	5.04	31.4	8.81	6.01	5.87	41.3	9.92
Dy	99.6	150	75.3	56.3	333	118	76.9	83.4	347	115
Ho	36.2	53.1	27.8	20.0	113	46.3	30.9	32.9	91.1	42.2
Er	172	245	133	97.8	491	235	156	173	317	194
Tm	38.5	53.3	28.2	20.8	97.6	55.8	34.7	42.2	53.4	42.3
Yb	350	474	257	193	820	530	340	409	411	386
Lu	66.6	87.3	51.0	39.2	153	103	69.3	78.5	67.2	73.1
Hf	12626	15208	9149	9609	7100	13944	9533	12452	12087	12030
Ta	4.35	7.05	0.98	0.92	5.30	9.33	0.72	6.77	2.65	5.53
Pb	1.27	1.50	0.45	0.30	7.16	1.83	13.2	0.79	4.64	2.40
Th	583	663	201	130	2964	664	96.4	335	2148	1060
U	2039	2095	481	364	1488	5285	98.39	3063	2091	2570

Spot (ppm)	TAU-23-1 161	TAU-23-1 162	TAU-23-1 163	TAU-23-1 164	TAU-23-1 165	TAU-23-1 166	TAU-23-1 167	TAU-23-1 168	TAU-23-2 001	TAU-23-2 002
Al	26.6	b.d.l.	103	20.0	b.d.l.	b.d.l.	423	37.1	1.31	773
P	1043	1082	955	401	149	165	804	177	350	215
Ti	7.49	3.26	4.42	3.30	3.99	3.17	14.6	4.98	7.93	9.64
Y	2490	2568	4526	1518	787	1277	10450	765	4602	2151
Nb	4.32	3.21	8.19	10.89	2.50	1.30	70.76	2.08	29.72	7.56
La	0.09	b.d.l.	0.09	0.18	b.d.l.	b.d.l.	3.77	0.10	0.07	0.23
Ce	5.11	1.53	29.14	7.66	4.41	5.38	186	4.77	254	76.22
Pr	0.11	0.04	0.71	0.14	0.11	0.36	5.74	0.16	0.73	0.49
Nd	1.44	0.74	10.8	1.40	1.77	6.38	82.3	2.54	12.7	7.41
Sm	4.41	3.09	20.6	3.67	3.85	10.8	137	5.39	28.1	14.9
Eu	0.45	0.14	0.50	0.56	0.70	1.45	7.45	0.96	10.9	5.60
Gd	37.1	29.2	105	22.7	20.4	43.6	519	24.8	132	66.1
Tb	14.5	13.2	35.7	9.55	6.06	12.3	136	7.26	39.7	19.9
Dy	203	195	424	125	72.3	128	1287	77.3	439	216
Ho	82.6	82.5	152	48.9	26.2	44.3	382	26.1	150	74.2
Er	407	430	682	247	123	192	1429	116	646	321
Tm	90.4	96.6	140	59.1	26.1	39.1	251	23.9	130	63.7
Yb	829	895	1193	556	239	333	1939	210	1085	527
Lu	158	175	210	107	46.4	62.2	315	39.8	190	97.4
Hf	11044	12185	11265	13688	9920	10174	10189	10143	8654	8657
Ta	2.88	2.54	3.65	9.71	1.26	0.86	11.63	1.06	6.38	3.33
Pb	8.58	2.58	26.4	1.12	0.57	0.91	42.3	1.41	8.32	3.86
Th	240	125	1295	527	246	411	18611	662	3703	1156
U	1262	1199	2142	3621	568	709	9646	903	2354	824

Spot (ppm)	TAU-23-2 003	TAU-23-2 004	TAU-23-2 005	TAU-23-2 006	TAU-23-2 007	TAU-23-2 008	TAU-23-2 009	TAU-23-2 010	TAU-23-2 011	TAU-23-2 012
Al	b.d.l.	4.46	b.d.l.	4.90	717	6.69	36.8	b.d.l.	1.84	61.9
P	77	171	165	887	2587	247	542	439	216	455
Ti	2.46	12.2	3.53	3.42	22.2	3.52	5.18	1.66	1.77	5.96
Y	334	2523	1540	1789	6609	1066	3806	1236	3710	5315
Nb	2.22	24.99	1.82	5.69	18.5	6.17	3.71	6.19	19.9	108
La	b.d.l.	0.11	b.d.l.	0.09	16.1	0.19	0.35	b.d.l.	0.07	0.19
Ce	4.71	227.43	21.81	19.56	45.3	9.14	13.32	3.91	39.95	130
Pr	0.02	0.67	0.33	0.13	5.63	0.15	1.20	0.03	0.89	1.10
Nd	0.29	13.1	5.10	1.67	31.0	1.80	19.7	0.50	15.5	21.0
Sm	0.98	27.6	10.1	3.99	26.0	4.19	37.2	2.20	29.4	48.5
Eu	0.25	10.3	4.27	1.54	2.74	0.84	6.39	0.23	4.57	6.59
Gd	6.13	107	48.1	27.2	132	23.8	146	16.8	126	207
Tb	2.17	28.3	14.1	10.9	49.8	8.19	40.3	7.07	36.1	57.6
Dy	27.0	272	151	149	618	98.8	392	96.9	371	580
Ho	11.0	84.6	52.8	57.8	219	36.1	127	39.7	119	180
Er	55.3	345	237	299	968	171	548	211	504	728
Tm	12.6	64.8	48.7	68.6	202	37.0	104	50.3	98.3	136
Yb	119	528	424	646	1730	334	876	487	799	1075
Lu	24.4	94.6	82.9	124	301	64.1	167	96.5	141	181
Hf	12754	8697	8439	10424	11413	9026	6901	12231	9437	10885
Ta	2.14	5.67	0.93	5.31	10.76	3.71	1.13	10.10	7.68	33.39
Pb	0.28	9.72	0.99	1.82	22.4	1.79	2.16	0.89	6.27	37.3
Th	109	3994	304	569	3566	544	826	379	2872	16167
U	566	1736	368	3452	8149	1616	949	2545	3953	13201

Spot (ppm)	TAU-23- 2 013	TAU-23- 2 014	TAU-23- 2 015	TAU-23- 2 016	TAU-23- 2 017	TAU-23- 2 018	TAU-23- 2 019	TAU-23- 2 020	TAU-23- 2 021	TAU-23- 2 022
Al	2.03	b.d.l.	16.4	50.6	3.31	2.52	b.d.l.	1654	143	b.d.l.
P	260	202	409	403	324	336	193	256	1069	145
Ti	7.64	4.37	5.98	8.70	3.32	8.55	6.93	13.8	1.95	1.90
Y	2802	873	767	1003	1152	3947	1468	2061	2652	476
Nb	2.43	2.97	1.52	2.61	5.89	12.03	7.51	9.35	26.49	2.49
La	0.10	b.d.l.	0.17	b.d.l.	b.d.l.	0.19	b.d.l.	20.6	0.18	b.d.l.
Ce	13.19	11.93	0.92	12.71	5.89	34.8	86.2	82.8	9.49	13.9
Pr	0.59	0.09	0.13	0.26	0.07	1.92	0.25	6.69	0.13	0.03
Nd	10.0	1.77	0.55	4.09	1.83	34.8	4.21	33.9	1.55	0.49
Sm	24.4	3.84	1.12	9.07	3.74	70.6	10.8	24.8	4.11	1.18
Eu	8.81	1.15	0.46	0.93	0.52	10.9	5.58	15.6	0.47	0.86
Gd	104	21.9	9.60	37.2	22.9	222	54.9	77.8	30.0	7.23
Tb	28.3	7.05	4.72	10.8	8.64	50.1	15.2	19.0	13.9	2.92
Dy	283	81.2	65.3	109	106	448	152	185	199	35.9
Ho	92.0	29.4	26.4	35.2	35.1	131	50.9	60.4	82.3	14.7
Er	387	136	129	147	167	535	209	269	435	76.9
Tm	79.2	30.2	31.6	28.4	43.7	101	41.4	61.0	108	18.6
Yb	676	278	322	236	405	826	347	634	1055	189
Lu	126	53.8	66.3	45.3	74.2	145	65.6	145	204	43.88
Hf	8131	9571	13416	10392	14008	9018	8308	8121	14713	10406
Ta	1.29	2.16	1.50	1.37	4.89	2.88	2.37	2.97	17.1	0.83
Pb	2.01	1.17	1.72	27.3	1.11	13.1	3.37	32.0	5.78	3.24
Th	967	465	52.0	227	463	6239	1405	9614	840	149
U	1011	937	673	638	2770	5249	863	4306	6796	469

Spot (ppm)	TAU-23- 2 023	TAU-23- 2 024	TAU-23- 2 025	TAU-23- 2 026	TAU-23- 2 027	TAU-23- 2 028	TAU-23- 2 029	TAU-23- 2 030	TAU-23- 2 031	TAU-23- 2 032
Al	1.80	b.d.l.	b.d.l.	231	2.47	1.93	417	5.42	1.43	2.69
P	101	297	22629459	23061186	76	117	400	163	143	185
Ti	3.77	4.95	b.d.l.	63.3	2.33	2.05	13.2	4.90	4.33	3.73
Y	328	2868	157173	274024	472	1013	3541	856	1310	1026
Nb	0.68	23.44	b.d.l.	1.58	1.52	1.53	20.65	3.82	1.62	1.67
La	b.d.l.	b.d.l.	291693	157491	b.d.l.	b.d.l.	1.65	0.15	b.d.l.	b.d.l.
Ce	3.90	87.1	669767	412942	7.01	9.40	195	13.49	16.74	13.34
Pr	0.04	0.34	49259	54137	0.03	0.11	0.96	0.11	0.35	0.21
Nd	0.71	8.01	209903	238286	0.46	2.54	9.21	1.65	5.56	3.56
Sm	1.52	21.6	81717	62284	1.46	6.00	15.7	3.53	11.5	7.58
Eu	0.57	4.72	5383	3004	0.47	1.70	5.46	1.18	3.87	2.65
Gd	8.54	97.1	62218	54429	9.20	29.4	82.3	17.6	47.5	34.8
Tb	2.66	27.1	5010	8209	3.26	8.74	25.8	6.19	13.0	9.81
Dy	30.4	285	27717	48173	40.7	98.0	302	73.7	138	106
Ho	11.1	93.3	5137	9244	15.4	35.0	114	28.2	45.5	35.9
Er	51.6	400	13479	24756	76.7	162	521	138	194	157
Tm	11.0	79.4	1708	3236	17.6	35.1	105	30.5	39.5	31.9
Yb	102	664	10361	19369	168	312	899	278	335	279
Lu	20.08	119	1275	2465	33.7	58.9	173	56.6	63.0	53.5
Hf	9387	10481	b.d.l.	b.d.l.	12043	11524	8677	9275	9733	9652
Ta	0.48	8.80	2.50	b.d.l.	1.63	1.34	3.49	1.86	0.90	0.93
Pb	0.20	11.7	1701	1940	0.27	0.78	8.45	1.05	1.00	0.78
Th	87.42	5340	4390	7145	139	348	3380	264	429	341
U	211	4707	981	2939	474	745	3534	565	597	551

Spot (ppm)	TAU-23-2 033	TAU-23-2 034	TAU-23-2 035	TAU-23-2 036	TAU-23-2 037	TAU-23-2 038	TAU-23-2 039	TAU-23-2 040	TAU-23-2 041	TAU-23-2 042
Al	4.64	2.68	10.8	1.88	b.d.l.	b.d.l.	b.d.l.	1.46	5.52	21.8
P	142	151	279	107	230	275	214	189	295	1633
Ti	1.78	1.59	3.53	2.22	5.61	3.07	7.16	5.98	5.31	2.36
Y	948	759	3750	514	1098	848	1784	1025	1889	991
Nb	1.04	1.76	9.21	1.84	3.07	5.07	1.23	2.83	3.84	2.29
La	0.05	b.d.l.	0.23	b.d.l.	b.d.l.	1.48	0.07	b.d.l.	b.d.l.	0.15
Ce	4.47	4.15	63.9	11.2	10.0	20.7	9.22	10.90	65.63	0.51
Pr	0.28	0.09	0.82	0.03	0.09	0.55	0.44	0.09	0.24	0.07
Nd	4.21	1.98	11.9	0.71	1.84	3.31	7.18	1.54	4.20	0.33
Sm	6.95	3.47	23.9	1.98	3.95	3.73	14.8	3.76	7.95	0.91
Eu	1.09	0.59	6.62	0.66	1.42	0.95	5.45	1.42	2.28	0.10
Gd	29.2	18.4	111	11.2	20.1	18.1	62.2	20.0	39.6	7.41
Tb	8.58	6.01	33.2	3.76	7.04	6.05	17.4	6.92	12.9	4.91
Dy	94.2	71.2	363	46.4	87.0	75.4	181	85.3	163	78.9
Ho	33.6	25.7	124	17.2	35.8	28.0	58.9	33.2	61.5	32.0
Er	149	122	546	82.7	178	134	256	166	297	175
Tm	30.6	25.8	109	18.0	39.8	30.0	52.2	36.6	64.0	47.7
Yb	267	235	927	164	369	271	450	332	585	548
Lu	51.6	44.9	169	32.9	77.2	52.6	87.2	66.7	119	116
Hf	9944	11496	9431	9668	9300	10271	8544	9103	9625	17619
Ta	0.62	1.29	3.87	1.06	1.51	2.82	0.79	1.41	1.35	4.06
Pb	0.48	0.45	5.81	0.27	0.92	1.17	1.18	0.83	19.64	0.32
Th	191	166	1232	109	415	451	490	376	297	30.4
U	427	524	1526	253	824	1068	592	673	281	3547

Spot (ppm)	TAU-23- 2 043	TAU-23- 2 044	TAU-23- 2 045	TAU-23- 2 046	TAU-23- 2 047	TAU-23- 2 048	TAU-23- 2 049	TAU-23- 2 050	TAU-23- 2 051	TAU-23- 2 052
Al	6.28	b.d.l.	19.5	3.54	1.80	18.6	b.d.l.	52.2	1.88	84.6
P	532	385	206	112	626	161	260	194	323	1306
Ti	2.95	3.16	8.45	4.96	1.46	3.04	2.89	4.22	3.21	119
Y	1044	1002	2589	1139	1930	1623	1576	790	2301	3646
Nb	1.08	1.16	3.21	1.54	5.00	11.41	8.34	3.30	6.20	6.82
La	b.d.l.	b.d.l.	0.09	0.04	b.d.l.	b.d.l.	b.d.l.	0.13	0.05	3.59
Ce	1.20	2.01	19.84	9.03	9.27	25.13	21.86	4.30	69.05	36.52
Pr	0.03	0.08	1.29	0.42	0.09	0.08	0.08	0.07	0.42	2.73
Nd	0.63	1.04	19.2	6.31	1.94	1.88	1.60	0.86	7.55	20.6
Sm	1.68	2.27	27.0	10.7	5.27	5.96	4.71	2.22	18.6	27.8
Eu	0.21	0.25	8.54	3.54	0.94	1.34	0.97	0.46	5.91	8.13
Gd	15.0	17.9	99.5	42.3	34.3	40.2	29.7	14.4	79.2	116
Tb	6.25	6.58	25.5	11.2	12.4	13.3	10.8	5.42	22.1	38.7
Dy	86.6	84.9	259	116	160	158	135	68.8	230	402
Ho	36.1	34.3	84.9	38.9	62.5	59.4	52.0	25.9	75.8	119
Er	182	167	363	172	309	271	251	126	326	493
Tm	40.1	35.6	70.4	34.7	67.6	57.0	54.5	27.9	66.6	97.4
Yb	375	322	624	298	626	526	488	254	577	825
Lu	77.8	63.9	118	57.08	124	96.1	94.9	51.6	107	145
Hf	9265	8306	8024	8351	10169	11834	9586	10332	9342	10038
Ta	0.63	0.66	1.43	0.88	3.59	6.17	3.60	3.19	2.24	3.32
Pb	1.05	1.48	1.21	0.56	1.04	2.03	1.42	1.21	3.43	39.3
Th	44.4	74.9	544	221	456	901	650	333	1503	741
U	320	338	531	261	1972	1954	1413	1140	1776	1156

Spot (ppm)	TAU-23-2 053	TAU-23-2 054	TAU-23-2 055	TAU-23-2 056	TAU-23-2 057	TAU-23-2 058	TAU-23-2 059	TAU-23-2 060	TAU-23-2 061	TAU-23-2 062
Al	16.4	7.51	5.86	3.03	1.54	1.69	5.49	7.70	b.d.l.	1.68
P	305	314	297	181	135	255	244	293	236	356
Ti	5.72	8.63	7.67	4.30	3.64	2.08	4.50	4.78	2.80	2.47
Y	766	1944	1628	1460	1106	687	1906	1077	2147	1211
Nb	2.17	1.85	2.05	1.60	1.15	4.72	2.38	3.69	6.92	7.44
La	0.21	0.08	b.d.l.	0.08	b.d.l.	b.d.l.	0.07	b.d.l.	b.d.l.	b.d.l.
Ce	9.32	8.18	8.82	8.43	8.61	6.86	10.6	7.91	38.4	10.7
Pr	0.12	0.43	0.25	0.25	0.20	0.04	0.64	0.13	0.20	0.05
Nd	1.49	6.48	4.27	4.02	3.20	0.64	10.6	2.26	3.53	1.01
Sm	2.64	14.4	9.61	9.94	6.55	1.91	17.2	4.58	9.53	3.15
Eu	0.89	5.70	3.89	3.35	1.87	0.38	3.39	0.82	3.19	0.62
Gd	14.6	67.3	47.6	50.5	31.0	11.2	65.5	27.2	51.2	19.5
Tb	4.98	18.6	14.1	14.0	9.45	4.25	18.7	8.77	16.6	7.78
Dy	64.5	194	156	149	106	57.4	191	104	193	103
Ho	25.5	63.8	53.2	49.0	38.0	23.2	63.9	37.0	69.9	40.5
Er	131	279	241	215	171	118	279	170	329	204
Tm	30.6	56.3	49.6	43.5	35.6	28.1	55.2	34.8	67.9	48.8
Yb	312	493	437	371	314	271	474	305	613	468
Lu	66.6	93.8	85.2	71.3	60.6	56.1	90.9	58.2	116	91.0
Hf	10214	8543	8572	9764	9781	13389	8039	9653	10194	12509
Ta	1.62	0.96	1.10	0.80	0.87	5.06	0.91	1.80	3.13	6.97
Pb	3.89	1.46	1.31	1.64	0.59	0.88	1.21	1.43	1.84	1.68
Th	165	637	590	714	260	305	507	650	790	624
U	506	711	706	657	509	1980	743	1026	1242	3307

Spot (ppm)	TAU-23- 2_063	TAU-23- 2_064	TAU-23- 2_065	TAU-23- 2_066	TAU-23- 2_067	TAU-23- 2_068	TAU-23- 2_069	TAU-23- 2_070	TAU-23- 2_071	TAU-23- 2_072
Al	50.4	3.10	b.d.l.	24978	5.07	b.d.l.	18.36	6.34	b.d.l.	17.9
P	629	79	154	5541361	153	257	309	183	236	490
Ti	10.9	3.51	6.44	32.8	6.62	7.62	2.39	4.15	1.85	3.86
Y	5900	256	1471	33574	1215	931	2666	1010	2190	704
Nb	36.2	0.63	8.12	1.44	1.00	2.55	10.1	1.00	3.31	0.87
La	1.75	0.15	b.d.l.	33214	0.09	b.d.l.	0.06	0.14	b.d.l.	b.d.l.
Ce	207	3.43	83.1	86721	10.55	3.31	20.2	2.40	5.28	0.53
Pr	2.80	0.09	0.16	11342	0.51	0.13	0.28	0.27	0.33	0.03
Nd	40.2	0.57	2.55	49081	8.33	2.22	6.13	3.54	4.91	0.60
Sm	69.5	1.14	7.26	11679	14.11	4.79	13.5	5.80	10.4	2.28
Eu	15.4	0.50	3.55	694	5.19	0.89	1.39	1.40	1.67	0.04
Gd	242	5.20	41.1	10752	53.7	22.6	64.3	27.5	52.1	16.3
Tb	65.7	1.74	13.1	1449	14.14	7.19	20.2	8.50	17.1	6.25
Dy	639	21.6	145	7933	138	83.0	238	96.9	201	72.9
Ho	197	8.11	51.0	1438	42.8	31.5	86.4	34.4	72.9	24.5
Er	790	41.7	225	3606	182	150	403	159	334	106
Tm	151	9.51	45.5	392	35.0	32.5	86.6	33.6	71.2	21.5
Yb	1174	93	388	2020	292	300	785	301	632	175
Lu	208	18.9	73.3	261	58.2	59.9	141	59.6	120	32.5
Hf	8005	11167	9282	629	8233	9072	13287	8612	9780	12681
Ta	8.94	0.77	3.03	0	0.46	1.07	5.37	0.80	2.41	0.59
Pb	20.9	0.33	2.09	411	0.79	0.50	4.12	0.60	0.86	0.71
Th	8961	57.0	969	2669	330	248	1943	139	394	35.3
U	4998	241	767	2127	422	675	3137	379	1343	392

Spot (ppm)	TAU-23- 2 073	TAU-23- 2 074	TAU-23- 2 075	TAU-23- 2 076	TAU-23- 2 077	TAU-23- 2 078	TAU-23- 2 079	TAU-23- 2 080	TAU-23- 2 081	TAU-23- 2 082
Al	29.1	368.68	1.45	10.04	86.04	b.d.l.	21.4	8.75	4.32	7.56
P	1411	1263	327	548	666	251	248	505	211	760
Ti	8.11	11.43	1.79	4.28	2.70	5.68	4.02	0.84	4.99	3.17
Y	3036	3564	2450	1830	2558	1642	1879	1466	1587	2420
Nb	1.65	13.3	20.2	5.97	4.64	9.44	4.89	6.66	1.98	8.00
La	b.d.l.	1.41	0.31	0.22	b.d.l.	b.d.l.	0.10	b.d.l.	b.d.l.	0.50
Ce	1.62	15.7	27.3	29.5	13.4	24.5	22.5	4.14	6.34	5.79
Pr	0.21	1.56	0.22	0.21	0.24	0.16	0.53	0.02	0.49	0.19
Nd	3.57	15.6	3.19	2.36	4.13	2.60	7.40	0.57	7.72	2.72
Sm	9.81	27.1	9.09	5.82	9.55	6.36	13.9	2.21	12.7	6.48
Eu	0.16	8.25	1.38	1.95	2.15	1.73	3.22	0.18	2.44	0.62
Gd	55.8	137	53.9	35.0	49.9	37.2	58.1	16.8	54.4	38.9
Tb	20.9	40.5	18.6	12.8	17.8	12.1	17.2	7.94	15.8	15.8
Dy	273.0	401.6	225.1	161.1	229.5	149.2	186.7	117.0	164.1	201.9
Ho	104	120	79.9	59.6	84.9	55.3	65.9	49.2	55.2	76.5
Er	483	497	373	290	412	255	280	260	237	380
Tm	100	97.8	74.4	64.7	93.8	54.4	56.0	62.4	47.8	83.9
Yb	875	844	662	584	880	482	466	600	401	768
Lu	157	153	125	111	162	91.7	88.3	119	75.4	139
Hf	11506	15345	10293	9951	12245	9989	9265	15297	8492	10039
Ta	0.99	15.94	9.33	3.74	3.39	4.40	1.64	6.19	0.77	6.47
Pb	2.64	16.3	3.62	2.23	1.22	2.26	2.02	0.73	0.79	1.51
Th	148	390	1498	809	546	987	832	296	335	661
U	650	1188	3063	1991	2847	1968	1904	2631	504	3181

Spot (ppm)	TAU-23-2 083	TAU-23-2 084	TAU-23-2 085	TAU-23-2 086	TAU-23-2 087	TAU-23-2 088	TAU-23-2 089	TAU-23-2 090	TAU-23-2 091	TAU-23-2 092
Al	21.5	18.5	1.33	3.51	16.7	b.d.l.	13.2	13.3	b.d.l.	b.d.l.
P	283	1105	133	189	245	597	1020	1676	221	222
Ti	4.77	7.02	3.90	3.94	4.77	2.38	2.22	4.16	17.7	5.15
Y	4049	1888	684	2043	2235	2402	1743	3731	514	1085
Nb	7.05	8.53	1.14	1.65	12.18	18.64	0.89	3.69	2.39	3.05
La	0.16	b.d.l.	b.d.l.	b.d.l.	b.d.l.	b.d.l.	b.d.l.	0.09	b.d.l.	b.d.l.
Ce	121	35.2	9.11	9.64	34.6	12.4	0.23	6.61	26.5	16.7
Pr	1.68	0.15	0.08	0.43	0.16	0.05	b.d.l.	0.14	0.10	0.13
Nd	29.0	2.71	1.33	5.94	2.40	1.04	0.30	2.00	1.99	2.45
Sm	49.8	6.98	3.04	11.6	6.55	3.42	1.21	5.55	3.50	4.94
Eu	18.6	0.80	1.26	3.76	1.63	0.72	0.05	0.12	0.65	1.83
Gd	182	38.2	16.8	60.7	37.9	28.4	12.5	43.8	14.4	25.5
Tb	45.8	13.5	5.43	17.8	13.4	12.9	7.11	20.6	4.10	8.09
Dy	442.8	166.2	64.7	194	176	192	122	296	51.5	97.0
Ho	137	61.8	23.6	64.8	68.6	79.5	54.9	119	17.6	36.9
Er	554	294	110	291	335	406	311	611	81.6	175
Tm	103	60.9	24.1	59.6	75.8	93.4	77.3	134	16.7	37.2
Yb	841	534	211	525	693	872	751	1210	146	339
Lu	150	107	41.8	99.0	136	163	148	224	30.4	68.9
Hf	9930	10431	9088	10106	11547	12529	13136	12215	8236	8340
Ta	1.81	3.02	0.67	1.22	4.91	10.18	1.23	2.30	0.90	1.51
Pb	4.45	20.2	1.15	1.64	2.56	1.13	0.39	12.23	4.11	0.79
Th	1991	323	94.3	692	1147	513	18.1	435	80.5	317
U	1224	335	195	952	2115	3198	728	1501	90.2	536

Spot (ppm)	TAU-23-2 093	TAU-23-2 094	TAU-23-2 095	TAU-23-2 096	TAU-23-2 097	TAU-23-2 098	TAU-23-2 099	TAU-23-2 100	TAU-23-2 101	TAU-23-2 102
Al	b.d.l.	3.16	25.0	8.47	9.26	21.2	167	1.30	1.19	2.49
P	208	220	537	560	313	241	324	572	142	347
Ti	2.71	6.29	4.18	6.49	2.41	4.16	7.19	2.94	5.48	3.11
Y	976	698	1702	5235	1642	2827	875	2641	1334	3173
Nb	3.85	1.36	7.74	6.74	10.29	11.37	1.81	18.53	1.14	6.43
La	b.d.l.	b.d.l.	0.08	0.14	0.06	0.29	10.64	b.d.l.	0.06	0.07
Ce	6.29	6.32	8.56	39.3	11.6	133	11.8	38.3	5.91	63.2
Pr	0.10	0.10	0.06	1.70	0.09	0.60	1.43	0.14	0.47	0.70
Nd	1.32	1.48	1.14	32.2	1.41	7.08	7.46	3.04	7.13	11.2
Sm	3.60	3.55	3.21	62.2	4.61	9.55	6.54	8.85	12.4	21.2
Eu	0.73	1.34	0.72	18.0	0.72	4.02	2.80	1.71	3.16	6.23
Gd	22.6	17.5	23.2	226	31.6	45.0	28.8	51.6	51.8	99.7
Tb	7.68	5.56	9.42	58.5	11.2	15.2	7.99	17.9	13.8	28.5
Dy	92.5	64.0	129	569	146	192	83.6	224	141	311
Ho	34.7	23.2	53.5	175	55.5	78.5	29.5	84.3	46.3	107
Er	161	108	279	715	269	420	133	414	193	477
Tm	34.1	22.7	66.9	139	57.6	103	27.7	90.2	38.0	95.4
Yb	301	209	651	1162	544	1008	238	812	324	828
Lu	59.6	42.2	128	208	104	211	48.0	154	60.5	157.1
Hf	8993	8859	11606	8250	11086	8044	8459	12948	8985	8261
Ta	2.54	0.95	5.19	1.86	7.66	3.75	0.92	10.59	0.59	2.81
Pb	1.33	0.94	0.83	6.72	1.47	5.17	0.94	3.03	1.04	3.02
Th	534	387	358	3070	671	1969	374	1459	423	1317
U	1214	542	2439	2106	2879	1717	702	6029	667	1508

Spot (ppm)	TAU-23- 2 103	TAU-23- 2 104	TAU-23- 2 105	TAU-23- 2 106	TAU-23- 2 107	TAU-23- 2 108	TAU-23- 2 109	TAU-23- 2 110	TAU-23- 2 111	TAU-23- 2 112
Al	31.7	36098	b.d.l.	9.20	79.9	12.8	3.35	b.d.l.	13.1	5.58
P	634	46	212	208	1043	339	254	156	242	209
Ti	2.24	4.32	9.12	3.59	4.85	10.9	5.19	6.16	6.05	8.70
Y	2368	126	1152	1334	4320	6539	4473	2852	4120	1149
Nb	18.8	0.24	5.09	1.50	47.0	17.7	10.6	3.84	6.65	3.45
La	0.25	11.3	b.d.l.	0.06	1.03	0.16	0.12	0.10	0.18	b.d.l.
Ce	10.6	3.83	36.8	9.42	35.2	206	115	72.2	74.2	6.15
Pr	0.14	1.99	0.21	0.28	0.51	2.42	0.91	0.81	1.84	0.16
Nd	1.61	7.72	4.34	4.93	5.04	38.2	15.2	15.5	31.3	3.16
Sm	4.85	2.73	11.7	9.66	11.8	62.7	29.7	28.1	55.0	6.94
Eu	0.63	1.69	4.63	2.48	1.27	25.4	12.3	12.6	17.5	1.59
Gd	33.6	4.03	46.1	42.2	74.3	242	140	112	187	29.5
Tb	13.7	1.11	12.3	12.2	29.1	66.8	41.5	29.8	46.0	8.80
Dy	191	11.9	123	131	370	700	440	294	445	104
Ho	75.4	3.96	39.2	45.0	141	224	149	92.4	139	38.6
Er	391	20.1	171	205	678	955	651	382	568	179
Tm	90.4	4.71	34.3	42.5	147	185	130	73.5	108	38.2
Yb	847	46.7	300	378	1293	1525	1084	609	887	337
Lu	165.3	9.36	53.6	74.1	240	270	199	111	162	66.7
Hf	14756	4808	9738	9194	12500	8104	8918	8919	8245	8337
Ta	16.15	0.49	1.99	1.18	21.24	2.85	2.87	1.44	1.89	1.35
Pb	2.97	248	8.49	1.08	15.2	4.23	2.80	2.29	5.12	1.53
Th	997	33.9	4013	456	2905	1886	1217	911	2333	656
U	6532	137	2446	735	9031	1069	1010	671	1844	1301

Spot (ppm)	TAU-23-2 113	TAU-23-2 114	TAU-23-2 115	TAU-23-2 116	TAU-23-2 117	TAU-23-2 118	TAU-23-2 119	TAU-23-2 120	TAU-23-2 121	TAU-23-2 122
Al	159	19.3	2.74	2.74	52.1	b.d.l.	b.d.l.	40.14	b.d.l.	1.49
P	302	306	1050	231	458	83	280	355	262	328
Ti	4.43	3.63	1.71	4.55	3.20	4.08	3.60	5.24	7.06	1.48
Y	3580	2091	3678	1848	1533	996	2302	1394	946	1304
Nb	9.61	4.27	33.9	5.99	6.66	0.88	9.60	1.44	1.75	4.40
La	0.20	b.d.l.	b.d.l.	b.d.l.	0.07	b.d.l.	b.d.l.	0.08	b.d.l.	b.d.l.
Ce	23.3	34.1	7.36	18.8	8.10	18.4	31.0	8.84	9.69	13.2
Pr	0.53	0.05	0.04	0.24	0.12	0.22	0.22	0.10	0.04	0.10
Nd	7.74	1.48	1.12	4.44	1.61	5.03	4.58	1.91	1.00	1.64
Sm	18.6	4.75	5.07	11.1	3.85	9.75	11.0	4.25	2.30	4.31
Eu	2.48	0.61	0.30	2.62	0.71	3.67	2.19	0.67	0.47	1.29
Gd	88.8	32.7	42.1	59.9	25.9	38.5	59.9	25.8	16.0	26.5
Tb	28.7	12.2	19.5	17.5	9.72	10.6	18.3	9.36	6.24	9.35
Dy	329	164	279	185	130	107	206	119	80.0	118
Ho	115	65.9	116	61.8	51.1	34.0	73.3	46.6	31.9	44.3
Er	537	331	606	270	256	143	333	225	156	214
Tm	113	73.6	143	53.4	56.9	28.2	69.4	48.4	33.4	44.3
Yb	988	680	1342	453	531	235	611	434	300	412
Lu	186	132	258	85.2	104.5	44.5	117	85.8	60.8	81.3
Hf	13073	12291	17300	8240	12079	8201	9298	9492	8832	9450
Ta	5.53	2.93	21.23	2.33	4.37	0.49	3.60	0.89	0.97	2.49
Pb	3.92	20.6	2.33	3.40	1.23	0.41	2.99	5.97	7.64	0.80
Th	1928	430	1090	1557	508	174	1292	143	170	324
U	4315	649	9129	1355	2050	194	1581	232	244	986

Spot (ppm)	TAU-23- 2 123	TAU-23- 2 124	TAU-23- 2 125	TAU-23- 2 126	TAU-23- 2 127	TAU-23- 2 128	TAU-23- 2 129	TAU-23- 2 130	TAU-23- 2 131	TAU-23- 2 132
Al	25.4	b.d.l.	6067	5.91	15.5	447	b.d.l.	4.80	4.69	6.95
P	186	297	191	197	130	2125	212	106	221	127
Ti	3.30	3.39	8.60	7.27	4.68	7.36	3.70	4.54	5.15	11.7
Y	1703	3051	1562	1820	1016	4640	952	337	1055	1873
Nb	13.16	3.30	3.28	1.43	1.09	19.53	3.93	0.74	3.27	1.93
La	b.d.l.	0.08	0.85	0.09	b.d.l.	10.02	b.d.l.	b.d.l.	b.d.l.	0.05
Ce	34.5	8.54	6.84	8.24	6.71	77.1	10.7	4.73	17.3	5.45
Pr	0.11	0.75	0.48	0.48	0.22	4.27	0.10	0.03	0.12	0.85
Nd	2.21	11.7	6.18	6.97	2.95	26.9	1.90	0.66	2.41	16.4
Sm	7.41	21.1	10.3	13.9	6.61	26.8	4.87	1.51	5.50	41.9
Eu	1.62	4.01	1.94	5.44	2.26	1.71	1.08	0.58	1.71	7.83
Gd	42.9	91.2	46.5	64.3	30.9	121	28.0	7.70	28.9	121
Tb	14.0	27.3	14.2	17.6	9.10	38.8	8.38	2.45	9.03	24.7
Dy	161	300	159	186	103	437	94.2	29.1	101	213
Ho	57.2	103	54.8	59.7	36.2	155	32.6	11.0	35.0	62.9
Er	259	458	242	253	162	680	143	53.7	158	257
Tm	53.6	92.1	48.2	50.8	34.4	139	29.3	12.0	33.2	48.7
Yb	453	793	423	450	304	1152	256	111	294	394
Lu	84.9	150	82.1	84.0	57.7	210	49.2	22.5	57.7	75.4
Hf	10262	8169	8041	8935	10345	10119	9862	10048	9720	8490
Ta	4.86	1.61	1.36	0.82	0.85	8.11	2.13	0.64	2.18	0.75
Pb	3.97	1.32	4.30	1.29	0.69	8.82	2.55	0.35	2.59	4.10
Th	1649	563	356	553	325	3727	1049	147	1248	1820
U	2093	1130	663	634	506	4915	1622	289	1255	2342

Spot (ppm)	TAU-23- 2 133	TAU-23- 2 134	TAU-23- 2 135	TAU-23- 2 136	TAU-23- 2 137	TAU-23- 2 138	TAU-23- 2 139	TAU-23- 2 140	TAU-23- 2 141	TAU-23- 3 001
Al	4.21	2.73	20.9	b.d.l.	b.d.l.	2.85	22.1	32032	21.0	1.98
P	331	322	369	189	138	420	239	1496	3376	109
Ti	4.90	3.00	2.74	4.33	3.06	3.84	2.91	199	2.27	5.08
Y	1189	2324	1128	2525	1865	4249	2169	1321	4531	1514
Nb	5.18	3.59	4.03	2.30	1.69	7.33	2.81	13.8	16.7	1.15
La	0.04	0.55	0.13	0.06	b.d.l.	0.13	b.d.l.	0.97	0.23	0.06
Ce	8.03	10.6	4.45	4.12	3.91	18.4	8.27	3.94	1.58	21.9
Pr	0.12	0.67	0.10	0.36	0.31	0.97	0.29	0.31	0.24	0.52
Nd	2.50	8.63	1.44	5.67	5.56	15.7	5.71	1.51	2.41	8.23
Sm	7.49	15.2	2.79	12.2	10.0	32.8	12.9	1.33	5.37	15.0
Eu	1.48	2.44	0.59	2.90	2.33	7.32	2.58	1.24	0.56	6.48
Gd	35.5	69.1	18.9	63.2	48.7	144	58.1	8.57	37.1	64.0
Tb	9.96	20.7	6.95	20.0	15.7	40.0	17.6	5.21	20.9	16.8
Dy	113	229	95.4	236	179	419	204	91.0	324	163
Ho	40.5	77.3	37.2	83.7	64.2	139	70.8	41.6	135	52.7
Er	188	344	186	384	300	609	328	248	754	216
Tm	41.6	69.0	43.2	79.0	61.3	122	67.1	66.8	201	41.2
Yb	393	591	405	701	546	1047	595	723	2100	347
Lu	75.8	112.0	79.6	137	107	193	120	145	405	65.6
Hf	11155	9055	9890	8605	8160	10102	12045	8618	15733	7988
Ta	3.42	2.05	8.55	1.34	1.01	2.39	1.97	6.48	28.3	0.62
Pb	3.22	1.15	0.54	0.83	0.62	5.47	2.14	52.81	2.18	0.59
Th	1367	517	208	367	268	2442	918	27.8	307	272
U	2510	1179	1131	809	632	2570	1690	3553	18870	277

Spot (ppm)	TAU-23-3 002	TAU-23-3 003	TAU-23-3 004	TAU-23-3 005	TAU-23-3 006	TAU-23-3 007	TAU-23-3 008	TAU-23-3 009	TAU-23-3 010	TAU-23-3 011
Al	12.0	7.44	1.29	15.5	1.79	2.62	15.8	11.4	1.54	2.80
P	106	624	804	374	348	156	523	541	552	617
Ti	5.35	9.82	7.93	6.08	7.09	6.27	1.09	9.35	5.64	5.27
Y	1431	1229	2153	1420	939	301	655	1074	1136	1331
Nb	0.91	0.69	0.91	5.88	2.60	1.89	1.24	1.23	2.03	1.99
La	b.d.l.	b.d.l.	b.d.l.	1.17	b.d.l.	b.d.l.	b.d.l.	b.d.l.	b.d.l.	b.d.l.
Ce	18.7	2.17	3.87	26.8	21.9	2.50	0.94	1.60	2.23	2.87
Pr	0.42	0.08	0.13	0.47	0.04	0.04	0.03	0.04	0.04	0.04
Nd	6.96	1.56	3.06	2.33	0.98	0.55	0.24	0.84	0.78	0.89
Sm	13.9	4.27	7.89	3.48	2.47	1.26	0.46	2.20	2.47	2.68
Eu	5.85	0.12	0.17	0.73	0.38	0.07	0.18	0.07	0.07	0.09
Gd	57.8	26.3	48.2	20.6	15.0	7.48	4.01	18.2	17.1	19.7
Tb	15.7	9.13	16.6	7.64	5.87	2.45	2.76	6.75	6.80	7.99
Dy	155	115	203	106	76.0	28.5	46.2	90.8	94.3	110
Ho	48.8	42.7	72.2	44.8	31.3	10.3	20.5	36.7	38.4	44.4
Er	202	197	322	239	157	47.4	131	175	191	224
Tm	38.9	40.1	63.1	56.3	34.5	9.94	35.2	37.1	42.0	48.5
Yb	325	349	523	562	317	90	384	338	379	442
Lu	60.9	66.5	95.6	122	66.0	18.6	81.7	66.1	74.6	87.6
Hf	8768	10951	11066	10866	10321	13251	12376	11213	11708	11414
Ta	0.57	0.47	0.56	2.54	1.38	1.51	1.02	0.72	1.29	1.39
Pb	0.56	6.11	16.6	20.9	14.4	6.42	0.57	1.62	2.31	2.97
Th	257	51.3	143	426	235	118	140	69.9	104	138
U	252	163	359	505	238	697	556	261	430	550

Spot (ppm)	TAU-23-3 012	TAU-23-3 013	TAU-23-3 014	TAU-23-3 015	TAU-23-3 016	TAU-23-3 017	TAU-23-3 018	TAU-23-3 019	TAU-23-3 020	TAU-23-3 021
Al	b.d.l.	6.18	1.31	5.84	1.45	1.64	7479	9.41	9.46	823
P	269	147	175	245	190	191	38774357	1913	809	4128
Ti	3.61	2.59	17.2	6.16	5.33	5.18	168	6.05	1.93	28.6
Y	3493	1386	453	1306	717	424	115273	3493	1337	10920
Nb	6.27	10.9	0.64	3.55	1.01	0.95	b.d.l.	7.26	0.64	21.2
La	0.09	0.09	b.d.l.	b.d.l.	b.d.l.	0.04	242592	0.07	b.d.l.	4.24
Ce	20.2	25.1	3.13	8.54	8.65	7.13	472481	15.4	0.33	49.3
Pr	0.56	0.16	0.06	0.16	0.18	0.10	83704	0.27	b.d.l.	4.33
Nd	10.9	2.51	1.22	2.80	2.81	1.60	389433	2.82	0.26	49.6
Sm	27.6	6.69	2.30	5.99	5.79	2.99	88101	7.02	0.98	138
Eu	5.52	0.88	0.15	1.64	0.92	0.52	9134	0.66	0.04	68.5
Gd	126	38.4	12.1	30.2	25.5	14.2	60920	45.7	11.0	670
Tb	34.3	11.9	3.85	9.42	7.03	3.90	5029	19.7	5.93	168
Dy	363	136	45.4	113	75.6	42.7	25027	283	99.1	1427
Ho	118	47.3	16.2	42.5	24.8	14.4	5419	115	44.0	365
Er	490	212	73.4	194	98.3	61.6	12941	556	243	1266
Tm	97.7	42.8	15.0	41.0	19.2	11.5	1471	123	60.8	204
Yb	803	370	136	365	155	93.7	7718	1109	600	1418
Lu	149	69.1	28.7	70.8	27.4	17.4	717	213	124	224
Hf	8517	11270	8294	8261	9185	8736	b.d.l.	12543	13089	9532
Ta	2.29	5.64	0.31	2.36	0.33	0.31	b.d.l.	3.89	0.83	4.86
Pb	2.67	3.17	0.93	1.38	10.41	7.94	1815	6.03	0.36	19.16
Th	1185	1391	9.61	598	71.9	57.7	13433	139	19.88	2355
U	1308	1745	26.9	975	77.8	66.1	2510	494	597	854

Spot (ppm)	TAU-23-3 022	TAU-23-3 023	TAU-23-3 024	TAU-23-3 025	TAU-23-3 026	TAU-23-3 027	TAU-23-3 028	TAU-23-3 029	TAU-23-3 030	TAU-23-3 031
Al	6.26	1.73	63.6	260	2.76	5.47	8.46	10.9	1.66	b.d.l.
P	235	223	411	991	224	158	579	1832	329	270
Ti	9.91	11.0	20.8	14.4	6.93	6.82	11.3	11.0	4.75	2.83
Y	396	550	976	2125	2292	1956	1146	4129	5180	4042
Nb	3.00	3.28	8.03	9.23	8.94	9.16	6.44	9.83	6.37	4.72
La	b.d.l.	0.06	0.21	42.55	0.18	0.07	b.d.l.	0.12	0.15	0.10
Ce	18.9	21.9	9.16	108	19.3	18.1	7.40	18.2	28.6	17.1
Pr	0.04	0.06	0.11	13.57	0.46	0.33	0.07	0.11	1.74	0.83
Nd	0.55	0.95	0.86	61.3	7.01	4.70	0.72	1.38	28.9	15.4
Sm	1.48	2.32	1.68	24.8	12.2	9.98	2.74	4.91	53.0	32.8
Eu	0.19	0.31	0.30	4.18	0.43	0.38	0.93	0.86	11.5	6.80
Gd	8.23	11.8	13.2	60.2	62.4	52.4	20.9	38.7	211	148
Tb	2.77	3.99	5.71	19.0	19.7	16.8	7.17	18.6	55.1	41.0
Dy	34.4	49.1	81.0	197	229	197	92.0	295	561	425
Ho	13.1	17.9	32.9	61.1	78.8	68.6	36.1	132	178	136
Er	61.8	87.0	167	289	335	295	202	728	742	572
Tm	13.4	18.4	36.3	66.1	62.6	54.4	49.5	169	141	112
Yb	120	165	326	654	484	429	515	1654	1164	931
Lu	24.6	33.6	61.9	136	83.2	75.0	110	330	210	173
Hf	10196	10432	11312	14978	7824	8365	11804	11806	7914	8399
Ta	1.27	1.47	4.54	7.92	2.76	2.76	4.60	3.55	1.68	1.73
Pb	5.81	6.82	21.4	4.10	8.70	7.78	3.58	7.37	3.59	2.34
Th	98.2	115	122	170	159	144	80.7	132	1569	1099
U	64.1	68.8	477	1648	253	251	971	822	1430	1254

Spot (ppm)	TAU-23-3 032	TAU-23-3 033	TAU-23-3 034	TAU-23-3 035	TAU-23-3 036	TAU-23-3 037	TAU-23-3 038	TAU-23-3 039	TAU-23-3 040	TAU-23-3 041
Al	b.d.l.	387	6.16	b.d.l.	b.d.l.	b.d.l.	b.d.l.	59.3	166	b.d.l.
P	378	281	175	236	60	269	253	603	574	9424083
Ti	6.84	9.19	3.64	3.13	5.62	10.7	7.78	7.23	6.84	b.d.l.
Y	853	654	1610	1118	155	862	791	1017	2086	21226
Nb	2.07	3.66	3.37	6.34	1.08	12.5	10.7	3.35	4.81	b.d.l.
La	b.d.l.	0.17	0.12	b.d.l.	b.d.l.	b.d.l.	b.d.l.	0.35	0.84	46579
Ce	29.1	17.5	7.76	14.5	5.90	18.6	15.5	5.08	6.74	108418
Pr	0.10	0.13	0.27	0.09	0.06	0.07	0.08	0.27	0.34	13476
Nd	1.80	1.03	3.69	1.33	1.06	1.45	1.19	1.87	3.89	56963
Sm	3.68	2.33	8.24	4.72	2.03	3.03	2.19	2.32	7.17	11943
Eu	1.08	0.69	1.63	1.22	0.32	0.15	0.20	0.05	1.38	1681
Gd	20.6	13.4	42.2	27.8	9.48	17.5	15.5	15.2	40.0	9259
Tb	6.33	4.20	13.00	9.46	2.33	5.97	5.15	6.27	14.5	1033
Dy	79.0	55.5	152	108	19.9	79.8	69.2	90.4	185	5239
Ho	30.7	22.1	54.7	38.7	4.98	30.7	26.6	36.6	67.7	830
Er	144	113	249	179	16.3	145	127	184	331	1670
Tm	30.4	26.1	51.0	37.1	2.82	30.9	28.8	44.6	74.9	233
Yb	278	258	451	325	20.9	269	259	450	719	1314
Lu	55.5	55.5	87.2	62.0	3.52	51.7	49.4	94.1	144	158
Hf	9673	11488	9029	10016	10760	12360	11043	14503	9529	b.d.l.
Ta	0.80	2.82	1.70	3.36	0.55	4.79	4.15	1.95	2.98	b.d.l.
Pb	17.8	11.0	0.88	1.69	1.44	17.0	17.9	7.43	1.31	286
Th	103	84.9	375	739	16.1	174	176	73.6	366	1147
U	72.8	252	770	1287	48.1	149	162	1096	1573	355

Spot (ppm)	TAU-23-3 042	TAU-23-3 043	TAU-23-3 044	TAU-23-3 045	TAU-23-3 046	TAU-23-3 047	TAU-23-3 048	TAU-23-3 049	TAU-23-3 050	TAU-23-3 051
Al	7.91	16.8	7.82	3.04	570	3.32	4.44	84.7	207	3.99
P	979	690	695	191	242	455	348	510	300	273
Ti	6.20	6.53	12.0	10.2	19.2	5.07	4.12	6.93	4.71	9.6
Y	1930	1254	1440	457	701	4087	3365	2925	3390	2441
Nb	1.54	0.67	1.89	2.00	3.29	3.67	2.83	13.2	6.57	10.9
La	b.d.l.	b.d.l.	b.d.l.	0.09	0.35	0.11	0.12	0.32	0.08	b.d.l.
Ce	2.99	0.80	4.10	30.7	44.5	13.8	10.3	73.7	39.4	88.4
Pr	0.11	0.03	0.06	0.07	0.23	1.02	0.80	0.40	1.50	0.36
Nd	1.61	0.61	1.07	1.43	1.94	19.1	13.6	4.44	22.8	5.49
Sm	4.37	2.44	3.63	1.94	3.20	42.7	31.4	10.9	33.0	13.1
Eu	0.10	0.04	0.21	0.60	0.65	7.71	5.54	1.52	11.6	6.26
Gd	29.5	20.5	26.1	10.7	15.6	163	127	62.0	127	72.5
Tb	11.28	8.62	9.24	3.67	5.27	42.4	33.9	22.0	34.0	21.1
Dy	153	119	126	43.0	63.6	426	344	258	338	230
Ho	61.7	42.3	48.4	15.3	23.1	134	109	92.8	109	79.9
Er	302	182	228	74.1	113	562	457	440	466	348
Tm	64.1	34.7	47.0	16.2	26.3	109	90.2	93.8	90.3	71.0
Yb	556	274	413	148	234	921	758	818	767	613
Lu	104	47.9	77.3	29.9	44.4	169	141	148	146	115
Hf	11508	12793	11967	10726	10669	7703	8076	11004	7425	8642
Ta	0.84	0.41	1.15	1.23	1.87	1.61	1.43	5.04	1.41	3.56
Pb	17.5	4.69	30.7	10.5	15.5	3.82	3.21	69.5	2.20	3.73
Th	135	35.3	168	110	161	1770	1411	1498	873	1739
U	312	169	441	154	224	1659	1477	1040	862	1092

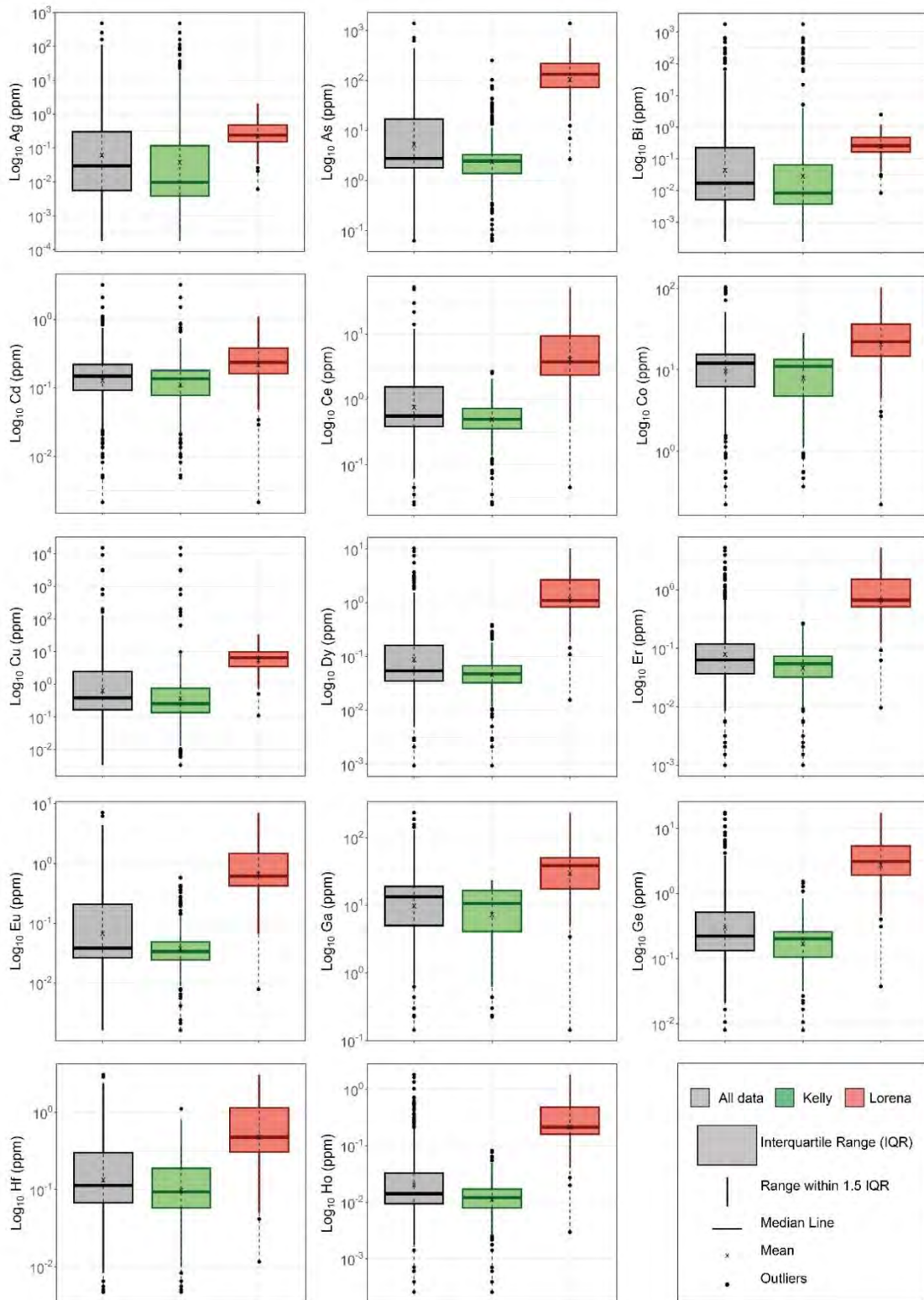
Spot (ppm)	TAU-23-3 052	TAU-23-3 053	TAU-23-3 054	TAU-23-3 055	TAU-23-3 056	TAU-23-3 057	TAU-23-3 058	TAU-23-3 059	TAU-23-3 060	TAU-23-3 061
Al	b.d.l.	b.d.l.	b.d.l.	2.59	143	b.d.l.	36.71	2.26	b.d.l.	b.d.l.
P	267	319	113	291	1737	310	572	135	183	155
Ti	9.1	5.04	7.24	8.06	37.4	3.04	10.4	4.72	5.48	5.74
Y	2698	1518	303	985	2062	714	960	1686	1781	2448
Nb	10.8	4.28	0.47	0.87	2.49	2.50	2.14	1.19	3.09	2.15
La	b.d.l.	b.d.l.	b.d.l.	b.d.l.	3.60	b.d.l.	0.53	b.d.l.	b.d.l.	0.09
Ce	86.7	40.5	4.81	8.44	17.1	9.50	10.7	21.9	44.1	41.5
Pr	0.44	0.21	0.02	0.21	1.99	0.10	0.33	0.48	0.48	0.66
Nd	7.21	3.79	0.29	2.89	11.6	1.57	2.61	7.65	8.27	10.1
Sm	14.8	8.12	0.74	5.60	8.29	4.00	4.26	15.1	17.2	18.5
Eu	6.86	3.82	0.07	0.54	0.70	0.37	0.49	6.67	7.35	9.24
Gd	78.6	42.4	4.79	24.6	37.6	19.4	21.9	67.4	72.5	77.2
Tb	22.9	12.0	1.89	7.83	13.5	5.96	7.27	17.8	18.9	22.3
Dy	254	136	23.3	91.5	167	69.4	87.9	179	191	240
Ho	87.2	50.2	9.9	33.9	63.6	25.0	32.9	56.4	60.4	82.2
Er	385	238	49.1	158	302	115	147	231	250	359
Tm	77.0	50.0	11.1	33.1	60.0	22.1	28.5	44.6	47.9	72.6
Yb	673	465	105	293	483	193	237	377	403	619
Lu	125	93.8	20.9	59.5	91.6	37.0	45.0	70.2	75.6	119
Hf	8575	8479	12202	9593	10280	10458	10557	8018	8418	7950
Ta	3.12	1.93	0.28	0.67	1.04	1.08	0.86	0.70	1.32	0.91
Pb	2.77	1.26	2.74	9.66	12.92	9.55	11.77	0.74	1.39	1.05
Th	1249	532	30.4	102	122	107	122	322	605	440
U	952	628	79.6	206	347	299	342	314	491	338

Spot (ppm)	TAU-23-3_062	TAU-23-3_063	TAU-23-3_064	TAU-23-3_065	TAU-23-3_066	TAU-23-3_067	TAU-23-3_068	TAU-23-3_069
Al	b.d.l.	1298	b.d.l.	2.89	3.45	b.d.l.	2.52	b.d.l.
P	192	211	168	338	363	163	194	226
Ti	5.41	19.8	6.03	3.87	3.87	5.39	5.53	6.58
Y	2855	1748	2250	2587	2811	2129	2517	1302
Nb	2.61	15.2	3.55	3.14	3.57	1.97	2.46	4.07
La	0.05	0.75	0.07	0.07	0.08	0.07	0.07	b.d.l.
Ce	49.8	95.7	51.9	8.12	10.3	34.3	37.7	52.3
Pr	0.71	0.28	0.38	0.76	1.04	0.61	0.68	0.25
Nd	12.0	3.29	6.51	11.6	15.3	11.1	11.9	3.77
Sm	21.3	6.92	12.8	20.6	23.9	20.8	24.0	8.06
Eu	10.9	2.94	6.53	3.84	4.23	9.21	10.4	3.73
Gd	91.0	41.0	64.8	85.7	96.0	89.5	101	43.3
Tb	26.1	13.6	19.3	24.1	26.4	23.2	26.4	12.6
Dy	285	163	217	255	276	229	266	135
Ho	96.1	58.3	75.8	86.2	93.7	71.7	82.2	44.7
Er	422	272	338	379	405	286	334	190
Tm	83.8	58.0	67.9	76.5	80.5	55.2	64.3	36.2
Yb	708	511	576	654	692	458	539	309
Lu	137	96.4	108	124	131	83.8	101	56.8
Hf	7909	11911	8606	8494	8612	7972	8127	8345
Ta	1.00	5.73	1.37	1.15	1.23	0.79	1.00	1.62
Pb	1.20	4.93	1.68	1.09	1.41	1.24	1.21	1.77
Th	539	1575	690	504	593	458	540	769
U	394	1321	467	604	669	384	471	580

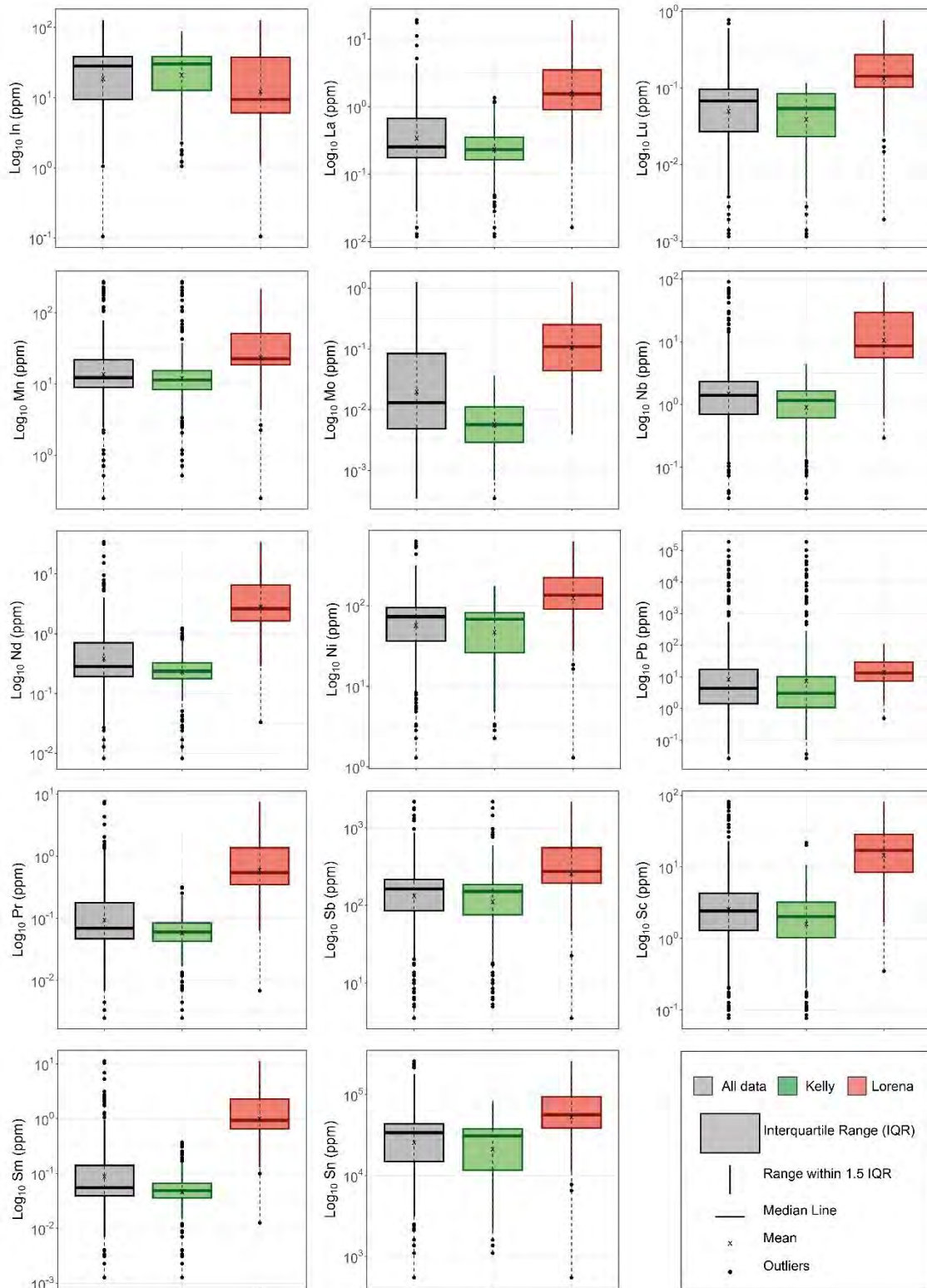


APPENDIX J

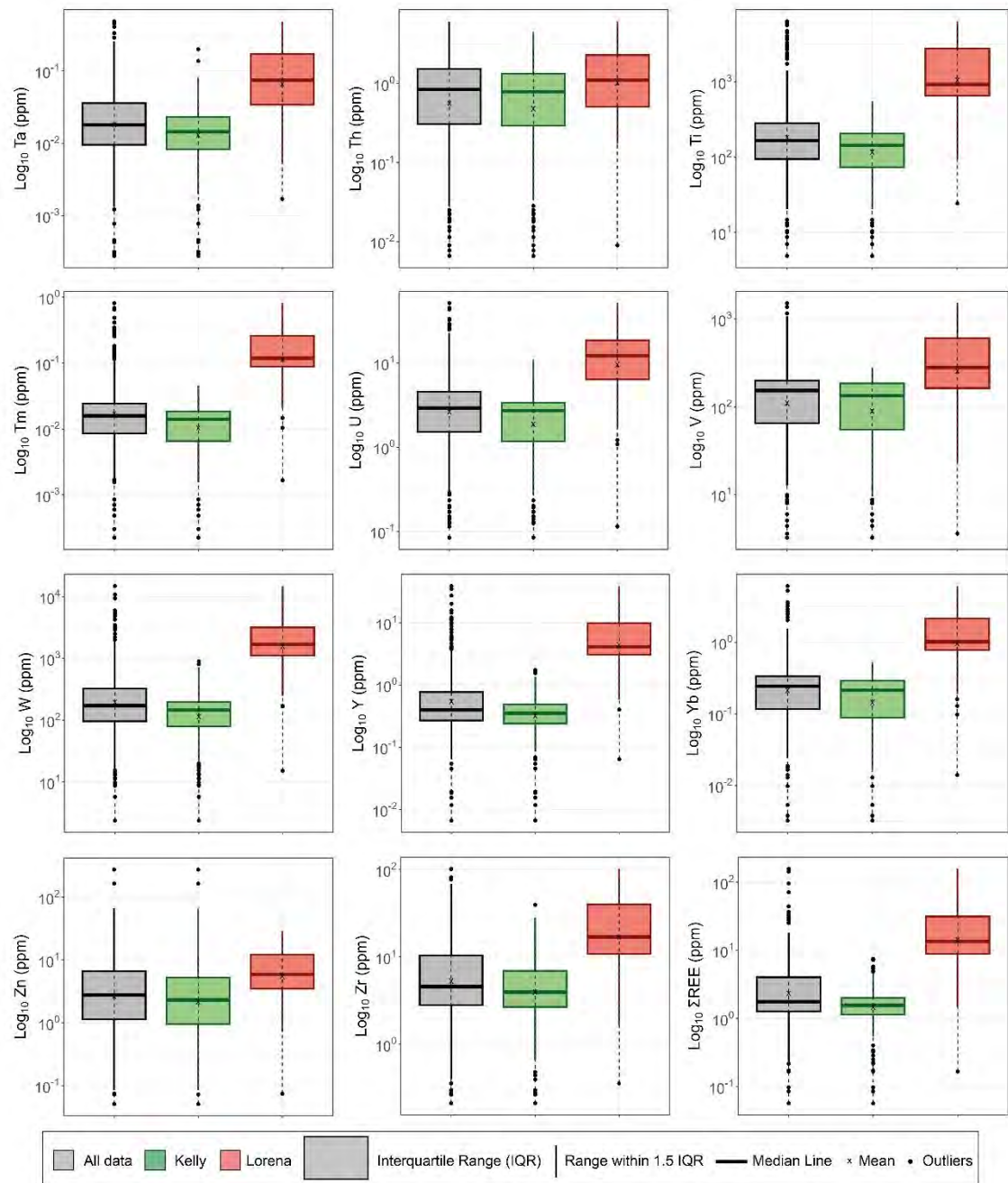
Boxplots of cassiterite trace element contents



Box plots showing element contents in cassiterite from Taucane (LA-ICP-SF-MS data)



Box plots showing element contents in cassiterite from Taucane (LA-ICP-SF-MS data)

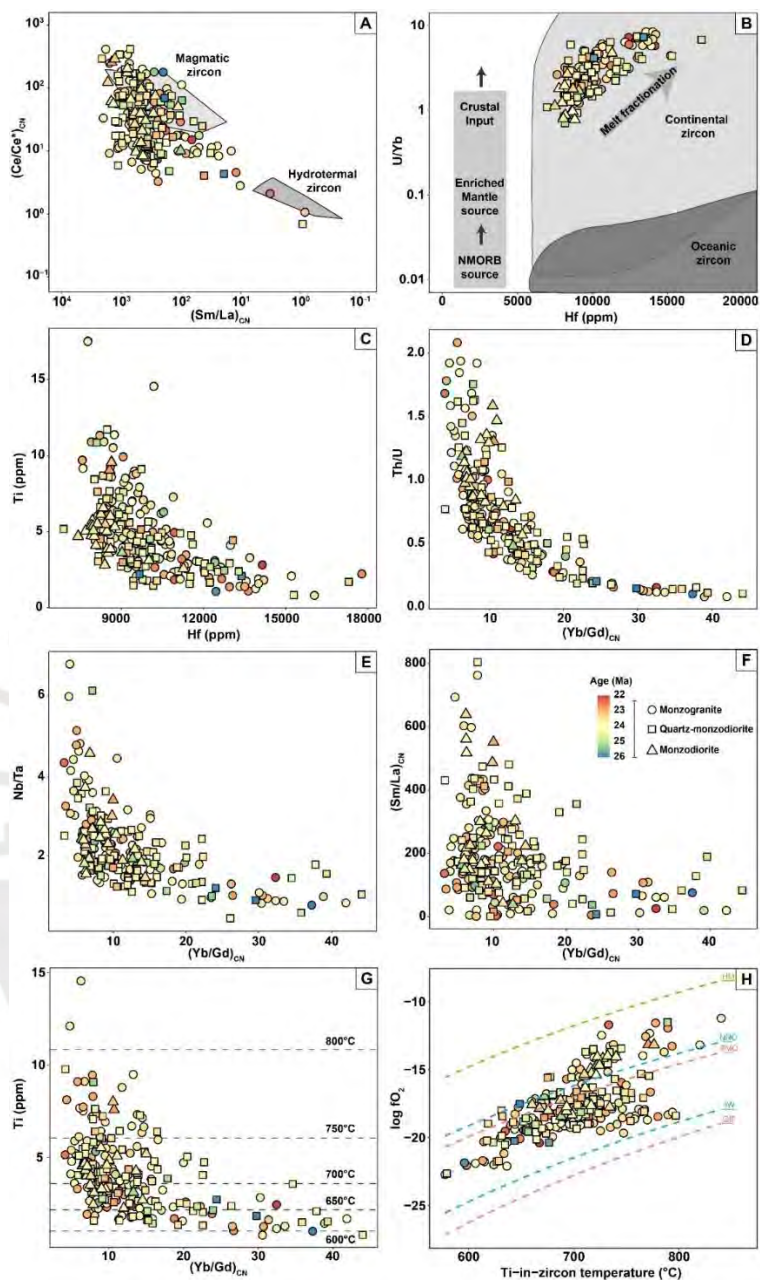


Box plots showing element contents in cassiterite from Taucane (LA-ICP-SF-MS data). The values for Gd and Tb were not included in the Σ REE since they are affected by polyatomic interference from tin oxides (see Yang et al. 2024)



APPENDIX K

**Binary diagrams of zircon trace
element contents**



Binary diagrams of trace elements and derived parameters for zircon grains from Taucane. (A) $(\text{Sm/La})_{\text{CN}}$ vs $(\text{Ce/Ce}^*)_{\text{CN}}$, with compositional fields after Hoskin (2005); (B) Hf vs U/Yb , with compositional fields after Grimes et al. (2015); (C) Hf vs Ti ; (D) $(\text{Yb/Gd})_{\text{CN}}$ vs Th/U ; (E) $(\text{Yb/Gd})_{\text{CN}}$ vs Nb/Ta ; (F) $(\text{Yb/Gd})_{\text{CN}}$ vs $(\text{Sm/La})_{\text{CN}}$; (G) $(\text{Yb/Gd})_{\text{CN}}$ vs $\text{Ti-in-zircon temperature}$; (H) $\text{Ti-in-zircon temperature}$ vs $\log f\text{O}_2$ with buffers calculated according to Frost (1991). $(\text{Ce/Ce}^*)_{\text{CN}}$, $(\text{Sm/La})_{\text{CN}}$, and $(\text{Yb/Gd})_{\text{CN}}$ values are normalized to chondrite $C1$ values of McDonough and Sun (1995). Temperatures are calculated following using the Ti-in-zircon thermometer of Ferry and Watson (2007). Abbreviations: FMQ–Fayalite-Magnetite-Quartz; HM–Hematite-Magnetite; IW–Iron-Wustite; NNO–Nickel-Nickel Oxide; QIF–Quartz-Iron-Fayalite